

WASM: Minerals, Energy, and Chemical Engineering

**Multi-scale Hydrodynamics of Multiphase Flow in
Vapour-Liquid Separation Processes**

Muhammad Dary Mahadika Priyambodo

0000-0001-8904-0137

**This thesis is presented for the Degree of
Doctor of Philosophy
of
Curtin University**

August 2023

Declaration

To the best of my knowledge and belief, this thesis contains no material previously published by any other person except where due acknowledgement has been made.

This thesis contains no material which has been accepted for the award of any degree or diploma in any university.

Signature:

Date: 18th of August 2023

Muhammad Dary Mahadika Priyambodo

Copyright

I warrant that I have obtained, where necessary, permission from the copyright owners to use any third-party copyright material reproduced in the thesis (e.g. questioners, artwork, unpublished letters), or to use any of my own published work (e.g. journal articles) in which the copyright is held by another party (publisher, co-author).

Signature:

Date: 18th of August 2023

Muhammad Dary Mahadika Priyambodo

Acknowledgement

The completion of my PhD study would not be possible without the support of many supportive and encouraging people around me.

First and foremost, I would like to express my sincere gratitude to my supervisor and my mentor, Associate Professor Tejas Bhatelia, with whom I had the pleasure to work with since my undergraduate research project in 2018. Over the years, his patience, guidance, motivation, knowledge, and the opportunities that has been given to me has helped me to become a better researcher.

I would also like to thank my supervisory team that includes my principal supervisor, Professor Vishnu Pareek, and co-supervisors, Dr. Milinkumar Shah and Dr. Biao Sun. It is honour and privilege to work together with them in the Process Intensification & Innovation Group.

I have also been fortunate to work in collaboration with Dr. Jim Patel and Dr. Maciej Mazur. They both have helped me in publishing two journal articles together.

Additionally, my sincere appreciation to all colleagues and faculty member in the WA School of Mines: Minerals, Energy & Chemical Engineering. It has been a great pleasure knowing and working together with all of you, which I cannot mention one by one.

I would also like to thank Curtin University and the Australian Research Council (ARC) for the given financial support towards the candidature of my PhD through the Curtin International Postgraduate Research Scholarship (CIPRS) program and the Research Stipend Scholarship program. (Project Number: LP160101181).

Last but not least, this thesis is dedicated to both my parents, who have sacrificed so much for my success and my sister, for her encouragement and support. They have been there along the way, through the good and bad times, and I look forward in sharing more success stories with them for many years to come.

Abstract

Due to stringent environmental regulations and increasing economic pressure, the interest in research and development of novel equipment used in the chemical and processing industry has increased by applying process intensification principles that rely on understanding the governing physiochemical phenomena of a given unit operation. Vapour-liquid separation is one of the key functions for unit operations in the chemical and processing industries that are typically carried out in a vapour-liquid separator (two-phase system). The objective of this thesis was to understand the hydrodynamics of the key components (inlet diverter and mist eliminator) at micro- and mili-scale, which is important in improving the overall efficiency of a vapour-liquid separator. A detailed multi-scale framework was developed that involves multiple numerical, experimental, and analytical research studies.

A vertical vapour-liquid separator typically features two key components with different governing physical phenomena to separate the vapour and liquid phases: An inlet diverter and a wire mesh pad. The first component, the inlet diverter, utilises baffles to promote equal fluid flow distribution inside the vessel. An inlet diverter is expected to enhance the separation efficiency of the mesh pad by maximising the contact area between the mesh pad and the feed and avoid local flooding or oversaturation in some regions of the mesh pad. In this thesis, the performance of an existing inlet diverter, the Schoepentoeter, was numerically investigated using CFD. It was found that the Schoepentoeter does not promote equal fluid flow distribution of the inlet feed. Consequently, a novel inlet diverter named the fractal flow mixer was proposed. The fractal flow mixer was designed using the concept of self-similar bifurcating channels and combines the function of a flow distributor and a mixer into a single device. The device has two inlets recursively bifurcated over four stages resulting in 16 outlet channels per pathway. The outlets from each of the two pathways are then combined to mix the two fluid streams. Initially, the hydrodynamic performance of the fractal flow mixer was numerically investigated by conducting CFD simulations (single-phase flow) with two gases of air and methane. The effect of Reynolds number and inlet flow ratio was investigated. uniform flow distribution was achieved with a maximum relative standard deviation of 8% (air-air).

The study was extended by investigating the hydrodynamics of a gas-liquid flow passing through the fractal flow mixer and the feasibility of producing Taylor flow within its microchannels. Experiments were conducted for a range of liquid-to-gas superficial velocity ratios (V_{SL}/V_{SG}). High-speed imaging was used to quantify the flow regimes inside the microchannels of the device. Four distinctive flow regimes were identified. As a result, a flow regime map was developed. Furthermore, an optical probe was used to measure the bubble

mean size and velocity. It was concluded that the fractal flow mixer was able to generate equal flow distribution across the 16 outlets and maintain a Taylor flow over a range of V_{SL}/V_{SG} . However, the bubble size varies to a certain extent, depending on the V_{SL}/V_{SG} that are governed by the capillary effect and the back-pressure. The result from these two studies shows the potential of the fractal flow mixer to be used as an inlet diverter at a larger scale, enhancing the separation efficiency of the mesh pad.

The second component of the vapour-liquid separator investigated in this thesis was the knitted mesh pad, which captures the entrained liquid droplets from the gas or vapour stream using metal or plastic wires. The fundamental understanding of the hydrodynamic phenomena and numerical representation of the droplet impact on a thin wire is critical for predicting the parameters that govern the capture of droplets. Predicting the maximum impact velocity that results in the droplet being captured on a horizontal, stationary wire ($V_{t,max}$) has previously been based on the solution of the force balance equation over an impacting droplet. However, these correlations were often based on varying simplifications, particularly in using a constant value of drag coefficient (C_d) in calculating the drag force in the force balance equations. The result of such simplifications has contributed to the discrepancy between predictions and experimental data, ranging from 15 to 40%. In this thesis, a new analytical model with a correlation was developed to predict the C_d as a function of fundamental physical properties of the fluid (the ratio of viscosities) and operating parameters (the ratio of diameters).

Droplet capture experiments with different wire materials and wire and droplet sizes were also carried out. High-speed imaging was used to measure the $V_{t,max}$. Results from the experiment were used to estimate the parameters in the newly developed correlation for the variable C_d using a hybrid genetic algorithm (GA) and the Levenberg-Marquadt algorithm (LMA) method. The new model was tested for a wide range of experimental data and was able to predict the experimental data more accurately than previously reported predictions. The model was also used to investigate the effect of wire size and fluid properties on the $V_{t,max}$. The model can be further improved by considering surface tension between different fluid properties of a droplet and different material properties of a wire in the empirical correlation to calculate the variable C_d . The empirical database of droplet capture can also be expanded using different wire materials and sizes and droplets with different fluid properties.

At macro-scale, a novel vapour-liquid separator design was proposed with a dual mesh configuration. In comparison to a single mesh pad configuration, an average of 26% recovery in performance can be achieved at industrially relevant conditions ($V_{in} = 11.03$ m/s) with a dual mesh pad configuration.

Publications by the Author

Journal publications:

- M.D.M. Priyambodo, M. Mazur, J. Patel, M. Shah, B. Sun, V. Pareek, M. Brandt, P.A. Webley, and T. Bhatelia, “Numerical evaluation of an additively manufactured uniform fractal flow mixer” *Chemical Engineering and Processing – Process Intensification*, vol. 179, p. 109047, 2022/09/01 2022, doi: <https://doi.org/10.1016/j.cep.2022.109047>.
- M.D.M. Priyambodo, M.T. Shah, T. Bhatelia, B. Sun, V. Pareek, “Analytical Model for Droplet Capture on a Thin Wire” *Industrial & Engineering Chemistry Research*, vol. 61, no. 51, pp. 18914-18927, 2022/12/28 2022, doi: <https://doi.org/10.1021/acs.iecr.2c03606>.
- M.D.M. Priyambodo, T. Bhatelia, M. Shah, J. Patel, M. Mazur, V. Pareek, “Gas-liquid hydrodynamics in a fractal flow mixer”, vol. 193, p. 109558, 2023/09/23, doi: <https://doi.org/10.1016/j.cep.2023.109558>

Conference publications:

- M.D.M. Priyambodo, B. Sun, T. Bhatelia, R. Utikar, V. Pareek, and G. Byfield, “CFD Simulations of Vapour-Liquid Separator in LNG Process” *Chemeca 2019: Chemical Engineering Megatrends and Elements*, Sydney, NSW, 2019. [Online]. Available: <https://search.informit.org/doi/10.3316/informit.700549525211132>.

Conference posters and presentations:

- M.D.M. Priyambodo, T. Bhatelia, B. Sun, M. Shah, and V. Pareek, “Effect of Wire Shape and Size in Droplet Impact on a Wire”, *Chemeca 2021: Advance, Disrupt, and Sustain*, Brisbane, Australia, 27th – 28th September 2021. (Online oral presentation)
- M.D.M. Priyambodo, T. Bhatelia, B. Sun, M. Shah, and V. Pareek, “Effect of Wire Shape and Size in Vapour-Liquid Separation”, *26th International Symposium on Chemical Reaction Engineering (ISCRE 26) and 9th Asia-Pacific Chemical Reaction Engineering Symposium (APCRE 9)*, New Delhi, India, 5th – 8th December 2021. (Online poster presentation)
- M.D.M. Priyambodo, A.P. Rao, T. Bhatelia, M. Mazur, J. Patel, and M. Shah, “Effect of mixing ratio on fractal flow mixer” *Chemeca 2022: Greener, Safer, Cleaner Chemical Engineering for the Next Century*, Melbourne, Australia, 25th – 27th September 2022 (Poster presentation + 3 minutes pitch)

Table of Contents

Declaration	i
Copyright	ii
Acknowledgement	iii
Abstract	iv
Publications by the Author	vi
Table of Contents	vii
List of Figures	ix
List of Tables	xii
Nomenclature	xiii
Chapter 1 Introduction	1
1.1. Gas/Liquid Separation Technologies in a Vapour-Liquid Separator	2
1.1.1. Inlet Diverter.....	2
1.1.2. Mist Eliminator.....	3
1.2. Multiphase Hydrodynamics in Vapour-Liquid Separator	4
1.3. Research Methodology.....	6
1.4. Research Objectives	7
1.5. Significance and Contributions of the Thesis.....	8
1.6. Thesis Outline and Organisation	0
Chapter 2 Hydrodynamics of Droplet Capture on Thin Wires	2
Abstract.....	2
Graphical Abstract.....	3
2.1. Introduction.....	3
2.2. Analytical Models to Calculate $V_{t,max}$	10
2.3. Improved Analytical Model to Calculate $V_{t,max}$	13
2.4. Contact Angle Measurement.....	14
2.5. Droplet Capture Experiment	17
2.6. Optimisation Methodology and Model Validation.....	20
2.7. Results and Discussion.....	22
2.7.1. Comparison of Analytical Models	22
2.7.2. Effect of Wire Size and Fluid Properties on $V_{t,max}$	25
2.8. Effect of Wire Shapes and Sizes (Numerical Simulation)	28
2.9. Conclusion	32
Chapter 3 Gas-gas Hydrodynamics of a Fractal Flow Mixer	34
Abstract.....	34
Graphical Abstract.....	35
3.1. Introduction.....	35
3.2. Methodology	38
3.2.1. Fractal Flow Distributor and Mixer Design	38
3.2.2. CFD Model	41
3.3. Results and Discussion.....	45
3.3.1. Manufacture.....	45

3.3.2.	Effect of Inlet Reynolds Number.....	47
3.3.3.	Effect of Inlet Flow Ratio (IFR)	54
3.4.	Conclusions.....	61
Chapter 4	Gas-liquid Hydrodynamics of a Fractal Flow Mixer	63
	Abstract.....	63
	Graphical Abstract.....	64
4.1.	Introduction.....	64
4.2.	Experimental	71
4.3.	Results and Discussion.....	74
4.3.1.	Flow Regimes	74
4.3.2.	Bubble Hydrodynamics	80
4.4.	Conclusions.....	88
Chapter 5	CFD Simulations of Vapour-Liquid Separator	90
	Abstract.....	90
5.1.	Introduction.....	91
5.2.	CFD Model	93
5.3.	Mesh Pad Modelling Methodology and Validation	95
5.4.	Results and Discussion.....	96
5.4.1.	Inlet Diverter.....	96
5.4.2.	Mesh Pad	98
5.4.2.1.	Single Mesh Pad with Inlet Diverter: Baseline Case Study	98
5.4.2.2.	Effect of Height and Opening.....	99
5.4.2.3.	3D Simulation of Dual Mesh-pad Configuration.....	101
5.5.	Conclusions.....	102
Chapter 6	Conclusions and Recommendations	103
6.1.	Conclusions.....	103
6.2.	Challenges and Recommendations.....	107
References	109
Appendices	117
	APPENDIX A: Experiment Study on Additively Manufactured Mesh Pads	117
	APPENDIX B: Copyrights.....	120
	APPENDIX C: Attribution of Authorship Statement.....	123

List of Figures

Figure 1: Schematic diagram of a (a) Vertical Vapour-Liquid Separator and a (b) Horizontal Vapour-Liquid Separator.....	1
Figure 2: (a) Different designs of inlet diverters (Bothamley, 2015) and the (b) Schoepentoeter, an example of a vane-type inlet diverter (Sulzer, 2023b)	2
Figure 3: Different types of mist eliminators (a) knitted mesh pad (Sulzer, 2023a), (b) vane-type (Sulzer, 2022), and (c) axial cyclone (Sulzer, 2022)	4
Figure 4: Diagram of the research methodology in this thesis	7
Figure 5: Flow diagram of thesis outline	0
Figure 6: Schematic diagram of a droplet impacting a wire (■ – wire, ● – droplet, ■ – intersection between wire and droplet); (a) The position of droplet just at the time of impact ($t = 0$); (b) a wire piercing the droplet; (c) the position of droplet when it is captured on the wire (time = $t + \Delta t$)	10
Figure 7: (a) Schematic diagram of experiment setup (b) Actual experiment setup.....	15
Figure 8: Images of contact angles of water droplets on Copper contact surface.....	15
Figure 9: Images of contact angles of water droplets on Stainless Steel contact surface	15
Figure 10: Images of contact angles of water droplets on Aluminium contact surface	16
Figure 11: Images of contact angles of water droplets on Tin contact surface.....	16
Figure 12: Images of contact angles of water droplets on a Brass contact surfaces	16
Figure 13: Schematic diagram of droplet impact experiment setup	18
Figure 14: Outcome of droplet impact on copper wire ($R_f/R_d = 0.53$): Captured ($R_f = 0.40$ mm; $V_1 = 0.490$ m/s)	18
Figure 15: Outcome of droplet impact on copper wire ($R_f/R_d = 0.53$) (a) Captured ($R_f = 0.40$ mm; $V_1 = 0.490$ m/s) and (b) Not Captured ($R_f = 0.40$ mm; $V_1 = 0.518$ m/s)	19
Figure 16: $V_{t,max}$ of droplet impact on a thin copper and stainless-steel wire at different values of R_f/R_d and R_f	20
Figure 17: Comparison of $V_{t,max}$ values between the predictions from the proposed analytical model (Eq. 2) with the experiment data for copper and stainless-steel wire	21
Figure 18: (a) Comparison of analytical model predictions ($R_f = 0.000350$ m), and (b) comparison of drag and surface contact force on the droplet under captured condition from different analytical model ($R_f = 0.000350$ m, $R_d = 0.00129$ m, Lorenceau et al. – Eq. T2 - 2, Safavi and Nourazar – Eq. T2 - 13, and Kim and Kim – Eq. T2 - 8).....	23
Figure 19: (a) Comparison of model predictions and experimental data of Lorenceau et al. (Lorenceau et al., 2004) (● – Lorenceau model Eq. T2 – 2, ○ – Safavi and Nourazar model, ● – Kim and Kim model), and (b) average error in predictions of Lorenceau et al.’s experimental data from different analytical models	24
Figure 20: Predictions of $V_{t,max}$ from the proposed model against different experimental data sets (Lorenceau et al., 2004), (Kim & Kim, 2016), (Safavi & Nourazar, 2019), and (Khalili et al., 2016).....	25
Figure 21: Predictions of (a) $V_{t,max}$, (b) drag coefficient, (c) drag force at different wire size and ratio of diameters (R_f/R_d) with water as the droplet (secondary phase); (d) Predictions of $V_{t,max}$ at different wire size and droplet size with water as the droplet (secondary phase).....	27
Figure 22: Predictions of (a) $V_{t,max}$ with different fluid properties of the droplet; (b) C_d at different ratio of diameters (R_f/R_d) with different fluid properties of the droplet.....	28
Figure 23: 2D Flow domain of droplet impact on a thin wire	29
Figure 24: Qualitative comparison of the droplet impact outcome for (a) Numerical simulation result (Present study) (b) Numerical simulation result (Zheng et al., 2018) (c) Experiment high-speed imaging result (Kim & Kim, 2016).....	30
Figure 25: Prediction of $V_{t,max}$ for different wire shapes at different ratios of diameter (wire-to-droplet): (a) Square; (b) Triangle; (c) Circle; (d) Inverted Triangle	31
Figure 26: Fractal flow distributor and associated parameters (a) Single bifurcation unit (b) Single bifurcation unit including wall thickness parameters (c) Section view of single channel path parameters (d) N=4 stage embodiment. Fractal self-similar unit of repeating detail comprising of j and $j + 1$ units (shaded) identified by “H” shaped lines on the projected two-dimensional unit connectivity schematic (from (Mazur et al., 2019))	40
Figure 27: Fractal flow distributor design with two independent channel pathways (a) Nesting arrangement of two channel pathways and associated pathway and device axes of symmetry (b) Single channel pathway indicating arrangement of inclined transition plane and outlet plane	41
Figure 28: (a) Flow domain of the fractal flow mixer; (b) Detail of tetrahedral mesh of the flow domain; (c) Top view of the flow domain with number labels (ID) on each outlet	42
Figure 29: Additively manufactured flow distributor and mixer devices: (a) 4-stage polymer device manufactured (b) 4-stage metal device (c) 6-stage metal device.....	47
Figure 30: RSD [%] of cross-sectional averaged species mass fraction at all 16 outlets at varying Inlet Re (Inlet ratio = 1)	49

Figure 31: Distribution index (DI) of species mass fraction within each outlet against different Inlet Re (Inlet ratio = 1) for (a) Air and air mixture (b) Air and methane mixture	49
Figure 32: Average pressure drop between all inlets and outlets at varying Inlet Re.....	50
Figure 33: Species mass fraction contour (from module-B) of each outlet at different inlet Re (IFR = 1) for (a) Re = 10 (b) Re = 100 (c) Re = 10000 (d) Re = 1000.....	50
Figure 34: The RSD [%] of local cell values of species mass fraction (from module-B) within each outlet at different Inlet Re (IFR = 1) for (a) Re = 10 (b) Re = 100 (c) Re = 1000 (d) Re = 10000.....	51
Figure 35: The RSD [%] of local cell values of velocity within each outlet (Air-Air and Air-Methane) at different Inlet Re (IFR = 1) for (a) Re = 10 (b) Re = 100 (c) Re = 1000 (d) Re = 10000	52
Figure 36: Species mass fraction contour (air from module-B) of all 16 channels at different Reynolds number; (a) Re = 10 (b) Re = 100 (c) Re = 10000 (d) Re = 10000.....	53
Figure 37: RSD [%] of cross-sectional averaged species mass fraction (from module-B) at all outlets at different IFR (Air and Air Mixture).....	55
Figure 38: Distribution index (DI) of species mass fraction within each outlet at different IFR (a) Re at module-A = 100 (b) Re at module-A = 1000 (c) Re at module-A = 10000.....	56
Figure 39: Average pressure drop between all inlets and outlets at varying IFR (Air and air mixture)	56
Figure 40: (a) Pressure drop comparison at a high IFR (b) velocity vector at an IFR of 0.01 (c) velocity vector at an IFR of 100.....	57
Figure 41: Species mass fraction contour (air from module-B) of each outlet at an IFR of 0.1; (a) Inlet Re at module-A = 100 (b) Inlet Re at module-A = 1000	58
Figure 42: Species mass fraction contour (air from module-B) of all 16 channels at an IFR of 0.1; (a) Inlet Re at module-A = 100 (b) Inlet Re at module-A = 1000	59
Figure 43: Species mass fraction contour (air from module-B) of each outlet at an IFR of 10; (a) Inlet Re at module-A = 1000 (b) Inlet Re at module-A = 10000	59
Figure 44: Species mass fraction contour (air from module-B) of all 16 channels at an IFR of 0.1; (a) Inlet Re at module-A = 100 (b) Inlet Re at module-A = 1000	60
Figure 45: The RSD [%] of local cell values of velocity within each outlet at different inlet ratio for (a) Re at module-A = 100 (b) Re at module-A = 1000 (c) Re at module-A = 10000.....	60
Figure 46: The RSD [%] of local cell values of species mass fraction (from module-B) within each outlet at different inlet ratio for (a) Re at module-A = 100 (b) Re at module-A = 1000 (c) Re at module-A = 10000	61
Figure 47: (a) The additively manufactured fractal flow mixer, (b) its geometrical parameters, and the (c) Outlet ID.....	71
Figure 48: Schematic diagram of experiment setup [A] LED Light [B] Light stand [C] Lead Screw [D] Optical probe [E] Fractal flow mixer [F] Metal stand [G] Water rotameter [H] Water inlet [I] Air mass flow controller [J] Air inlet [K] Water tank [L] Custom aluminium frame [M] Bypass valve [N] Camera tripod [O] High speed camera [P] Laptop 1 (for HSI) [Q] Optoelectronic module [R] Laptop 2 (For optical probe)	72
Figure 49: Regime map for a gas-liquid in a circular micro-channel ($d_i = 1.097$ mm) (Triplett et al. 1998) with dots representing tested flow conditions in the current study.....	73
Figure 50: Identified flow patterns from high-speed imaging experiments [a] Bubbly flow [b] Slug flow [c] Annular flow [d] Churn flow.....	78
Figure 51: High-speed imaging experiment results of flow pattern combinations in the front four tubes of the fractal flow mixer ($d = 1.00$ mm): (a) low flow, (b) low flow and slug flow, (c) low flow and bubbly flow, (d) low flow and annular flow, (e) slug flow, (f) slug and bubbly flow, (g) slug and annular flow, (h) slug and churn flow, (i) churn flow.....	79
Figure 52: Identified flow patterns in the outlet channels ($d_i = 1.000$ mm) of the fractal flow device plotted against the flow regime map by Triplett et al. 1999 (Triplett et al., 1999) for a single circular channel ($d_i = 1.097$ mm). The solid black lines correspond to flow regime transition lines by Triplett et al. 1999 (Triplett et al., 1999) and the dashed and solid blue lines correspond to flow regime transition lines from this study.....	80
Figure 53: Averaged (a) bubble mean size and (b) bubble mean velocity across all 16 outlets combined against V_{SL} at different V_{SG}	81
Figure 54: RSD of bubble mean size across all 16 outlets for (a) $V_{SG} = 0.265$ m/s, (b) $V_{SG} = 0.531$ m/s, and (c) $V_{SG} = 0.796$ m/s.....	82
Figure 55: RSD of bubble mean velocity across all 16 outlets for (a) $V_{SG} = 0.265$ m/s, (b) $V_{SG} = 0.531$ m/s, and (c) $V_{SG} = 0.796$ m/s.....	82
Figure 56: Bubble mean size at each outlet for (a) $V_{SG} = 0.265$ m/s, (b) $V_{SG} = 0.531$ m/s, (c) $V_{SG} = 0.796$ m/s.....	83
Figure 57: High-speed imaging experiment results at different V_{SL}/V_{SG} : (a) $V_{SL}/V_{SG} = 1$; (b) $V_{SL}/V_{SG} = 1.5$; (c) $V_{SL}/V_{SG} = 2$	84
Figure 58: Averaged bubble mean velocity at each outlet for (a) $V_{SG} = 0.265$ m/s, (b) $V_{SG} = 0.531$ m/s, and (c) $V_{SG} = 0.796$ m/s.....	84
Figure 59: Bubble frequency at each outlet for (a) $V_{SG} = 0.265$ m/s (b) $V_{SG} = 0.531$ m/s (c) $V_{SG} = 0.796$ m/s..	86

Figure 60: Relative standard deviation of the bubble size at each outlet for (a) $V_{SG} = 0.265$ m/s, (b) $V_{SG} = 0.531$ m/s, and (c) $V_{SG} = 0.796$ m/s	87
Figure 61: Relative standard deviation of the bubble velocity at each outlet for (a) $V_{SG} = 0.265$ m/s, (b) $V_{SG} = 0.531$ m/s, and (c) $V_{SG} = 0.796$ m/s	88
Figure 62: CAD Model of Schoepentoeter	93
Figure 63: Fluid domain of a vapour-liquid separator with a Schoepentoeter and a single mesh pad configuration	93
Figure 64: Diagram of vapour-liquid separator with a dual mesh pad configuration in 2D	94
Figure 65: Fluid domain of a vapour-liquid separator with a Schoepentoeter and dual mesh pad configuration	94
Figure 66: Comparison of Literature Experimental Data against CFD Simulation Result.....	96
Figure 67: 3D Fluid Domain of Inlet Diverter with Location of Iso-surfaces and Velocity Contours	97
Figure 68: Velocity Contours at Various Inlet Velocities/Re Number	97
Figure 69: Fraction of Velocity above $V_{t,max}$ on the Mesh Pad Inlet against Various Inlet Velocity.....	99
Figure 70: Fraction of Velocity above $V_{t,max}$ against Various Distances between Mesh Pads ($v=0.46$ m/s; $Re=5.69 \times 10^6$).....	100
Figure 71: Fraction above $V_{t,max}$ on the Mesh Pad Inlet against Various Inlet Velocity (Dual Mesh Pad Configuration 3D Model)	101

List of Tables

Table 1: Previous studies on droplet impact and droplet detachment on a thin wire.....	8
Table 2: Published analytical model to calculate $V_{t,max}$	11
Table 3: Average contact angle values of water droplets on different contact surfaces	16
Table 4: Physical Property of Different Fluids at 20°C	27
Table 5: Geometric parameters for fractal flow mixer.....	42
Table 6: Governing equations, constitutive equations, and spatial discretization schemes used in the CFD model	43
Table 7: Simulated flow conditions	44
Table 8: Previous studies on multi-channel micro-structured device	68
Table 9: Variables of 2D Dual Mesh Pad Configuration Parametric Study	95
Table 10: Standard Deviation of Velocities at Different Heights of the Vessel	97
Table 11: Area-weighted Average Velocity at different Heights of the Fluid Domain	98

Nomenclature

Symbol or units	Definition
A_p	Projected area of the droplet normal to the wire upon impact [m ²]
a_1	Constant no. 1 in correlation for variable C_d
Bo	Bond number
b_1	Constant no. 2 in correlation for variable C_d
C_d	Drag coefficient
c_1	Constant no. 3 in correlation for variable C_d
C_{t_u}	u -axis linear offset of transition plane centreline
C_{t_v}	v -axis linear offset of transition plane centreline
d	Diameter [m]
d_i	Internal diameter [mm]
d_j	Channel diameter at stage j [m]
D_{j_i}	Inlet diameter of bifurcation unit j
D_{j_o}	Outlet diameter of bifurcation unit j
F_b	Buoyancy force [N]
F_d	Drag force [N]
F_s	Surface tension force [N]
g	Gravity acceleration [m/s ²]
G_B	gas bubbles dispersing from the outlet of the fractal flow mixer [μm]
G_S	Gas slugs inside the microchannels
H_j	Height of bifurcation unit j
H_t	Linear offset of transition plane from outlet plane
k	Constant for a given fibre/wire and liquid from Lorenceau et al. [1]
L	Length [m]
L_S	Liquid slugs inside the microchannels
L_x	X axis edge length for rectangular outlet channel array
L_y	Y axis edge length for rectangular outlet channel array
M	Mass of the droplet [kg]
\overline{M}_i	Mean velocity or species mass fraction (from module-B).
N	Total number of bifurcation stages
O	Number of channel outlets in a single channel pathway
p	Arc of a circle [m]
q	Mass fraction of a species in a combined flow from the two modules

R	Ratio of bifurcation unit inlet to outlet diameters
R_d	Droplet radius [m]
R_{Dj}	Bifurcation unit j inlet to outlet diameter ratio
Re	Reynold number
R_f	Wire radius [m]
R_M	Characteristic length of droplet or maximum threshold droplet radius that can be captured by a particular wire size [m]
RSD	Relative standard deviation [%]
s	Standard deviation
S_j	Spacing of bifurcation unit j
S^2	Variance of the real mixture
S_0^2	Variance of a totally unmixed system
t	Time [s]
T	Channel wall thickness of bifurcation unit j
U	Number of copies of a self-similar object
v	Velocity [m/s]
V_m	Characteristic velocity [m/s]
V_{SG}	Gas superficial velocity [m/s]
V_{SL}	Liquid superficial velocity [m/s]
$V_{t,max}$	Maximum impact velocity / threshold velocity [m/s]
We	Weber number
x_i	Cross-sectional averaged mass fraction of a species at a particular outlet
Z	Height [m]

Greek letter	Definition
α_j	Bifurcation deviation angle
ΔP	Pressure loss [Pa]
Δt	Elapsed time/time duration [s]
δ	Fractal dimension
μ_1	Viscosity of the primary phase [kg/(m·s)]
μ_3	Viscosity of the secondary phase [kg/(m·s)]
ρ_1	Density of the primary phase [kg/m ³]
ρ_2	Density of the wire medium/material [kg/m ³]
ρ_3	Density of the secondary phase [kg/m ³]
σ	Fractal scaling factor
θ	Bifurcation angle [degrees]
θ_a	Advancing contact angle [°]
θ_j	Centreline bifurcation angle
θ_r	Receding contact angle [°]
$\theta_{t_{xz}}$	Inclination angle of transition plane relative to plane XZ
$\theta_{t_{yz}}$	Inclination angle of transition plane relative to plane YZ

Term	Definition
AM	Additive Manufacturing
BMS	Bubble Mean Size [μm]
BMV	Bubble Mean Velocity [m/s]
CFD	Computational Fluid Dynamics
DI	Distribution Index
IFR	Inlet Flow Ratio
L-PBF	Laser Powder Bed Fusion
MI	Mixing Index
RSD	Relative Standard Deviation
SIMPLE	Semi-Implicit Method for Pressure-Linked Equation
VP	Vat Photo polymerisation
VLS	Vapour-liquid Separator

Chapter 1 Introduction

Increasing environmental and economic pressures on improving the efficiencies of the chemical and processing industry have sparked a renewed interest in developing novel equipment used in these processes. One common strategy is to develop intensified processing equipment with smaller footprints and higher through puts. However, the efficient use of process intensification principles solely relies on understanding the governing physiochemical phenomena of a given unit operation within the process. These unit operations perform a function that could be classified into four main categories: Heat transfer, mass transfer, separations, and pressure changes. The majority of these functions involve more than one phase (multiphase), which is required to be separated for further processing. Typically, this function is carried out in phase separators. Phase separators can be of several types depending on the number and types of phases they separate. However, the most common type of separators includes a vapour-liquid or liquid-liquid separator for a two-phase system or a vapour-liquid-liquid separator for a three-phase system. In some instances, vapour-liquid-solid separation is also performed but is hardly configured as a single-unit operation.

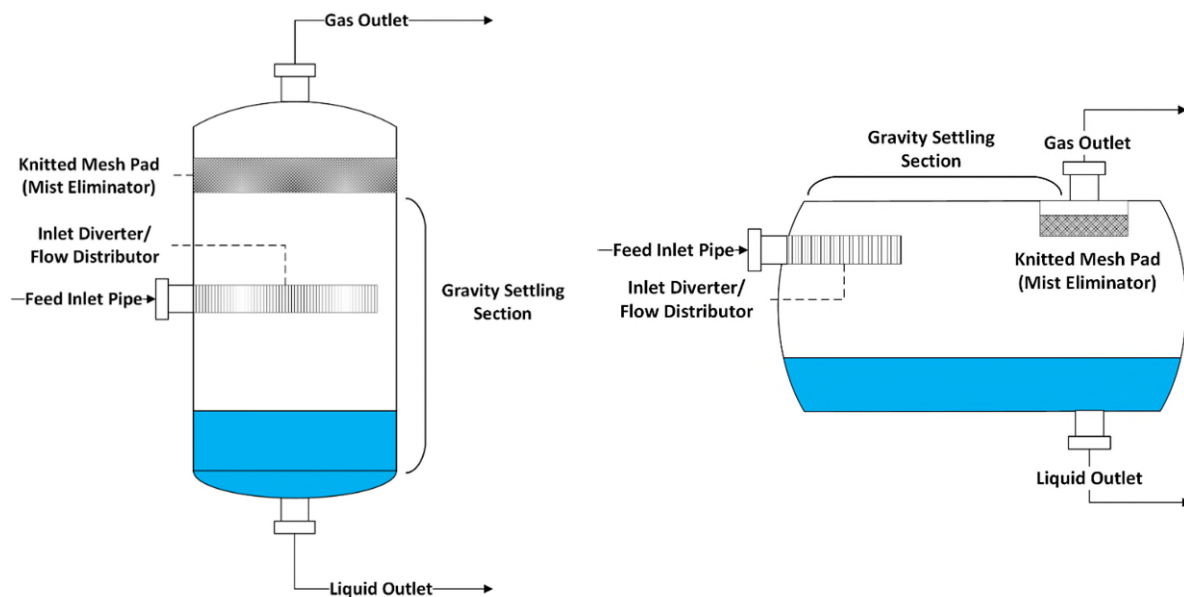


Figure 1: Schematic diagram of a (a) Vertical Vapour-Liquid Separator and a (b) Horizontal Vapour-Liquid Separator

A vapour-liquid separator (VLS) is a multiphase system where the interaction between the phases occurs at multiple scales (millimetre or metre scale). Depending on the application, there are different configurations of vapour-liquid separators. They can be designed as horizontal or vertical vessels with different internal components inside the vessel (Mokhatab et al., 2015; Stewart & Arnold, 2008). As shown in Figure 1, a typical VLS would consist of a feed pipe, an inlet diverter/flow distributor, a gravity-settling section, a mist eliminator, a gas outlet, and a liquid outlet.

1.1. Gas/Liquid Separation Technologies in a Vapour-Liquid Separator

1.1.1. Inlet Diverter

The first component of the VLS is the inlet flow distributor or diverter. It typically utilises baffles to firstly carry out the bulk separation of the two phases (gas and liquid) by gravity and secondly promote equal fluid flow distribution and controlled droplet size inside the vessel of the VLS. An inlet diverter is expected to enhance the separation efficiency of a mist eliminator (i.e. knitted mesh pad) by maximising the contact area between the inlet feed with the mesh pad and to avoid local flooding or oversaturation in some regions of the mesh pad. It is a critical component in a VLS because an ineffective fluid flow distributor and mixer can affect up to 20-25% of the efficiency of the process (Sinnott & Towler, 2019b). An inlet flow distributor can have a simple design, such as a diverter plate, a half-pipe design, and a dished-head design, or it can be in the form of complex designs, such as a vane-type or a cyclonic design (Bothamley, 2015).

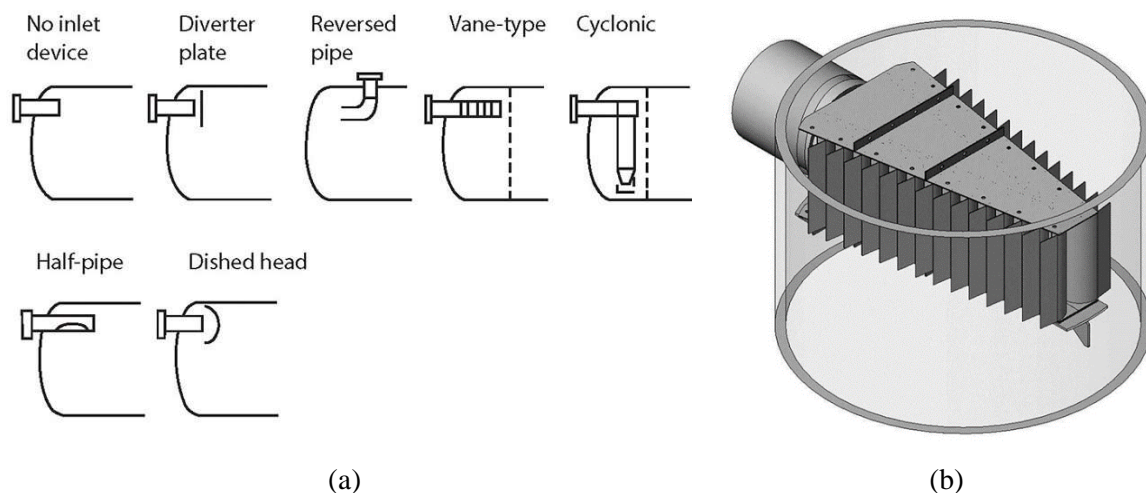


Figure 2: (a) Different designs of inlet diverters (Bothamley, 2015) and the (b) Schoepentoeter, an example of a vane-type inlet diverter (Sulzer, 2023b)

Different designs of inlet diverters are shown in Figure 2[a-b]. A baffle or plate design reduces the inertia of the inlet feed, inducing the liquid phase of the feed to fall with gravity. The baffles can be designed in many different ways (i.e. dished head, diverter plate, half-pipe, etc.) as long as the structural integrity of the inlet diverter is maintained to cope with the momentum of impact. A cyclonic inlet diverter utilises centrifugal to separate the two phases of the inlet feed. The cyclonic inlet diverter is limited by its sensitivity towards the inlet flow rate, where the separation efficiency is significantly reduced at lower and unstable inlet flow rates. A vane-type inlet diverter utilises an arrangement of multiple vanes/baffles to not only promote bulk separation of the two phases, but it is also utilised to enhance the equal fluid flow distribution inside the VLS vessel. As shown in Figure 2[b], a well-known example of a complex vane-type design is the Schoepentoeter, which consists of banks of swept vanes that are proportionally oriented and distributed to slice the mixed-phase feed into a series of flat jets (Sulzer, 2022)

After the inlet diverter, there is the gravity settling section of the VLS, where the separation between the two phases occurs from simply utilising the gravity force. Large and heavy liquid particles will settle at the bottom of the vessel, and the predominantly gas phase will rise to the top before being subjected to the mist eliminator. In the gravity settling section, droplets greater than 140 μm are removed to prevent overload on the mist eliminator.

1.1.2. Mist Eliminator

The second component of the VLS is the mist eliminator that is used to remove small droplets (<140 μm). There are different types of mist elimination devices, including knitted mesh pads, vane-type separators, and axial cyclone separators, as shown in Figure 3[a-c]. For the knitted mesh pad, as shown in Figure 3[a], according to (Stewart & Arnold, 2008), the knitted mesh pads consist of metals or plastic wires with a diameter of 0.10 – 0.28 mm that impinges and capture the entrained liquid droplets from the gas or vapour stream. The knitted mesh pad typically has a high void volume fraction (95-99%) and a high surface area. Different operating parameters govern the performance of the mesh pad at the macro-scale, including the mesh pad thickness, packing density, velocity of the feed, wire diameter, supporting grid, and construction material (El-Dessouky et al., 2000). A vane-type separator utilises banks of vanes that forces directional changes of the fluid flow, causing the flow to become laminar and impinges the droplets through inertial interception, eventually coalescing the droplets into forming a liquid film and draining through the liquid collection section (Koopman et al., 2014). Additionally, an axial cyclone separator separates the droplet by

centrifugal forces. As shown in Figure 3[c], the axial flow cyclone has swirl vanes near the bottom of the unit that induces the swirling flow where the liquid phase will exit via the drainage slit located on the wall of the unit, and the gas phase will exit through the top centre part of the unit. The axial cyclone separator has a very high separation efficiency but is very sensitive to small changes in the flow and requires a high flow rate to induce the centrifugal force required to separate the phases (Stewart & Arnold, 2008).

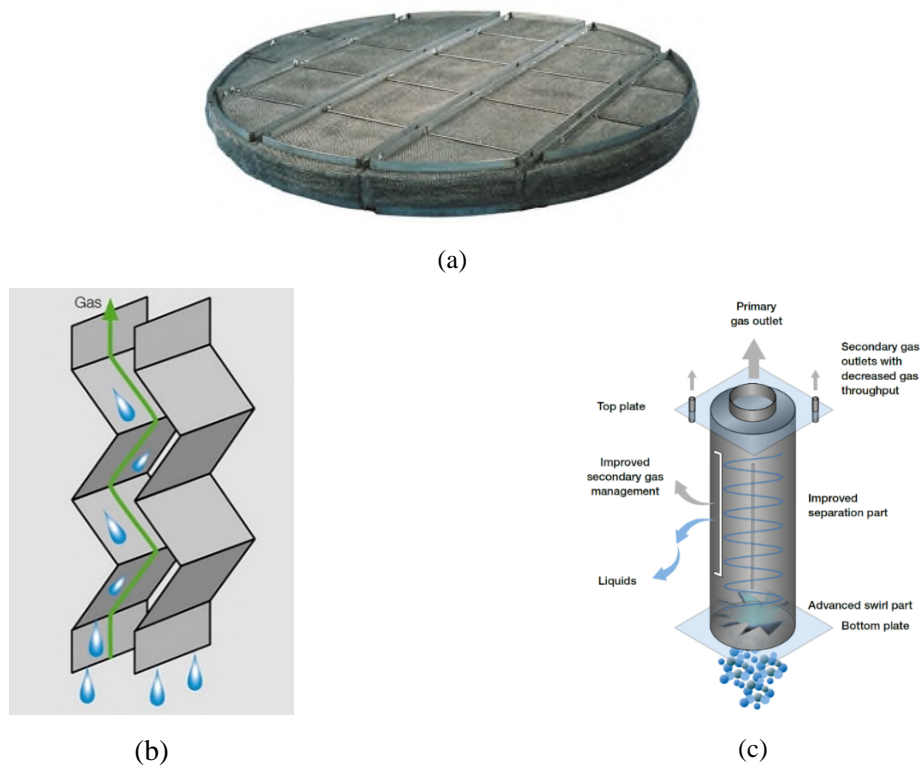


Figure 3: Different types of mist eliminators (a) knitted mesh pad (Sulzer, 2023a), (b) vane-type (Sulzer, 2022), and (c) axial cyclone (Sulzer, 2022)

Whilst these mist-eliminating devices vary in geometry and complexity, their role is to primarily agglomerate the small droplets of liquid that cannot be separated by gravity. Depending on the liquid droplet size distribution and the amount of liquid in the multiphase flow post-inlet diverter, different mist eliminators can be used in a single VLS vessel to achieve complete separation.

1.2. Multiphase Hydrodynamics in Vapour-Liquid Separator

The multiphase hydrodynamic characterisation for understanding the governing physics of separation has been a topic of research for both the inlet diverters and mist eliminators. However, the approach for characterising the inlet diverters have been contrasting

because the performance of the inlet diverters can be easily measured using experimental techniques but are very difficult to characterise due to the low spatial and temporal resolution of experimental techniques. Thus, researchers have tried to use numerical tools, including Computational Fluid Dynamics (CFD), to model these systems (Haghshenasfard et al., 2007; Pham et al., 2018; Rahimi & Abbaspour, 2008). However, these models have been limited to a single phase and only provide information about the continuous phase, limiting their ability to predict the separation efficiency of the dispersed phase.

On the other hand, understanding the governing hydrodynamics within the mist eliminator (i.e., the impact of droplets on solid surfaces) has been the subject of several numerical and experimental studies. However, a limited validity of the models to the experimental data can be found in the literature. In addition, researchers have focused on understanding the effect of different operating parameters and packing density, mesh pad thickness, the material of construction, vapour velocity, wire diameter, and supporting grids have been reported by many researchers (Al-Dughaiter et al., 2011; Al-Dughaiter et al., 2010; El-Dessouky et al., 2000; Kouhikamali et al., 2014; Rahimi & Abbaspour, 2008). These studies can be used to quantify the overall separation efficiencies. However, the fundamental understanding of the hydrodynamic phenomenon and the numerical representation of the droplet impact on a thin wire that governs the separation is still unclear.

The key property of a droplet that impacts a solid surface, such as a thin wire, and governs whether it dissipates all its kinetic energy and becomes stationary, is the maximum terminal velocity ($V_{t,max}$). In other words, if a droplet travels at or below $V_{t,max}$, its probability of becoming stationary at impact is 100%. The prediction of $V_{t,max}$ is based on the solution of the force balance equation over an impacting droplet with four forces acting upon a droplet when it travels downwards and impacts a wire. These forces include the gravity force, surface tension force, drag force, and buoyancy force. Previous studies have proposed/provided different models and correlations to calculate the $V_{t,max}$ by integrating the force balance equation (Gu et al., 2020; Kim & Kim, 2016; Lorenceau et al., 2004; Safavi & Nourazar, 2019). However, these models were based on varying simplifications, integration methods, and assumptions. One assumption that is the same across all models is using a constant drag coefficient (C_d) value to calculate the drag force. Another assumption is using a constant value to calculate the projected area of wire that interacts with the droplet. The result of such simplifications has contributed to the discrepancy between predictions and experimental data, ranging from 15 to 40%.

1.3. Research Methodology

In this thesis, we investigated the multiphase fluid dynamics to understand the governing hydrodynamics in a vertical VLS for both the inlet diverter and a mist eliminator. At first, CFD was used to investigate the distribution performance of the Schoepentoeter. It was found that the Schoepentoeter was unable to provide an equal fluid flow distribution, which is further discussed in Chapter 5. Furthermore, the design of inlet diverters is constrained by traditional manufacturing methods. Consequently, novel additively manufactured flow distributors have been proposed (Barbosa et al., 2023; Barbosa et al., 2021; Cao et al., 2018; Liu et al., 2012; Mazur et al., 2019). These flow distributors, including the fractal flow mixer proposed in this thesis, has a potential to be used as an inlet diverter. The hydrodynamics performance of the fractal flow mixer was numerically investigated by conducting CFD simulations with a single-phase flow and with two gases, air and methane. The effect of Reynolds number and inlet flow ratio was investigated. Experiments were conducted for a range of liquid-to-gas superficial velocities (V_{SL}/V_{SG}). High-speed imaging and optical probe were respectively used to qualitatively and quantitatively characterise the flow regimes generated by the fractal flow mixer.

In order to characterise the multi-scale and multi-phase hydrodynamics of the mist eliminator (knitted mesh pad), numerical and experimental tools were used to elucidate the relationship between the physical properties of the phases, the topology of the mesh and the momentum of the phases. Using these data sets, a new analytical model was proposed and validated against the literature and experimental data.

Overall, the research methodology used a combination of high-fidelity experimental tools, numerical tools, and phenomenological modelling and computational fluid dynamics modelling to develop and validate the hypothesis that allows the understanding of multiphase fluid dynamics in a VLS. The diagram of the research methodology is shown in Figure 4.

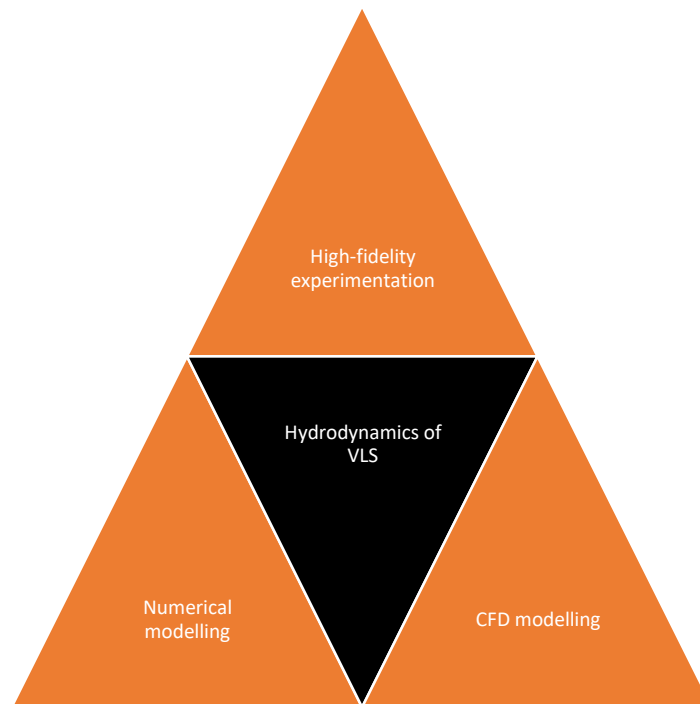


Figure 4: Diagram of the research methodology in this thesis

1.4. Research Objectives

The primary focus of this thesis is to understand the underlying fluid dynamics/hydrodynamics of two components in a vapour liquid separator, that includes the inlet diverter and the knitted mesh pad.

The following key objectives were addressed and pursued in this research work:

- i. To investigate the hydrodynamics of droplet capture on thin wires with different wire sizes, wire materials, and physical properties of droplets.
- ii. To propose a new analytical model that utilises a variable value of C_d to predict the $V_{t,max}$ between a single droplet and a single wire under controlled flow conditions.
- iii. To propose a novel additively manufactured inlet diverter/flow distributor, called the fractal flow mixer.
- iv. To investigate the hydrodynamics of a gas-gas and gas-liquid flow passing through the fractal flow mixer. The feasibility of producing Taylor flow within its microchannels was also investigated for the gas-liquid flow.

- v. To investigate the hydrodynamic performance of an existing inlet flow distributor design (Shell Schoepentoeter) in providing/promoting equal fluid flow distribution in a vapour-liquid separator vessel.
- vi. To investigate the vapour-liquid separation performance of a novel dual mesh pad vapour-liquid separator configuration.

1.5. Significance and Contributions of the Thesis

The outcome of the studies conducted in this thesis contributes to the body of knowledge by providing a better understanding towards the underlying fluid dynamics of two physical systems in a vapour-liquid separator. The first physical system was the fluid distribution of an inlet diverter. For existing inlet diverters, the design and performance are typically constrained by traditional manufacturing methods. However, the advancement of additive manufacturing has enabled the construction of novel high-performance flow distribution devices. In this thesis, a novel additively manufactured inlet flow distributor was proposed, called the fractal flow mixer, that combines the function of an inlet flow distributor and a mixer into a single device. Experiments and computational fluid dynamics studies were carried out to characterise the hydrodynamics of the fractal flow mixer. These studies have proven that the fractal flow mixer can be used as an alternative to existing inlet flow distributor designs. Results obtained from these studies can be used as a foundation for future development of the fractal flow mixer at different scale and configurations. The second physical system of the vapour-liquid separator was the interaction between a droplet and a wire of a mesh pad. The fundamental understanding of the hydrodynamic phenomena and numerical representation of the droplet impact on a thin wire is very critical in predicting the parameters that govern the capture of droplets. From this study, a new analytical model was proposed to predict the $V_{t,max}$. Unlike previously proposed analytical models, the proposed model includes a correlation that was developed to predict the C_d as a function of fundamental physical properties of the fluid (the ratio of viscosities) and operating parameters (ratio of diameters). As a result, with the inclusion of the variable C_d value, the proposed analytical was able to predict the $V_{t,max}$ more accurately than previous analytical models. Being able to accurately predict the $V_{t,max}$ can eventually benefit in quantifying the separation performance of a vapour-liquid separator. Furthermore, both studies, while distinct, converge towards enhancing the overall separation efficiency of the vapour-liquid separator at macro-scale and is expected to benefit many chemical and processing industries.

1.6. Thesis Outline and Organisation

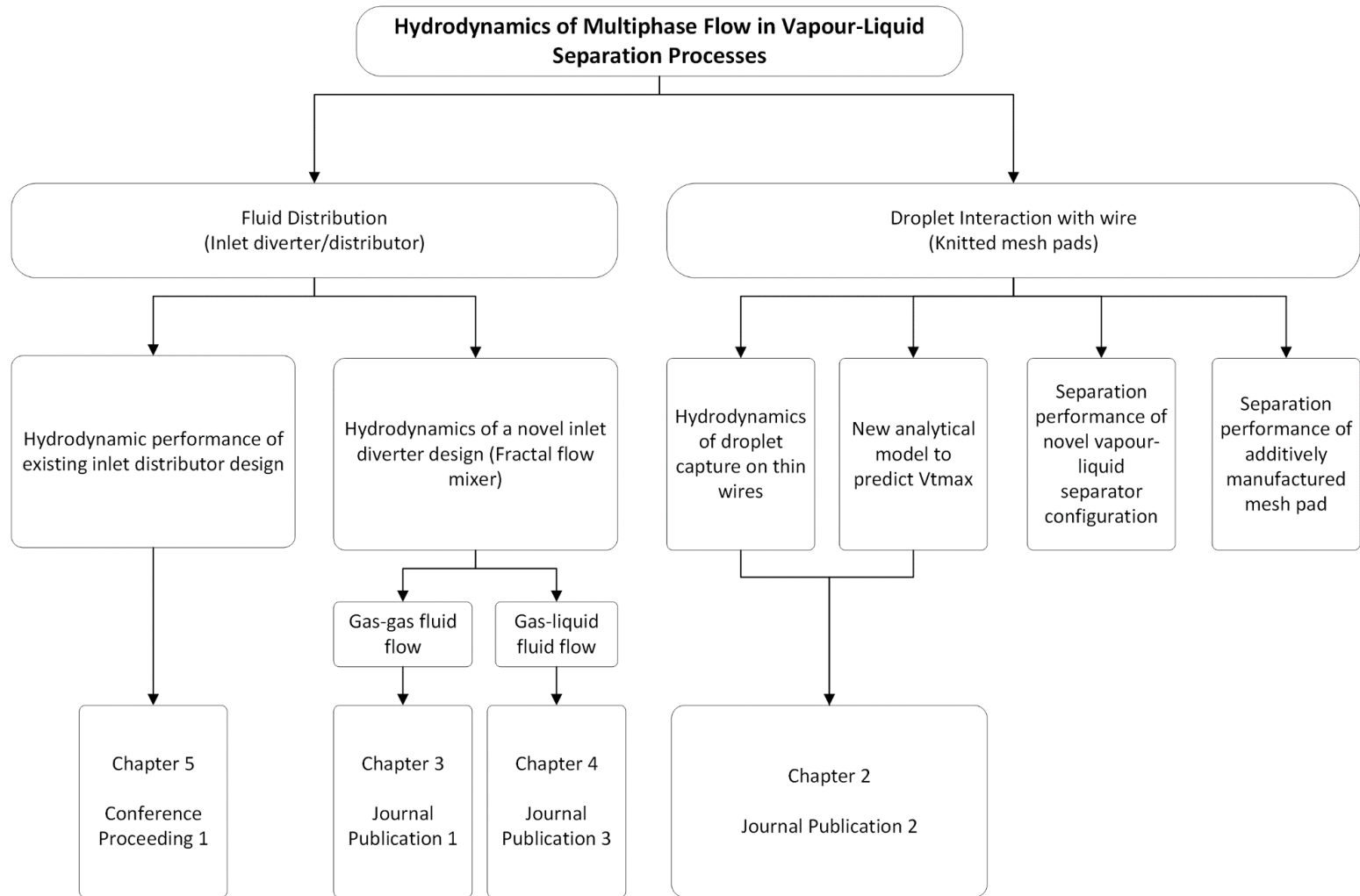


Figure 5: Flow diagram of thesis outline

The outcome of the research studies conducted are presented in different chapters of this thesis and communicated through different publications and proceedings, as shown by the flow diagram of thesis outline in Figure 5. The following list outlines the six chapters in this thesis:

Chapter 1 – Introduction

Provides a brief introduction of the thesis in regards to the gas/liquid separation technologies and the multiphase hydrodynamics in a vapour-liquid separator. This chapter also presents the research methodology, objectives, significance and contributions of the thesis, and the thesis outline and organisation.

Chapter 2 – Hydrodynamics of Droplet Capture on Thin Wires

Investigates the hydrodynamics of droplet impact and capture on a horizontal stationary wire with different process parameters that include the effect of wire size, wire materials, and physical properties of a droplet. High-speed imaging was used to measure the contact angle of different surface materials and the maximum impact velocity at which a droplet is being captured on a horizontal stationary wire ($V_{t,max}$). A new analytical model was also proposed to predict the $V_{t,max}$. This analytical model includes an empirical correlation that was developed to predict a variable value of drag coefficient as a function of fundamental physical properties and operating parameters. Additionally, a numerical simulation study was conducted to study the effect of wire shapes and sizes towards the $V_{t,max}$.

Chapter 3 – Gas-gas Hydrodynamics of a Fractal Flow Mixer

Demonstrates the capability of additive manufacturing in producing devices with inherently complex designs, such as the fractal flow mixer, which is presented in this thesis. The mixing performance and hydrodynamics of the fractal flow mixer was characterised by investigating the effect of Reynolds number and inlet flow ratio (IFR) with two gases (air and methane) through numerical CFD simulations. Additionally, an experiment study was conducted to understand the hydrodynamics of bubble flow after passing through the fractal flow mixer.

Chapter 4 – Gas-liquid Hydrodynamics of a Fractal flow mixer

Investigates the hydrodynamics of a gas-liquid flow passing through the fractal flow device and the feasibility of producing Taylor flow within its microchannels. High-Speed Imaging (HSI) was used to identify the gas-liquid flow regimes in the multi-microchannel outlet tubes of the fractal flow mixer. An optical probe was used to analyse the flow uniformity of the device by measuring the bubble mean size and velocity across all 16 outlet channels after passing through the fractal flow mixer at different inlet velocities (air and water).

Chapter 5 – *CFD Simulations of Vapour-Liquid Separator*

Whilst Chapter 2 until Chapter 4 focused on research studies of vapour-liquid separation processes at mili-/micro, Chapter 5 numerically investigates the separation performance of an existing inlet diverter design (Schoepentoeter) and the knitted mesh pad at macro-scale. Additionally, a novel dual-mesh pad VLS configuration was proposed in this Chapter.

Chapter 6 – *Conclusions and Recommendations*

Summarises the key findings presented in this thesis and provides recommendations for further work related to the presented topics.

Chapter 2 Hydrodynamics of Droplet Capture on Thin Wires

The content of Chapter 2 is reprinted (adapted) with permission and modified from the following publication:

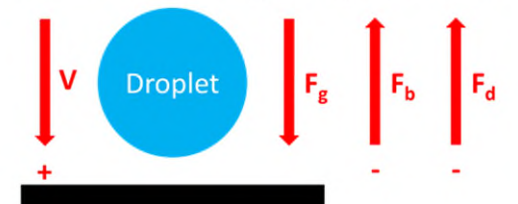
- M.D.M. Priyambodo, M.T. Shah, T. Bhatelia, B. Sun, V. Pareek, "Analytical Model for Droplet Capture on a Thin Wire" *Industrial & Engineering Chemistry Research*, vol. 61, no. 51, pp. 18914-18927, 2022/12/28 2022, doi: <https://doi.org/10.1021/acs.iecr.2c03606>.

Abstract

Mist elimination is a widely used separation technique in many industrial processes and is commonly carried out using knitted wires. The droplet impact and capture on these wires are governed by the impact hydrodynamics. Predicting the maximum impact velocity, that results in the droplet being captured on a horizontal, stationary wire ($V_{t,max}$) has previously been based on the solution of the force balance equation over an impacting droplet. However, these correlations were often based on varying simplifications, particularly in using a constant value of drag coefficient (C_d) in calculating the drag force in the force balance equations. The result of such simplifications has contributed to the discrepancy between predictions and experimental data ranging from 15 to 40%. The current work proposes a new analytical model with a correlation that was developed to predict the C_d as a function of fundamental physical properties of the fluid (the ratio of viscosities) and operating parameters (ratio of diameters). Droplet capture experiments with different wire materials and different wire and droplet sizes were also carried out. High-speed imaging was used to measure the $V_{t,max}$. Results from the experiment were used to estimate the parameters in the newly developed correlation for the variable C_d using a hybrid genetic algorithm (GA) and Levenberg-Marquadt algorithm (LMA) method. The new model was tested for a wide range of experimental data. The predictions from the proposed model were in agreement with the experimental data within the range of an $V_{t,max}$ between 0.35 to 0.65, with discrepancies within $\pm 25\%$. The model was also used to investigate the effect of wire size and fluid properties on the $V_{t,max}$. For all fluids tested, it was found that the increase of the droplet-to-wire ratio resulted in the increase of the $V_{t,max}$ and the decrease of the C_d value. Additionally, a fluid with a higher viscosity resulted in higher $V_{t,max}$, which is expected, and the proposed model was able to predict it. The study concluded that the proposed model provides a higher accuracy in predicting the $V_{t,max}$ than previously reported predictions and provides a deeper understanding of the key variables governing droplet capture on thin wires, which can be valuable for further optimisation of wire mesh systems in a diverse field of application that is not limited to only mist elimination.

Graphical Abstract

Force Balance of Droplet Impact on a wire



$$M \frac{dv}{dt} = -F_d - F_s + F_g - F_b$$

$$= -\frac{1}{2} \rho_3 v^2 C_d A_p - 4\pi\sigma R_f + Mg - \frac{\rho_1}{\rho_3} Mg$$

Common assumption in previous models:
Fixed value of drag coefficient

Newly Developed Correlation for a Variable C_d

$$C_d = a_1 \left(\frac{R_f}{R_d} \right)^{b_1} \left(\frac{\mu_3}{\mu_1} \right)^{c_1}$$

- The C_d is correlated as a function of the ratio of wire radius to droplet radius and the ratio of fluid viscosities.
- The optimal values of the constants ($a_1, b_1,$ and c_1) were estimated using a hybrid genetic algorithm – Levenberg Marquardt algorithm method to match the droplet capture experiment data presented in this study.

2.1. Introduction

The impact and capture of a droplet on a thin wire is a key phenomenon that dictates many natural and industrial separation processes (such as filtration and mist elimination). A typical mist elimination process involves the impact of droplets on knitted wires. Knitted wires forms a mesh pad, which is widely used for separation in equipment such as phase separators, packed columns, flash drums, etc (American Petroleum Institute, 2008; Don & Robert, 2008; Duroudier, 2016; Gas Processors Suppliers Association, 2004; Mokhatab et al., 2015; Stewart & Arnold, 2008). The fundamental understanding of the hydrodynamic phenomena and numerical representation of the droplet impact on a thin wire is critical for predicting the parameters that govern the capture of droplets.

The hydrodynamics of droplet impact would be highly dependent on the surface and shape of impact. Extensive studies for droplet impact on planar surfaces that has an impact surface larger than the droplet have been made (Chandra & Avedisian, 1991; Harlow & Shannon, 1967; Levin & Hobbs, 1971) and a comprehensive review of the hydrodynamics of droplet impact on both liquid and solid surfaces was presented by (Rein, 1993). (Hung & Yao, 1999) conducted the first study to understand the hydrodynamics of droplet impact on a wire with comparable droplet and wire sizes. They observed two possible outcomes – dripping of single droplet from wire and disintegration or splitting of a droplet in two. (Hung & Yao, 1999) represented the hydrodynamics of droplet impact on a wire by dimensionless parameters such as the Weber number (We), the ratio of droplet diameter to fibre diameter, and the Bond number (Bo). Based on their experimental data, a regime map was developed to classify the droplet

impact velocity that might result in either dripping or splitting. (Hung & Yao, 1999) used the experimental data and calculated dimensionless numbers to develop a semi-empirical model to predict the size of a dripping droplet after impacting the wire. (Hung & Yao, 2002) further extended their investigation to study the effect of the wettability of fibre on the droplet impact phenomena. Several studies (Gu et al., 2020; Kim & Kim, 2016; Lorenceau et al., 2004; Safavi & Nourazar, 2019) have experimentally investigated the maximum impact velocity that results in droplet capture or a hanging droplet on a horizontal, stationary wire. This maximum impact velocity is referred to as threshold velocity and denoted in this work as $V_{t,max}$.

Several other studies have been conducted to understand interactions between a single droplet and a single wire under controlled flow conditions or between intersecting wires. These studies have been summarised in Table 1, which provides a comprehensive overview of the different types of investigations conducted and the different scales at which the studies were conducted. These studies have focused on the effect of wire orientation (Gilet et al., 2010; Mullins et al., 2004; Piroird et al., 2009), the flexibility of a wire (Comtet et al., 2016; Dressaire et al., 2016; Zhu et al., 2019), wire shape (Merdasi et al., 2018; Wang & Desjardins, 2018), wire temperature (Lee et al., 2019), wire wettability, influence of external forces (Amrei et al., 2016; Aziz et al., 2018; Farhan & Tafreshi, 2018; Sahu et al., 2013) and the eccentricity of impact (Lorenceau et al., 2009; Safavi & Nourazar, 2019, 2021; Sher et al., 2013) on the droplet capture or detachment phenomena. Discussing some of the literatures shown in Table 1, (Mullins et al., 2004) investigated the effect of fibre orientation on the surface wettability and proposed an equation to calculate the optimum angle of fibre that would enhance the efficiency of the wet filtration process. (Piroird et al., 2009) showed that an inclined fibre increases droplet capture efficiency. (Comtet et al., 2016) and (Dressaire et al., 2016) investigated the effect of fibre flexibility on droplet capture efficiency and concluded that an optimal fibre length and tuning of the fibre mechanical properties were critical to maximising droplet capture efficiency. (Zhu et al., 2019) investigated the effect of fibre oscillations on the droplet capture phenomena. (Wang & Desjardins, 2018) numerically investigated the effect of contact angle and fibre shape. The droplet detachment from different fibre shapes was quantified using the Eotvos number, which is the ratio of the weight of the drop to the surface tension force. (Lorenceau et al., 2009), (Sher et al., 2013), and (Safavi & Nourazar, 2021) concluded that droplet impact eccentricity (off-centre impact) can improve the droplet capture efficiency of a fibre. (Safavi & Nourazar, 2019) showed that increasing the ratio of droplet radius to fibre ratio along with increasing the droplet impact eccentricity on hydrophilic fibres would decrease the droplet capture efficiency of the fibre. (Weyer et al., 2017) experimentally studied the droplet motion

on a fibre network and how to control its motion. Two critical parameters in fibre-based microfluidics were concluded that includes the fibre diameter and the fibre steepness. A model to predict the droplet detachment volume was also introduced based on the interacting forces acting upon the film that wets both fibre with a single fitting parameter.

From Table 1, there are also studies that focuses on the effect of external forces. (Amrei et al., 2016) introduced a novel ferrofluid-based method to experimentally measure the force required to detach a droplet from a single fibre and intersecting fibres. A magnet at varied heights was used to exert an external force to the ferrofluid droplets and a scale was used to measure the peak value of force before the magnet completely detaches from the fibre. This experimental method was then used to investigate the effect of the droplet properties, the fibre diameter, and the Young-Laplace Contact Angle (YLCA) towards the droplet detachment force required from a fibre (Farhan & Tafreshi, 2018) and towards the volume of droplet residue left on a fibre after droplet detachment (Aziz et al., 2018). (Sahu et al., 2013) conducted a series of experiments to study the effect of an air jet towards the motion of an oil droplet on a single filament and through a series of filament in parallel, with the air blowing either in parallel or perpendicular to the filament. Different droplet motion and shapes were observed, and a simplified model was presented to interpret the physical origin of the observed droplet motion and shapes.

Numerical simulation studies have also been conducted to investigate the hydrodynamics of droplet impact on thin wires. (Gac & Gradoń, 2012) studied the effect of Weber number, contact angle, and capillary number towards the kinetics of central and eccentric droplet impact using the two-colour lattice-Boltzmann method (LBM). The model was in good agreement with the presented experimental data. However, the model was only valid for a capillary number (Ca) value less than one. For greater values of Ca, the model was unable to predict the droplet deformations near the fibre. (Ojaghlou et al., 2018) used nonequilibrium molecular dynamic simulations to numerically investigate the mechanism of water droplet detachment and volume of water residue on a smooth hydrophilic fibre and predict the external force required for droplet detachment. (Merdasi et al., 2018) numerically studied the effect of surface tension, gravity magnitude, and viscosity towards the deformation rate of the droplet after impacting rectangular obstacles in a vertical channel. The LBM was used in conjunction with He-Chen-Zhang (He et al., 1999) method for two phase flow. It was found that the increase in the droplet deformation rate was caused by the decrease of surface tension or viscosity and the increase of gravity force. (Khalili et al., 2016) conducted a 2D computational fluid dynamics (CFD) study using the volume-of-fluid (VOF) method with

process parameters similar to the experimental study by (Lorencean et al., 2004). The result of this study was quantitatively and qualitatively comparable to the theoretical and experimental results presented by (Lorencean et al., 2004). However, over a range of operating conditions, the deviations from the model were relatively large. (Abishek et al., 2019) studied the effect of contact angle dynamics and fibre wettability towards droplet capture and re-entrainment on a thin fibre using the volume of fluid (VOF) method on OpenFOAM. From this study, droplet capture regime maps were established based on the dynamics of contact angle, that includes the individual and advancing hysteresis, total contact angle hysteresis, and equilibrium contact angle. (Wang et al., 2021) conducted a numerical study to investigate the effect on wire wettability, droplet eccentricity, and the fibre tilt angle toward the $V_{t,max}$. It was found that the droplet capture rate, $V_{t,max}$, and wetting length all decreased with the increase in eccentricity and increased with the increase in tilt angle. Despite several models have been proposed in the literature, there is a lack of a fundamental analytical model that predicts the experimentally observed $V_{t,max}$ across a wide range of operating conditions.

(Lorencean et al., 2004) proposed an analytical model to calculate $V_{t,max}$ and compared their calculated values with their experimental data. (Kim & Kim, 2016) presented a simplified analytical model to calculate the $V_{t,max}$ that included dimensionless parameters similar to the model of (Hung & Yao, 1999). (Kim & Kim, 2016) also compared the fidelity of their model by comparing the calculated $V_{t,max}$ with their experimental data and provided a regime map for droplet capture and splitting phenomena. Despite of the simplicity of the model, the Kim and Kim model was not able to predict the threshold velocity at higher fibre to wire diameter ratios. (Gu et al., 2020) proposed a force balance equation and also included the buoyancy term. (Safavi & Nourazar, 2019) proposed an analytical and CFD model with surface contact angle and provided experimental data. The model was unable to predict the experimental data at low fibre to droplet ratios.

The previously proposed analytical models for $V_{t,max}$ carry several different assumptions, and as a result, their predictions at different system conditions are inconsistent. One of the key assumptions that all models make is the use of a fixed value for the drag coefficient in their calculation of drag force. In this work, we critically reviewed widely used previous models (Gu et al., 2020; Kim & Kim, 2016; Lorencean et al., 2004; Safavi & Nourazar, 2019) to highlight the reasons why they cannot predict the published experimental data (Kim & Kim, 2016; Lorencean et al., 2004; Safavi & Nourazar, 2019). Consequently, a new analytical model is proposed in this work to calculate $V_{t,max}$. This newly developed model

does not take a fixed value of the drag coefficient (C_d). The C_d is correlated as a function of the ratio of wire radius to droplet radius and the ratio of fluid viscosities.

Droplet capture experiments were carried out for different ratio of wire to droplet size and different wire materials. High-speed imaging was used to measure the $V_{t,max}$. Results from the experiment was then used to estimate the parameters in the newly developed correlation for the variable C_d . The parameter estimation was conducted using the genetic algorithm (GA) for global optimisation and coupled with the Levenberg-Marquardt algorithm (LMA) for local optimisation in MATLAB. Using the estimated parameters in the newly developed correlation for the variable C_d , the proposed analytical model was then tested for a wide range of experimental data (Khalili et al., 2016; Kim & Kim, 2016; Lorenceau et al., 2004; Safavi & Nourazar, 2019). The proposed analytical model was also used to investigate the effect of droplet and wire properties on the droplet capture velocity as well as different forces acting on an impacting droplet.

Authors	Droplet direction	Fibre radius	Droplet radius	Impact vel.	Material		Investigations
					Liquid	Wire	
		(μm)	(μm)	(cm/s)			
Lorenceanu et al. (2004) ^{*#^}	(I)	80 – 350	500 – 1500	10 – 100	Water, silicon oil	Nylon	(a), (b), (c)
Lorenceanu et al (2009) ^{*#^}	(I)	250 \pm 20	1250	10 – 150	Water	Stainless steel	(e), (h)
Piroird et al. (2009) ^{*#^}	(I)	250	1000 – 1150	10 – 100	Silicon oil, water + glycerol, aqueous solution	Nylon	(b), (c), (e), (f)
Khalili et al. (2016) ^{#^}	(I)	350	500 – 1500	10 – 100	Water, silicon oil	Nylon	(a), (b), (c)
Kim and Kim (2016) ^{*#^}	(I)	20 – 1000	1350	~ 170 – 290	Water	Copper fiber (86°), coated with teflon (114°), coated with polyethyleneimine in ethylene chloride (58°)	(a), (d), (e)
Gu et al. (2019) ^{*#^}	(II)	60	10	30 – 600	Iso octane	Polypropylene	(e)
Wang and Desjardins (2018) ^{#^}	(I)	Triangle sides: 160, 350, and 700; Circle: 350	1000	unspecified	Unspecified, density = 971 kg/m ³ ; surface tension = 0.0214 N/m	Unspecified range, contact angle = 10 – 80°	(d), (g)
Hung and Yao (1999) ^{*#^}	(I)	56.5 – 794	55 – 340	100 – 700	Water	Stainless steel	(a), (b), (d), (e)
Hung and Yao (2002) ^{*#^}	(I)	70 – 1600	175	280	Water	Stainless steel	(a), (d)
Mullins et al. (2004) ^{*#^}	(III)	7 \pm 0.1	2.8 \pm 0.8	~ 100	Water	Glass	(f)
Comtet et al. (2016) ^{*#^}	(I)	750 – 1000			Silicon oils	Nitinol	(a), (b), (e), (i)
Dressaire et al. (2016) ^{*#^}	(I)	400	410 – 1050	10 – 80	Silicon oils	Unspecified, linear density = 1.2 mg/cm; bending stiffness = 4.34x10 ⁻⁵ Nm ²	(a), (b), (e), (i), (j)
Zhu et al. (2019) ^{*#^}	(I)	54 – 1200	1260 – 1470	19.8 – 280	Water	Nylon	(a), (b), (e), (i)
Sher et al. (2013) ^{*#^}	(I)	145 - 395	1110 – 2360 \pm 50	40 – 150 \pm 0.3	Water	Stainless steel	(a), (b), (e), (h)
Safavi and Nourazar (2019) ^{*#^}	(I)	300 – 500	500 – 2000	16 – 150	Water	Nylon and Steel	(a), (b), (d), (e), (h)

Safavi and Nourazar (2021) ^{*#^}	(I)	500	1300	20 – 200	Water	Nylon	(d), (h)
Sahu et al. (2013) ^{*#^\$}	(III)	90	400 – 580	330 – 2270	Silicon oils (10, 20, 50, and 100 cst) and PEO	Flexible fused silica capillary tubings	(b), (c), (e), (j), (l)
Weyer, Duchesne, and Vandewalle (2017) ^{*#\$}	(I)	80 – 225	Unspecified range (volume = 0.5 – 10 μ l)	-	Dow Corning silicone oil and soapy water	Nylon	(a), (b), (c), (f), (k)
Amrei et al. (2016) ^{*#\$}	(III)	107.5	Unspecified range (infusion rate = 0.73 – 1200 μ L/h)	-	Water-based ferrofluid and ferrofluid + glycerol	Nylon (Monofilament fishing line)	(b), (c), (d), (f), (k), (l)
Farhan and Tafreshi (2018) ^{*#\$}	(I)	190.5	Unspecified range	-	Water-based ferrofluid	Nylon (Monofilament fishing line)	(a), (b), (c), (d), (l)
Aziz et al. (2018) ^{*\$}	(I)	81 – 264	Unspecified range (infusion rate = 0.73 – 1200 μ L/h)	-	Water-based ferrofluid	Nylon (Fluorocarbon fishing line)	(a), (b), (c), (d), (l)
Gac and Gradon (2012) [#]	(III)	Unspecified range (ratio of fiber diameter to droplet diameter = 0.5 – 2)	Unspecified range (ratio of fiber diameter to droplet diameter = 0.5 – 2)	Unspecified range (Weber number = 0 – 50)	Unspecified	Unspecified	(a), (b), (c), (e), (h)
Merdasi et al. (2017) ^{#\$}	(I)	Unspecified range	Unspecified range	Unspecified range	Unspecified	Unspecified	(a), (b), (c), (e), (g)
Ojaghloou et al. (2018) ^{#\$}	(I)	6.4×10^{-4} and 12.8×10^{-4}	Unspecified, (volume = 2000 – 17000 water molecules)	-	Water	Rigid carbon nanotube	(a), (b), (d), (l)
Droplet direction I. Falling II. Rising III. Horizontal (i.e. left to right)	Type of study * Experiment # Numerical ^ Droplet impact \$ Droplet detachment only (deposited on fiber)	Investigations: (a) Effect of wire size (b) Effect of droplet size (c) Effect of liquid property (i.e. density, viscosity, etc.) (d) Effect of wire property (i.e. contact angle, wettability, etc.) (e) Effect of impact velocity			(f) Effect of wire angle (g) Effect of wire shape (h) Effect of eccentricity (i) Effect of wire flexibility (j) Effect of wire dynamics (k) Effect of wire intersection/cross (l) Effect of external force (i.e. air, magnet, etc.)		

2.2. Analytical Models to Calculate $V_{t,max}$

A schematic diagram of droplet impact and its capture on a thin wire for a droplet moving downward under a stationary medium is shown in Figure 6. The position of the droplet just at the time of impact ($t = 0$) is shown in Figure 6[a], a wire piercing the droplet is shown in Figure 6[b], and the position of the droplet when it is captured on the wire (time = $t + \Delta t$) is shown in Figure 6[c].

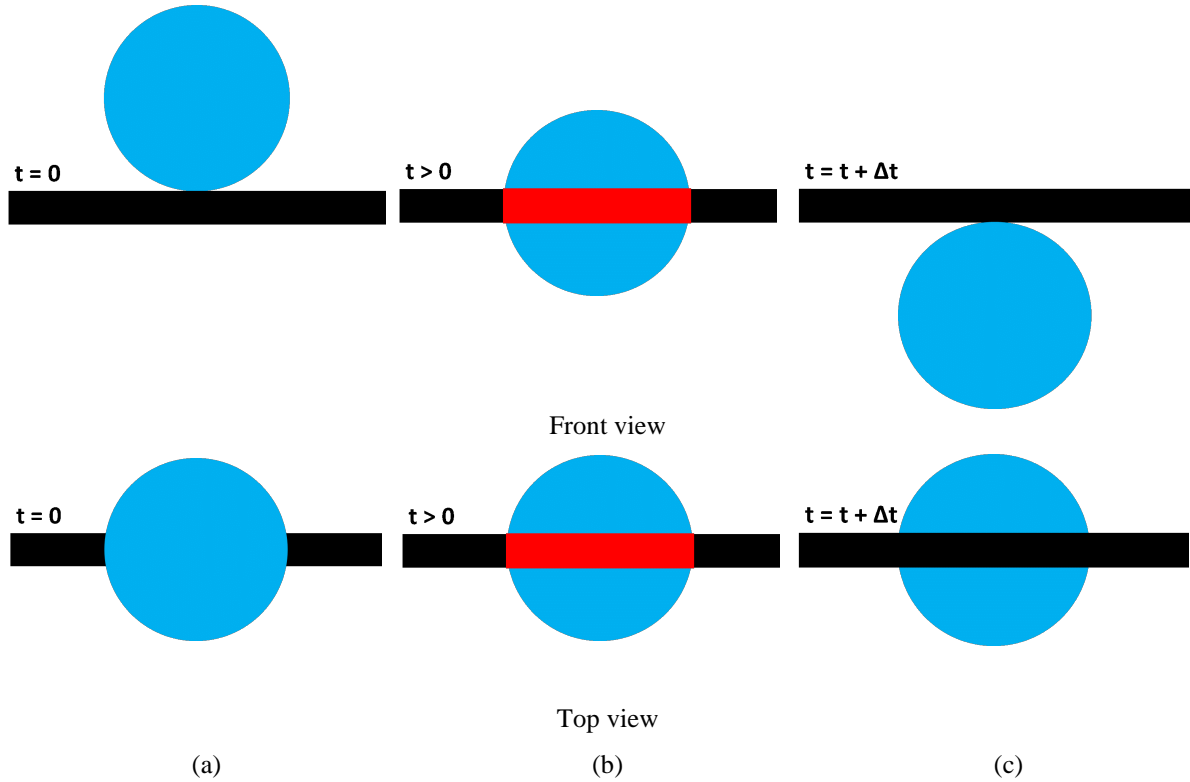


Figure 6: Schematic diagram of a droplet impacting a wire (■ – wire, ● – droplet, ■ – intersection between wire and droplet); (a) The position of droplet just at the time of impact ($t = 0$); (b) a wire piercing the droplet; (c) the position of droplet when it is captured on the wire (time = $t + \Delta t$)

The maximum impact velocity at which a droplet would be captured on a wire can be calculated by balancing different forces on an impacting droplet. The force balance equation can be written as:

$$M \frac{dv}{dt} = -F_d - F_s + F_g - F_b = -\frac{1}{2} \rho_3 v^2 C_d A_p - 4\pi\gamma R_f + Mg - \frac{\rho_1}{\rho_3} Mg \quad \text{Eq. 1}$$

where M is the mass of the droplet, F_d is the drag force, F_s is the surface tension (contact) force, F_g is the gravity force, and F_b is the buoyancy force. Furthermore, g is gravity acceleration, ρ_1 is the density of the primary phase (i.e. air), ρ_3 is the density of the secondary phase (i.e. water), v is the droplet impact velocity, C_d is the drag coefficient, A_p is the projected area of the droplet

normal to the wire upon impact, γ is the surface tension, R_f is the wire radius, and R_d is the droplet radius. The sign convention of each force would depend on the direction of the droplet movement and note that droplet movement in the downward direction is assumed in this discussion. To calculate $V_{t,max}$, the force balance equation (Eq. 1) is integrated for the distance travelled by the droplet in the time duration Δt with the boundary conditions of (i) droplet velocity being $V_{t,max}$ at $t = 0$ and (ii) droplet velocity being 0 at $t + \Delta t$. This boundary condition also infers that the distance travelled by the droplet in time duration Δt is equal to the wire diameter. (Lorencean et al., 2004), (Kim & Kim, 2016), (Safavi & Nourazar, 2019), and (Gu et al., 2020) provided the models to calculate $V_{t,max}$ by integrating the force balance equation (Eq. 1). These models are summarised in Table 2.

Table 2: Published analytical model to calculate $V_{t,max}$	
Lorencean et al. (Lorencean et al., 2004)	
$V_{t,max} = V_m \sqrt{\frac{e^{kR_M/R_d-1}}{kR_M/R_d} \left[\left(\frac{R_M}{R_d} \right)^2 - \frac{R_d}{R_M} \right]}$	Eq. T2 - 1
or	
$V_{t,max} = V_m \sqrt{\left[\left(\frac{R_M}{R_d} \right)^2 - \frac{R_d}{R_M} \right]}$	Eq. T2 - 2
$k = 12C_D R_f / (\pi R_M)$	Eq. T2 - 3
$R_m = \sqrt[3]{3R_f \left(\frac{\sigma}{\rho_3 g} \right)}$	Eq. T2 - 4
$V_m = \sqrt{4gR_m}$	Eq. T2 - 5
$F_D = \frac{1}{2} \rho_3 v^2 C_d A_p = \frac{1}{2} \rho_3 v^2 (2)(4R_f R_d) = \rho_3 v^2 (4R_f R_d)$	Eq. T2 - 6
$F_C = 4\pi\sigma R_f$	Eq. T2 - 7
Kim and Kim (Kim & Kim, 2016)	
$V_{t,max} = \sqrt{\frac{We \times \sigma}{\rho_3 \times R_d}}$	Eq. T2 - 8
$We = \frac{6 \left(\frac{R_f}{R_d} \right) - 2Bo}{1 - \left(\frac{3}{\pi} \right) \left(\frac{R_f}{R_d} \right)}$	Eq. T2 - 9
$Bo = \frac{\rho_3 g R_d^2}{\sigma}$	Eq. T2 - 10
$F_D = \frac{1}{2} \rho_3 v^2 C_d A_p = \frac{1}{2} \rho_3 v^2 (1)(4R_f R_d) = \frac{1}{2} \rho_3 v^2 (4R_f R_d)$	Eq. T2 - 11
$F_C = 4\pi\sigma R_f$	Eq. T2 - 12

Safavi and Nourazar (Safavi & Nourazar, 2019)	
$V_{t,max} = V_m \sqrt{-2 \frac{R_d}{R_m} + \frac{\frac{R_m^2}{R_d^2} [\cos \theta_r + \cos \theta_a]}{\left(1 - \frac{3R_f}{\pi R_d}\right)}}$	Eq. T2 - 13
$V_m = \sqrt{4gR_m}$	Eq. T2 - 14
$R_m = \sqrt[3]{3R_f \left(\frac{\sigma}{\rho_3 g}\right)}$	Eq. T2 - 15
$F_D = \frac{1}{2} \rho_3 v^2 C_d A_p = \frac{1}{2} \rho_3 v^2 (L) (4R_f R_d) = \frac{1}{2} \rho_3 v^2 (2R_d) (4R_f R_d)$	Eq. T2 - 16
$F_C = \sigma p L (\cos \theta_r - \cos \theta_a) = \sigma (2\pi R_f) (2R_d) (\cos \theta_r - \cos \theta_a)$	Eq. T2 - 17
Gu et al. (Gu et al., 2020)	
$V_{t,max} = \left[\frac{1}{a} \left(c + bR_d + \frac{b}{a} \right) - \frac{1}{a} \left(c - bR_d + \frac{b}{2a} \right) e^{2aR_d} \right]^{\frac{1}{2}}$	Eq. T2 - 18
$a = \frac{3\rho_1 C_d}{2\pi\rho_3} \cdot \frac{2R_f + \pi R_d/2}{R_d^2}$	Eq. T2 - 19
$b = \frac{6\sigma}{\rho_3} \cdot \frac{R_f}{R_d^4}$	Eq. T2 - 20
$c = \frac{2g(\rho_1 - \rho_3)}{\rho_3}$	Eq. T2 - 21
$F_D = \frac{1}{2} \rho_1 v^2 C_d A_p = \frac{1}{2} \rho_1 v^2 C_d (4R_f R_d + \pi R_d^2)$	Eq. T2 - 22
$F_C = 4\pi\sigma R_f$	Eq. T2 - 23

Despite using the same force balance equation (Eq. 1), the models to predict the $V_{t,max}$ that were presented by different authors are significantly different to each other, as summarised in Table 2. (Lorenceanu et al., 2004) introduced the characteristic length of droplet R_M , which represents the maximum threshold of droplet radius that can be captured by a particular wire size. (Kim & Kim, 2016) assumed a linear relation between the droplet velocity and time, dV/dt was calculated as a ratio of the finite difference in the droplet velocity ($V_{t,max} - 0$) to the wire diameter (as a distance travelled in the time duration). It is notable that both (Lorenceanu et al., 2004) and (Kim & Kim, 2016) did not consider buoyancy force on the droplet in their force balance equation. Furthermore, (Lorenceanu et al., 2004) used a C_d value of 2 whereas (Kim & Kim, 2016) used a C_d value of 1. (Safavi & Nourazar, 2019) also adopted the model derivation approach of (Kim & Kim, 2016); however, they used the characteristic length of the droplet as suggested by (Lorenceanu et al., 2004). (Safavi & Nourazar, 2019) also used a different

treatment for the surface tension force term. They considered the slowing of droplet motion while during droplet impact (advancement) and the slowing of droplet detachment from the wire (receding). The surface tension force equation of Safavi and Nourazar's model has two contact angles – one for an advancing droplet and the other for a receding droplet. Another difference in the surface tension force by Safavi and Nourazar is the addition of $2R_d$ into the equation, where other models only considers R_f . (Gu et al., 2020) developed a model for a rising droplet where they accounted for buoyancy force in the force balance equation. Surprisingly, (Gu et al., 2020) used the density of the continuous medium in the drag force closure instead of the density of droplet phase. For the value of C_d , (Lorenceanu et al., 2004) used 2, (Kim & Kim, 2016) used 1, and (Safavi & Nourazar, 2019) used a variable value equal to $2R_d$. The majority of models used $4R_fR_d$ as the projected area (see Figure 6) in the drag calculation, whereas (Gu et al., 2020) considered $(4R_fR_d + \pi R_d^2)$ as the projected area. Since the assumptions, integration approach and the values of constants used in the previous models are different, they result in inconsistent predictions of droplet capture velocity. The comparison of these models and their ability to predict experimental data is covered in the results and discussion section (Section 2.7). The inability of previous models in capturing the experimental data (discussed in the results of Section 2.7) can be attributed to the treatment of drag force in these models. A constant value of drag coefficient (C_d) value was used in the drag force calculation, and it is not clear how a particular value of C_d was selected in previous studies. In addition, there is no consensus on the value of C_d among different studies. Typically, the value of C_d is calculated based on the particle Reynolds number which is based on the droplet diameter and slip velocity between the droplet and wire. Thus, one value of C_d cannot be applied to all systems. Furthermore, the droplet capture phenomena are rather complex, and it involves impacting, piercing, and hanging of droplet on a thin wire.

2.3. Improved Analytical Model to Calculate $V_{t,max}$

To alleviate the shortcoming of previous models (Gu et al., 2020; Kim & Kim, 2016; Lorenceanu et al., 2004), in this work, a semi-empirical approach was adopted and presented in Eq. 2-7. In this approach, a force balance equation that includes gravitational, drag, surface tension and buoyancy forces was considered with the closure models of drag and surface tension forces as given in Eq. 2-7. This force balance equation was then integrated for the droplet capture phenomena where droplet is travelling downward. In this work, the following equation was derived for $V_{t,max}$.

$$V_{t,max}^2 = \frac{1}{a} \left(c - bR_d + \frac{b}{2a} \right) - \frac{1}{a} \left(c + bR_d + \frac{b}{2a} \right) e^{-4aR_d} \quad \text{Eq. 2}$$

$$a = \frac{\rho_3 C_d A_p}{M} = \frac{\rho_3 C_d (4R_f R_d)}{M} \quad \text{Eq. 3}$$

$$b = \frac{8\pi\sigma R_f}{M \cdot R_d} \quad \text{Eq. 4}$$

$$c = \frac{2g(\rho_3 - \rho_1)}{\rho_3} \quad \text{Eq. 5}$$

$$b = \frac{8\pi\sigma R_f}{M \cdot R_d} \quad \text{Eq. 6}$$

$$M = \frac{4}{3}\pi\rho_3 R_d^3 \quad \text{Eq. 7}$$

Instead of using a fixed value of C_d , variable C_d was proposed and used depending on the size of droplet, size of wire and viscosities. The parameters in C_d (a_1 , b_1 , and c_1) were estimated using the experimental data presented in this study, that was available for several different wire sizes and droplet sizes. The methodology of the parameter estimation is discussed in Section 4.0. The empirical correlation among C_d , R_f , R_d and two viscosities (μ_3 and μ_1) can be derived as:

$$C_d = a_1 \left(\frac{R_f}{R_d} \right)^{b_1} \left(\frac{\mu_3}{\mu_1} \right)^{c_1} \quad \text{Eq. 8}$$

$$a_1 = 1.00732 \pm 0.0015 \times R_f \text{ (in meter)}, b_1 = -1.999 \text{ and } c_1 = 0.01$$

where μ_1 is the viscosity of the primary phase (droplet phase) and μ_3 is the viscosity of the secondary phase (stationary medium). The ability of this model in predicting various experimental data sets was investigated and discussed in the results and discussion (Section 2.7)

2.4. Contact Angle Measurement

An experiment was carried out to measure the static contact angle of contact surfaces (wires) of the droplet capture experiment. The experiment setup, shown in Figure 7[a-b], consists of a syringe pump, a DSLR camera (Nikon D750), an optical macro lens, a needle, an LED light, a height control system using trapezoidal lead screws, distilled water, and five contact surfaces. The five contact surfaces included in this experiment were copper, stainless steel, aluminium, tin, and brass plates. The syringe pump was set to 60 $\mu\text{l}/\text{min}$ and attached to a tube that was terminated with a 18G needle to produce a droplet with a diameter of 1.54 mm. For each contact surface, the experiment was repeated three times. To measure the contact angle of each image taken, the *DropSnake* plugin in ImageJ was used. The *DropSnake* plugin

was developed by (Stalder et al., 2006) to measure contact angle that combines gradient information and statistical region based energy function with cubic-spline image interpolation (B-spline snakes/active contours) . The image results of the contact angles of water droplets on different contact surfaces are shown in Figure 8 until Figure 12. An average contact angle value was taken from the three images for each contact surface tested, which is tabulated in Table 3.

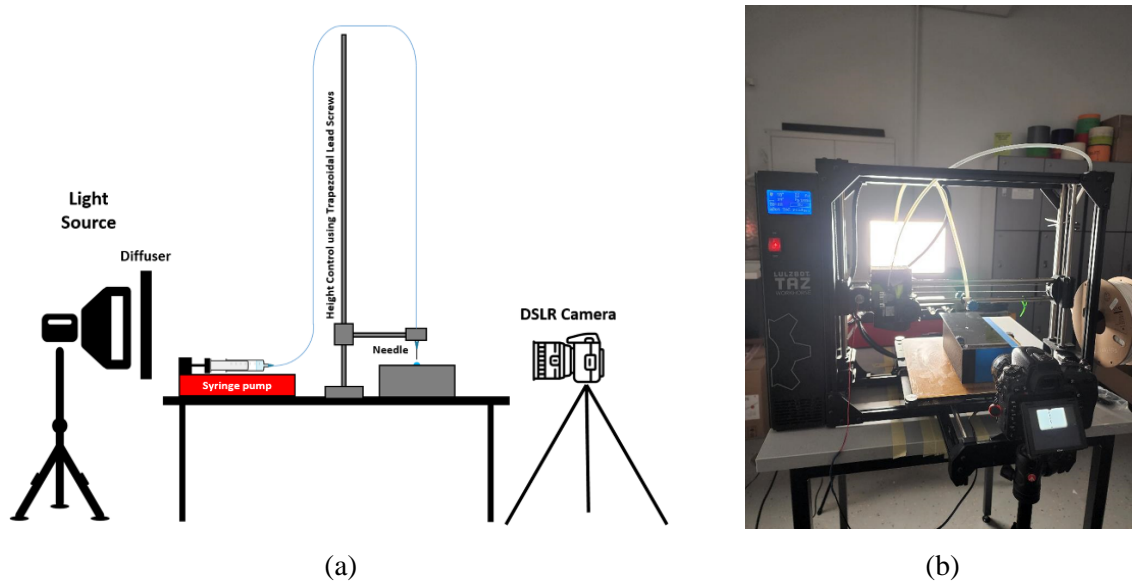


Figure 7: (a) Schematic diagram of experiment setup (b) Actual experiment setup

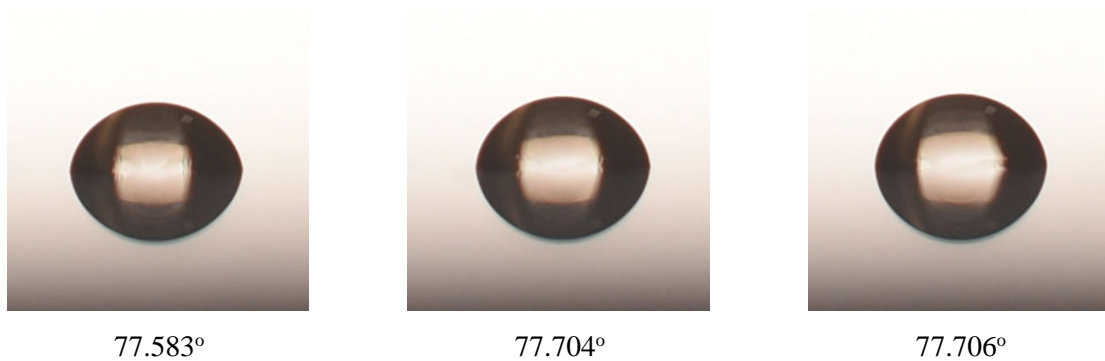


Figure 8: Images of contact angles of water droplets on Copper contact surface

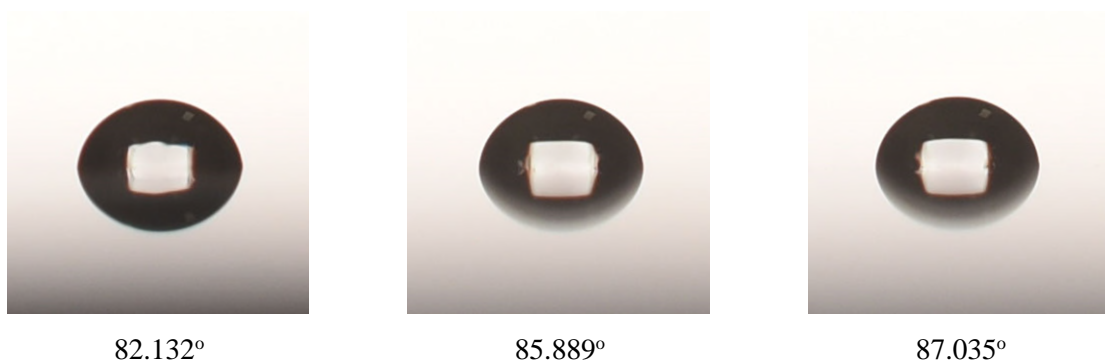
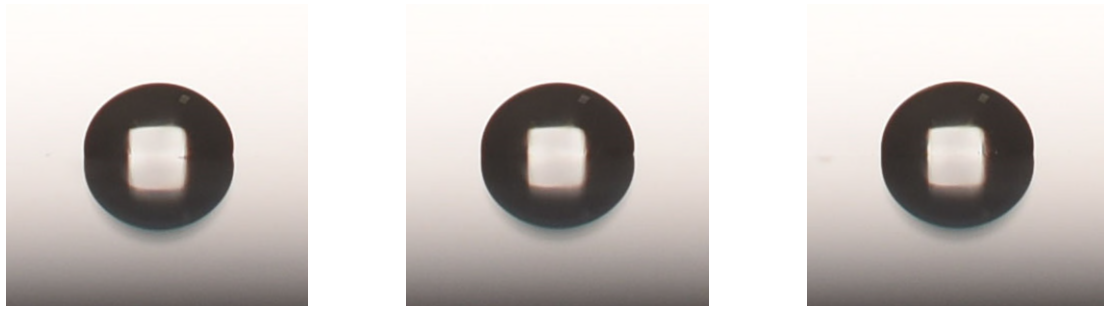


Figure 9: Images of contact angles of water droplets on Stainless Steel contact surface

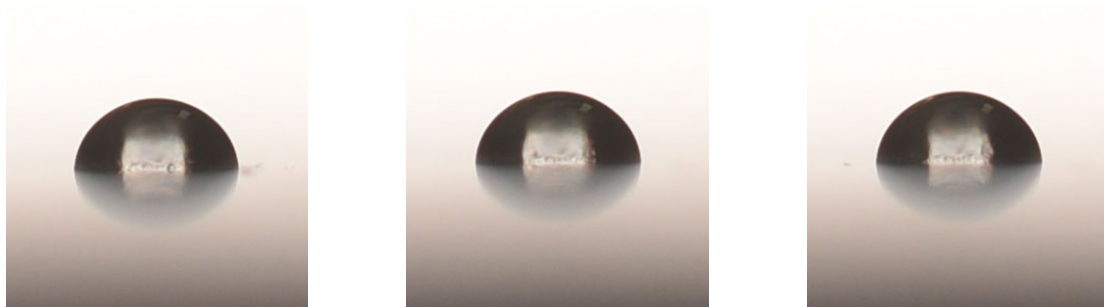


93.271°

94.534°

95.554°

Figure 10: Images of contact angles of water droplets on Aluminium contact surface

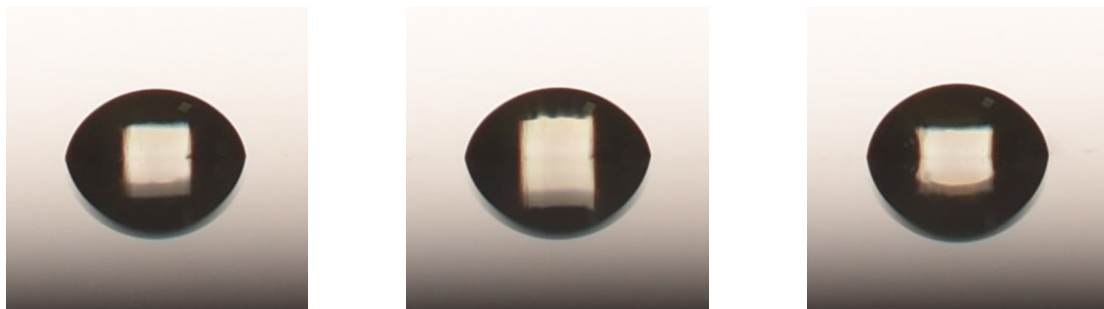


82.873°

84.156°

83.298°

Figure 11: Images of contact angles of water droplets on Tin contact surface



75.611°

76.122°

77.462°

Figure 12: Images of contact angles of water droplets on a Brass contact surfaces

Table 3: Average contact angle values of water droplets on different contact surfaces	
Contact Surface	Average contact angle
Copper	77.664
Stainless Steel	85.018
Aluminium	94.453
Tin	83.442
Brass	76.398

2.5. Droplet Capture Experiment

Droplet capture experiments were carried out for different ratio of wire to droplet size (R_f/R_d). The impact velocity for droplet capture ($V_{t,max}$) was measured using high-speed imaging technique with a recording speed of 2000 frames per second (fps). The experimental setup (Figure 13) comprised of a syringe pump, needle, light source (dimmable LED video light), trapezoidal lead screws, clamps, a high-speed camera (Photron Fastcam SA4), an optical macro lens, and an image acquisition system. These experiments were conducted using distilled water as the droplet medium in conjunction with copper and stainless-steel wires. The static contact angle of the copper wire and stainless-steel wire was measured to be 77° and 85° , respectively. Initially, syringe pump settings and needle size were calibrated to get specific droplet sizes ($R_d = 0.75, 0.81, 0.95, 1.23, 1.41, \text{ and } 1.54 \text{ mm}$). The droplet was made to impact a copper wire that was tightly strung between the prongs of the clamp. The wire was horizontally aligned using the gridlines from the image acquisition system and the wire was aligned with the needle using a line laser level to ensure central impact. Furthermore, the distance between the needle tip and copper wire was adjusted using trapezoidal lead screws in order to achieve a specific impact velocity. In a particular experiment with a specific wire size, this distance was varied from 5 mm to 180 mm, corresponding to a droplet impact velocity (V_1) from 0.23 m/s to 1.77 m/s. The experiments were conducted for two wire sizes ($R_f = 0.4 \text{ mm}$ and $R_f = 0.625 \text{ mm}$). Each experiment with a specific wire size and a calibrated distance between the wire and needle tip was repeated ten times. Once the maximum distance (between the wire and needle tip) at which the capture rate was 100% from the 10 repetitions was determined, the recorded images of that experiment was post-processed to calculate $V_{t,max}$. For example, Figure 14 and Figure 15 shows the droplet impact phenomena observed in the recorded images at $R_f = 0.40 \text{ mm}$, $V_1 = 0.490$ and 0.518 m/s , and $R_f/R_d = 0.53$. From Figure 14, the droplet was captured at a V_1 value of 0.490 m/s . Increasing V_1 from 0.490 m/s to 0.518 m/s has resulted in the droplet no longer being captured by the wire, as shown by Figure 15.

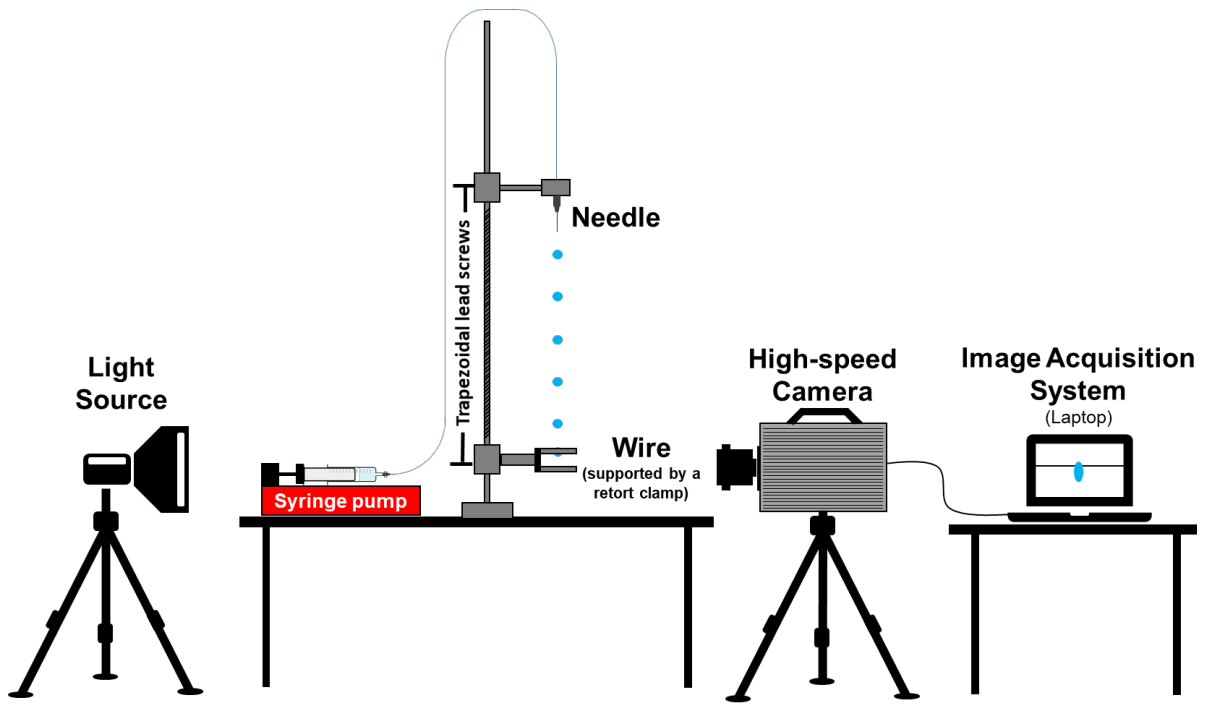


Figure 13: Schematic diagram of droplet impact experiment setup

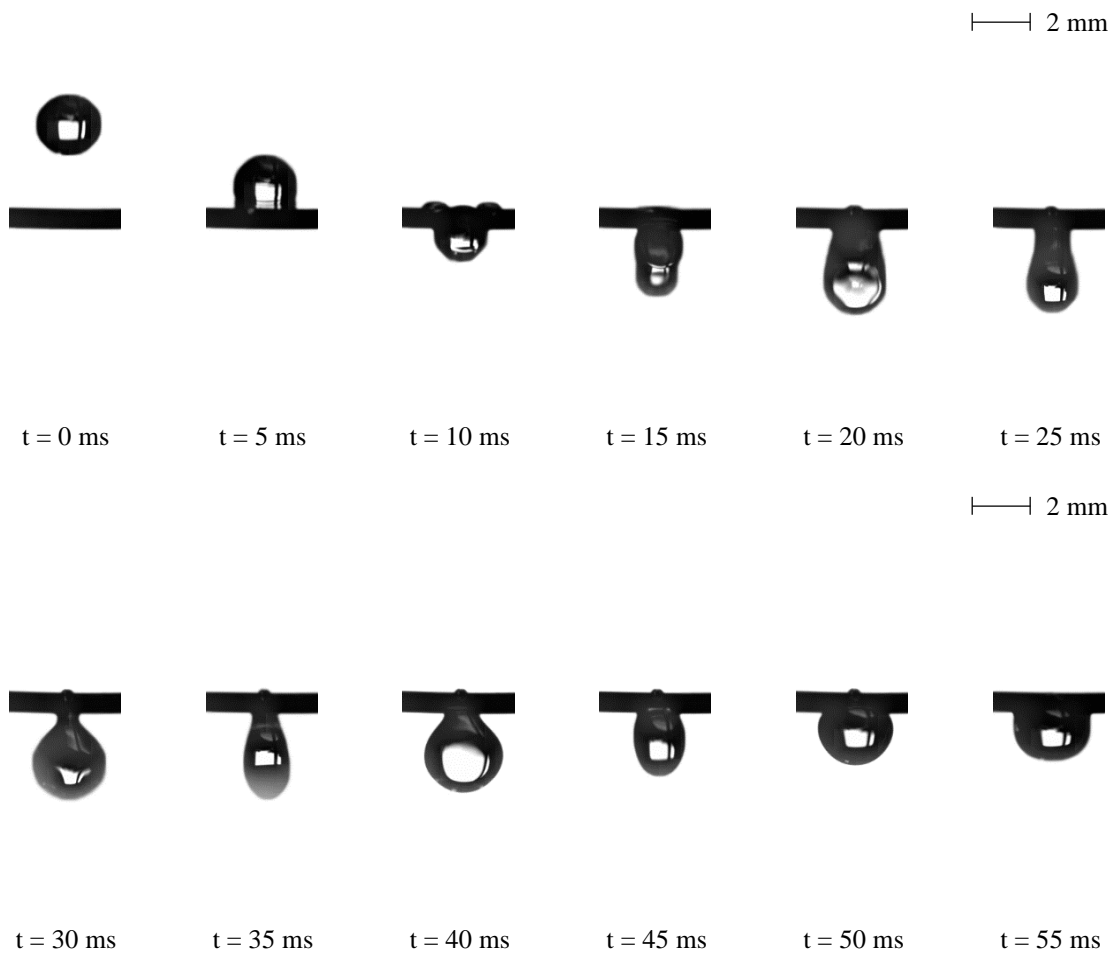


Figure 14: Outcome of droplet impact on copper wire ($R_f/R_d = 0.53$): Captured ($R_f = 0.40$ mm; $V_1 = 0.490$ m/s)

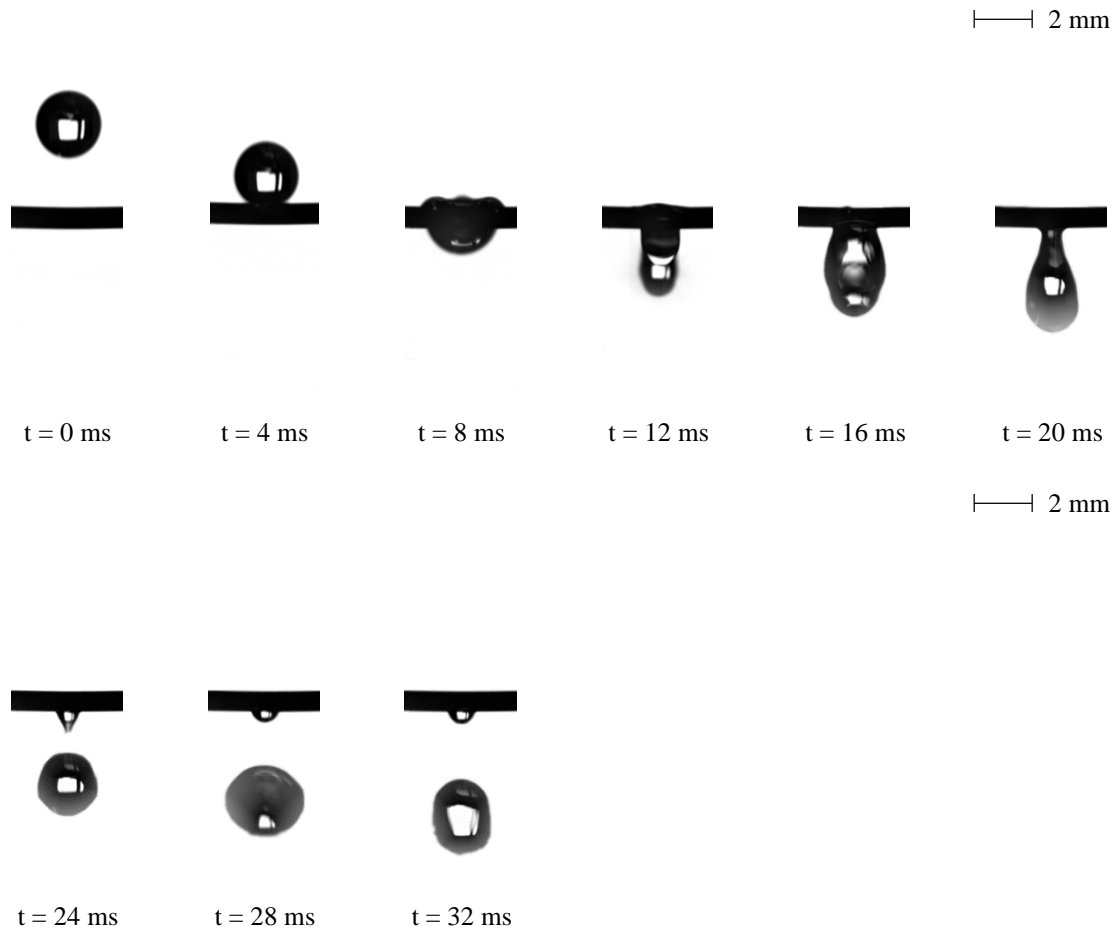


Figure 15: Outcome of droplet impact on copper wire ($R_f/R_d = 0.53$) (a) Captured ($R_f = 0.40$ mm; $V_1 = 0.490$ m/s) and (b) Not Captured ($R_f = 0.40$ mm; $V_1 = 0.518$ m/s)

The $V_{t,max}$ of droplet impact on a thin copper and stainless steel wire at different values of R_f/R_d (0.26 – 0.83) and R_f (0.4 and 0.625 mm) is shown in Figure 16, where it can be seen that the increase of R_f/R_d has resulted in the increase of $V_{t,max}$ for both cases using copper and stainless steel wire. From Figure 16, comparing the $V_{t,max}$ between the two wire size tested ($R_f = 0.4$ and 0.625 mm), for both copper and stainless steel wire, at the same R_f/R_d value of ~ 0.4 , the $V_{t,max}$ is higher at a lower value of R_f ($R_f = 0.4$ mm). This can be the result of larger droplet size at an R_f value of 0.625 mm. Figure 4 also shows the $V_{t,max}$ using stainless steel wire is lower than using copper wire, on average, it was $\sim 10\%$ lower for $R_f = 0.4$ mm and $\sim 5.5\%$ lower for $R_f = 0.625$ mm. The lower $V_{t,max}$ for stainless steel wire was the result of the higher static contact angle (85°) of stainless steel in comparison to copper wire (77°).

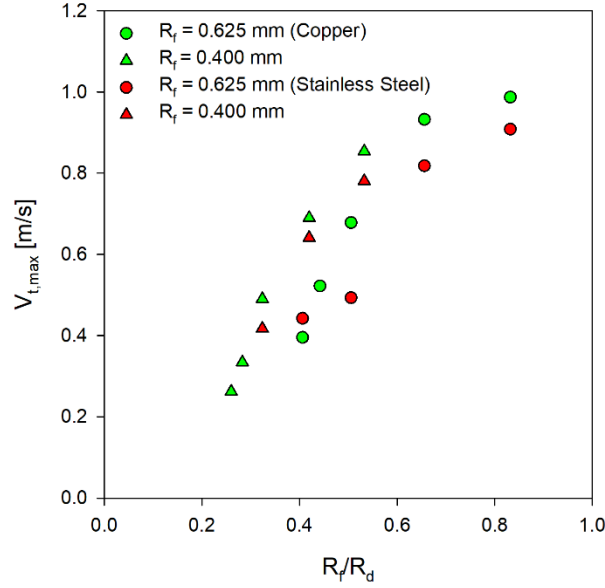


Figure 16: $V_{t,max}$ of droplet impact on a thin copper and stainless-steel wire at different values of R_f/R_d and R_f

2.6. Optimisation Methodology and Model Validation

In this study, the hybrid genetic algorithm (GA) (Holland, 1992) and Levenberg-Marquardt algorithm (LMA) (Levenberg, 1944; Marquardt, 1963) method was used to estimate the optimal values of the three constants (a_1 , b_1 , and c_1) in the empirical correlation of C_d (Eq. 8) by minimising the following objective function:

$$F = \sum_{i=1}^{R_{fn}} \sum_{j=1}^{R_{dn}} [V_{t,max(i,j)}^{exp} - V_{t,max(i,j)}^{cal}]^2 \quad \text{Eq. 9}$$

where R_{fn} is the number of wire sizes (0.4 and 0.625 mm; $R_{fn} = 2$) and R_{dn} is the number of droplet sizes (0.75, 0.81, 0.95, 1.24, 1.41, and 1.54 mm; $R_{dn} = 6$). $V_{t,max(i,j)}^{exp}$ and $V_{t,max(i,j)}^{cal}$ are the experimental and calculated values of $V_{t,max}$ at different combinations of wire sizes (i) and droplet sizes (j), respectively.

The stochastic GA (Holland, 1992) was chosen used due to its ability in discovering global optima in a complex fitness landscape, solving multi objective function, and does not require any initial guesses for the parameters (Sivanandam & Deepa, 2008). However, the GA has a limited function in identifying local minima and required to be coupled with a local search technique. Thus, GA was coupled with the LMA (Levenberg, 1944; Marquardt, 1963), which is a deterministic local optimisation tool that are applicable in solving smooth and relatively

well-conditioned objective functions. The estimated parameters from the GA were used as initial guesses in the LMA to find the local minima.

Using the hybrid GA-LMA method, at each iterative step, the change in the objective function (Eq. 9) was checked against the tolerance limit and stopping criteria which was set to 1×10^{-10} with a maximum number of iterations of 10000. After using the hybrid GA-LMA method against the $V_{t,max}$ data of copper wire, the three constants to be used in the empirical correlation of Cd (Eq. 8) were found to be: $a_1 = 1.00744936$, $b_1 = -1.9998$, and $c_1 = 0.01$.

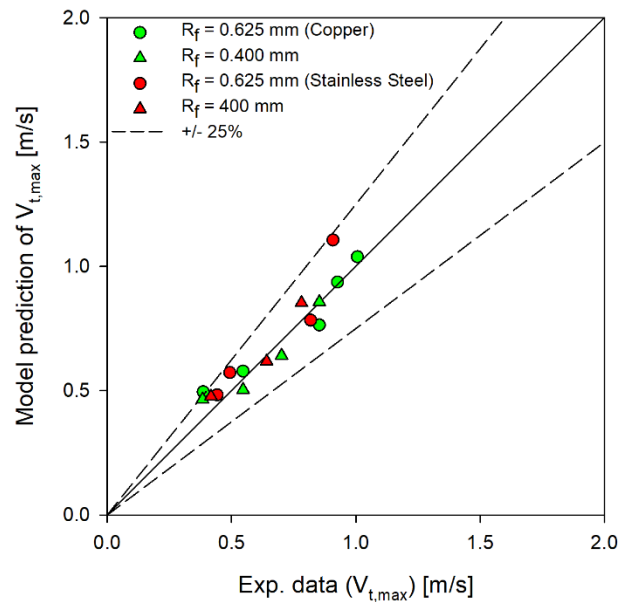


Figure 17: Comparison of $V_{t,max}$ values between the predictions from the proposed analytical model (Eq. 2) with the experiment data for copper and stainless-steel wire

Figure 17 shows a 25% parity plot that compares the values of $V_{t,max}$ between the predictions from the proposed analytical model (Eq. 2) with the experiment data for both copper wire and stainless steel). For copper wire, the proposed model resulted in predictions with the average error of $\pm 17\%$. This was expected since the constants in the empirical correlation of C_d (Eq. 8) were estimated using the $V_{t,max}$ experiment data of copper wire as a basis. The same coefficients that were previously obtained from the copper experiment data was also used to predict the $V_{t,max}$ experiment data of stainless steel. For stainless steel wire, the proposed model resulted in predictions with the average error of $\pm 11\%$.

2.7. Results and Discussion

2.7.1. Comparison of Analytical Models

The predictions of droplet capture velocity by the analytical models from different literatures (Gu et al., 2020; Kim & Kim, 2016; Lorenceau et al., 2004) for a set of system parameters (stationary medium = air, droplet = water, wire = nylon, $R_f = 0.00035$ m, variable R_d , $\sigma = 0.072$, $C_d = 2$, experimental data of (Lorenceau et al., 2004)) is shown in a 25% parity plot in Figure 18[a]. As the derivation method of these models are different, their predictions significantly vary for fixed system parameters. The difference between the model by Lorenceau et al. (Eq. T2 – 2) and the model by Kim and Kim remained constant over the range of droplet diameter, whereas the divergence between the Lorenceau model (Eq. T2 – 2) and Safavi-Nourazar model increases with the decrease in droplet diameter. Safavi and Nourazar's model provided predictions closer to the experimental data compared to the other two models. Additionally, using the other model by Lorenceau (Eq. T2 – 1), where there is an extra term added to take into account a constant (k), has yielded a significantly higher $V_{t,max}$ value in comparison to other models at a lower range of droplet radius ($R_d \sim 0.6 - 0.8$ mm). The significant difference in the prediction of the $V_{t,max}$ value can be attributed the higher value of the calculated drag force when using Eq. T2 – 1 by Lorenceau. For a particular droplet diameter of 0.00129 m, the comparison of predicted $V_{t,max}$ and the calculated values of by the three different analytical models (Gu et al., 2020; Kim & Kim, 2016; Lorenceau et al., 2004) shown in Figure 18[b]. These models have predicted different values of drag and contact forces. For the drag force, the two models presented by Lorenceau et al. (Eq. T2 – 1 and Eq. T2 – 2) have calculated two different values of drag force. Eq. T2 – 1 has calculated a drag force value that is ~ 3.35 times higher than Eq. T2 – 2. The drag force calculated by the Kim and Kim model was comparable to that of Lorenceau et al. (Eq. T2 – 2). There was no significant difference in the calculated value of contact force from the Lorenceau et al. model and Kim-Kim model, while the difference in the order of magnitude was observed in the value of drag and contact forces calculated by Safavi and Nourazar's model and those from the other two models. Additionally, in most cases, within each study, the drag force and surface tension force are comparable. As highlighted earlier, Lorenceau et al. (Lorenceau et al., 2004) and Kim and Kim (Kim & Kim, 2016) used C_d value of 2 and 1 respectively, whereas Safavi and Nourazar (Safavi & Nourazar, 2019) considered a variable C_d which was equal to $2R_d$. The variation in C_d with the droplet diameter is critical for reasonable agreement between the predictions from Safavi and Nourazar's model and experimental data.

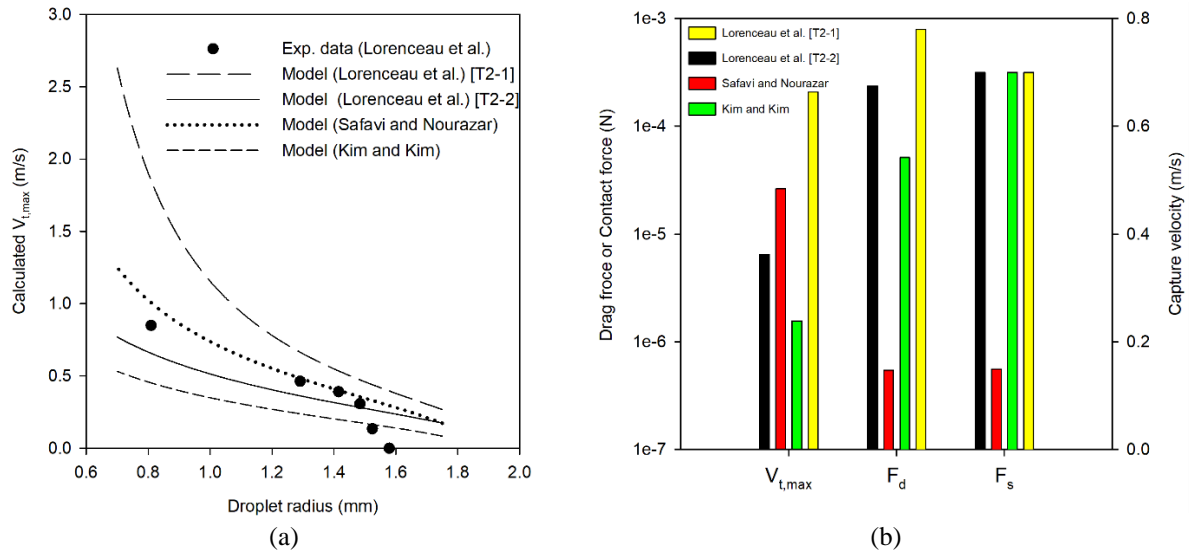


Figure 18: (a) Comparison of analytical model predictions ($R_f = 0.000350$ m), and (b) comparison of drag and surface contact force on the droplet under captured condition from different analytical model ($R_f = 0.000350$ m, $R_d = 0.00129$ m, Lorenceanu et al. – Eq. T2 - 2, Safavi and Nourazar – Eq. T2 - 13, and Kim and Kim – Eq. T2 - 8)

Due to the differences in the predicted capture velocity and calculated forces, it is important to compare these models against different experimental data sets. The comparison of the calculated values of droplet capture velocity by (Lorenceanu et al., 2004) (Eq. T2 – 2), (Kim & Kim, 2016), and (Safavi & Nourazar, 2019), against the experimental data of (Lorenceanu et al., 2004) is shown in a 25% parity plot in Figure 19[a]. For fibre diameter of $350 \mu\text{m}$, all three models predicted the experimental data with a discrepancy more than $\pm 20\%$. For fibre diameters of 250 and $150 \mu\text{m}$, the predictions from Safavi and Nourazar’s model were closer to the experimental data with a discrepancy of less than $\pm 20\%$, whereas the other two models resulted in significant higher discrepancy. Figure 19[b] shows the average error from each of the three models for each of the three experimental data sets ($R_d = 350, 250$ and $150 \mu\text{m}$). Note that the average error was calculated as $|V_{t,max,exp.} - V_{t,max,predicted}| / V_{t,max,exp.}$. The Lorenceanu model and Kim-Kim model resulted in an average error of 30 to 40% for all three data sets, whereas the Safavi and Nourazar model resulted in an average error in the range of 15 to 40%.

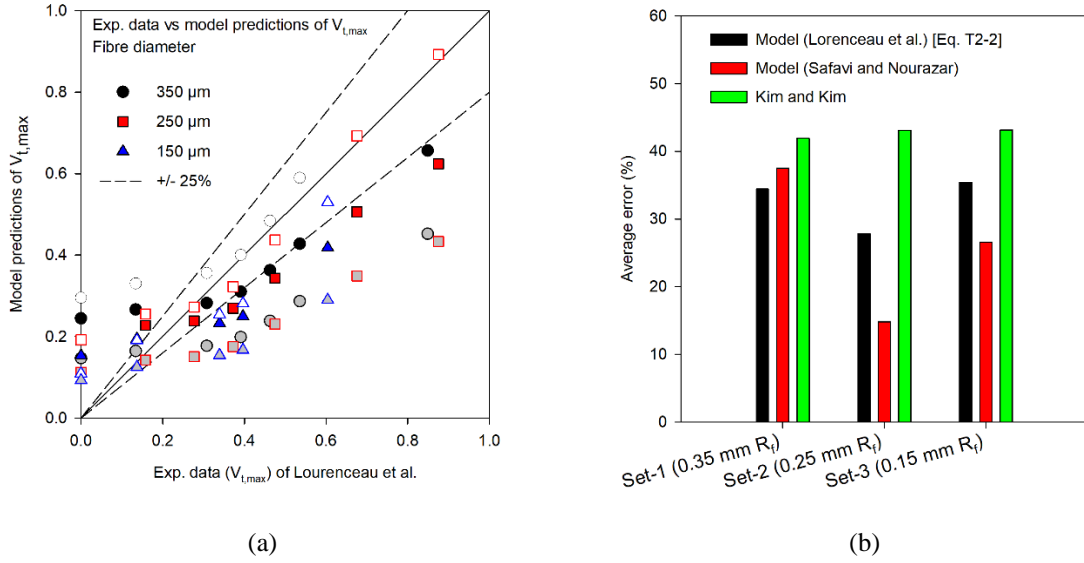


Figure 19: (a) Comparison of model predictions and experimental data of Lorenceau et al. (Lorenceau et al., 2004) (\bullet – Lorenceau model Eq. T2 – 2, \circ – Safavi and Nourazar model, \bullet – Kim and Kim model), and (b) average error in predictions of Lorenceau et al.’s experimental data from different analytical models

The current study proposed a new analytical model (Eq. 2) with variable C_d value (Eq. 8). The predictions of $V_{t,max}$ from the proposed model against multiple experiment data (Lorenceau et al., 2004); (Kim & Kim, 2016); (Safavi & Nourazar, 2019); (Khalili et al., 2016) are shown in a 25% parity plot in Figure 20. The predictions from the proposed model were in agreement with the experimental data within the range of an $V_{t,max}$ value between 0.35 m/s to 0.65 m/s, with discrepancies within $\pm 25\%$. To be able to predict $V_{t,max}$ values below 0.35 m/s or above 0.65, the coefficient a_1 in Eq.8 needs to be adjusted and optimised to accommodate different wire materials since the constants in Eq.8 ($a_1, b_1,$ and c_1) were obtained through the parameter estimation using the hybrid GA-LMA method, which was from the experiment data presented in this study using copper wires.

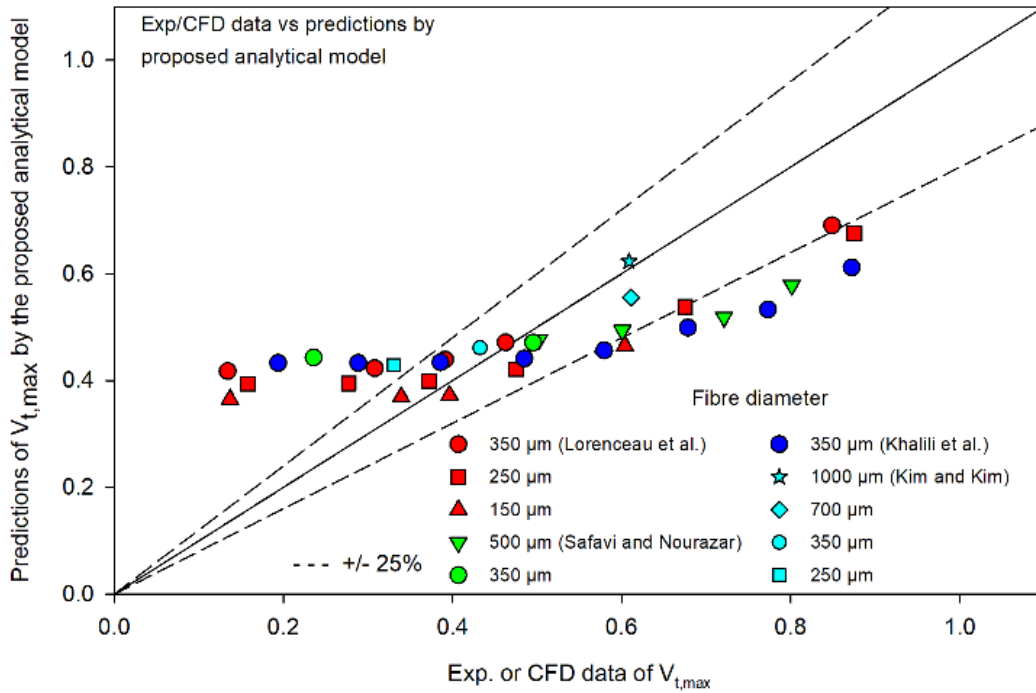


Figure 20: Predictions of $V_{t,max}$ from the proposed model against different experimental data sets (Lorencean et al., 2004), (Kim & Kim, 2016), (Safavi & Nourazar, 2019), and (Khalili et al., 2016)

2.7.2. Effect of Wire Size and Fluid Properties on $V_{t,max}$

Figure 21[a] shows the effect of wire radius on the predictions of $V_{t,max}$ by the proposed analytical model. For all three simulated wire diameters (350 μm , 250 μm and 150 μm), the predicted values resulted in minima with the values increasing at either side of the minimum value in each profile. Interestingly, the minimum $V_{t,max}$ in each profile coincided with the value of R_m calculated by Eq. T2-4. R_m represents the threshold droplet radius for which a droplet can be captured at an impact velocity of zero (0 m/s). In other words, it represents the maximum radius of the droplet that can be captured by balancing only gravity and surface tension forces. This proves the ability of the proposed model to capture R_m , referred to as the characteristic length scale of a droplet in previous studies (Lorencean et al., 2004; Safavi & Nourazar, 2019), for different wire diameters. Additionally, noteworthy that previous studies (Lorencean et al., 2004; Safavi & Nourazar, 2019) have reported the variation in $V_{t,max}$ only for $R_d < R_m$. However, in this study, the variation in $V_{t,max}$ for an R_f/R_d value between 0 to 1 is shown in Figure 21[a]. At $R_f/R_d > R_f/R_m$, the increase in wire radius resulted in a significantly decreased value of the predicted $V_{t,max}$. For example, at an R_f/R_d of 0.5 the value of $V_{t,max}$ was ~ 2.2 m/s for 150 μm wire and that was ~ 0.7 m/s for 350 μm wire. The effect of wire size on $V_{t,max}$ can be attributed to the variation in the drag force and surface tension force. For a given wire size, the surface tension force remains constant with the variation in droplet

size; however, the drag force varies with both droplet and wire size. This can be achieved by having the variable C_d as a function of C_d , R_f , R_d and two viscosities (μ_1 and μ_3). The variation in C_d value for three wire sizes and the range of droplet diameters are shown in Figure 21[b]. The C_d declined with wire sizes, and for a given wire size, it declined rather steeply with the decrease in droplet size. Figure 21[c] shows the predictions of drag force and Figure 21[d] shows the $V_{t,max}$ at different wire sizes and the ratio of diameters (R_f/R_d) with water as the droplet (secondary phase). From Figure 21[c], it can be seen that the drag force decreases along with the increase of R_f/R_d , which is a similar trend to the prediction of the C_d , as shown in Figure 21[b]. From Figure 21[d], the effect of R_m can also be seen, where R_m coincides with an R_d value of ~ 0.001 at all simulated wire sizes, which is a similar trend to Figure 21[a].

Consequently, the ability of the proposed analytical model to capture $V_{t,max}$ was also tested for different liquids as a secondary phase. The selected liquids and their properties were summarised in Table 4. The selection of liquids was made to cover a wide range of viscosity (from 0.0009 to 0.97 kg/m.s) and surface tension (from 0.021 to 0.0727 N/m). The variation in the predicted $V_{t,max}$ for these four liquids and with an R_f of 350 μm is shown in Figure 22[a]. The value of $V_{t,max}$ increased with the increase in liquid viscosity. For example, $V_{t,max}$ for water at an R_f/R_d of 1 was found to be ~ 4.3 m/s; whereas that value for highly viscous silicone oil was ~ 17.3 m/s. The variation in the predicted value of C_d for the four different liquids is shown in Figure 22[b]. It can be seen that the C_d value for all four liquids are similar to each other, which can be attributed to the low coefficient value of c_1 in Eq. 8. The low coefficient value of c_1 in Eq. 8 has made it less sensitive to the changes of different viscosities of different liquids. Further fine-tuning of the c_1 coefficient is required in order to accurately predict the changes of $V_{t,max}$ for different liquids.

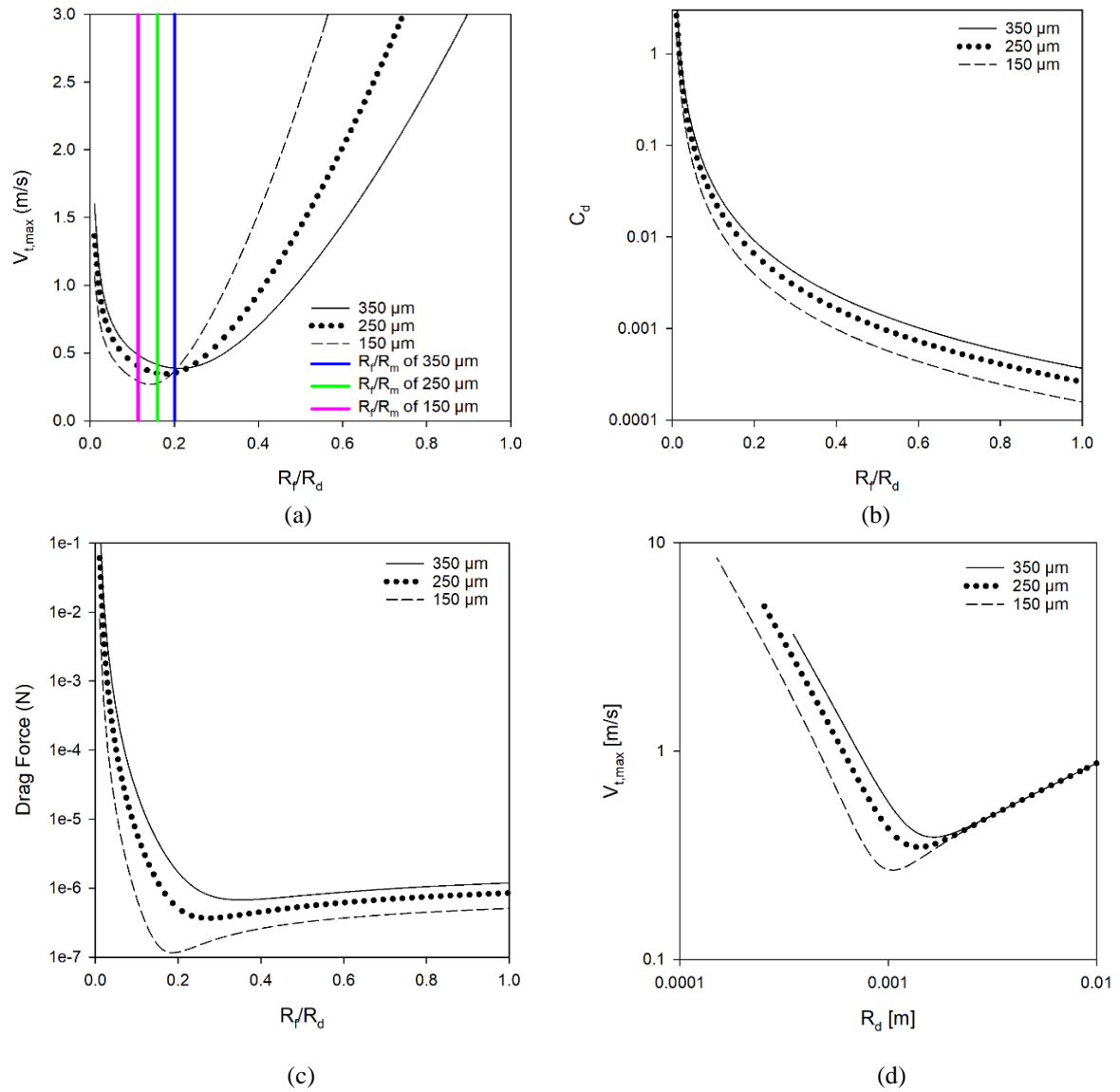


Figure 21: Predictions of (a) $V_{t,max}$, (b) drag coefficient, (c) drag force at different wire size and ratio of diameters (R_f/R_d) with water as the droplet (secondary phase); (d) Predictions of $V_{t,max}$ at different wire size and droplet size with water as the droplet (secondary phase)

Table 4: Physical Property of Different Fluids at 20°C			
	Density [kg/m ³]	Surface Tension [mN/m]	Viscosity [kg/ms]
Water	1000	72.7	0.00091
Ethylene Glycol	1113	48.4	0.0161
Ethanol	789	24.8	0.001095
Silicon Oil SO-1000	971	21	0.97

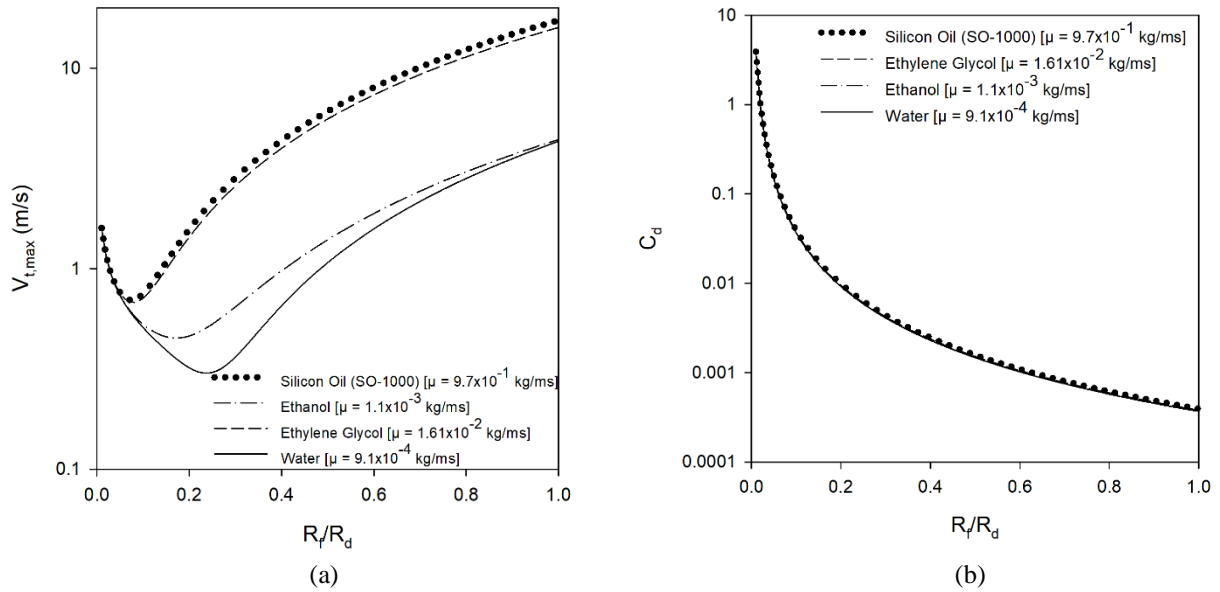


Figure 22: Predictions of (a) $V_{t,max}$ with different fluid properties of the droplet; (b) C_d at different ratio of diameters (R_f/R_d) with different fluid properties of the droplet

Exclusively for Section 2.7, it is adapted and modified from the following conference poster and presentation:

- M.D.M Priyambodo, T. Bhatelia, B. Sun, M. Shah, and V. Pareek, “Effect of Wire Shape and Size in Droplet Impact on a Wire”, *Chemeca 2021: Advance, Disrupt, and Sustain, Brisbane, Australia, 27th – 28th September 2021*. (Online oral presentation)
- M.D.M Priyambodo, T. Bhatelia, B. Sun, M. Shah, and V. Pareek, “Effect of Wire Shape and Size in Vapour-Liquid Separation”, *26th International Symposium on Chemical Reaction Engineering (ISCRE 26) and 9th Asia-Pacific Chemical Reaction Engineering Symposium (APCRE 9), New Delhi, India, 5th – 8th December 2021*. (Online poster presentation)

2.8. Effect of Wire Shapes and Sizes (Numerical Simulation)

In addition of the numerical and experimental research studies presented in previous sections of Chapter 2 (Section 2.2 – Section 2.7.2), a parametric numerical CFD study using ANSYS Fluent was conducted to investigate the effect of wire shapes and sizes towards the $V_{t,max}$ in a system of a single droplet impacting upon a single thin wire. The dimension of the rectangular 2D computational domain, as shown in Figure 23, was 3 mm in width and 6 mm in height, which was equivalent to 15 x droplet diameter in width and 30 x droplet diameter in height. For the mesh resolution, a single droplet of 200 μm was resolved using 90 cells in the radial direction.

The volume of fluid (VOF) multiphase model was used, and the air-water surface tension was set to be 0.072 N/m with the wall adhesion forces included, and a wall contact angle of 90° was used. The laminar viscous model was used since the maximum Reynolds number tested was 812 at an inlet air velocity of 4 m/s. The inlets were modelled using the velocity-inlet boundary condition, and the outlet were configured as pressure-outlets. The

simulated wires with different shapes were modelled as a hollow object with walls in the middle of the fluid domain. Wall adhesion forces along with a wall contact angle of 90° was included to the walls of the simulated wires. A no-slip boundary condition was assigned to the other walls that form the rectangular fluid domain. The SIMPLE scheme was used for the pressure-velocity coupling, and the pressure staggering option scheme (PRESTO) was used for the pressure interpolation. The least-square cell-based method was used for the evaluation of gradients. A second-order upwind discretisation was applied for the momentum equation. The geo-reconstruct solution method was used for the volume fraction discretisation, and the first order implicit discretisation was applied for the transient formulation. To minimise truncation errors, a double-precision solver was used. The results for each timestep were converged with the continuity residuals below 1×10^{-3} , the velocity residuals below 1×10^{-5} , and the global mass fluxes were balanced.

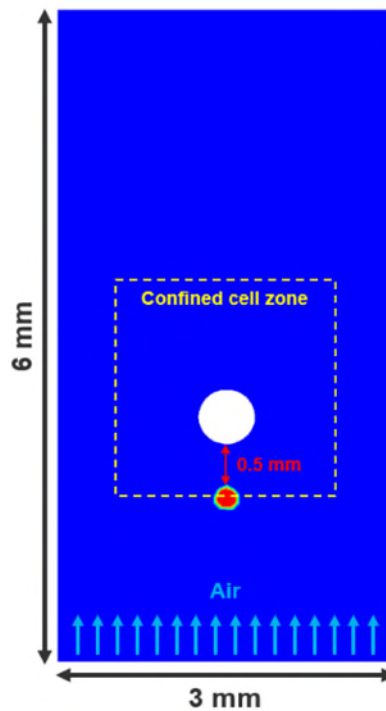


Figure 23: 2D Flow domain of droplet impact on a thin wire

The CFD model was qualitatively validated against images of droplet impact outcome that shows the splitting phenomena from two experimental and analytical studies. Figure 24[a] shows images of droplet impact from the numerical CFD simulation from this study, while Figure 24[b] and Figure 24[c] show the numerical simulation result from (Zheng et al., 2018) and the experiment result by (Kim & Kim, 2016), respectively. The numerical CFD model presented in this study focused on a droplet impact system against gravity (rising droplet), while the literature data (Kim & Kim, 2016; Zheng et al., 2018) focused on a droplet

impact system in the direction of gravity (falling droplet). Comparing Figure 24[a] with Figure 24[b] and Figure 24[c], the numerical CFD model presented in this study produced results of droplet impact outcome showing the splitting phenomena similar to both studies (Kim & Kim, 2016; Zheng et al., 2018).

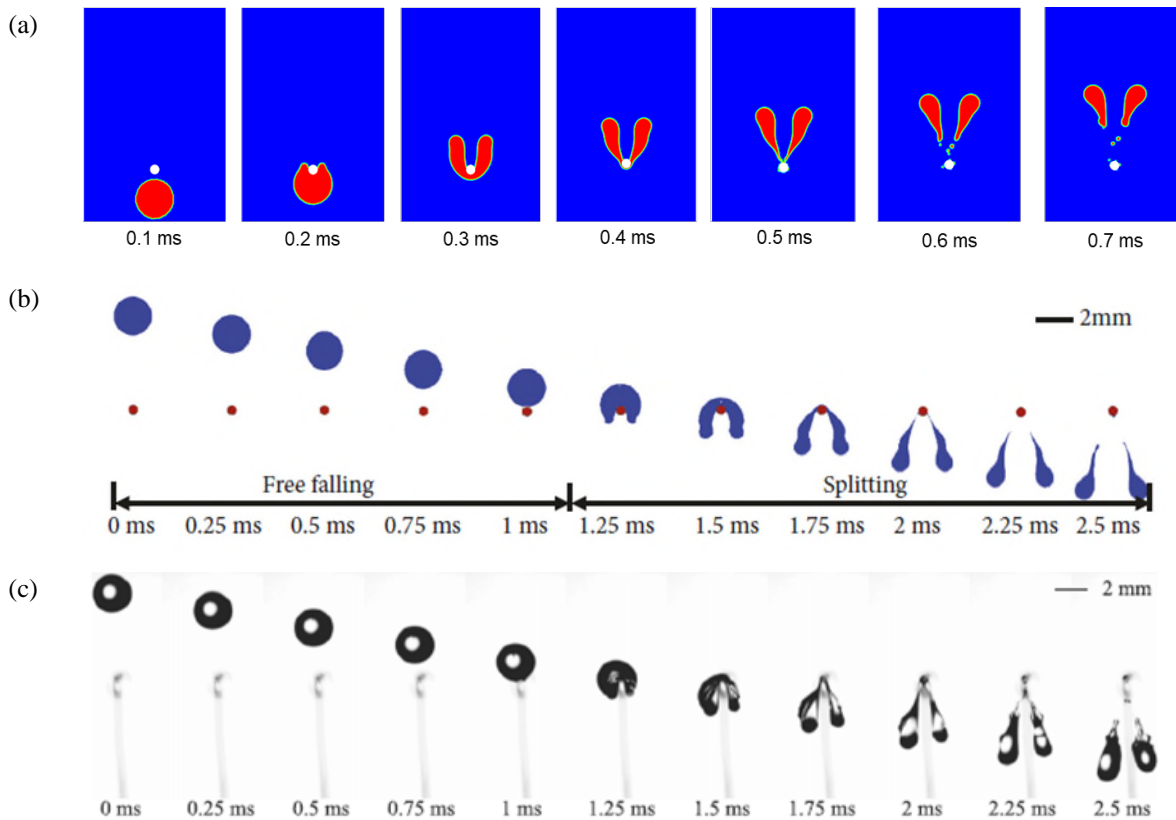


Figure 24: Qualitative comparison of the droplet impact outcome for (a) Numerical simulation result (Present study) (b) Numerical simulation result (Zheng et al., 2018) (c) Experiment high-speed imaging result (Kim & Kim, 2016)

In this numerical CFD study, the $V_{t,max}$ was determined at the maximum air inlet velocity, at which 100% of the droplet mass was still attached to the surface after impacting the wire. A confined cell zone was introduced to measure the mass of the water attached to the wire surface, which is the yellow dashed box, as shown in Figure 23. Using this method, only the mass of the water attached to the surface will be reported, and the remaining mass of the water attached to other parts of the fluid domain (i.e. outer wall) will be ignored.

Through the parametric study, the $V_{t,max}$ for different wire shapes at different ratios of diameter (wire-to-droplet) were calculated, as shown in Figure 25[a-d]. From these figures, the effect of surface topology was observed; it can be seen that the $V_{t,max}$ increases with the increase of the ratios of diameter. Additionally, for a square wire (Figure 25[a]) and triangle wire (Figure 25[b]), the droplet impact is normal to the wire surface/plane, producing similar

$V_{t,max}$ values, from 1.50 m/s to 2.50 m/s, across all R_f/R_d tested. However, a different trend was observed for a circle wire (Figure 20[c]) and an inverted triangle (Figure 20[d]), where the droplet impact is not normal to the wire surface. The calculated $V_{t,max}$ values for a circle wire (Figure 25[c]) and an inverted triangle wire (Figure 25[d]) ranges from 0.75 m/s to 4.0 m/s and 0.75 m/s to 2.00 m/s, respectively. The highest $V_{t,max}$ observed was 4.00 m/s using the circle wire at an R_f/R_d of 5. However, it must be taken into account that a higher R_f/R_d also implies a mesh pad specification with low porosity, potentially resulting in a higher pressure drop.

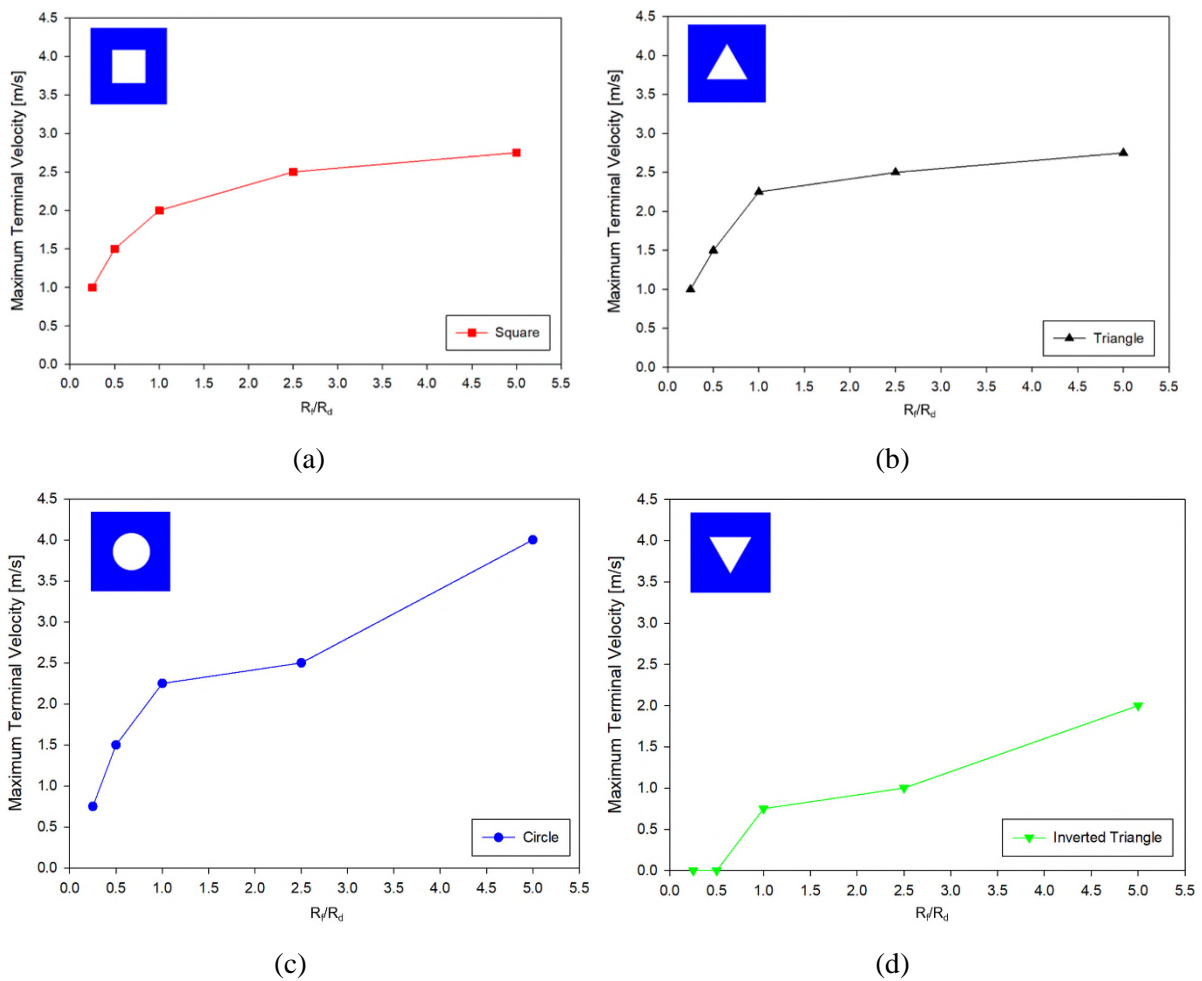


Figure 25: Prediction of $V_{t,max}$ for different wire shapes at different ratios of diameter (wire-to-droplet): (a) Square; (b) Triangle; (c) Circle; (d) Inverted Triangle

2.9. Conclusion

In this work, the previously proposed analytical models (Lorenceanu et al., 2004)(Gu et al., 2020; Kim & Kim, 2016) to calculate the $V_{t,max}$ of droplet capture on a wire were critically reviewed. The consequence of using a fixed value of drag coefficient along with the other simplifications presented in the previous models has resulted in an average error of up to 40%, when comparing the predicted $V_{t,max}$ with the available experiment data. A new analytical model was proposed to calculate $V_{t,max}$ that includes a correlation that was developed to predict the C_d as a function of fundamental physical properties of the fluid (the ratio of viscosities) and operating parameters (ratio of diameters). Contact angle was measured for different types of surfaces, that includes, copper, stainless steel, aluminium, tin, and brass. Once the contact angles were measured, droplet capture experiments were carried out using different wire material (copper and stainless steel), different droplet sizes, and different wire sizes. The $V_{t,max}$ was measured using high-speed imaging technique. From the experiment, it was found that the increase of R_f/R_d has resulted in the increase of $V_{t,max}$. It was also found that comparing the $V_{t,max}$ between the two wire size tested ($R_f = 0.4$ and 0.625 mm), at the same R_f/R_d value of ~ 0.4 , the $V_{t,max}$ is higher at a lower value of R_f ($R_f = 0.4$ mm). This can be the result of larger droplet size at an R_f value 0.625 mm. The $V_{t,max}$ using stainless steel wire is lower than using copper wire, on average, it was $\sim 10\%$ lower for $R_f = 0.4$ mm and $\sim 5.5\%$ lower for $R_f = 0.625$ mm. The lower $V_{t,max}$ for stainless steel wire is because stainless steel has a higher static contact angle (85°) in comparison to copper wire (77°).

The $V_{t,max}$ data from the experiment was also used to estimate the parameters in the newly developed correlation for the variable C_d . The parameter estimation was conducted using the GA-LMA method and it was found that the three constants to be used in the empirical correlation of C_d (Eq. 8) were: $a_1 = 1.00744936$, $b_1 = -1.9998$, and $c_1 = 0.01$. Using these constants in the empirical correlation of C_d (Eq. 8), the proposed analytical model (Eq. 2) was tested for different experiment data (Khalili et al., 2016; Kim & Kim, 2016; Lorenceanu et al., 2004; Safavi & Nourazar, 2019). The prediction from the proposed analytical model (Eq. 2) was in agreement with the provided experiment data within the range of an R_f/R_d value between $0.26 - 0.83$, with discrepancies within $\pm 25\%$.

The proposed analytical model was also used to study the effect of wire size. It was found that for all of the simulated wire diameters, the predicted $V_{t,max}$ decreased significantly with the increase of wire radius (R_f). This phenomenon can be attributed to the variation in the drag force and surface tension force for different combinations of wire size and droplet size. The variation in drag force was able to be captured in the proposed analytical model by

having a variable C_d value. The variation of C_d with respect to different wire sizes were also calculated. It was found that the value of C_d declined with the decrease of wire size and droplet size. Additionally, the predicted minimum values of $V_{t,max}$ for all simulated wire diameters coincided with the value of R_m , which represents the maximum radius of droplet that can be captured by balancing only gravity and surface tension forces.

Additionally, since the proposed analytical model has included a term for the ratios of viscosities (μ_3/μ_1), the effect of fluid properties on $V_{t,max}$ was also studied. It was concluded that the predicted $V_{t,max}$ increased with the increase of liquid viscosity. The variation of the predicted C_d value for all of the four different liquids were minimal, which can be attributed to the low value of coefficient c_1 , making it less sensitive towards the change in the viscosity of different liquid. To increase the accuracy in predicting changes of $V_{t,max}$ for different liquids, further fine-tuning of the c_1 coefficient is required.

For the numerical simulation study on the effect of wire shapes and sizes towards the $V_{t,max}$, it can be concluded that an optimum combination of ratio of diameters, mesh pad porosity, and wire shape can lead to a knitted mesh pad specification with an improved separation efficiency and reduced pressure drop. Additionally, an optimised wire geometry from this numerical simulation study can be used to conduct a multi-scale shape optimisation study that can improve the separation efficiency and reduce the pressure drop in vapour-liquid separators.

Chapter 3 Gas-gas Hydrodynamics of a Fractal Flow Mixer

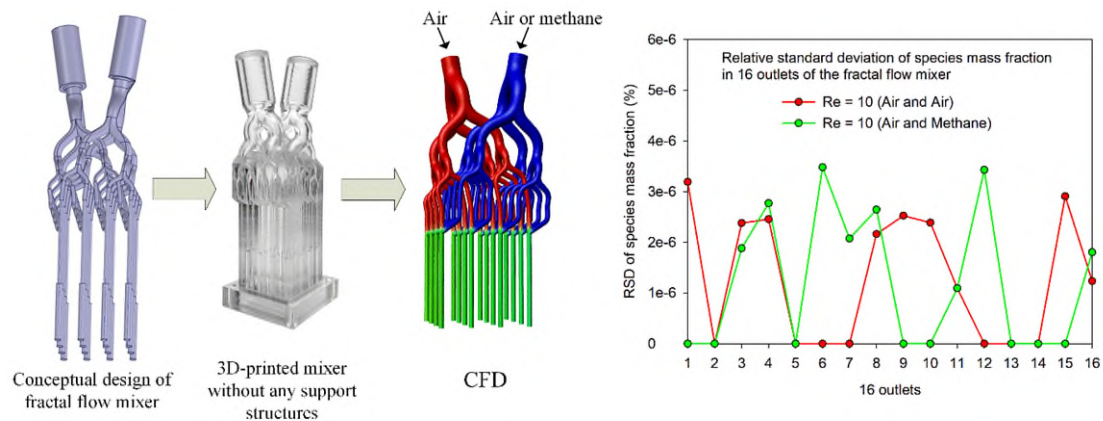
The content of Chapter 3 is reprinted (adapted) with permission from the following publication:

- M.D.M. Priyambodo, M. Mazur, J. Patel, M. Shah, B. Sun, V. Pareek, M. Brandt, P.A. Webley, and T. Bhatelia, "Numerical evaluation of an additively manufactured uniform fractal flow mixer" *Chemical Engineering and Processing – Process Intensification*, vol. 179, p. 109047, 2022/09/01 2022, doi: <https://doi.org/10.1016/j.cep.2022.109047>.

Abstract

The uniform distribution and mixing of fluids are a common functional requirement in a range of process intensified fluid handling applications. Traditional manufacturing processes have limited the design and performance of flow distributors and mixers. However, the maturing of additive manufacturing (AM) has increased the range of manufacturable geometries, enabling the construction of novel high-performance flow distribution devices. In this work, a novel flow distributor design was proposed, called the fractal flow mixer, which combines the function of a flow distributor and a mixer into a single device. The fractal flow mixer was designed using the concept of self-similar bifurcating channels that symmetrically bifurcates a flow into multiple channels, achieving flow uniformity through a series of sequential stages. After four stages of bifurcation, a y-junction on each channel was introduced before the outlet, mixing the flow from two modules. The bifurcating angle of the fractal flow mixer was carefully selected to remove the requirement of support structures when manufactured. The fractal flow mixer was successfully manufactured using vat photopolymerisation (VP) and laser powder bed fusion (L-PBF) techniques without any supports, minimising material waste and eliminates the procedure of the removal of support materials on the internal part features, which is a complex procedure, especially at mili-scale. Computational fluid dynamics (CFD) simulations were carried out to characterise the hydrodynamics and mixing performance of the newly designed mixer over a range of operating conditions and for mixing two gases. Effect of inlet Reynolds numbers (Re) and flow ratio was studied, the maximum relative standard deviation (RSD) was found to be ~8%, and majority of the flow was uniformly mixed with a distribution index close to unity. Additionally, the mixing performance for the fractal flow mixer was found to be highly governed by the inlet Re , which caused flow segregation at a higher inlet Re , even at varying IFRs. Whilst the mixing performance is governed by the inlet Re , due to the y-junction geometry at the mixing point of the fractal flow mixer, the pressure drop was primarily governed by the IFR. The ability of the fractal flow mixer to mix two different gases, and maintaining uniform flow distribution at different inlet flowrates, can be beneficial for a wide range of industrial applications.

Graphical Abstract



3.1. Introduction

The efficiency of many industrial and domestic processes, such as reactors, heat and mass transfer equipment, separators, air conditioners, irrigations systems and gas burners, are governed by the effectiveness of the fluid flow system to uniformly distribute and/or mix multiple fluids (Afshari et al., 2017; Ascough & Kiker, 2002; Barbosa et al., 2021; Bassiouny & Martin, 1984; Karki & Patankar, 2006; Lu et al., 2008; Luo et al., 2007; Luo et al., 2008; Park et al., 2016; VanGilder & Schmidt, 2005; Wang, 2008; Wang et al., 2016; Wen et al., 2006; Wichangarm et al., 2020; Zhao et al., 2016). Depending on the application and nature of the fluids involved, two approaches are used to achieve flow distribution and mixing. These involve premixing the fluids using a mixer followed by a flow distributor or vice versa. Regardless of the approach, an ineffective fluid flow distributor and mixer can affect up to 20-25% of the efficiency of the process (Sinnott & Towler, 2019a).

Flow distributor systems can generally be classified into three categories: (i) parallel with a high number of flow divisions per stage (i.e. manifold distributors); (ii) sequential with a low number of divisions per stage but a high number of stages based on self-similar bifurcating channels, also known as *fractal*; and (iii) a combination of both sequential and parallel schemes (Mazur et al., 2019). Traditionally, the flow distribution performance through manifold distributors is characterised analytically using the simple energy balance (the Bernoulli equation) and momentum conservation theorems. However, to fully understand and optimise the manifold distributors, it is important to estimate the frictional losses and conserve energy in all streamlines of the fluid flow inside the manifold. Using the Bernoulli equation is challenging because every division of the streamline would require a specific energy equation, which adds complexity (Wang et al., 2001). To avoid such complexity, previous studies

(Bajura, 1971; Bassiouny & Martin, 1984; Shen, 1992) introduced a momentum equation along the length of porous pipe and included either a constant pressure recovery and friction factors or a semi-empirical form of performance parameters. Whilst these approaches can predict the experimental data; they do not provide a detailed understanding that would allow optimisation of manifolds for reduced pressure loss and even distribution of the flow. (Tomor & Kristóf, 2016) developed a discrete model for flow distribution in manifolds (Wang et al., 2001). (Tomor & Kristóf, 2016) compared the results from the discrete model with the predictions from Computational Fluid Dynamics (CFD) study against experimental data and found reasonable agreement at low Re. Both CFD and discrete models from this study had some deviations at higher Re. (Barbosa et al., 2021) proposed a manifold with prismatic channels named the channelCOMB for mesoreactors. The channelCOMB design was tested at different Re and geometric parameters to analyse the flowrate distribution. It was found that the distributor was suited to be operated at a lower flow rate (laminar flow). In the channelCOMB design, the flow distribution performance was governed by the main chamber expansion and the length of the outlet channels. The accuracy of the manufacturing technique governs the distribution of the outlet channel widths, which also significantly impacts the flow distribution performance. Although manifold distributors have been studied for several decades, this type of distributor is often characterised by large-diameter ratios between the inlet and the outlet resulting in significant pressure loss and uneven distribution (Lu et al., 2008; Pigford et al., 1983).

On the other hand, self-similar bifurcating channels or *fractal* approach utilises a design that symmetrically bifurcates a flow into multiple channels to achieve flow uniformity through a series of sequential stages. In nature, there are several examples of such natural fractals, including but not limited to rivers, branches of trees, channels in human lungs, distribution of nerves, arteries and veins, etc. (Bejan, 2000). From a point source, an extensive network of 2^n flow streams can be created, with n being the number of bifurcations (Barbosa et al., 2021). Self-similar bifurcating channels can be designed in two and three-dimensional flow distributor arrangements with multiple flow channels. Such bifurcated channels have been applied to many engineering applications, including heat exchangers (Luo et al., 2007; Luo et al., 2008), microchannel reactors, and fluid distributors (Mazur et al., 2019; Wechsato et al., 2002) (Wechsato et al 2002) developed and optimised a radial flow distribution system that sequentially bifurcates flow from a central inlet to many equidistant, radially distributed outlets. (Luo et al., 2007; Luo et al., 2008) conducted an experimental and CFD study comparing pressure drop and thermal performance of different mini crossflow heat exchanger

configurations equipped with a combination of a novel constructal (bifurcating) distributor and a conventional pyramid distributor at the inlet and the outlet. It was found that the heat transfer performance was dominated by the type of the distributor and a combination of a constructal (bifurcating) collector, and a pyramid distributor showed an improved heat transfer performance. However, the effect of the distributor on the pressure drop, degree of non-uniformity and parametric constraints were not provided. Constructal or bifurcating distributors have been studied extensively, for the effect of bifurcating stages, angles of bifurcation, fluid flow conditions and topology minimisation (Cao et al., 2018; Liu et al., 2012). In general, these studies have shown that being able to operate multiple flow channels uniformly would result in lower pressure losses by minimising energy dissipation and can improve the overall uniformity and performance of industrial devices. However, with such extensive theoretical work, the optimum configurations often remain difficult to manufacture at a large scale as the relationship between the hydrodynamic and geometrical parameters does not take into account the challenges associated with additive manufacturing of these distributors. Some of the authors of this work have previously developed such correlations and showed how practically a uniform fluid flow distributor could be designed that is scalable and manufacturable (Mazur et al., 2019).

In addition to flow distributors, when more than one fluid is present in the process, inline static mixers are used with the distributor to mix two or more miscible fluids (Goldshmid et al., 1986). The material and design of static mixers depend on their application and flow regime (laminar or turbulent). The physical phenomena of mixing can be divided into mesomixing, micromixing, and macro mixing (Ghanem et al., 2014). Whilst, numerous variants of static mixers show a wide range of mixing performance for an exhaustive list of operating and fluid conditions, the major challenge lies in the ability of the fluid flow distributors to feed the multiple fluids to the mixer in controlled flow ratios with minimum pressure loss. Similar to flow distributors, the design of the static mixers is often limited to traditional manufacturing techniques. For many industrial applications and processes, the fluid distributors and static mixers are two separate equipment, which may add to the complexity of the overall process. In this work, AM and CFD simulations were used to design, manufacture, and investigate the hydrodynamic performance of a novel fractal flow mixer design. The fractal flow mixer presented in this study has the ability to provide uniform flow distribution and mixing using a single device. With a scale-up strategy, the fractal flow mixer would have a potential to be used for different industrial applications, reducing the need and complexity of using multiple equipment for fluid distribution and mixing.

3.2. Methodology

3.2.1. Fractal Flow Distributor and Mixer Design

In their prior work (Mazur et al., 2019), the authors presented a flow distributor design based on a fractal-like recursive bifurcation scheme (Mazur et al., 2019) (Figure 26[a-d]). The design was shown to exhibit high levels of outlet flow uniformity over a wide range of flow rates and outlet channel configurations due to inherent bifurcating flow path symmetry. In the current work, the uniform flow distributor design was duplicated to form a flow distribution and mixer system comprising of two nested flow distributors (referred to as modules) (Figure 26), enabling the distribution and/or mixing of two independent fluids in close proximity with high uniformity. Concurrently the design satisfies the following design objectives:

- High outlet channel packing density.
- Symmetry of module fluid pathways to provide equivalent flow conditions and reduced design effort.
- The separation distance between pathway channels is sufficient to allow channel wall thickness to satisfy structural and manufacturability requirements.
- The separation distance between the module inlets is sufficient to ensure no interference between associated connection fittings.
- A straight flow path at each module inlet prior to entering the initial bifurcation stage, to avoid bend-induced shear flows which could reduce bifurcation uniformity.

In addition to the characteristics defined in previous work, which apply to each flow distribution module (Mazur et al., 2019), the extended design is subject to a series of additional geometric parameters required to integrate the two independent flow distribution modules without interference. The modules are inclined at a *transition plane* and symmetrically mirrored around the *outlet plane*, normal axis of symmetry. The modules are located on the transition plane such that the axis of symmetry of the module (also referred to as the transition plane centreline) is linearly offset along the transition plane axes to avoid channel pathways interference. The potential for interference depends on several parameters including: the number of stages (N), the position of the transition plane, the associated bifurcation unit spacing (S_j), and channel wall thickness (T_{ji}) and (T_{jo}) (Figure 26[a-c]). The transition plane inclinations and centreline offsets provide degrees of freedom for achieving a desired separation distance between the inlets of both channel pathways while avoiding channel interference. The outlet plane comprises a uniformly interspaced array of channel

outlets for both modules. Located between the *outlet* and *transition planes* is an array of connecting channels which compensate for the inclined modules above, realigning the flow to the *outlet plane* normal. The connecting channels are tangential to the normal vectors of the outlet and transition planes. For the designs considered in this work, the transition plane is positioned at the outlet of stage $j = 4$ of the flow distributor (Figure 26[d]); however, the plane can be positioned at different stage locations if desired. Positioning at lower values of j results in fewer required connecting channels for realigning the flow, which decreases modelling effort as each channel has a unique geometry. However, positioning the transition plane at lower values of j can also increase the required inclination plane angles in order to avoid interference between channel pathways, as upper stage units are nested comparatively closer than downstream units. Furthermore, this can also increase the size of the device for the reasons explained below.

Directional changes in the connecting channels between the inclined transition plane and the horizontal outlet plane can introduce axial asymmetry in the flow path. Excess axial asymmetry in the flow subsequently entering a bifurcation unit can compromise the downstream uniformity of flow distribution (Mazur et al., 2019). The recovery to uniform axisymmetric flow following deviations introduced by turns in the flow path is typically proportional to the length to diameter ratio of the associated fluid channel (Narayana N. Pillai & Ramakrishnan, 2006). For a given length to diameter ratio, the connecting channel length will increase when positioning the transition plane at lower values of j due to the larger associated diameter. This in turn will increase the overall size of the device. As such it is desirable to position the transition plane at larger values of j in order to minimise device packaging space. To balance the compromise between modelling effort, channel pathway interference and packaging space, the transition plane was positioned at the outlet of stage $j = 4$.

Furthermore, although a symmetric layout of modules achieves equivalent flow conditions and simplifies design effort (as analysis is only necessary for a single channel pathway), the layout can also be structured asymmetrically to achieve intentionally different flow conditions. Finally, further stages can be added to the flow distributor design in both single and dual channel pathway configurations in order to target desired application requirements, such as a larger outlet area.

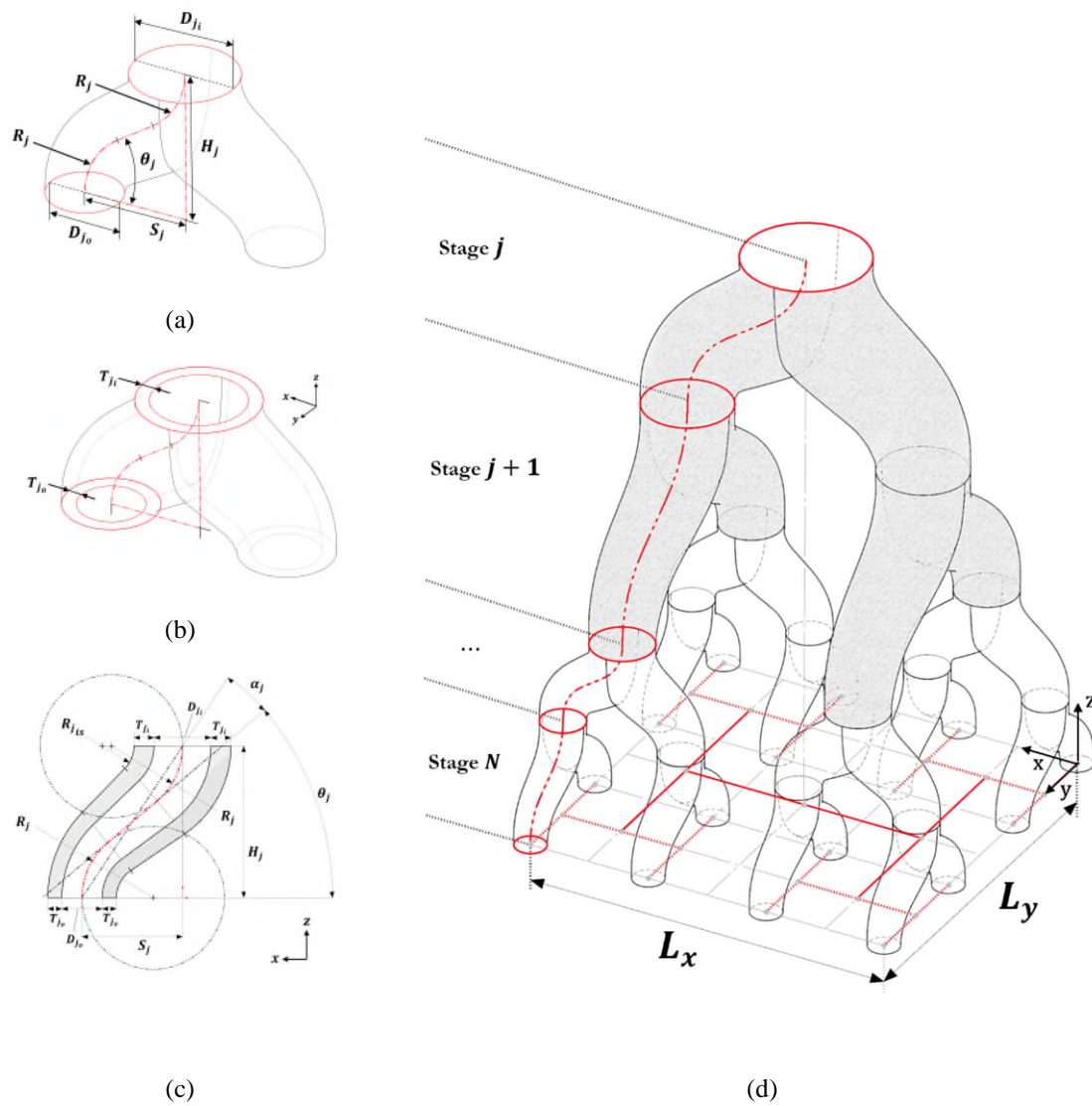


Figure 26: Fractal flow distributor and associated parameters (a) Single bifurcation unit (b) Single bifurcation unit including wall thickness parameters (c) Section view of single channel path parameters (d) $N=4$ stage embodiment. Fractal self-similar unit of repeating detail comprising of j and $j + 1$ units (shaded) identified by “H” shaped lines on the projected two-dimensional unit connectivity schematic (from (Mazur et al., 2019))

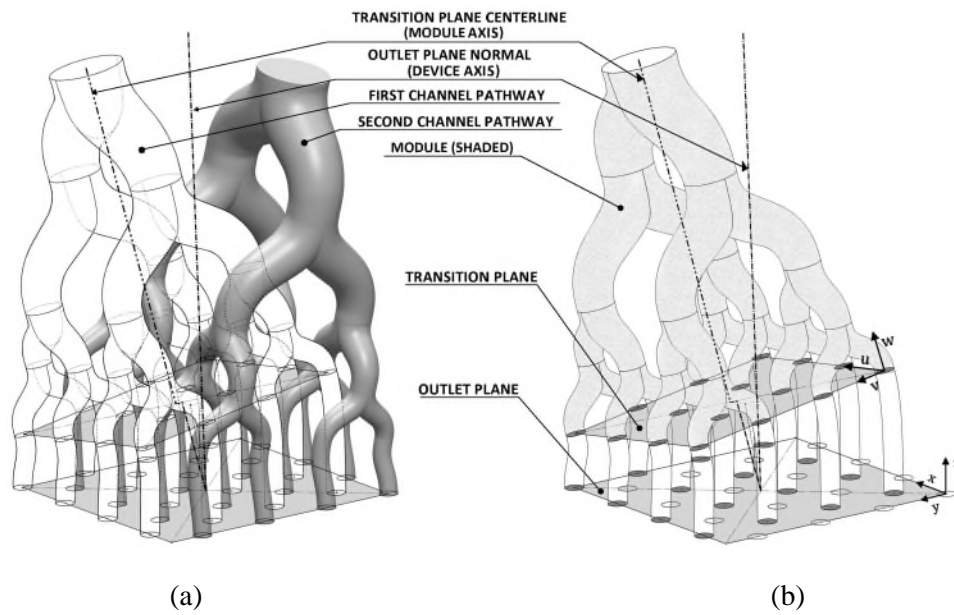


Figure 27: Fractal flow distributor design with two independent channel pathways
 (a) Nesting arrangement of two channel pathways and associated pathway and device axes of symmetry
 (b) Single channel pathway indicating arrangement of inclined transition plane and outlet plane

3.2.2. CFD Model

The hydrodynamic performance of the fractal flow mixer was investigated by conducting CFD simulations using the commercial package ANSYS-Fluent. The computational domain of the fractal flow mixer (Figure 28[a]) was developed based on the CAD model design shown in Figure 27[i-ii] with the addition of mixing points (y-junction) before each outlet. The device has two inlets (referred to as module-A and module-B, see Figure 28[a]), which are recursively bifurcated over four stages resulting in 16 outlet channels per pathway. The outlets from each of the two pathways are then combined to mix the two fluid streams. The 16 outlet channels were labelled accordingly, as shown in Figure 28[c]. The geometric parameters for the fractal flow mixer are summarised in Table 5. This geometry was discretised using a tetrahedral mesh, as shown in Figure 28[b]. Initially, simulations were conducted to study mesh dependency of simulation predictions by using the geometry with 1.2, 1.5 and 2 million cells. It was found that the pressure drop predictions from 1.5 and 2 million cells were in close agreement, with the variation being less than 1%. Consequently, the geometry with 1.5 million cells was used for subsequent simulations.

Parameter	Value
Inlet diameter	4mm
Outlet diameter	1mm
Number of stages	4
Number of outlets per module	16
Number of mixed channels	16
Y-junction angle	60°

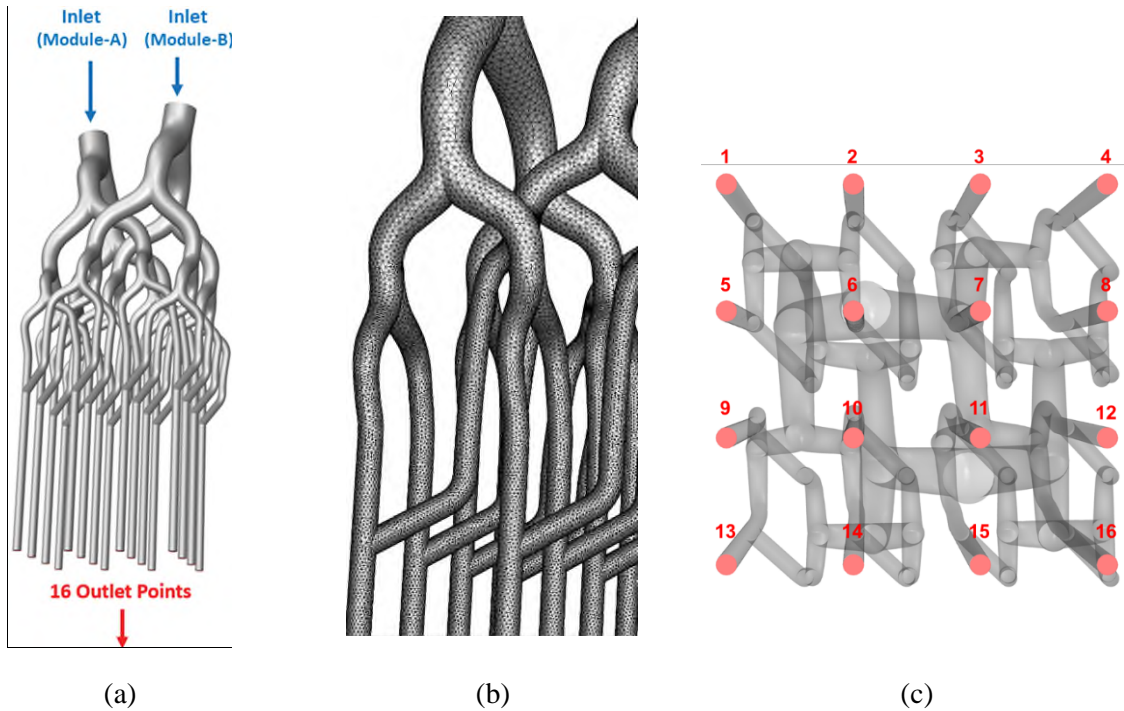


Figure 28: (a) Flow domain of the fractal flow mixer; (b) Detail of tetrahedral mesh of the flow domain; (c) Top view of the flow domain with number labels (ID) on each outlet

Steady-state simulations of the flow of a gas mixture of air ($\rho_{air} = 1.225 \frac{kg}{m^3}$; $\mu_{air} = 1.81 \times 10^{-5} Pa.s$) and methane ($\rho_{CH_4} = 0.657 \frac{kg}{m^3}$; $\mu_{CH_4} = 1.107 Pa.s$) were conducted using a pressure-based solver. The model solved continuity, momentum balance and species balance equations. The laminar model was used to resolve viscous forces in the flow, whereas species diffusion was resolved without chemical reactions. The laminar viscous model was selected since wall friction and surface tension forces were dominant in this type of channel flow, and the effect of turbulence in the channels would be negligible (Berk, 2018). The standard k- ϵ turbulent model with standard wall functions was used specifically for simulation No. 4 in Table 7 since the Re number at the outlets were in the turbulent regime. Inlets were modelled by using the velocity-inlet boundary condition, where inlet velocity calculated from

the simulated Reynolds numbers (see Table 7) was assigned along with inlet species concentration. The outlets were configured as pressure-outlets and a no-slip boundary condition was assigned to the walls. The SIMPLE scheme was used with the Rhie-Chow (distance-based) flux for the pressure-velocity coupling and the pressure staggering option scheme (PRESTO) was used for the pressure interpolation. A first-order upwind was applied for the turbulent kinetic energy and dissipation rate. A second-order upwind discretisation was applied for the momentum equation and the species transport. The mixture template in the species transport model was solved using the ideal gas law (incompressible). To minimise truncation errors, a double-precision solver was used. The results were converged with all residuals below 1×10^{-3} and the global mass fluxes were balanced. The governing equations, constitutive equations, and spatial discretization schemes used in the CFD model are summarised in Table 6.

Table 6: Governing equations, constitutive equations, and spatial discretization schemes used in the CFD model
Continuity equation: $\frac{\partial p}{\partial t} + \nabla \cdot (\rho \vec{v}) = 0$
Momentum balance equation: $\frac{\partial}{\partial t} (\rho \vec{v}) + \nabla \cdot (\rho \vec{v} \vec{v}) = -\nabla p + \nabla \cdot (\bar{\tau}) + \rho \vec{g}$
Stress tensor: $\bar{\tau} = \mu \left[(\nabla \vec{v} + \nabla \vec{v}^T) - \frac{2}{3} \nabla \cdot \vec{v} I \right]$
Species balance equation: $\frac{\partial}{\partial t} (\rho Y_i) + \nabla \cdot (\rho \vec{v} Y_i) = -\nabla \cdot \vec{J}_i$
Diffusion flux of a species: $J_i = -\rho D_{i,m} \nabla Y_i - D_{T,i} \frac{\nabla T}{T}$
Transport equations for the standard k-ε turbulent model (kinetic energy and dissipation energy): $\frac{\partial}{\partial t} (\rho k) + \frac{\partial}{\partial x_i} (\rho k u_i) = \frac{\partial}{\partial x_j} \left[\left(\mu + \frac{\mu_t}{\sigma_k} \right) \frac{\partial k}{\partial x_j} \right] + G_k + G_b + \rho \varepsilon + Y_M + S_k$ <p>and</p> $\frac{\partial}{\partial t} (\rho \varepsilon) + \frac{\partial}{\partial x_i} (\rho \varepsilon u_i) = \frac{\partial}{\partial x_j} \left[\left(\mu + \frac{\mu_t}{\sigma_\varepsilon} \right) \frac{\partial \varepsilon}{\partial x_j} \right] + C_{1\varepsilon} \frac{\varepsilon}{k} (G_k + C_{3\varepsilon} G_b) - C_{2\varepsilon} \frac{\varepsilon^2}{k} + S_\varepsilon$

In these simulations, two different gases were injected from two inlets (modules A and B in Figure 28[a]) and the distribution and mixing of these two gases at each of the 16 outlets were investigated from the simulation predictions. In order to characterise the performance of the fractal flow mixer at different flow conditions, simulations were carried out by varying the inlet Re from 100 to 10000, corresponding to the variation of 0.1 to 10 in the ratio of inlet

flow rate in module-A to module-B. Henceforth, the ratio of inlet gas flow rates will be referred to as the inlet flow ratio (IFR). Furthermore, one set of simulations was conducted with air entering from both the modules and the other set of simulations was conducted with air entering from module-A and methane from module-B. Methane and air were selected to assess the potential use of the fractal flow mixer as a gas burner. Table 7 summarises the simulated flow conditions.

Set-1				Set-2			
Sim.	module-A (Re)	module-B (Re)	Inlet Flow Ratio (IFR)	Sim.	module-A (Re)	module-B (Re)	Inlet Flow Ratio (IFR)
No.	Air	Air	(module-A/module-B)	No.	Air	Methane	(module-A/module-B)
1	10	10	1	9	10	9.0405	1.106
2	100	100	1	10	100	90.405	1.106
3	1000	1000	1	11	1000	904.05	1.106
4	10000	10000	1	12	10000	9040.5	1.106
5	100	1000	0.1				
6	1000	100	10				
7	1000	10000	0.1				
8	10000	1000	10				

To assess the velocity and distribution of species in the total flow coming out from the device, cross-sectional averaged mass fraction of one species (from module-B) and velocity was calculated in the flow from each of the 16 outlets. Then, the RSD of these 16 values was calculated using Eq. 10. Additionally, to assess the velocity and species distribution in each outlet, the RSD of local cell values of velocity and species mass fraction (from module-B) was also calculated using Eq. 10. Note that higher standard deviation values would mean higher non-uniformity of species or velocity distribution in the flow.

$$RSD = \frac{s}{\bar{M}_i} \quad \text{Eq. 10}$$

In Eq. 10, s is the standard deviation of velocity or species mass fraction (from module-B) and \bar{M}_i is the mean velocity or species mass fraction (from module-B). Another parameter

used to assess the flow uniformity was the distribution index (DI), which is defined by Eq. 11 (Berk, 2018),

$$DI = 1 - \frac{S^2}{S_0^2} = 1 - \frac{(x_i - q)^2}{q(1 - q)} \quad \text{Eq. 11}$$

where S^2 is the variance of the outlet mixture, S_0^2 is the variance of a completely unmixed system, q is the mass fraction of a species in a combined flow from the two modules, and x_i is the cross-sectional averaged mass fraction of a species at a particular outlet. The value of DI can vary between zero and one, with zero representing a completely segregated mixture and one representing a completely well-mixed mixture (Berk, 2018). The DI was used to compare the fluid flow composition between the inlet and the outlet. Theoretically, based on the design of the fractal flow mixer, with an IFR of 1 at the inlet for both modules, it is expected that the fluid composition at each outlet would have the same fluid flow ratio of 1, where the composition would be 50% from module-A and 50% from Module-B. The DI was initially defined by (Lacey, 1954) as the mixing index (MI), which assesses the quality of mixing of a real mixture. Since then, multiple studies (Aubin et al., 2010; Camarri et al., 2020; Hessel et al., 2005; Kukukova et al., 2009; Kumar et al., 2011; Mariotti et al., 2019) have reported different experimental and numerical methods to characterise mixing quality and investigate the mixing phenomenon in different designs of micromixers. The experimental methods to characterise mixing quality includes dilution of coloured dyes, dilution of fluorescent species, reactions yielding coloured species, competing parallel reactions, monitoring species concentration, and acid-base of pH indicator reactions (Aubin et al., 2010). In this study, the mixing index (MI) was used as a parameter to assess the flow uniformity, as opposed to the mixing quality/mixing degree at each channel, which was originally proposed by (Lacey, 1954). Hence, the name mixing index (MI) has been changed to the distribution index (DI) in this paper.

3.3. Results and Discussion

3.3.1. Manufacture

AM processes are based on a layer-by-layer approach to part manufacture, which effectively decomposes a complex and difficult to manufacture 3D part geometry into a series of comparatively simple to manufacture 2D layers. AM processes such as L-PBF or VP present an attractive manufacturing solution for the geometrically complex flow distribution system under consideration. L-PBF is an AM process that uses a laser heat source to

selectively melt metal powder in a layered manner in order to build up solid three-dimensional parts (Campanelli et al., 2010). L-PBF is compatible with a broad range of metals, including steel, nickel, aluminium and titanium alloys (Frazier, 2014). Similarly, VP is a polymer AM process based on selective light exposure of photopolymeric resins (Gibson et al., 2015). The process is capable of manufacturing high-resolution parts from a range of polymeric materials, including translucent materials, which is useful for flow visualisation purposes in flow device design applications such as the focus of this work. However, VP polymer materials exhibit a limited ability to resist demanding service environments subject to elevated temperatures, pressures, and reactive flow media encountered in chemical engineering applications. In such cases, L-PBF components may be required.

The quality and manufacturability of L-PBF and VP components are dependent on the geometry and orientation of the manufactured parts relative to the build platform. The successful manufacture of the desired part geometry often requires the use of support structures which comprise of temporary additional material built along with the part. Support structures ensure the part material layers remain in the correct position during the build by preventing sagging of unsolidified overhanging material layers, dissipating heat from hot layers, and reducing distortions induced by thermomechanical stresses (Gan & Wong, 2016). The structures have intentionally fragile geometry so that they may be separated from the part with relative ease following the build. Support structures are typically required for overhanging surfaces that are not able to be self-supporting. For processes such as L-PBF and VP, this is typically for surfaces with an incline below 30 ~ 40 degrees from the horizontal. Although support structures increase the range of manufacturable part geometries, they are undesirable due to increasing material usage, post-processing effort, and build duration. Furthermore, support structures cannot be easily removed from inaccessible internal part features. Consequently, parts designed for VP and L-PBF manufacture should be designed in order to minimise the need for support structures; by considering modifying overhanging geometry, incorporating self-supporting features or by changing the build orientation of the part.

These requirements were incorporated into the flow distribution and mixer design in this work when considering the selection of the bifurcation angle since the design comprises internal part features, which would make support structure removal infeasible. A series of devices were made to evaluate the manufacturability of the flow distributor and mixer devices using VP and L-PBF processes, including a 4-stage translucent polymer device and Ti-6Al-4V alloy devices with 4- and 6-stages Figure 29[a-c]. Ti-6Al-4V alloy was used for the metal

devices due to its high specific strength and high compatibility with L-PBF processing (Boyer et al., 1994; Brandt et al., 2013). The VP and L-PBF devices were manufactured on ProJet 7000 HD and an SLM Solution 125 HL machines, respectively. For both VP and L-PBF processes, the devices were entirely self-supporting when orientated with the inlet channel at the base of the build platform (i.e., a vertically inverted orientation to that of Figure 29[a-c]). All devices were manufactured successfully, and the self-supporting nature means that the devices can be manufactured with minimal material waste.

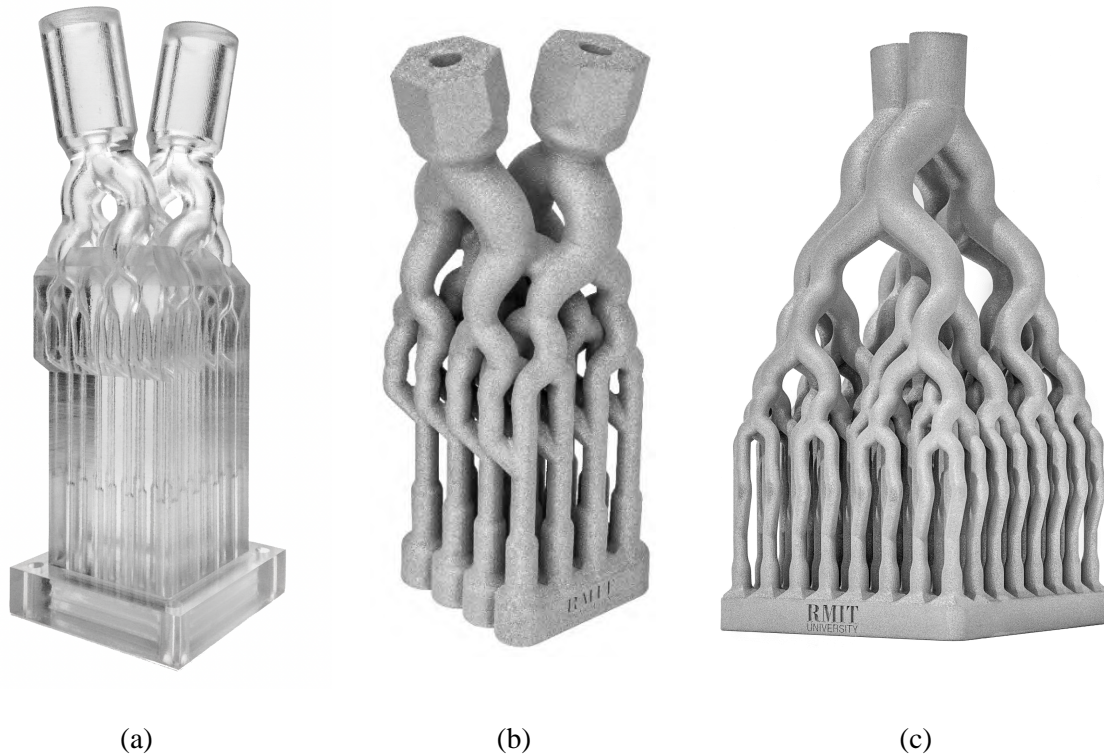


Figure 29: Additively manufactured flow distributor and mixer devices: (a) 4-stage polymer device manufactured (b) 4-stage metal device (c) 6-stage metal device.

3.3.2. Effect of Inlet Reynolds Number

For simulations with an IFR of 1 (Table 7 simulations 1-4 and 9-12), Figure 30 shows the RSD of the cross-sectional averaged species mass fraction at all 16 outlets for a range of inlet Re and both mixtures (air-air and air-methane). The maximum RSD observed at all the outlets was $\sim 8\%$ for the air-air mixture and $\sim 10.5\%$ for the air-methane mixture. It can also be seen that the increase in inlet Re resulted in the decrease in the RSD values, which translates to the increase of uniformity of the species distribution across the cross-section of all 16 outlets. This can be attributed to the bifurcating and symmetrical nature of the device topology, resulting in a reasonably identical performance at all the outlets. These results also

imply that the increase in inlet Re resulted in better mixing at the Y-junction and this may be attributed to micro-turbulence generated at higher Reynolds number. Even though the laminar flow ($Re = 10, 100, \text{ and } 1000$) resulted in slightly higher non-uniformity, the values of RSD were still relatively low, indicating uniformity of species at all 16 outlets.

Another parameter that was used to assess the flow uniformity was the DI. Theoretically, the fractal flow mixture with an IFR of 1 (same inlet flow rate from the two modules) would result in an equal amount of two species in each of 16 outlets. The DI for all 16 outlets for simulated flow conditions are shown in Figure 31. Similar to the pattern shown in Figure 30, the increase of the inlet Re resulted in the decrease in the variation of DI values, inferring higher flow uniformity within one outlet. The DI (as shown in Figure 31) at each outlet for the two mixtures (air-air and air-methane) behaved quite differently, where it can be seen that the DI value for the air-air mixture ranges from ~ 0.98 to ~ 1 , while the DI for the air-methane mixture ranges from ~ 0.83 to ~ 0.97 . The lower DI value and uneven distribution between the outlets for the air-methane mixture were most likely due to the mixing being affected by the diffusivity of two different gasses.

It can be envisioned that the mixing performance can be improved at the cost of higher-pressure loss by inducing turbulences. Thus, it is essential to investigate the overall pressure drop in the fractal flow mixer. The average pressure drop between all inlets and outlets at different inlet Re is shown in Figure 32. It can be seen that the calculated pressure drop for the fractal flow mixer ranged between ~ 1 to 8000 Pa. For example, a typical gas-liquid distributor with an inlet Re of ~ 3000 using an orifice can have pressure drops of up to 5000 Pa (Don & Robert, 2008). When compared at the same Re , the fractal flow mixer showed a pressure drop of <1000 Pa. The significantly low-pressure drop can be attributed to the topology of the fractal flow mixer, where there are no sharp changes in the flow area throughout the device.

Although Figure 30 shows the uniform distribution of the species mass fraction at all 16 outlets, it is important to understand the local distribution of the flow and species in each outlet. The contours of species mass fraction at all 16 outlets are shown in Figure 33[a-d]. It can be seen from Figure 33[a], that at lower inlet Re ($Re = 10$), the flow was well-mixed with species mass fraction varying between 0.4 and 0.5. As the inlet Re increased, there was an increase in the level of flow segregation, which was prominent at a high inlet Re of 10000 (Figure 33[d]). Additionally, at all 16 outlets, the pattern of species mass fraction contour was also identical.

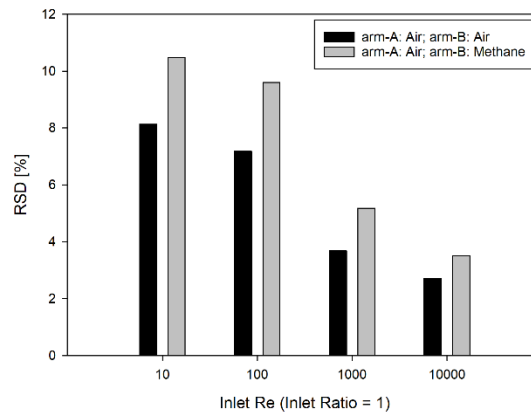


Figure 30: RSD [%] of cross-sectional averaged species mass fraction at all 16 outlets at varying Inlet Re (Inlet ratio = 1)

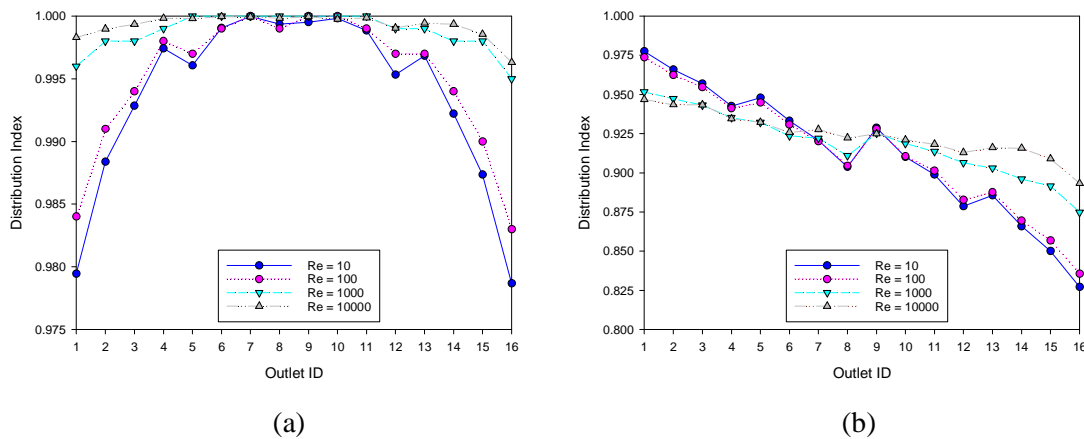


Figure 31: Distribution index (DI) of species mass fraction within each outlet against different Inlet Re (Inlet ratio = 1) for (a) Air and air mixture (b) Air and methane mixture

Quantitatively, Figure 33[a-d] shows the RSD of the local cell values of species mass fraction at each outlet at different inlet Re. It can be seen that increasing the inlet Re from 10 to 10000 increased the species mass fraction from ~0 % to ~47%. The significant increase of RSD signified the high level of flow segregation within each outlet occurring at higher inlet Re (i.e. Re = 10000), which was also shown by Figure 33[d]. This can be attributed to the level of turbulence that increased with the increase of the Inlet Re.

Figure 35[a-d] shows the RSD of local cell values of gas velocity at each outlet at different inlet Re. It can be seen that increasing the inlet Re from 10 to 10000 decreased the RSD of velocity from ~56% to ~22%, indicating uniform flow distribution at a higher inlet Re (i.e. Re = 10000). This was because the fluid flow was fully developed when it passed through the channels at a higher inlet Re (i.e. Re = 10000). Despite the high level of

uniformity, the contour (side-view) of the species mass fraction in 16 outlet channels, as shown in

Figure 36[a-d], showed that the increase of the inlet Re would increase the mixing length required to achieve complete mixing. Additionally, it can be seen in Figure 35 that the increase of inlet Re significantly affected the flow uniformity in each outlet for both the mixtures. However, a higher inlet (Re = 10000) resulted in a higher non-uniformity in species mass fractions. The effect of mixture composition in each outlet was almost identical in terms of both local distributions of flow and species.

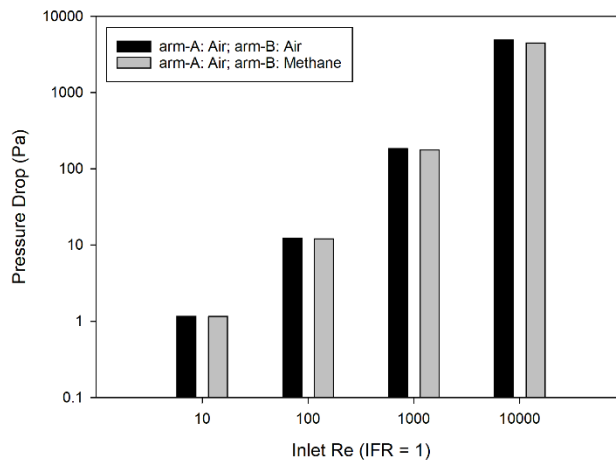


Figure 32: Average pressure drop between all inlets and outlets at varying Inlet Re

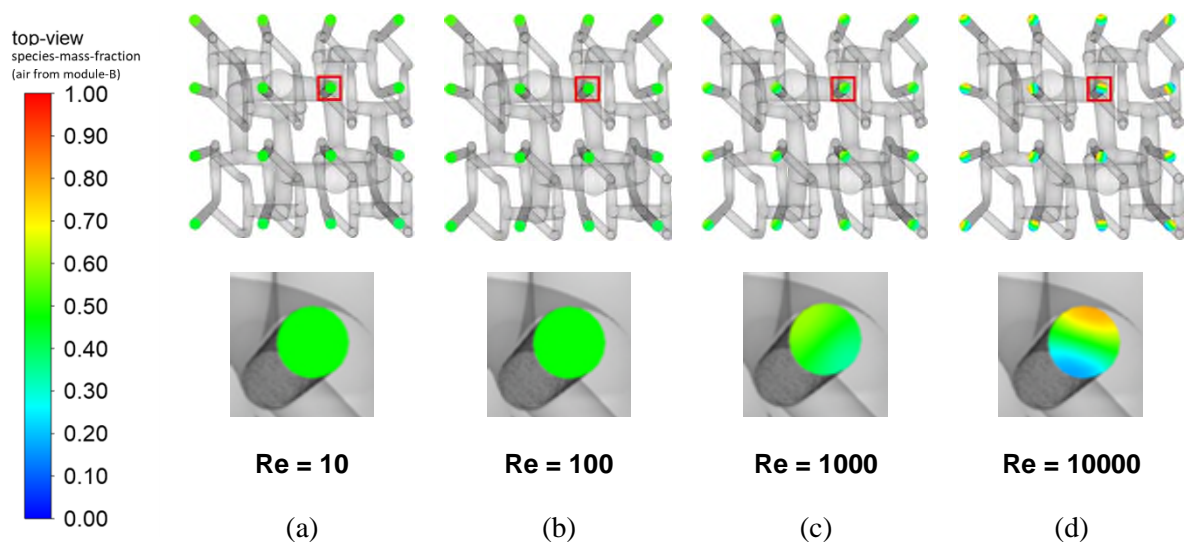
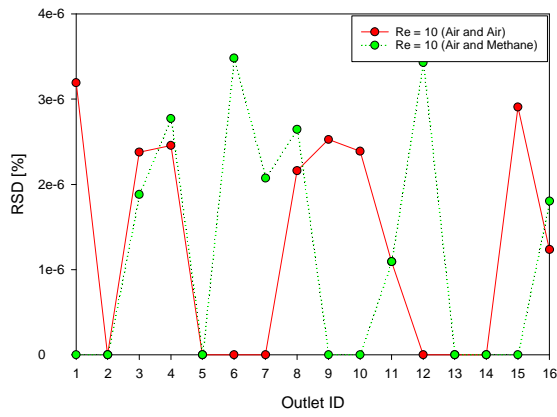
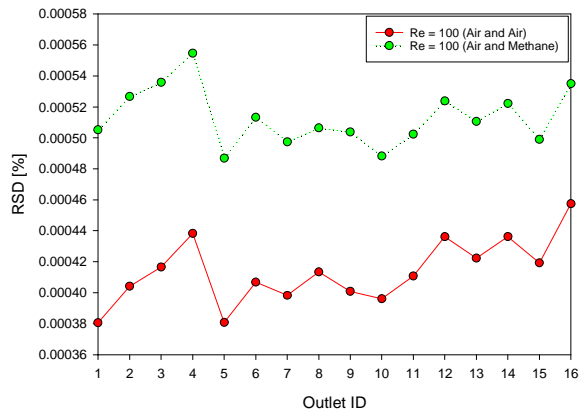


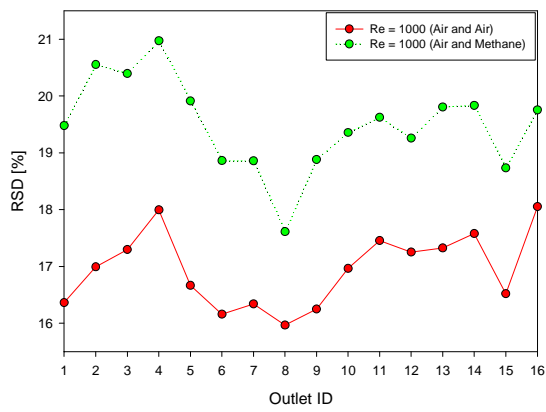
Figure 33: Species mass fraction contour (from module-B) of each outlet at different inlet Re (IFR = 1) for (a) Re = 10 (b) Re = 100 (c) Re = 10000 (d) Re = 1000



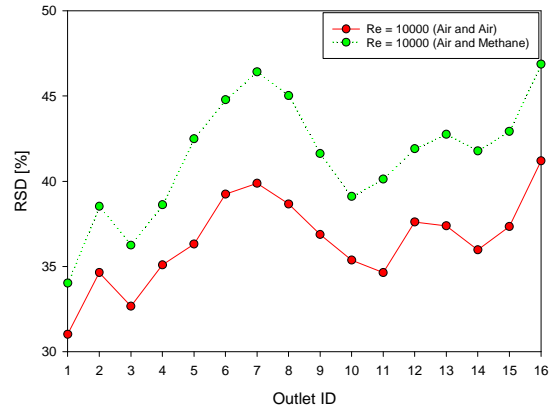
(a)



(b)

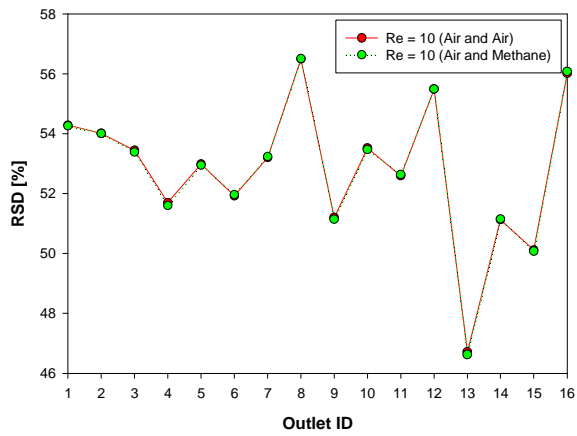


(c)

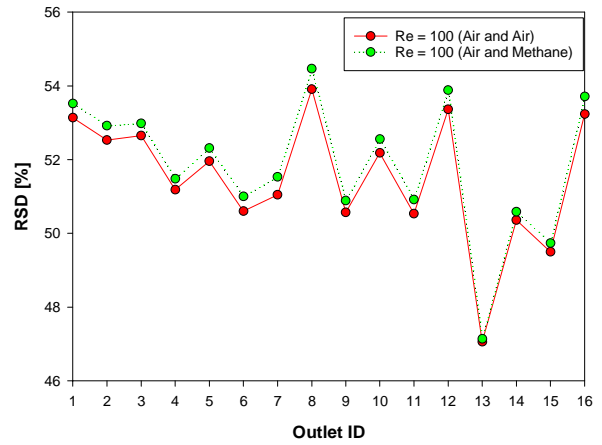


(d)

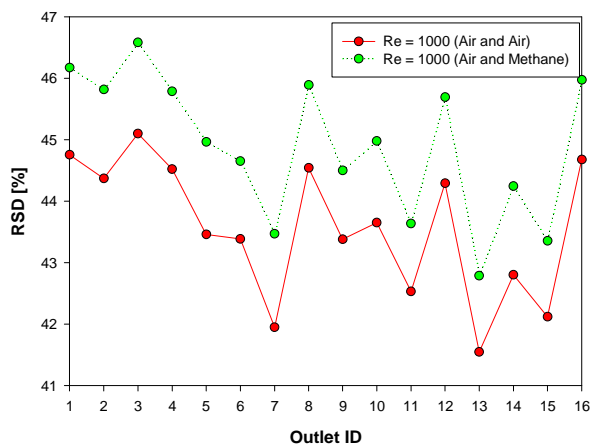
Figure 34: The RSD [%] of local cell values of species mass fraction (from module-B) within each outlet at different Inlet Re (IFR = 1) for (a) Re = 10 (b) Re = 100 (c) Re = 1000 (d) Re = 10000



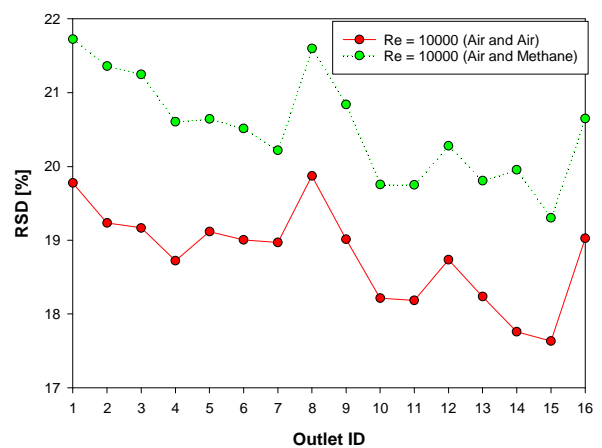
(a)



(b)



(c)



(d)

Figure 35: The RSD [%] of local cell values of velocity within each outlet (Air-Air and Air-Methane) at different Inlet Re (IFR = 1) for (a) Re = 10 (b) Re = 100 (c) Re = 1000 (d) Re = 10000

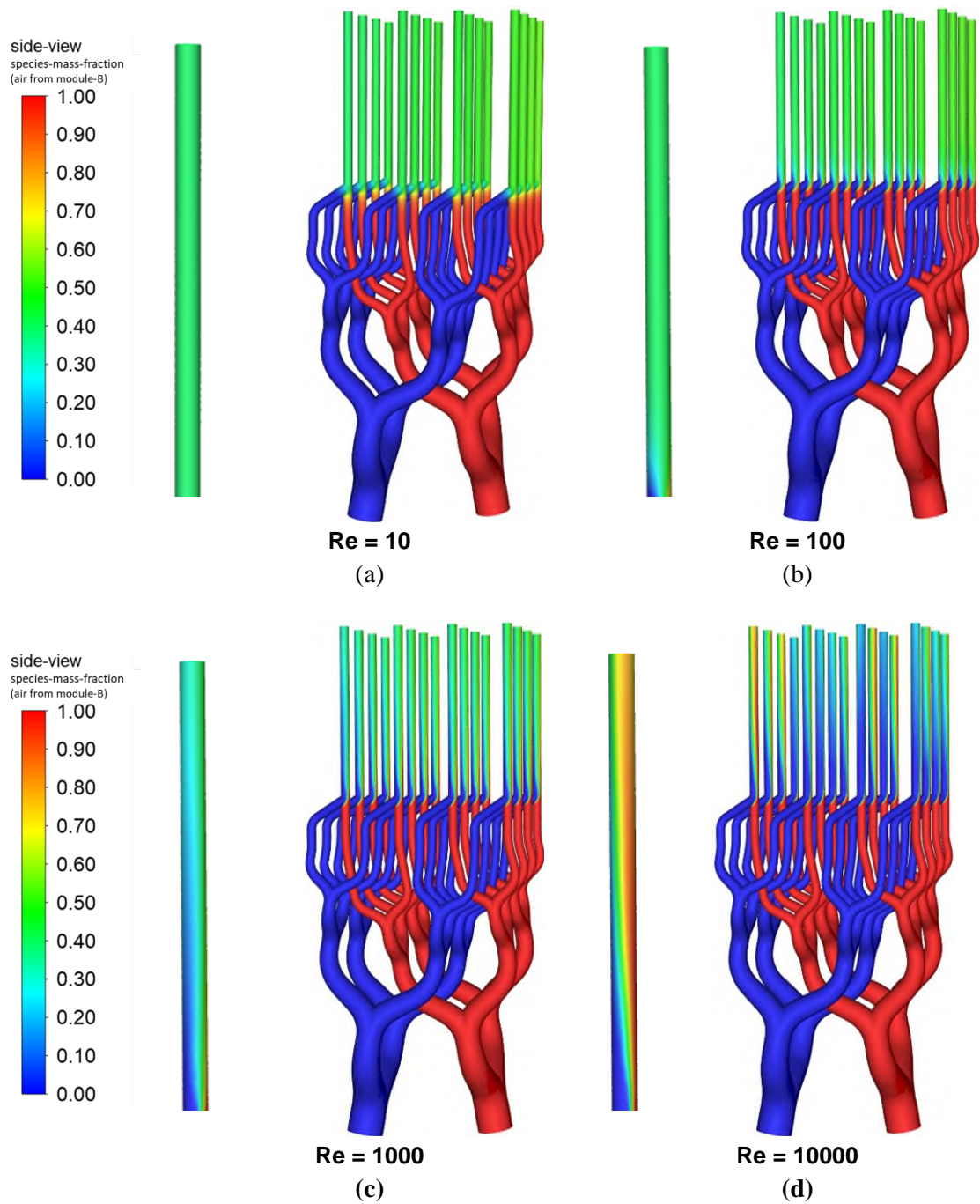


Figure 36: Species mass fraction contour (air from module-B) of all 16 channels at different Reynolds number; (a) $Re = 10$ (b) $Re = 100$ (c) $Re = 10000$ (d) $Re = 10000$

3.3.3. Effect of Inlet Flow Ratio (IFR)

The influence of the IFR on the mixing performance and uniformity of the fractal flow mixer was investigated by varying both the inlet Re and IFR (as shown in Table 7 Sim. No. 1-8). It must be noted that some specific values of the inlet ratio were not investigated as the resulting inlet Re on either of the modules would be unrealistic. For example, an inlet ratio of 100 and an inlet Re of 100 at Module-A would result in a very low inlet Re of 1 in Module-B. In addition, as presented in the previous section, since the density and diffusivity of the two different gases had minimal impact on the uniformity and mixing performance of the fractal flow mixer, only the air-air mixture was simulated for this investigation. Figure 37 shows the RSD of the cross-sectional averaged species mass fraction at all 16 outlets. At parity, where the IFR is 1, the increase in the inlet Re resulted in the decrease in RSD values which inferred an increase in the distribution of species across the cross-section. It can also be seen that the increase in IFR from 0.1 to 100 significantly increased the RSD from ~1.2% to ~21% correspondingly. However, it must be noted that the RSD of species mass fraction was calculated based on the mass fraction of a component entering from module-B. For example, when the IFR is 0.1, the inlet Re at module-B was higher than the inlet Re at module-A, resulting in a lower RSD value compared to an IFR of 10 where the inlet Re at module-A was higher than the inlet Re at module-B. This implies that the inlet Re predominantly governs the distribution of species, not the inlet ratio. IFR of 0.1 and 10 also introduced a disparity of flow rate passing through the two modules. The fluid flow with the higher Re from one module dominated all 16 channels. When the IFR was 0.1 and 10, inlet Re had less effect on the cross-sectional distribution of species in the fractal flow mixer.

To compare the fluid composition ratio between the inlet and the outlet at varying IFRs, the DI was calculated. The value of DI within each outlet at varying IFRs is shown in Figure 38 (a-c). At an IFR of 0.1 and 10, where there is a disparity of flow rate passing through the two modules, the DI was found to be consistent and closer to 1. Again, this was because the single module with the higher inlet Re was dominating the flow passing through all 16 outlet channels. For example, at an inlet Re of 10000 with an IFR of 10 (as shown in Figure 38[c]), the inlet flow compositions at the inlet of Module-A and Module-B were 91% and 9%, respectively. At this particular IFR, the DI values for all 16 outlets were close to 1, indicating that the fluid flow composition did not change from the inlet to outlet channels. Additionally, at all IFRs, the DI values were close to 1, indicating a high level of flow uniformity. This shows that the fractal flow mixer can be adapted to various applications requiring mixing at

different IFRs since the topology of the fractal flow mixer did not alter the consistency of the flow from the inlet to the outlet. The effect of the IFR on pressure drop is shown in Figure 39. It can be seen that the pressure drop was also governed by the IFR, and it increases with the increase in Re . In addition, it was evident that the bifurcating geometry, which did not have sharp bends or large diameter ratios, had relatively very low-pressure drops and achieved high flow uniformity and mixing.

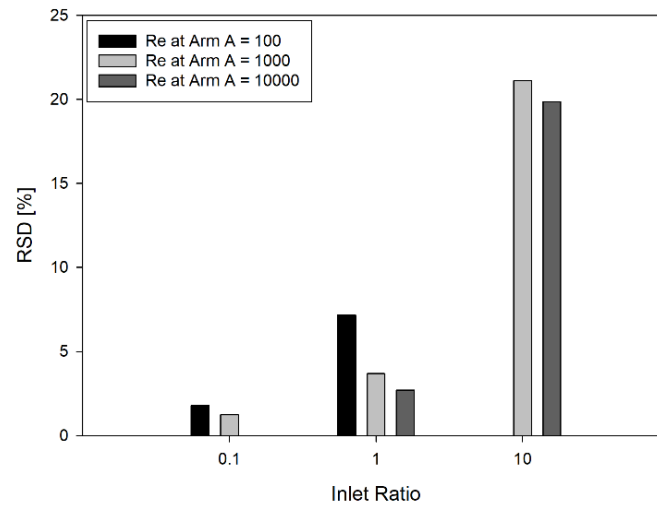
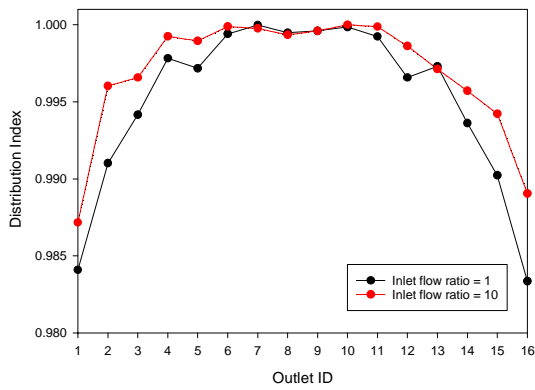
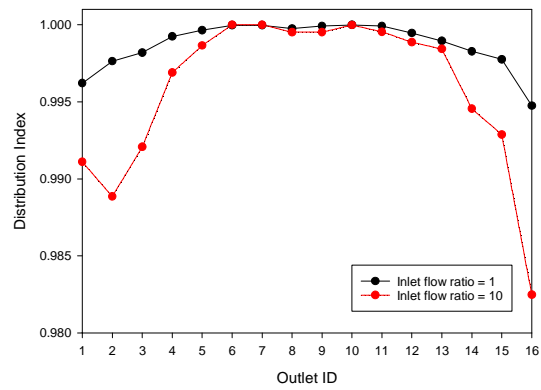


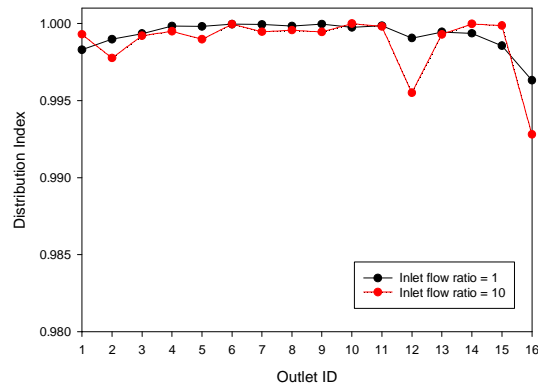
Figure 37: RSD [%] of cross-sectional averaged species mass fraction (from module-B) at all outlets at different IFR (Air and Air Mixture)



(a)



(b)



(c)

Figure 38: Distribution index (DI) of species mass fraction within each outlet at different IFR (a) Re at module-A = 100 (b) Re at module-A = 1000 (c) Re at module-A = 10000

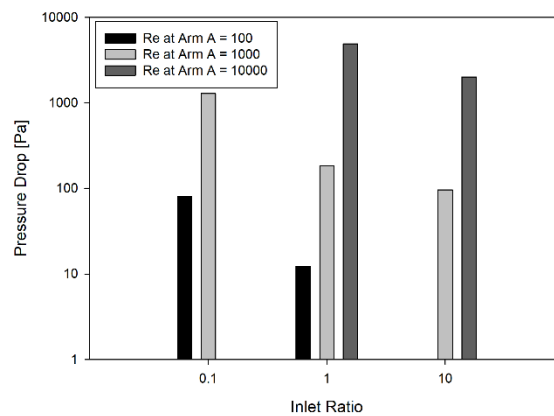


Figure 39: Average pressure drop between all inlets and outlets at varying IFR (Air and air mixture)

To study the effect of the mixing at the y-junction of the fractal flow mixer, the pressure drop at high IFRs of 0.01 and 100 were compared (Figure 40). It can be seen that the pressure drop was 76% higher when the inlet Re at module-A was 100 times higher than that in module-B. This was due to the fact that after passing through four stages of bifurcation, the flow from module-A passed through the y-junction at an angle, while the flow from Module-B passed through the y-junction in a straight channel. Hence, if the fractal flow mixer was to be used in a setting where a flow disparity is introduced between the two modules, it is best to have the flow with a higher inlet Re in Module-B.

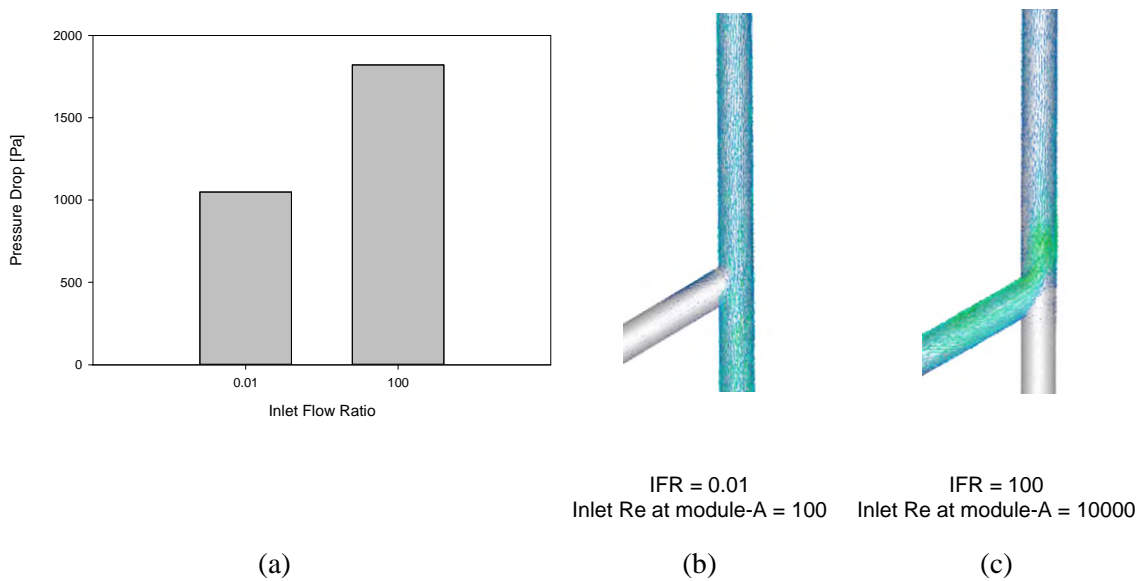


Figure 40: (a) Pressure drop comparison at a high IFR (b) velocity vector at an IFR of 0.01 (c) velocity vector at an IFR of 100

To understand the effect of IFR on the local distribution of flow and species, contours of species mass fraction at all 16 outlets at different inlet ratios were analysed (Figure 41 and Figure 43 [a-b]) along with the species contours of all 16 channels (Figure 42 and Figure 44). From Figure 41[a] and Figure 42[a], it can be seen that the flow from module-B highly dominated the flow, but the flow was well-mixed. However, from Figure 41[b] and Figure 42[b] shows that the flow was segregated. Despite having the same inlet ratio of 0.1, the module with the higher inlet Re (i.e. $Re = 10000$) caused flow segregation at the outlet, requiring a longer mixing length to achieve a well-mixed flow. A similar pattern was observed at an IFR of 10, as shown in Figure 43 and Figure 44.

Quantitatively, Figure 45[a-c] shows the RSD of local cell values of velocity at each outlet at different IFRs. This figure shows that at all IFRs, the increase of the inlet Re decreased the RSD of velocity. It also shows that the effect of IFR at higher inlet Re (i.e. $Re = 10000$) was negligible. Figure 46[a-c] shows the RSD of local cell values of species mass fraction within each outlet at different IFRs. This figure shows that at all IFRs, the increase of the inlet Re increased the RSD of the mass fraction. Thus, from these figures (Figure 45[a-c] and Figure 46[a-c]), it was evident that even with varying IFRs, the mixing performance of the fractal flow mixer was highly governed by the inlet Re, which caused flow segregation at a higher inlet Re. In addition, when there was a flow disparity between the modules, the flow was highly dominated by the fluid flow from a single module. Hence, less mixing was happening at the Y-junction.

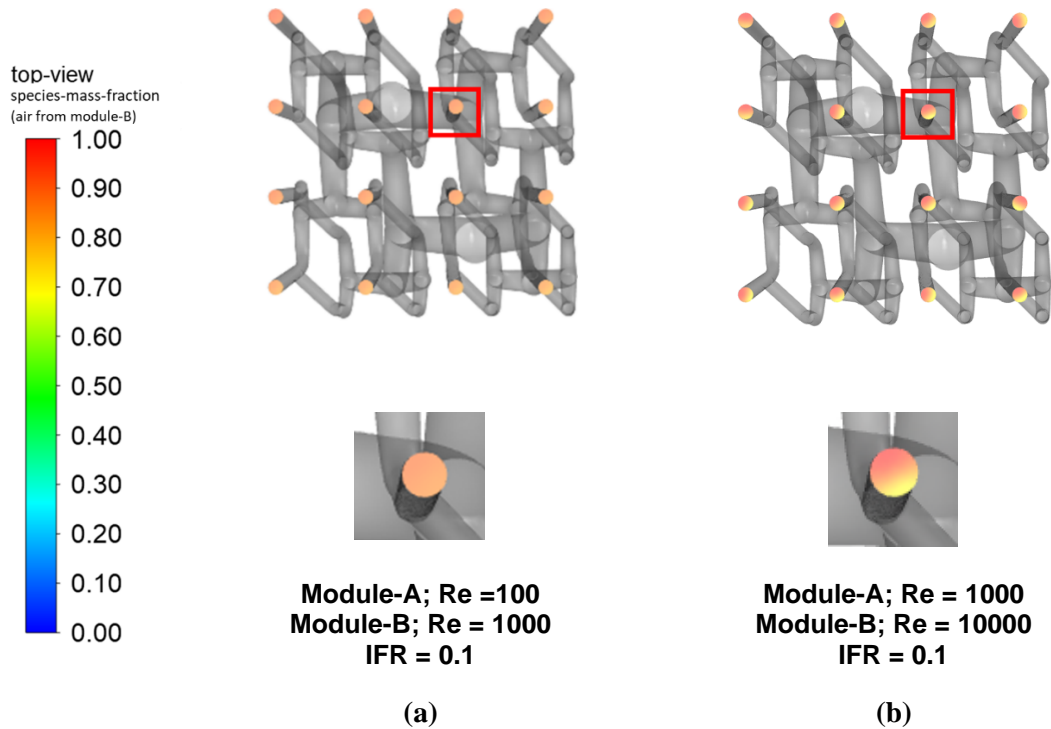


Figure 41: Species mass fraction contour (air from module-B) of each outlet at an IFR of 0.1; (a) Inlet Re at module-A = 100 (b) Inlet Re at module-A = 1000

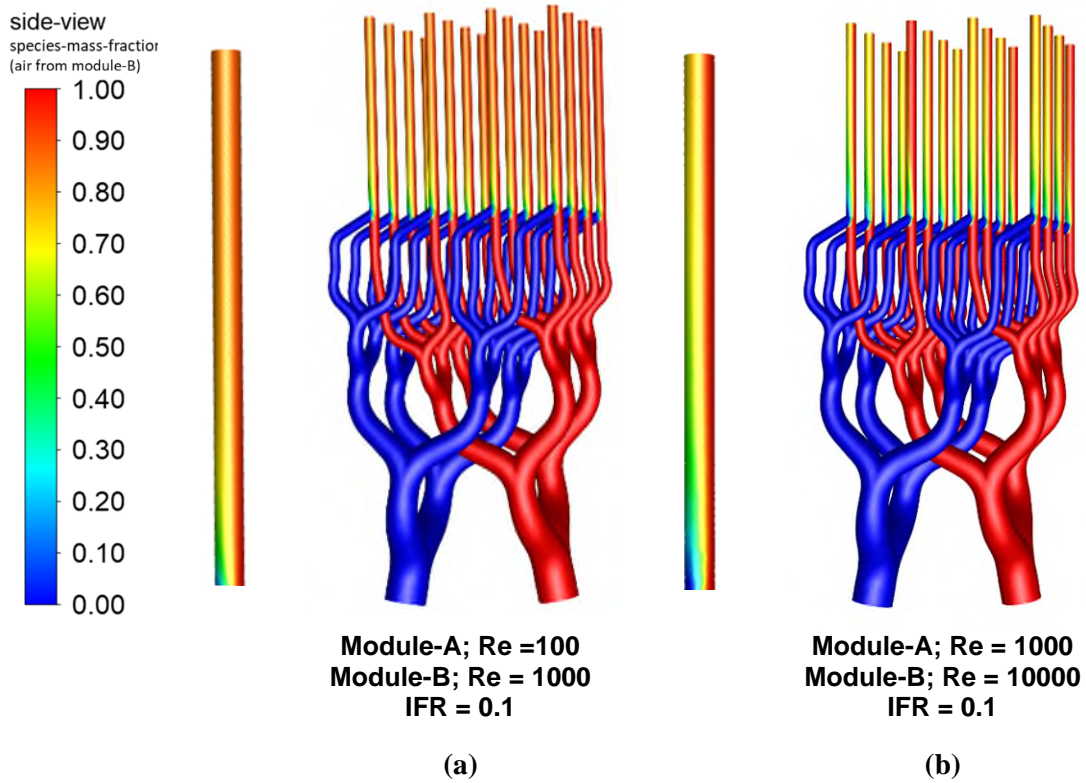


Figure 42: Species mass fraction contour (air from module-B) of all 16 channels at an IFR of 0.1; (a) Inlet Re at module-A = 100 (b) Inlet Re at module-A = 1000

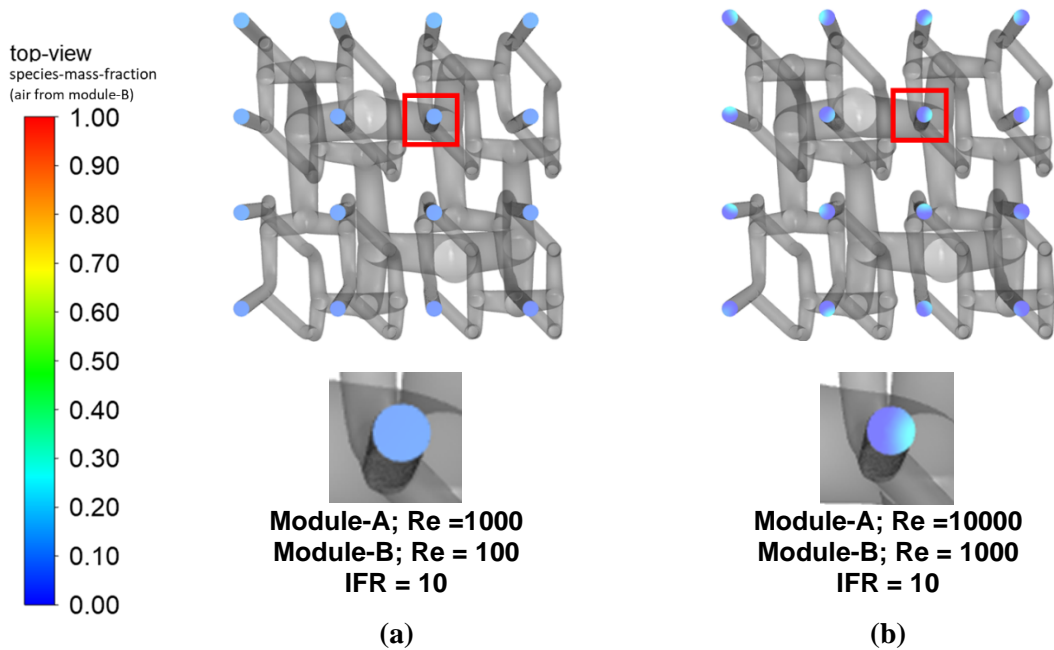


Figure 43: Species mass fraction contour (air from module-B) of each outlet at an IFR of 10; (a) Inlet Re at module-A = 1000 (b) Inlet Re at module-A = 10000

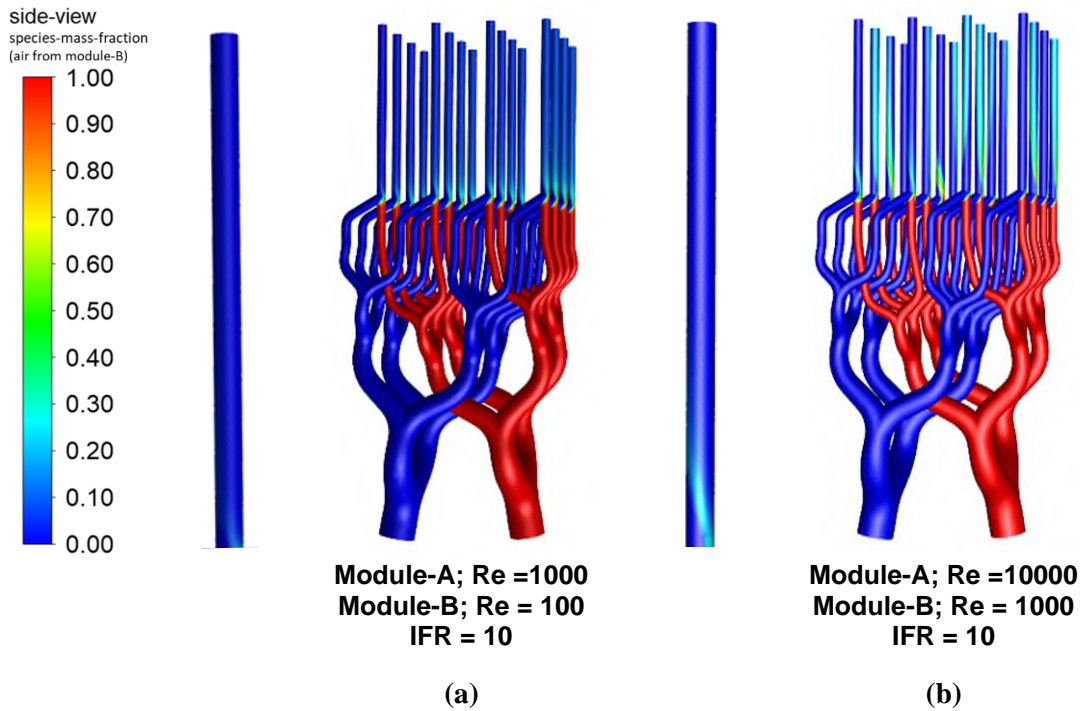


Figure 44: Species mass fraction contour (air from module-B) of all 16 channels at an IFR of 0.1; (a) Inlet Re at module-A = 100 (b) Inlet Re at module-A = 1000

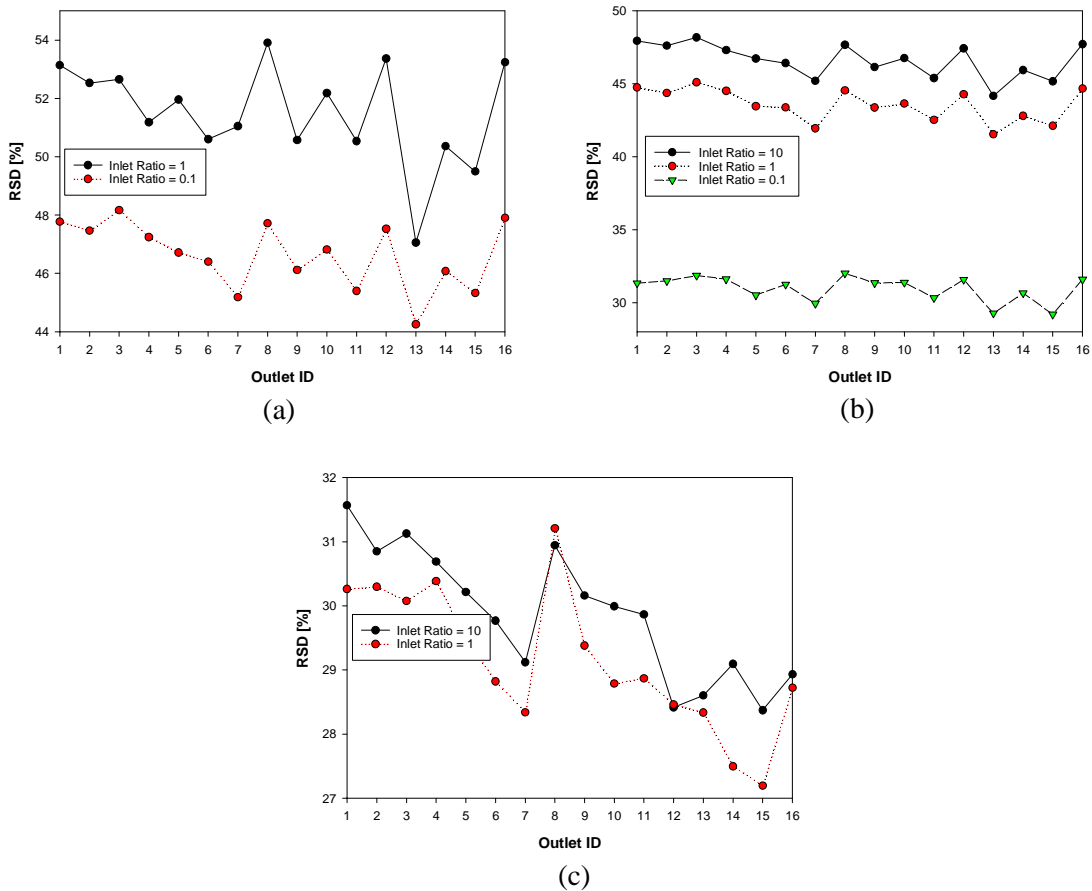


Figure 45: The RSD [%] of local cell values of velocity within each outlet at different inlet ratio for (a) Re at module-A = 100 (b) Re at module-A = 1000 (c) Re at module-A = 10000

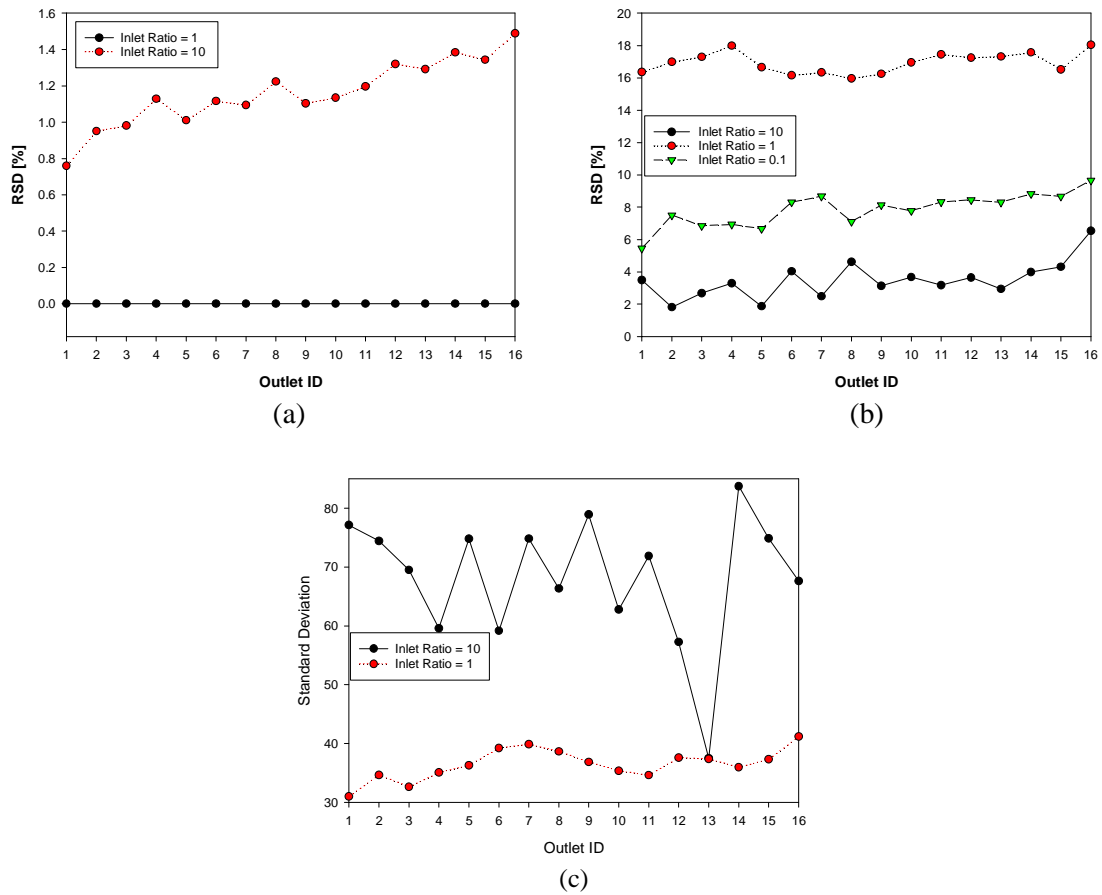


Figure 46: The RSD [%] of local cell values of species mass fraction (from module-B) within each outlet at different inlet ratio for (a) Re at module-A = 100 (b) Re at module-A = 1000 (c) Re at module-A = 10000

3.4. Conclusions

In this work, an additively manufactured high-density uniform flow distributor and mixer were proposed. The proposed distributor was designed and simulated using CFD modelling for hydrodynamic characterisation and quantifying mixing performance. The proposed fractal flow mixer used the concepts of bifurcation, and by optimising the bifurcation angle, the fractal flow mixer presented in this work was successfully manufactured without any support structures (self-supporting). Two techniques of AM were demonstrated, VP using a transparent resin as a precursor and L-PBF using Ti-6Al-4V alloy.

CFD simulation was carried out using two different combinations of gases to investigate the effect of density and diffusion on the mixing performance. It was found that the fluid mixtures had minimum impact on the mixing and was mainly governed by the micro-turbulence generated at the point of mixing. Furthermore, the effect of inlet Re number was studied on the overall fluid flow distribution, localised mixing (each channel) and overall

mixing. It was found that maximum RSD at all outlets was ~8% for the air-air mixture and ~10.5% for the air-methane mixture, at the lowest inlet Re number. This implies that in the laminar flow regime, the streamlines have a small effect on the overall mixing performance. However, in almost all of the simulated conditions, the localised mixing was even, and the lowest calculated DI was ~0.98 for the air-air mixture and ~0.83 for the air-methane mixture. The lower DI value and uneven distribution between the outlets for the air-methane mixture were most likely due to the mixing being affected by the diffusivity of two different gasses. For the pressure drop, comparing the fractal flow mixer against a typical gas-liquid distributor (orifice design), at an inlet Re of 3000, the orifice distributor can have pressure drops up to 5000 Pa, while the fractal flow mixer showed a pressure drop of only <1000 Pa.

It was evident that even with varying IFRs, the mixing performance of the fractal flow mixer was highly governed by the inlet Re, which caused flow segregation at a higher inlet Re. At all IFRs, the increase of the inlet Re decreased the non-uniformity and the maximum RSD was ~54%. It was found that between the IFR 1 and 10 for inlet Re of 100 ~ 1000, the fractal flow mixer showed a highly uniform flow distribution and mixing. Whilst the mixing performance is governed by the inlet Re, due to the y-junction geometry at the mixing point of the fractal flow mixer, the pressure drop was primarily governed by the IFR.

Chapter 4 Gas-liquid Hydrodynamics of a Fractal Flow Mixer

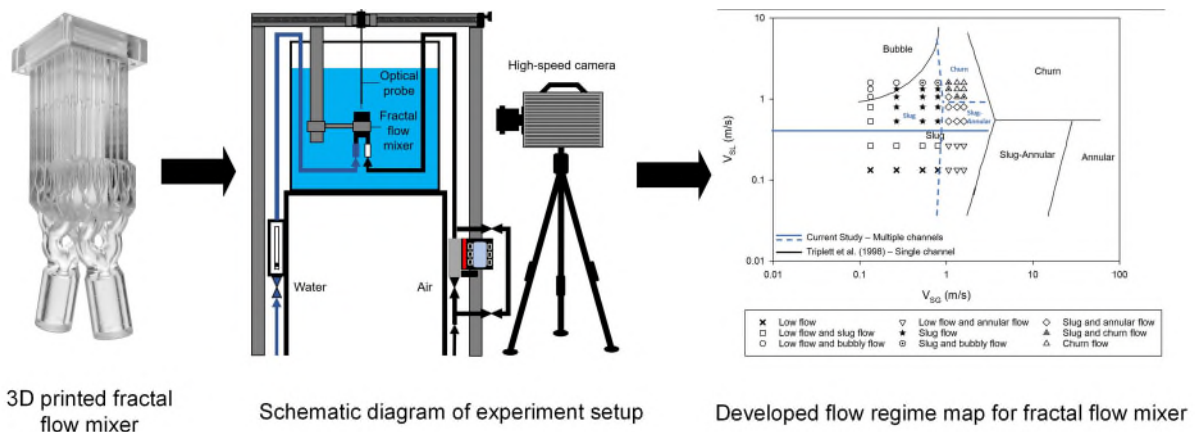
The content of Chapter 4 is reprinted (adapted) with permission from the following publication:

- M.D.M Priyambodo, T. Bhatelia, M. Shah, J. Patel, M. Mazur, V. Pareek “Gas-liquid hydrodynamics of a fractal flow mixer” *Chemical Engineering Processing – Process Intensification*, vol. 193, p. 109558, 2023/09/23, doi: <https://doi.org/10.1016/j.cep.2023.109558>.

Abstract

Gas-liquid hydrodynamics of a micro structured device (fractal flow mixer) were experimentally investigated. Experiments were conducted for a range of liquid-to-gas superficial velocities (V_{SL}/V_{SG}). High speed imaging was used to quantify the flow regimes inside the microchannels of the device at different V_{SL}/V_{SG} . Four distinctive flow regimes were identified, that includes bubbly flow, slug flow, annular flow, and churn flow. Due to the inherent properties of the slug flow, the ability to control and maintain a slug flow over a certain range combined volumetric flux ($V_{SL} + V_{SG}$) would be advantageous for different mass and heat transfer applications. The dominant forces that govern the transition of flows includes the inertial force, surface tension, bubble size distribution, and homogeneity of the fluid flow. At different V_{SL}/V_{SG} , two or more flow regimes were observed simultaneously in different micro channels. Consequently, a flow regime map was developed with transition lines of the V_{SL} and V_{SG} to indicate different flow regimes. It must be noted that the current flow regime map is only valid for a specific design of a fractal flow mixer that was presented in this study. Once the range of V_{SL} and V_{SG} to generate the slug flow was identified, an optical probe was used to measure the bubble mean size and velocity at different V_{SL} and V_{SG} within the slug flow regime. It was found that the increase of the V_{SL}/V_{SG} resulted in the decrease of the bubble mean size and the increase of the bubble mean velocity. Additionally, the global relative standard deviation (RSD) of bubble mean size decreases with the increase of the V_{SL}/V_{SG} , which can be attributed to uniform shearing of gas slugs across all channels. Increased liquid build-up in the channels occurs at a higher liquid-to-gas ratio. The fractal flow mixer was able to generate equal flow distribution across the 16 outlets and maintain a Taylor flow over a range of V_{SL}/V_{SG} . However, the bubble/slug size varies to a certain extent, depending on the V_{SL}/V_{SG} that are governed by the capillary effect and the backpressure. Additionally, further studies can be conducted on the fractal flow mixer for different applications at different scales. The fractal flow mixer has a potential to be used as an aeration device, a burner, a monolith reactor, a flow distributor, etc.

Graphical Abstract



4.1. Introduction

Micro-structured channels (including monolithic structures) are characterised by small diffusion paths, high surface-area-to-volume ratio, efficient process control, and smaller footprint (Gupta et al., 2009; Jähnisch et al., 2004), making them highly efficient for heat transfer (Asadolahi et al., 2012; Mohiuddin Mala et al., 1997; Ohadi et al., 2013) and mass transfer (Abiev et al., 2017; Guo et al., 2019; Ma et al., 2023) applications. It is often assumed that these channels are highly modular and in a multi-channel device, a uniform and controlled inlet fluid flow can be achieved. These inlet devices vary in shape and size depending on the type of application of a micro-structured channel. For example, chamber type (Dong et al., 2021) and honeycomb designs (Jiang et al., 2022; Ma et al., 2023; Zhang et al., 2018) have specifically been proposed as microreactors, whereas manifold distributors (Barbosa et al., 2023; Barbosa et al., 2021; Dong et al., 2017) and fractal devices (Liu et al., 2012; Mazur et al., 2019; Priyambodo et al., 2022; Zhang et al., 2021) have been used for achieving flow uniformity in heat and mass transfer applications. However, there are very limited large-scale applications of micro-structured channels in the industry, primarily due to the complexity of establishing even and controlled inlet fluid flow in multi-channels.

Table 1 summarises several studies on multi-channel micro-structured devices designed for different applications. Some of these studies have focused on the design and manufacture aspect, whereas a few studies aimed to characterise either single-phase flow or gas-liquid multiphase flow within the microchannels of the devices. There are different geometries of such devices, that includes fractal, parallel/consecutive, and honeycomb. A fractal design has a sequential design with a low number of divisions per stage but a high number of stages based on self-similar bifurcating channels, while a parallel/consecutive design has a high number of

flow divisions per stage (Mazur et al., 2019). Additionally, a honeycomb design has several divisions in the shape of hexagonal prismatic channels. In the case of single-phase flow through such devices, studies have been conducted to investigate the fluid flow distribution and/or mixing between multiple components. For example, the authors have previously designed and additively manufactured a novel fractal device (Mazur et al., 2019) and tested the flow distribution of the device using a single gas (air). Barbosa et al. (Barbosa et al., 2021) proposed a distributor named the *channelCOMB*, a manifold with prismatic channels. To analyse the flow distribution performance, a numerical simulation study with a single gas (air) was carried out to study the effect of the different Reynolds number and geometric parameters. It was found that the main chamber expansion and the length of the outlet channels mainly governs the distribution performance of the device. Barbosa et al. (Barbosa et al., 2023) then extended the study to investigate the effect of different additive manufacturing techniques towards the flow distribution performance of the *channelCOMB*. It was found that the stereolithography (SLA) technique was better in comparison to fused deposition modelling (FDM) technique due to the better material permeability and fabrication tolerance. Liu et al. (Liu et al., 2012) and Cao et al. (Cao et al., 2018) conducted studies using a single-gas (air) to study the effect of fluid properties, channel design (bifurcating stages and angle), operating parameters, and topology optimisation. These single-gas multi-channel distributor studies showed that an equal flow distribution can be achieved with different designs, leading to lower pressure losses.

When such devices are used with a multiphase gas-liquid flow, previous studies have focused on flow characterisation by defining flow regimes and measuring flow features (local and global) within the microchannels. As shown in Table 8, high-speed imaging, particle image velocimetry, and numerical techniques have been extensively used to understand the gas-liquid hydrodynamics inside multi-channel micro-structured devices.

The drag force between the two phases and the contact forces between the phases with the wall at a junction dictate the flow pattern in the microchannel. As a result, inlet flow rates, fluid properties, channel size, channel geometry, and material of construction of the channel are key parameters to optimise the flow inside a microchannel. Several studies have developed flow regime maps based on superficial gas and liquid velocities and have characterised the flow regimes in microchannel as bubbly flow, slug flow or Taylor flow, churn flow, annular flow, and transition flows (i.e. bubbly-slug, churn-annular, etc.) (Chen et al., 2006; Mishima & Hibiki, 1996; Triplett et al., 1999; Yue et al., 2007; Yue et al., 2008). Among these flow patterns, the slug flow or Taylor flow has gained more interest due to its unique feature where elongated, cylindrical gas bubbles occupy the entire cross-sectional area, separated by liquid

slugs, and a thin liquid film separates the gas bubbles from the wall of the tube (Abadie et al., 2012; Triplett et al., 1999). The fluid inside the liquid slug generates recirculation, which induces a higher rate of transport phenomena (mass transfer and heat transfer) (Abadie et al., 2012; Gupta et al., 2010; Leung et al., 2010). Despite its advantages, producing and controlling the Taylor flow within microchannels is rather a challenging task. There are studies that focused on the production of slug flow and investigating its hydrodynamics in a single channel (Abiev et al., 2017; Angeli & Gavriilidis, 2008; Etminan et al., 2021; Gupta et al., 2009; Gupta et al., 2010). Typically, T- junction (Liu & Zhang, 2009; Yue et al., 2007; Yue et al., 2008) or Y- junction (Lei et al., 2022; Lim & Lam, 2021) geometries are used to produce the slug flow in microchannels. However, only a few studies investigated the production and hydrodynamics of Taylor flow in multi-channel bifurcation geometries. As shown in Table 8, Zhang et al. (Zhang et al., 2021) conducted a numerical and an experimental study to provide a theoretical basis to scale up microreactors effectively and to characterise the gas-liquid Taylor flow in a fractal microchannel network with two inlets, four stages of bifurcations, and four outlets. The effect of Reynolds number, the gas-liquid flow rate ratio (j_G/j_L), and the gas inlet direction towards the stability of the Taylor flow, the gas-liquid interface, the flow distribution, and the swirling strength distribution were investigated. Tiwari et al. (Tiwari et al., 2019) conducted an experimental study to investigate the hydrodynamics of gas-liquid flow in a T-splitting distributor with two inlets, four stages of bifurcations, and a single outlet. Oil and air were used, and the effect of gas-liquid flow ratio towards the splitting mechanisms, flow regimes, the bubble/slug formation dynamics, and the corresponding relative lengths of bubbles/slugs were investigated. Three splitting mechanisms were identified at different gas-liquid flow ratios, including obstructed, partially-obstructed, and non-obstructed. Guo et al. (Guo et al., 2019) experimentally investigated the effect of different operating parameters and conditions towards the hydrodynamics of a gas-liquid flow in a tree-shaped microchannel. The flow distribution passing through the microchannels was governed by the hydrodynamic feedback effect at the end of branches and the capillary number (Ca) at the T-type bifurcation. Four flow regimes were identified: compact slug flow, slug flow, slug-foam flow, and bubbly foam. Additionally, in order to maintain a high-rate of mass transfer, a critical ratio of gas flow rate to liquid flow rate was determined.

In this work, the authors further extend the previous studies that have been carried out for the fractal flow mixer (Mazur et al., 2019; Priyambodo et al., 2022) by investigating the hydrodynamics of a gas-liquid flow passing through the fractal flow mixer and also the feasibility of producing Taylor flow within its microchannels. The fractal flow mixer was

submerged in a water tank with two inlets of air and water. At first, high-speed imaging (HSI) was used to identify the flow patterns within the microchannels of the fractal flow mixer over a range of air and water inlet flowrate or superficial velocity, which was chosen based on the flow regime map by Triplett et al. (Triplett et al., 1999) to target the slug flow or Taylor flow regime. Once the range of inlet velocities that exclusively produce the Taylor flow regime was identified, an optical probe was used to calculate the bubble size and velocity coming out of each outlet. The flow uniformity across all 16 outlets was analysed from the optical probe experiment. By tuning the slug size produced, it is expected that the fractal flow mixer can be used for different mass transfer applications while being simultaneously being used as a distributor.

Table 8: Previous studies on multi-channel micro-structured device								
Authors	Type of device	Application/purposes	Manufacturing method and material	Channel size	Operating parameters		Experiment/measurement method	Investigation
					Flow	Velocity		
Zhang et al. 2021	Fractal tree microchannel network (t-splitting)	Microreactor	Manufacturing method: template replication method Material: polydimethylsiloxane (PDMS) bonded with polyethylene terephthalate (PET)	0.3 – 2.4 mm	Gas-liquid, Gas: Nitrogen Liquid: Anhydrous ethanol with fluorescent polystyrene tracer particles	0 to 20 ml/min	μ-PIV, high-speed imaging, and CFD.	Taylor flow hydrodynamics and flow uniformity
Zou et al. 2021	Honeycomb	Microreactor	Manufacturing method: Stereo lithography (SLA) Material: photosensitive resin model VisiJet SL Clear	3.7 mm	Liquid-liquid Castor Oil and deionized water	0.3 to 5.4 mL/min	Camera (30fps) and numerical	Taylor flow hydrodynamics and flow uniformity
Guo et al. 2019	T-type bifurcation	Microreactor	Material: polymethyl methacrylate (PMMA)	0.4 mm	Gas-liquid Gas: CO2 Liquid: 2-amino-2-methyl-1-propanol	Gas to liquid flowrate ratio = 12	High-speed imaging and numerical	Fluid flow hydrodynamics, flow uniformity, and mass transfer performance.
Jiang et al. 2022	Honeycomb	Microreactor	Manufacturing method: template replication method Material: polydimethylsiloxane (PDMS) bonded with polyethylene terephthalate (PET)	1 mm	Gas-liquid, Gas: Nitrogen Liquid: Deionized water with tracer particles	0 to 10 mL/min	μ-PIV and CFD	Taylor flow hydrodynamics and flow uniformity
Zhang et al. 2018	Honeycomb	Microreactor	Manufacturing method: SLA 3D printing	2 – 3 mm	Gas-liquid,	Gas: 40 – 80 ml/min Liquid: 5 – 20	Experiment and CFD	Fluid flow hydrodynamics, flow uniformity,

			Material: Transparent resin		Gas: CO ₂ and N ₂ mixture Liquid: MEA solution			and mass transfer performance.
Tiwari et al. 2019	T-junction splitting distributor	Hydrodynamic performance (microreactor?)	Material: PMMA	1 – 2 mm	Gas-liquid Gas: Air Liquid: Oil (Kerosene)	Gas: 3 ml/min Liquid: 3 – 16 ml/min)	High-speed imaging	Taylor flow hydrodynamics
Ma et al. 2023	Honeycomb	Microreactor	Manufacturing method: Precision milling Material: PMMA	0.4 – 0.8 mm	Gas-liquid Gas: CO ₂ Liquid:	Gas-liquid flow ratio: 34	μ-PIV	Fluid flow hydrodynamics, flow uniformity, and mass transfer performance.
Dong, Xu, and Xu 2017	Modular manifold multi-stage channel (t-junction splitting)	Modular manifold for a fuel cell stack	-	3.2 (outlet) – 8.0 mm	Gas (single) Gas: air	Flowrate: 24000 – 54400 sccm Vel: 4.0 – 14.2 m/s	CFD	Flow uniformity
Cao et al. 2018	Multi-angle bifurcating channel distributor	Fluid flow distributor	-	Outlet: 1 mm Inlet: 16 mm	Liquid (single) Liquid: water	0.01 – 0.1 m/s	CFD	Flow uniformity Effect of inlet velocity and bifurcation angle
Liu et al. 2011	Circular and tee bifurcating channel distributor	Fluid flow distributor	Manufacturing method: CNC Material: Plexiglass	Outlet: 0.77 mm Inlet: 4.52 mm	Gas (single) Gas: Air	1.13 – 5.66 m ³ /h	Experiment	Flow uniformity
Liu, Li, Wang 2012	Tree-shape bifurcation channel	Fluid flow distributor	-	Outlet: 3.48 mm Inlet: 4.52 mm	Gas (single) Gas: Air	-	CFD	Flow uniformity
Barbosa et al 2021 and 2023	Parallel/consecutive flow distributor	Mesostructured reactor		Outlet: 0.994 – 1.036 mm	Gas (single) Gas: Air		CFD and experiment	Flow uniformity

Priyambodo et al. 2022	Fractal flow mixer	Fluid flow distributor	Manufacturing method: Vat-photopolymerisation (VP) and laser powder bed fusion (L-PBF) Material: Transparent resin (polymer) precursor and Ti-6Al-4V alloy	Inlet: 4 mm Outlet: 1mm	Gas Gas: Air and Methane	Re = 10 - 10000	CFD	Manufacturing method and flow uniformity
Mazur et al 2019	Fractal flow mixer	Fluid flow distributor	Manufacturing method: Vat-photopolymerisation (VP) and laser powder bed fusion (L-PBF) Material: Transparent resin (polymer) precursor and Ti-6Al-4V alloy	Inlet: 4 mm Outlet: 1mm	Gas (single-phase) Gas: Air	Re = 1000 - 10000	CFD and experiment	Manufacturing method and flow uniformity

4.2. Experimental

The fractal flow mixer, as shown in Figure 47[a], consists of self-bifurcating channels. It was additively manufactured using the vat-photopolymerisation (VP) technique with a transparent resin (polymer) precursor. The fractal flow mixer combines the function of a flow distributor and a mixer into a single device. In their prior work, the authors have presented the design and the additive manufacturing process of the fractal flow mixer (Mazur et al., 2019; Priyambodo et al., 2022). The geometric parameters of this device are also summarised in Figure 47[b]. The fractal flow mixer has two inlets or modules with a diameter of 4 mm, which go through four stages of bifurcation. It means that each module is symmetrically bifurcated into a total of 16 channels. These 16 channels from each module were then merged by 16 Y-junctions, resulting in 16 microchannel outlets of 1 mm diameter each, which is shown in Figure 47[c]. Due to the inherent microchannel geometry of these 16 outlets, it is expected that certain combinations of inlet flow of gas and liquid from the two inlet modules would produce a Taylor flow or a controlled slug flow in the microchannel outlets and produce gas bubbles after the fluid flow is dispersed through the microchannel outlets. In this work, the device was operated using air and water. High-speed imaging was used to observe the gas-liquid flow in the outlet microchannels qualitatively. The combinations of air and water flow rates, which resulted in a Taylor flow in the outlets, were identified. Moreover, the slug sizes were quantified by post-processing the high-speed images and measuring the bubble sizes using an optical probe.

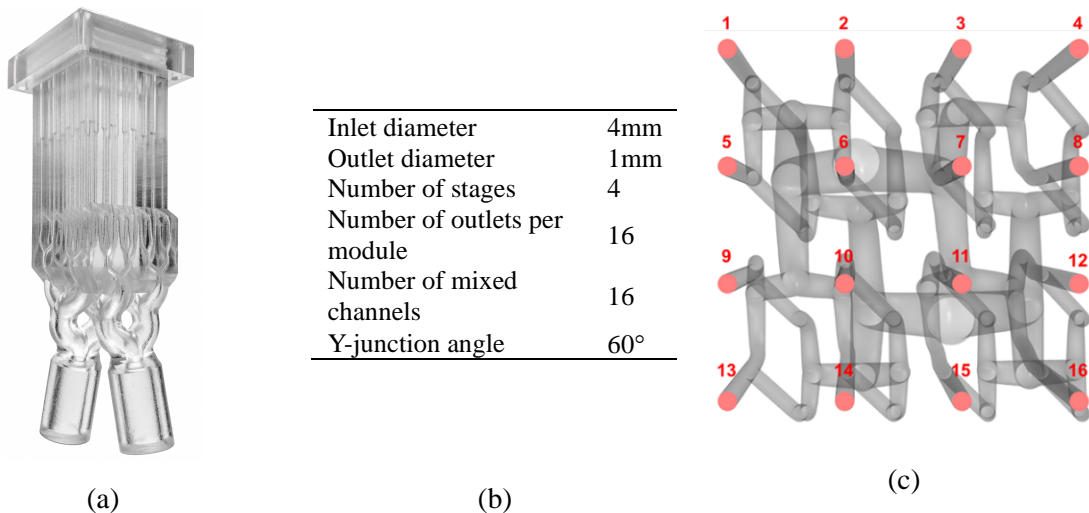


Figure 47: (a) The additively manufactured fractal flow mixer, (b) its geometrical parameters, and the (c) Outlet ID

The schematic diagram of the experimental setup is shown in Figure 48. A custom aluminium frame was used to support the optical probe, lead screw, and the fractal flow mixer. The fractal flow mixer was submerged in a square tank filled with water. The inlet modules were connected to air and water lines. The air and water flow rate were controlled using a mass flow controller and a rotameter. A bypass valve was installed around the air mass flow controller to avoid the channels being flooded with water, especially the air line. In this study, the gas and liquid slugs inside the microchannels will be referred to as G_S and L_S , respectively. Additionally, the gas bubbles dispersing from the outlet of the fractal flow mixer will be referred to as G_B .

The Photron FASTCAM SA4 high-speed camera with a Sigma 105mm f/2.8 EX DG macro lens was used to capture high-speed images of the fluid flow passing through the microchannels of the fractal flow mixer. The high-speed camera was placed perpendicular to the four visible outlets, and an LED video light was used for illumination. Images were recorded for 0.5 seconds at 5000 frames per second with a shutter speed of 1/25000s.

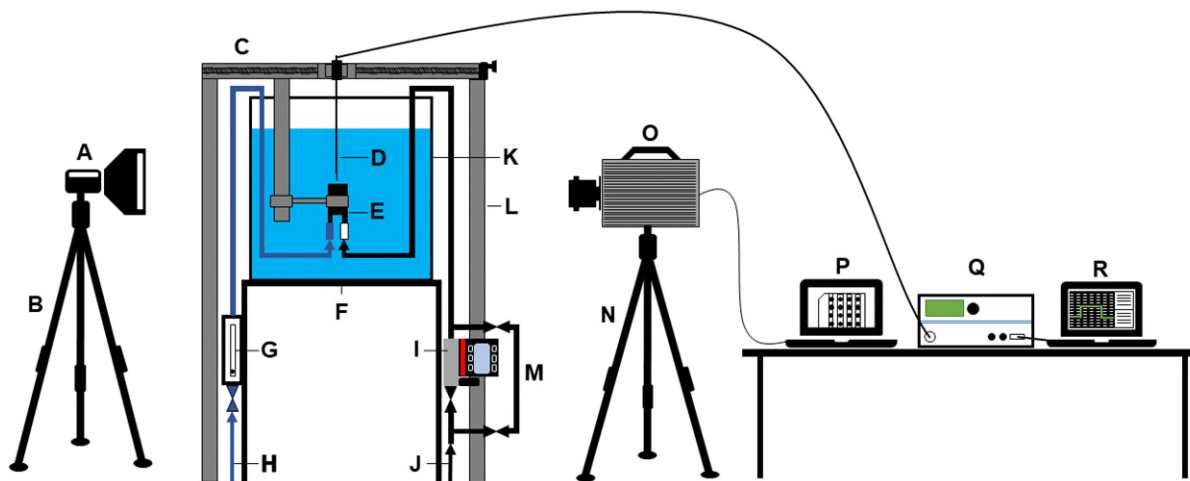


Figure 48: Schematic diagram of experiment setup [A] LED Light [B] Light stand [C] Lead Screw [D] Optical probe [E] Fractal flow mixer [F] Metal stand [G] Water rotameter [H] Water inlet [I] Air mass flow controller [J] Air inlet [K] Water tank [L] Custom aluminium frame [M] Bypass valve [N] Camera tripod [O] High speed camera [P] Laptop 1 (for HSI) [Q] Optoelectronic module [R] Laptop 2 (For optical probe)

The range of inlet flow rates of both water and air for the experiments conducted in this study was selected based on the flow regime map of Triplett 1998 (Triplett et al., 1999), as shown in Figure 49. The regime map was deduced for a gas-liquid flow in a single circular microchannel with an internal diameter of 1.097 mm. The regime map represented a wide range of gas superficial velocity (V_{SG}) and liquid superficial velocity (V_{SL}) on the X-axis and Y-axis,

respectively. The region on the map was divided into different flow types, including slug flow, slug-annular flow, annular flow, bubbly flow, and churn flow. As the current experimental study intended to produce a slug flow or Taylor flow in the microchannels of the fractal flow mixer, a range of V_{SG} and V_{SL} was selected that was within the slug flow region, as denoted by circular symbols in Figure 49. The selected range of V_{SG} and V_{SL} was then converted accordingly to the corresponding combinations inlet gas and liquid flowrate for the experiment.

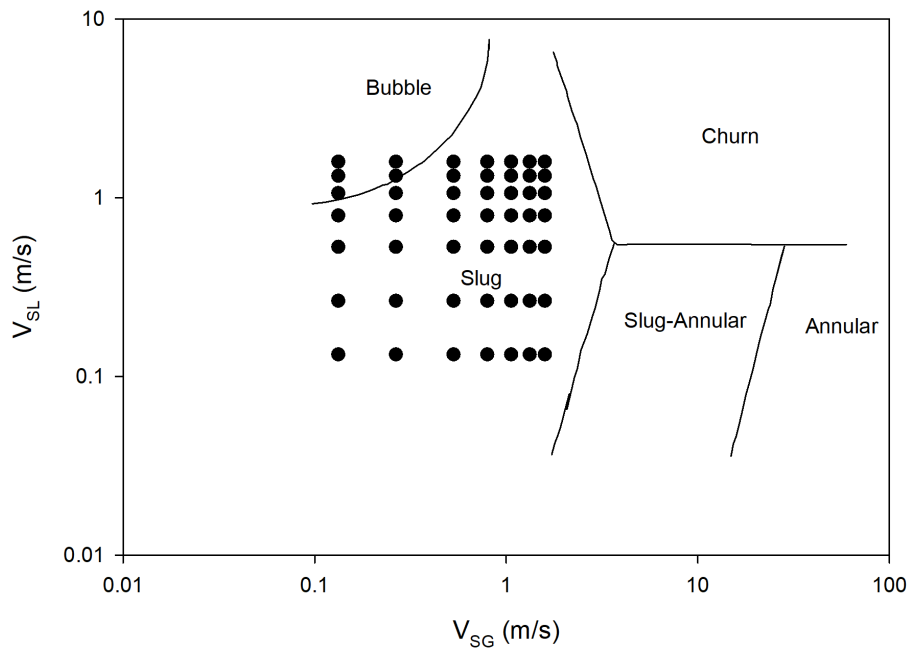


Figure 49: Regime map for a gas-liquid in a circular micro-channel ($d_i = 1.097$ mm) (Triplett et al. 1998) with dots representing tested flow conditions in the current study.

It is important to note that, theoretically, the fractal flow mixer was designed to maintain the same velocity at the inlet and on each outlet tube. Although the tube size is reduced from 4 mm at the inlet to 1 mm at the outlet tubes, the fluid flow is divided into 16 outlet tubes, maintaining the same superficial velocity between each inlet module and the outlet channels. Hence, the inlet velocity or the superficial velocity in the microchannels of air and water will be referred to as the V_{SG} and V_{SL} , respectively. In addition to high-speed imaging, the slug size in the outlet microchannel was measured by characterising the G_B size coming out from each outlet. For this, an optical probe was placed 0.5 cm above an outlet. To measure G_B from 16 different outlets of the fractal flow mixer using the optical probe, the position of the optical probe was changed by operating a lead screw, as shown in Figure 48. Each outlet was accordingly labelled, as shown in Figure 47[c].

The optical probe used in this work was a custom-made, single-tip, straight Doppler probe, along with a data acquisition system consisting of an optoelectronic module and post-processing software supplied by A2 Photonic Sensors. The construction and working principle of this optical probe was described in studies previously conducted by Prakash et al. (Prakash et al., 2019; Prakash et al., 2018). The data acquisition system utilises a block system to capture invalid and valid gas bubble events. To determine the optimum number of blocks, a block independence test was conducted at a V_{SG} of 0.531 m/s and a V_{SL} of 1.061 m/s. Three blocks were tested, that includes 1000, 2000, and 3000 blocks. From the three blocks tested, it was found that the difference in the averaged value (from 3 runs) of Bubble Mean Size (BMS) and Bubble Mean Velocity (BMV) between 2000 blocks and 3000 blocks was 0.69 % and 2.33%, respectively. Hence, 2000 blocks were chosen for each experiment run conducted in this study. Depending on the velocity tested, on average, 2000 blocks equals $\sim 2150 G_B$. At a lower velocity (i.e. $V_{SG} = 0.265$ m/s and $V_{SL} = 0.531$ m/s), it would be equal to 100-200 G_B and at a higher velocity (i.e. $V_{SG} = 0.796$ m/s and $V_{SL} = 1.326$ m/s), it would be equal to 6800 G_B . The experiment was conducted at least in triplicate for each combination of water and air inlet velocities at each outlet tube, totalling 6000 blocks per velocity tested. At lower velocity (i.e. $V_{SG} = 0.265$ m/s and $V_{SL} = 0.531$ m/s), it was repeated 5 to 6 times to capture at least 200 G_B in total. Since the block-based system was used in these experiments, the time to complete the pre-determined blocks (2000 blocks) varies from one experiment to another.

4.3. Results and Discussion

4.3.1. Flow Regimes

Initially, HSIs of gas-liquid flow in the front four outlet channels at different gas and liquid operating flow rates were analysed. The HSI method can only be used to identify the flow patterns in the external outlet channels of the fractal flow mixer. A full tomography must be conducted to qualitatively identify the flow regime of four internal outlet channels of the fractal flow mixer, which is not in the current scope of the study.

The dominant forces that govern the transition of flow regimes includes the inertial force, surface tension, bubble size distribution, and homogeneity of the fluid flow. For the inertial force, the increase of the V_{SG} would result in the increase to the inertial force, which eventually increases the probability and frequency of bubble coalescence (bubble-to-bubble collision). On the other hand, the surface tension is the force that resists the bubble coalescence. A distribution of smaller bubble sizes within the tube would have a higher surface tension per

unit volume, while a distribution of larger bubble sizes would have a reduced surface tension and would be prone to be coalesced. Additionally, the homogeneity of the fluid flow also contributes to the generated fluid flow regime within the tube. An unequal fluid flow distribution can lead to localised zones of high bubble concentration, creating a hub that would expedite the coalescence of bubbles.

Out of 49 gas and liquid flow rate combinations, the images with distinct flow regimes are shown in Figure 50[a-d]. Four different types of flow regimes were identified: bubbly flow, slug flow, annular flow, and churn flow. Bubbly flow was identified at a high liquid-to-gas ratio of the superficial velocity (low void fraction) (i.e. $V_{SG} = 0.133$ m/s and $V_{SL} = 1.326$ m/s). It is a flow regime where the gas phase is distributed in the tube as dispersed non-spherical bubbles that are smaller in diameter than the diameter of the channel. The low V_{SG} contributes to the distribution of small bubbles in this flow regime, as it would not be able to overcome the surface tension and inertia of the liquid flow. The small bubbles in this flow regimes have a high surface tension per unit volume that would resist the coalescence of the bubbles. If the V_{SG} is increased, the slug flow was identified (i.e. $V_{SG} = 0.531$ m/s and $V_{SL} = 0.796$ m/s). The increase in the V_{SG} would be able to overcome the surface tension of liquid and produced elongated cylindrical gas slugs, also known as Taylor bubbles, which occupies almost the entire cross-sectional area of the channel. A thin liquid film separates the gas slugs from the wall of the channel, and a liquid slug exists between the gas slugs. These gas slugs/Taylor bubbles would rise through the liquid driven by buoyancy and inertia, displacing smaller bubbles. If the ratio of the superficial velocity was swapped, where the V_{SG} is significantly higher than the V_{SL} (high void fraction) (i.e. $V_{SG} = 1.061$ m/s and $V_{SL} = 0.531$ m/s), the annular flow was identified. The annular flow is a flow regime that occurs when the gas phase was seen travelling at the centre of the channel as a continuous phase with a thin liquid film separating the gas phase from the wall of the channel. It is a result of the centrifugal force from the gas flow that pushes the gas to the centre. Whilst the high V_{SG} induces the annular, a constant V_{SL} is also important to maintain the presence of the thin liquid film on the wall. A very low V_{SL} would lead to cause the liquid film to break down and result in a different flow regime, potentially a wavy annular flow that was not observed in this study. The churn flow was observed at an increased volumetric flux of the mixture ($V_{SG} + V_{SL}$) (i.e. $V_{SG} = 1.592$ m/s and $V_{SL} = 1.326$ m/s). The churn flow is a flow regime that occurs when the Taylor gas bubbles deteriorates at higher flowrates due to the transition of a continuous liquid phase into a continuous gas phase. The considerable increase of the volumetric flux causes the surface tension between the liquid and gas phase of the fluid flow to break, generating irregular shapes and sizes of gas slugs within the tube.

Furthermore, at different combinations of velocities, two or more flow patterns (low flow, annular flow, slug flow and churn flow) were observed simultaneously in different outlet microchannels of the fractal flow mixer. Hence, a specific range of V_{SG} and V_{SL} is not exclusively related to a particular flow regime, with the exception of the slug flow regime. Figure 46 shows the high-speed imaging experiment results of flow pattern combinations in the front four tubes of the fractal flow mixer ($d = 1.00$ mm). Starting from the lower V_{SG} and V_{SL} (i.e. $V_{SG} = 0.133$ m/s and $V_{SL} = 0.133$ m/s), low flow (Figure 51[a]) was identified. The low flow occurs when the V_{SG} is too low to overcome the pressure head in the water tank. Gas slugs are occasionally seen in 1 or 2 channels at this flow regime. Increasing the V_{SG} yet maintaining the V_{SL} (i.e. $V_{SG} = 0.133$ m/s and $V_{SL} = 0.531$ m/s), generated the low flow and slug flow regime (Figure 51[b]). Gas slugs were identified in several tubes at this flow regime, while the other tubes were still in the low flow regime. Further increase of the V_{SL} (i.e. $V_{SG} = 0.133$ m/s and $V_{SL} = 1.326$ m/s) led to a lower void fraction, resulting in the low flow and bubbly flow regime (Figure 51[c]). On the other hand, at a condition where the V_{SG} was significantly higher than the V_{SL} (i.e. $V_{SG} = 1.592$ m/s and $V_{SL} = 0.265$ m/s), the low flow and annular flow (Figure 51[d]) was identified. At an increased volumetric flux of the mixture ($V_{SG} + V_{SL}$) and at a specific combination of V_{SG} and V_{SL} range (i.e. $V_{SG} = 0.265 - 0.796$ m/s and $V_{SL} = 0.535 - 1.326$ m/s), the slug flow (Figure 51[e]) was identified. At higher V_{SL} , beyond the range of slug flow regime, yet maintaining the V_{SG} within the range of the slug flow regime (i.e. $V_{SG} = 0.531$ m/s and $V_{SL} = 1.592$ m/s), resulted in the slug and bubbly flow (Figure 51[f]), where either gas slugs or bubbles were identified across the four tubes. On the other hand, increasing the V_{SG} beyond the range of the slug flow regime, yet maintaining the V_{SL} within the range of the slug flow regime (i.e. $V_{SG} = 1.061$ m/s and $V_{SL} = 0.531$ m/s), resulted in the slug and annular flow (Figure 51[g]), where either gas slugs or an annular gas flow were identified across the four tubes. At the highest range of mixture volumetric flux tested (i.e. $V_{SG} = 1.592$ m/s and $V_{SL} = 1.326$ m/s), the fluid flow fully transitions into a churn flow (Figure 51[i]) across all four tubes. In general, qualitatively, the cause of the simultaneous occurrence of different flow regimes within the tubes are caused by the different volumetric flux of the mixture ($V_{SG} + V_{SL}$). Additionally, although the geometry of the fractal flow mixer was inherently designed to provide equal fluid flow distribution across all of the 16 outlets, the geometry might require further fine tuning to achieve a better fluid flow distribution across all of the outlets.

Figure 52 shows the observed flow patterns in this study plotted against the flow regime map by (Triplett et al., 1999) for a single circular channel ($d_i = 1.097$ mm). The experiment conducted by (Triplett et al., 1999) had two inlets with a T-junction to mix the two phases of air and water into a single channel/tube. On the other hand, the present study had two inlets, four stages of bifurcation, a Y-junction, and 16 outlet channels/tubes. Another difference between the two studies would be the material of construction of the microchannels, where the study by (Triplett et al., 1999) used a Pyrex circular channel (Ace Glass Pyrex Part No. 7740), while the fractal flow mixer presented in this study was additively manufactured using a transparent resin (polymer) precursor. The difference in the surface roughness between the two studies would also contribute to the generated flow regime map. Additionally, from Figure 52, the scalability of the existing single-channel regime map to be used for multiple channels was observed. It was found that the range of V_{SG} and V_{SL} to produce the slug flow regime has decreased. There is also a shift in the transition lines between the churn flow and the slug-annular flow, starting at a lower value of V_{SL} (i.e. $V_{SL} = 1$), shown by the dashed blue lines in Figure 52. Additionally, in order to maintain the presence of G_S in the microchannels, a minimum threshold value was identified for V_{SL} , which is >0.531 m/s. Consequently, a new flow regime map and transition lines (solid and dashed blue lines in Figure 52) was developed for the fractal flow mixer, which is a device with multiple outlet channels. It must be noted that the current flow regime map is only valid for a specific design of a fractal flow mixer that was presented in this study, which was additively manufactured using the vat-photopolymerisation (VP) technique with a transparent resin (polymer) precursor. Different additive manufacturing techniques and materials would result in the microchannel walls of the fractal flow mixer to have different wetting properties, surface roughness, and friction, affecting the generated divisions of flow regimes from the fractal flow mixer.

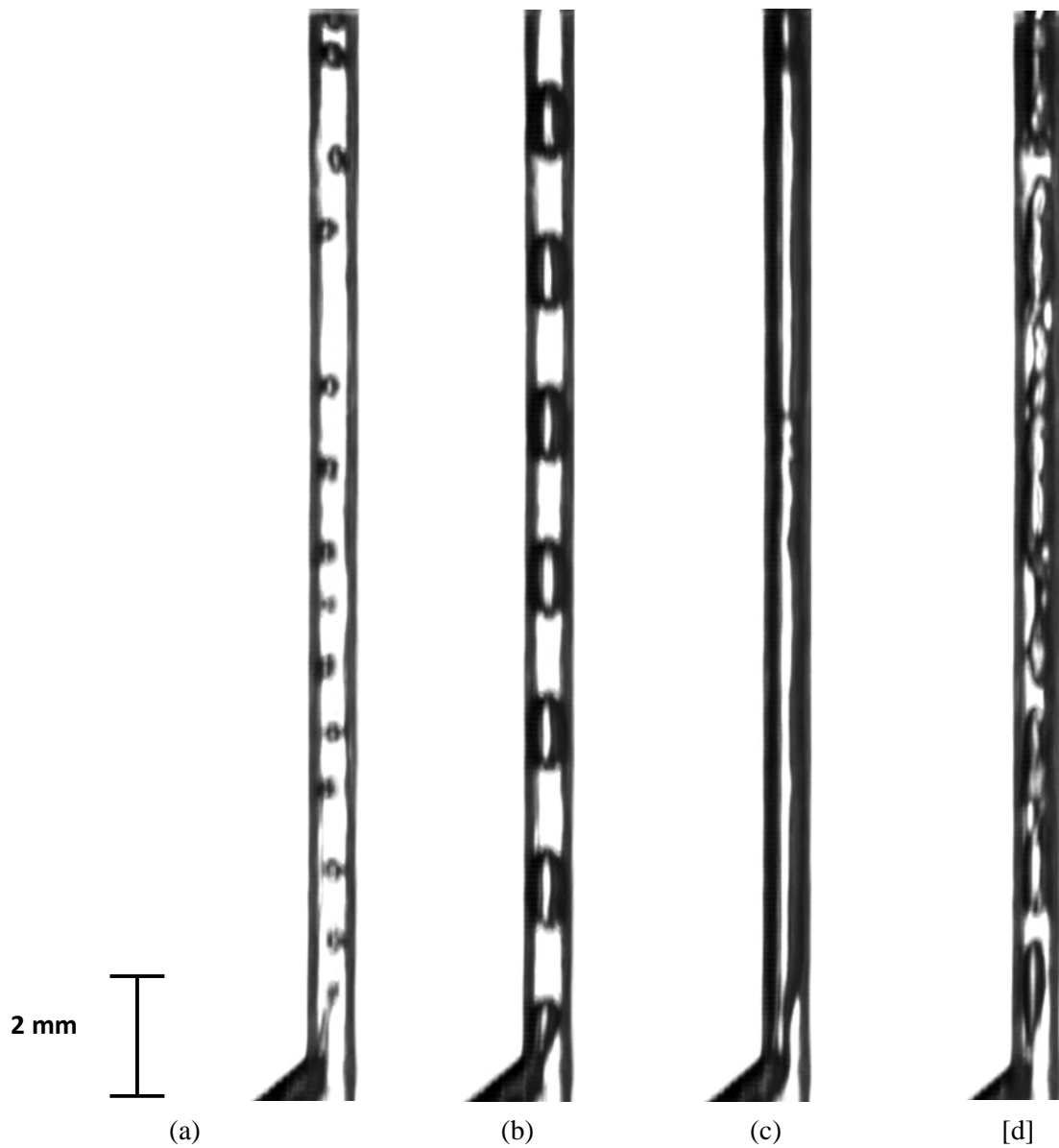


Figure 50: Identified flow patterns from high-speed imaging experiments [a] Bubbly flow [b] Slug flow [c] Annular flow [d] Churn flow

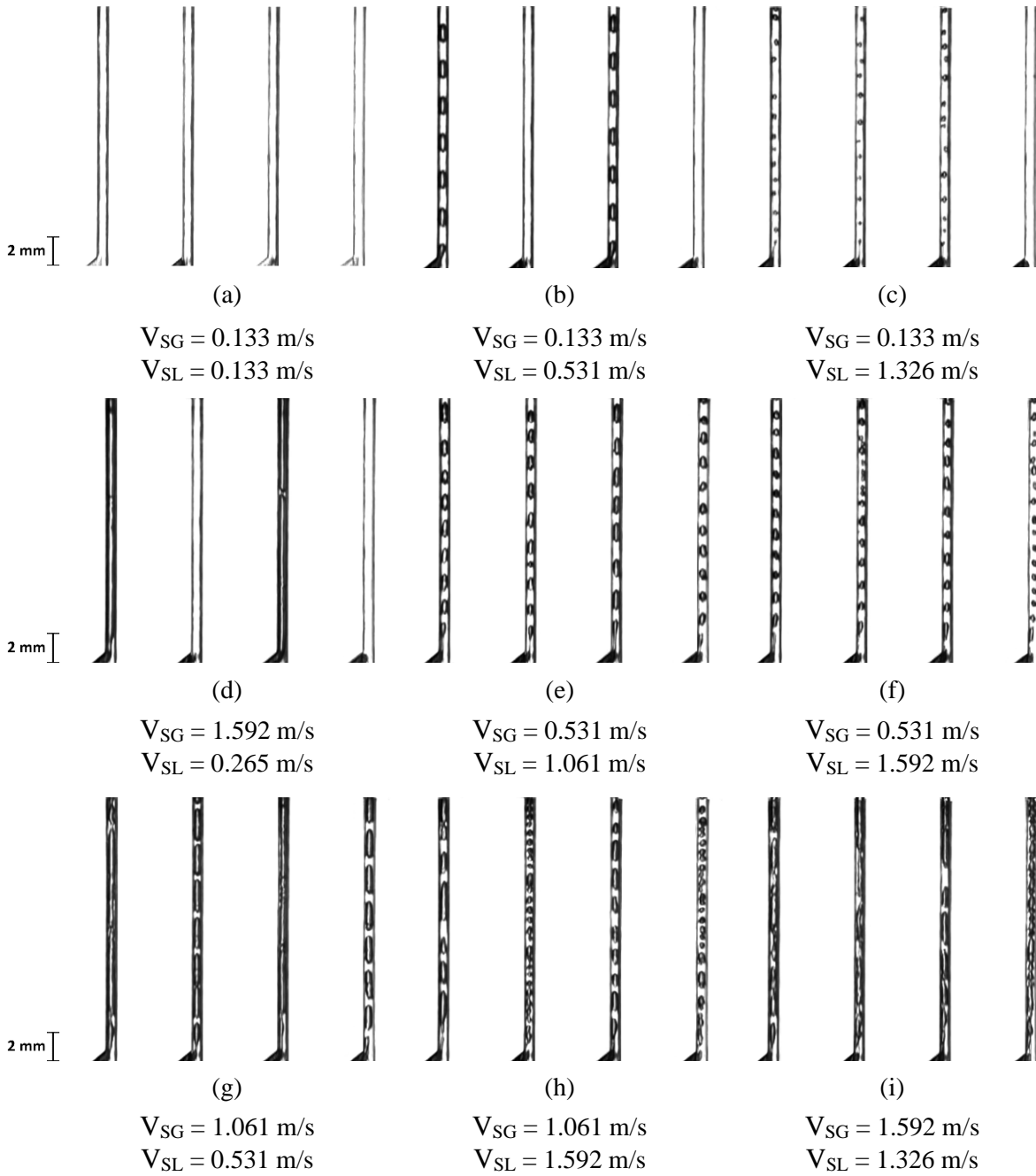


Figure 51: High-speed imaging experiment results of flow pattern combinations in the front four tubes of the fractal flow mixer (d= 1.00 mm): (a) low flow, (b) low flow and slug flow, (c) low flow and bubbly flow, (d) low flow and annular flow, (e) slug flow, (f) slug and bubbly flow, (g) slug and annular flow, (h) slug and churn flow, (i) churn flow

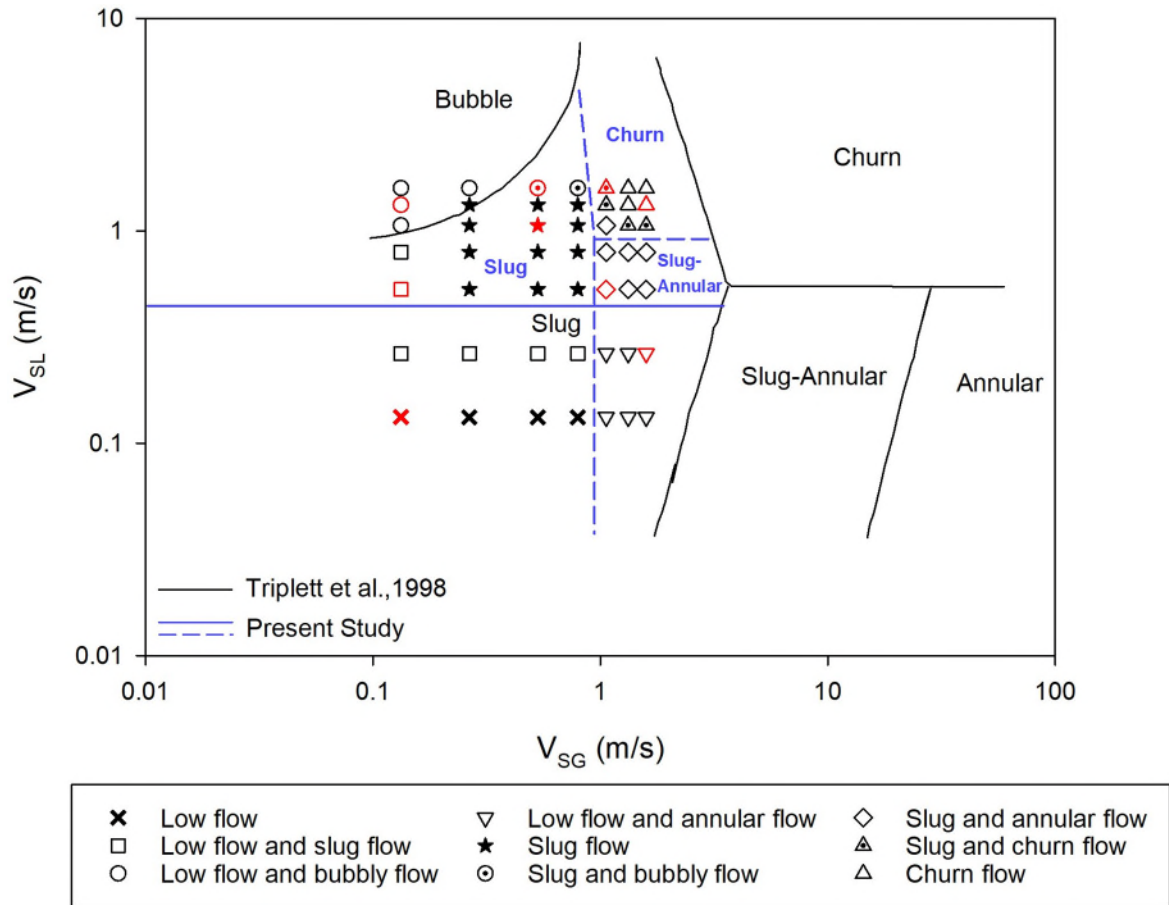


Figure 52: Identified flow patterns in the outlet channels ($d_i = 1.000$ mm) of the fractal flow device plotted against the flow regime map by Triplett et al. 1999 (Triplett et al., 1999) for a single circular channel ($d_i = 1.097$ mm). The solid black lines correspond to flow regime transition lines by Triplett et al. 1999 (Triplett et al., 1999) and the dashed and solid blue lines correspond to flow regime transition lines from this study.

4.3.2. Bubble Hydrodynamics

The results from the optical probe experiment that measures the BMS and BMV of the gas bubbles (G_B) dispersing from the outlet of the fractal flow mixer were further analysed in this section. The optical probe experiment was conducted over the range of V_{SG} and V_{SL} that exclusively produce slug flow ($V_{SG} = 0.265 - 0.796$ m/s and $V_{SL} = 0.531 - 1.326$ m/s). The term *averaged* used in this section refers to the average value from three experiment runs of the optical probe experiment. Meanwhile, the term *global average* refers to the average result from the 16 outlet channels combined. Figure 53 [a-b] shows the global of the BMS and BMV against the V_{SL} at different V_{SG} . Each data point in Figure 53[a-b] is an average value from 48 experiments. From Figure 53[a], the global average of BMS decreased with the increase of V_{SL} . This phenomenon occurred at all V_{SG} tested. Furthermore, at all V_{SG} tested, the global

average of BMS decreased by ~54% when the V_{SL} was increased from 0.531 m/s to 1.326 m/s. For the global average of BMV, as shown in Figure 53[b], the global average of BMV increased by two times (~244%) when the V_{SL} was increased from 0.531 m/s to 1.326 m/s.

Figure 54[a-c] shows the global average of the Relative Standard Deviation (RSD) of the BMS. It can be seen that the RSD decreases with the increase of the liquid-to-gas superficial velocity ratio (V_{SL}/V_{SG}). This phenomenon can be attributed to the constant shearing of G_s inside the channels due to the liquid build-up in the channels that occur at a higher V_{SL}/V_{SG} . At a lower V_{SL} and lower V_{SL}/V_{SG} , the kinetic energy in the liquid balances out the capillary force required for shearing the G_s , which is also why the consistency of the flow over the pre-determined number of blocks (2000 blocks) is better at a higher V_{SL}/V_{SG} .

Additionally, the reason of the non-uniformity across the sixteen channels could be due to the fact that the topology of the device is not highly symmetrical. Even though the design philosophy of the device is inherently symmetrical, the distribution of the gas and the liquid can be affected by the upstream velocity pathlines prior to the mixing point. Figure 55[a-c] shows the global average RSD of BMV across all 16 outlets. For all V_{SG} and V_{SL} tested, the RSD is relatively low (i.e. 5 – 10%), showing that the fractal flow mixer can provide uniform flow distribution across all sixteen outlet channels.

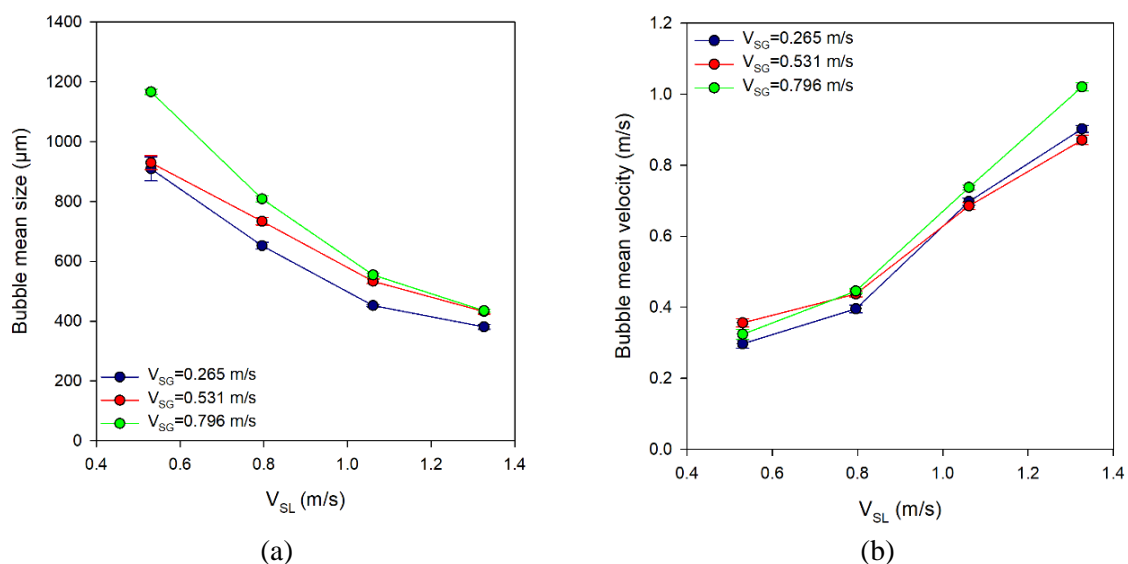


Figure 53: Averaged (a) bubble mean size and (b) bubble mean velocity across all 16 outlets combined against V_{SL} at different V_{SG} .

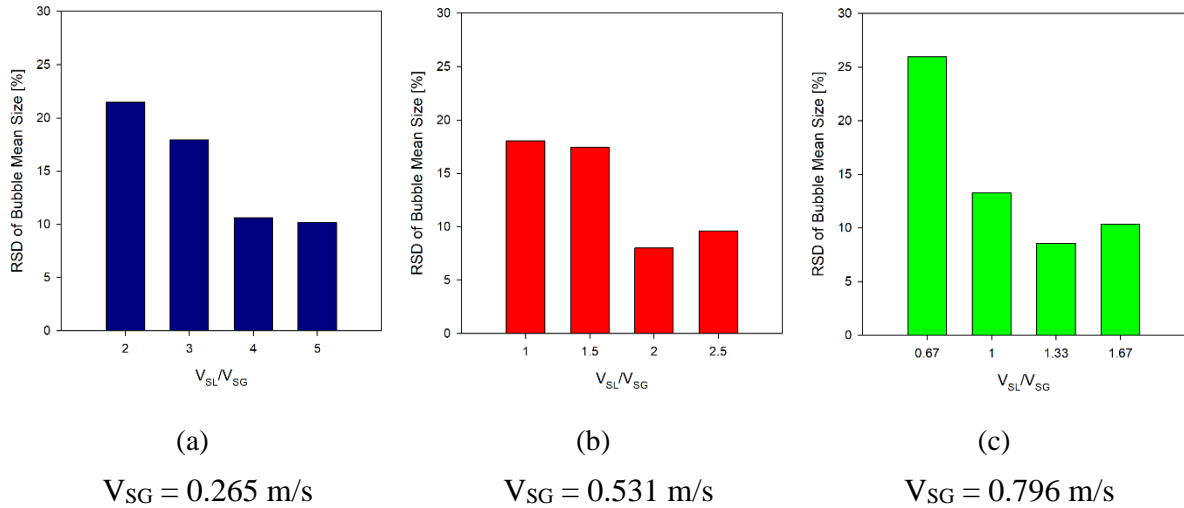


Figure 54: RSD of bubble mean size across all 16 outlets for (a) $V_{SG} = 0.265$ m/s, (b) $V_{SG} = 0.531$ m/s, and (c) $V_{SG} = 0.796$ m/s

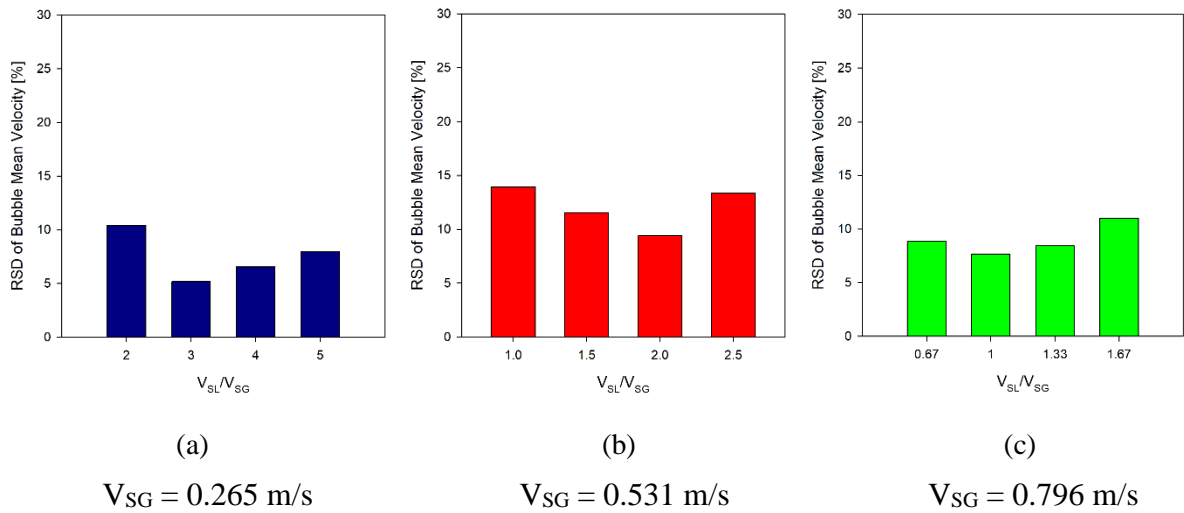


Figure 55: RSD of bubble mean velocity across all 16 outlets for (a) $V_{SG} = 0.265$ m/s, (b) $V_{SG} = 0.531$ m/s, and (c) $V_{SG} = 0.796$ m/s

Figure 56[a-c] and Figure 58[a-c] shows the averaged BMS and BMV at each outlet (local average) for different air inlet velocity, respectively. The error bars in Figure 56[a-c] and Figure 58[a-c] shows the standard deviation between the three experiment runs conducted for each outlet. From Figure 56[a-c], as previously shown in Figure 53[a], the BMS decreases with the increase of the V_{SL}/V_{SG} . Additionally, at lower water inlet velocity (i.e. $V_{SL} = 0.531$ m/s) and lower ratio of liquid-to-gas (i.e. 1), the G_B distribution among the 16 outlets is uneven. For example, as shown in Figure 56[b], at $V_{SL} = 0.531$ m/s and $V_{SG} = 0.531$ m/s, the difference in G_B size between the smallest (Position ID = 4) and the largest G_B size (Position ID = 11) is $\sim 58.5\%$. At a higher V_{SL} ($V_{SL} = 0.531$ m/s and $V_{SG} = 1.326$ m/s), the difference between the

smallest (Position ID = 4) and the largest G_B size (Position ID = 5) is $\sim 37.12\%$. This phenomenon was also shown in Figure 54[a-c]. Additionally, the effect of the V_{SL}/V_{SG} towards the size distribution of the of G_S at the front four channels were also qualitatively shown in Figure 57. Figure 58[a-c] shows that the bubble mean velocity is relatively constant at lower V_{SL} (i.e. 0.531 – 0.796 m/s) tested. However, variations exist across the sixteen outlets at higher V_{SG} and V_{SL} , which is caused by the random path of bubbles upon exiting the fractal flow device into the water tank, resulting in the bubbles not piercing the optical probe properly.

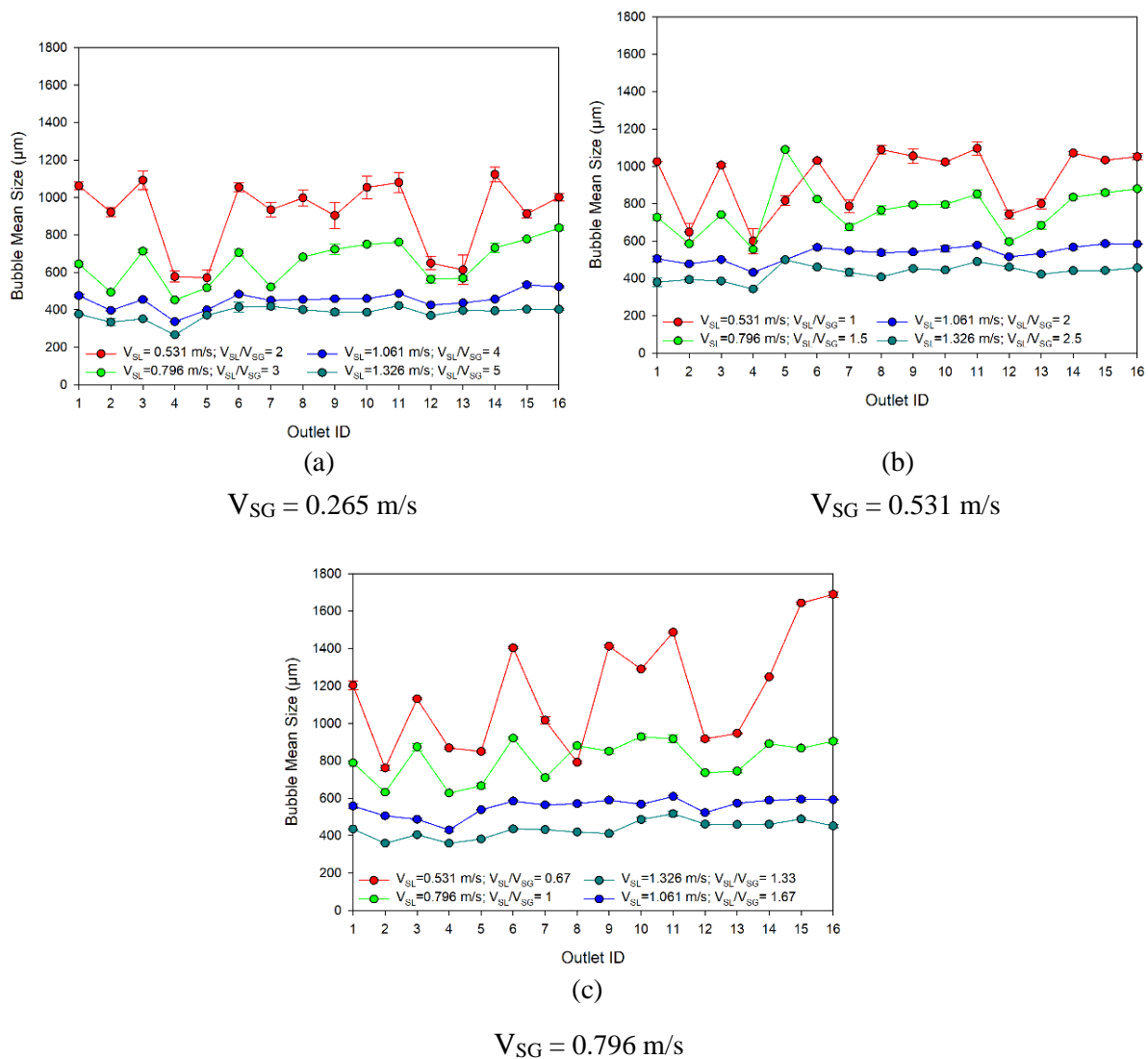
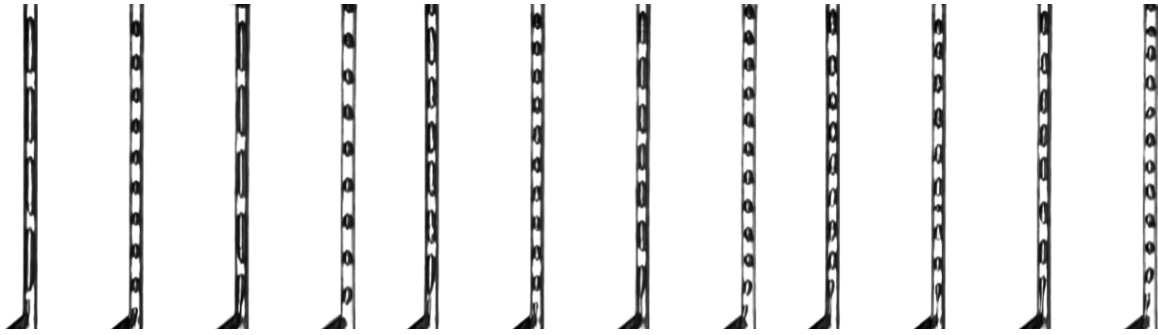


Figure 56: Bubble mean size at each outlet for (a) $V_{SG} = 0.265$ m/s, (b) $V_{SG} = 0.531$ m/s, (c) $V_{SG} = 0.796$ m/s



(a) $V_{SG} = 0.531$ m/s
 $V_{SL} = 0.531$ m/s
 $V_{SL}/V_{SG} = 1$

(b) $V_{SG} = 0.531$ m/s
 $V_{SL} = 0.796$ m/s
 $V_{SL}/V_{SG} = 1.5$

(c) $V_{SG} = 0.531$ m/s
 $V_{SL} = 1.061$ m/s
 $V_{SL}/V_{SG} = 2$

Figure 57: High-speed imaging experiment results at different V_{SL}/V_{SG} : (a) $V_{SL}/V_{SG} = 1$; (b) $V_{SL}/V_{SG} = 1.5$; (c) $V_{SL}/V_{SG} = 2$

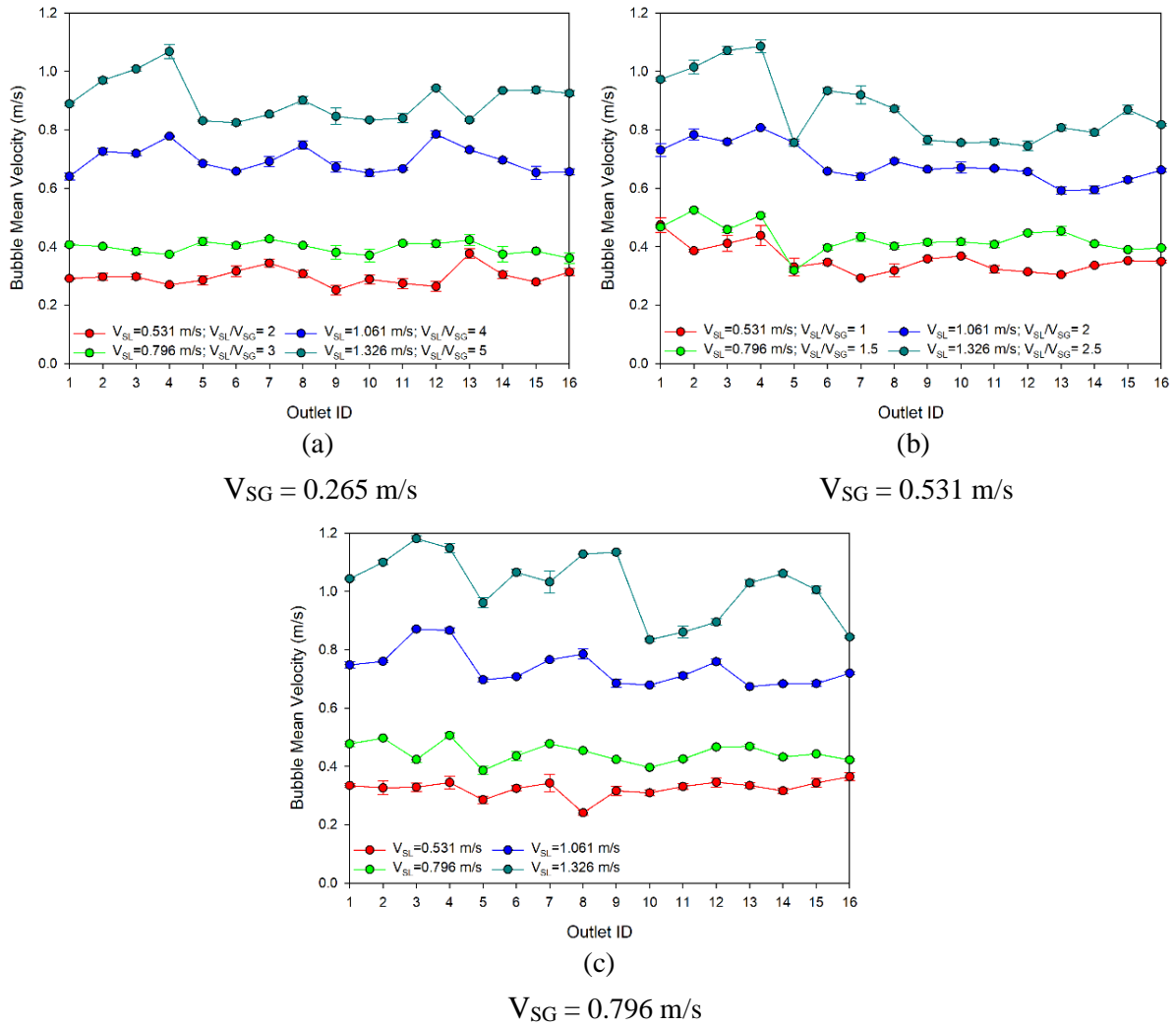
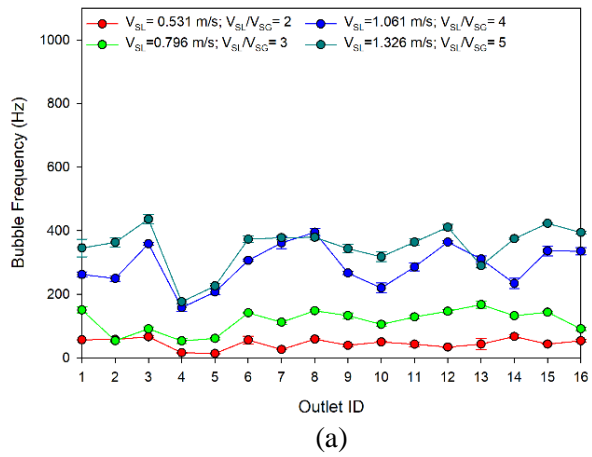


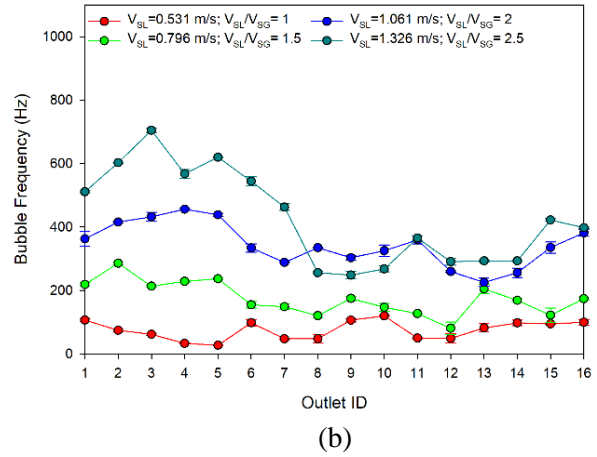
Figure 58: Averaged bubble mean velocity at each outlet for (a) $V_{SG} = 0.265$ m/s, (b) $V_{SG} = 0.531$ m/s, and (c) $V_{SG} = 0.796$ m/s

The flow distribution performance of the fractal flow mixer in producing G_B was also analysed using the data of bubble frequency at each outlet at different V_{SG} , as shown in Figure 59(a-c). It can be seen that at all V_{SG} tested, the bubble frequency increases with the V_{SL} , which is expected. The increase of V_{SL} also results in the variation of bubble frequency at different outlets, which is more apparent at higher V_{SG} and V_{SL} (i.e. $V_{SG} = 0.796$ m/s and $V_{SL} = 1.326$ m/s). Qualitatively, the trend of fluctuation at each outlet between the graphs of bubble mean size (Figure 56[c]) and the graphs of bubble frequency (Figure 59[c]) is similar, suggesting that the difference in bubble frequency at each outlet is caused by the difference of bubble size produced at each outlet at higher V_{SG} and V_{SL} .

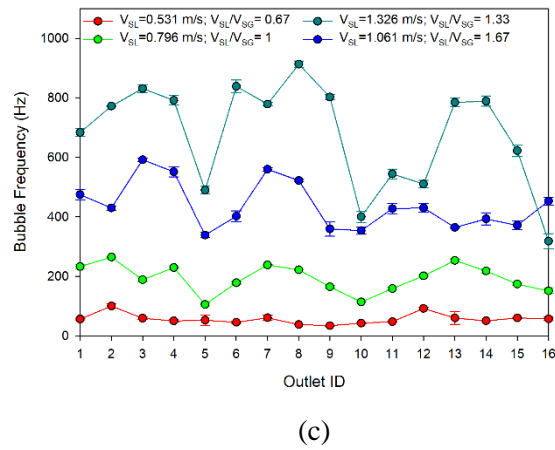
Besides the use of standard deviation in the form of error bars from the three experiment runs and analysing the bubble frequency, another parameter, the Relative Standard Deviation (RSD), was also used to assess the consistency of the fractal flow mixer in producing G_B at individual outlets (local) over a certain number of blocks (i.e. 2000 blocks). The RSD was calculated based on the total number of bubbles produced on a single experiment run at each outlet, which shows the range of variation of BMS and BMV from the respective average BMS and BMV values at each outlet. The RSD for the size and velocity of the G_B is shown in Figure 60[a-c] and Figure 61[a-c], respectively. Both figures shows that the RSD at higher V_{SL} is more consistent (i.e. $V_{SL} = 1.061 - 1.326$ m/s) in comparison to lower V_{SL} (i.e. $V_{SL} = 0.531 - 0.796$ m/s).



$V_{SG} = 0.265 \text{ m/s}$

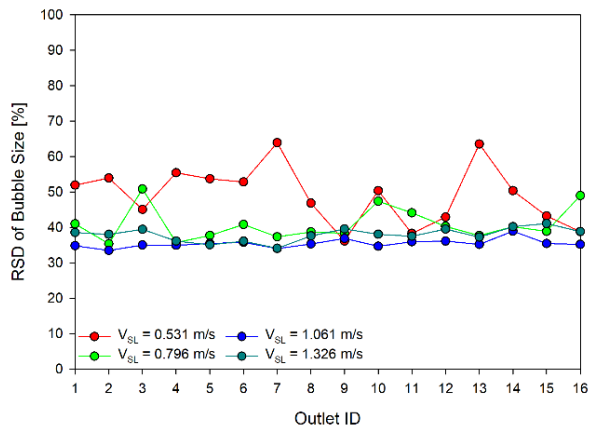


$V_{SG} = 0.531 \text{ m/s}$



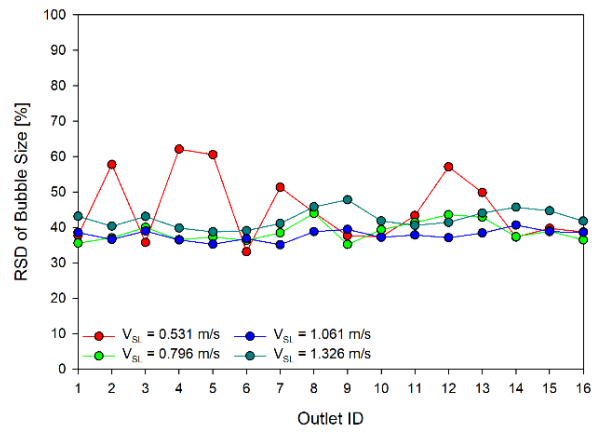
$V_{SG} = 0.796 \text{ m/s}$

Figure 59: Bubble frequency at each outlet for (a) $V_{SG} = 0.265 \text{ m/s}$ (b) $V_{SG} = 0.531 \text{ m/s}$ (c) $V_{SG} = 0.796 \text{ m/s}$



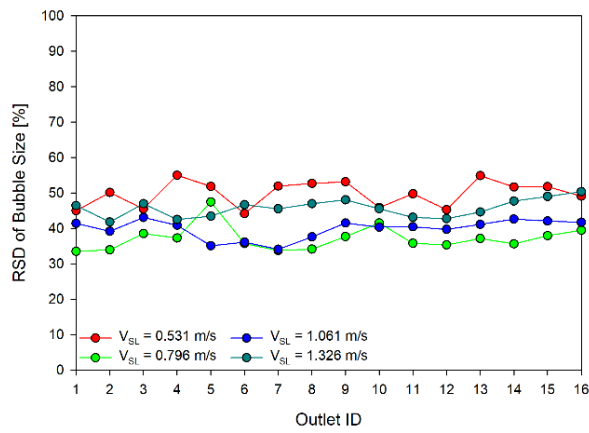
(a)

$V_{SG} = 0.265 \text{ m/s}$



(b)

$V_{SG} = 0.531 \text{ m/s}$



(c)

$V_{SG} = 0.796 \text{ m/s}$

Figure 60: Relative standard deviation of the bubble size at each outlet for (a) $V_{SG} = 0.265 \text{ m/s}$, (b) $V_{SG} = 0.531 \text{ m/s}$, and (c) $V_{SG} = 0.796 \text{ m/s}$

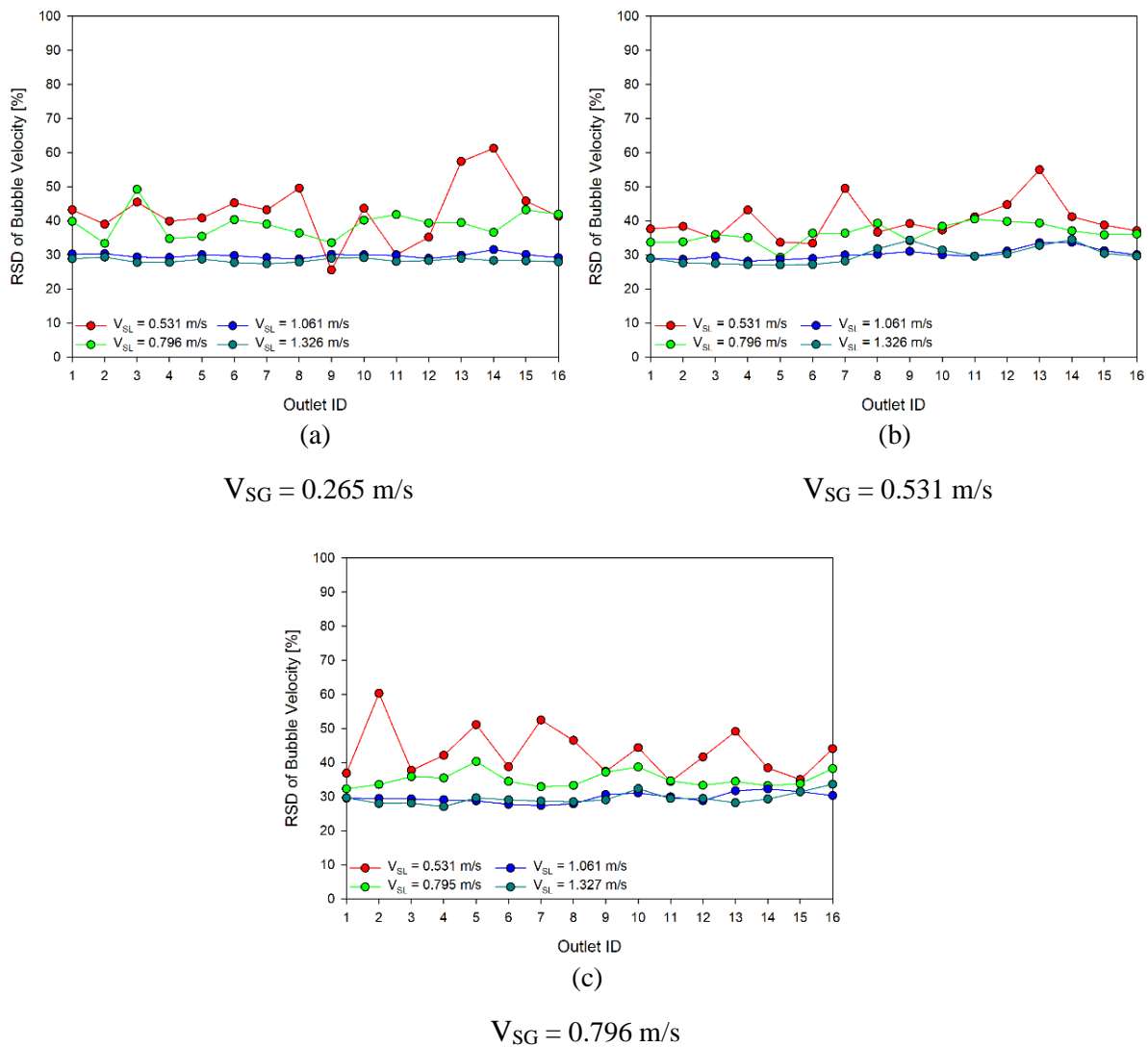


Figure 61: Relative standard deviation of the bubble velocity at each outlet for (a) $V_{SG} = 0.265 \text{ m/s}$, (b) $V_{SG} = 0.531 \text{ m/s}$, and (c) $V_{SG} = 0.796 \text{ m/s}$

4.4. Conclusions

In this work, the gas-liquid hydrodynamics of the fractal flow mixer was investigated. High-speed imaging (HSI) was used to identify the flow regimes and to measure the size of the gas slugs generated within the front four microchannels of the device. Four distinctive flow regimes were identified: Bubbly flow, slug flow, annular flow, and churn flow. At different combinations of velocities, two or more flow regimes (low flow, annular flow, slug flow and churn flow) were observed simultaneously in different outlet microchannels, resulting in nine combinations of flow patterns observed across the four channels. In future studies, a full tomography can be done to identify the flow regimes on the internal outlet channels.

Furthermore, comparing the identified flow regimes from the HSI experiment conducted against the flow regime map by (Triplett et al., 1999) for a single circular channel ($d_i = 1.097$ mm), it was found that the slug flow regime has decreased in size to a smaller range of V_{SG} and V_{SL} . There is also a shift in the transition lines between the churn flow and the slug-annular flow, starting at a lower value of V_{SL} (i.e. $V_{SL} = 1$), shown by the dashed blue lines in Figure 52. Additionally, in order to maintain the presence of G_S in the microchannels, a minimum threshold value was identified for V_{SL} , which is >0.531 m/s. Consequently, a new flow regime map and transition lines (solid and dashed blue lines in Figure 52) was developed for the fractal flow mixer. It must be noted that the current flow regime map is only valid for a specific design of a fractal flow mixer that was presented in this study, which was additively manufactured using the vat-photopolymerisation (VP) technique with a transparent resin (polymer) precursor.

Once the V_{SG} and V_{SL} combinations in the slug flow regime were identified, an optical probe was used to measure the bubble mean size and velocity coming out of each sixteen outlet channels of the fractal flow mixer. The experiment was carried out at different V_{SL}/V_{SG} . From the optical probe experiment, it was concluded that the increase of the V_{SL}/V_{SG} resulted in the decrease of the global average of the BMS and the increase of the global average of the BMV. Similar trends were observed from the averaged BMS and the local BMV within each outlet. From the global average of RSD of the BMS across all 16 outlets, it was found that the RSD decreases with the increase of the V_{SL}/V_{SG} , which can be attributed to the constant shearing of gas slugs due to the liquid build-up in the channels that occur at a higher liquid-to-gas ratio. Looking at the local RSD of bubble size and bubble velocity at each outlet, the RSD is more consistent at higher V_{SL} . Thus, it was concluded that the fractal flow mixer was able to generate an equal flow distribution across the 16 outlets and maintained a Taylor flow over a certain range of V_{SL}/V_{SG} . However, depending on the V_{SL}/V_{SG} , the G_B and G_S vary to a certain extent, governed by the capillary effect and the back-pressure. Additionally, further studies can be conducted on the fractal flow mixer for different applications at different scales. The fractal flow mixer can potentially be used as an aeration device, a burner, a monolith reactor, a flow distributor, etc.

Chapter 5 CFD Simulations of Vapour-Liquid Separator

The content of Chapter 5 is adapted and modified from the following publication:

- M.D.M. Priyambodo, B. Sun, T. Bhatelia, R. Utikar, V. Pareek, and G. Byfield, “CFD Simulations of Vapour-Liquid Separator in LNG Process” *Chemeca 2019: Chemical Engineering Megatrends and Elements*, Sydney, NSW, 2019. [Online]. Available:

<https://search.informit.org/doi/10.3316/informit.700549525211132>.

Abstract

In natural gas processing, a vapour-liquid separator (VLS) is one of the most commonly used unit operations. In this paper, a series of Computational Fluid Dynamics (CFD) simulations were conducted on an industrial scale VLS. Initially, simulations were carried out to evaluate the performance of an existing inlet diverter design (Schoepentoeter) by studying the effect of inlet Reynolds number on the cross-sectional variance of velocity. It was found that the flow was highly symmetrical and evenly distributed with a variance nearly zero at a very low Reynolds number ($Re = 1000$), but as the inlet Reynolds number increased, the variance increased to 0.03 and the flow was highly dominated towards the wall. To simulate the knitted mesh pad, porous media was used with inertial and viscous resistance calculated and validated using previously published experimental data (Rahimi & Abbaspour, 2008).

When a full scale VLS was simulated, it was found that at industrially relevant condition the effect of inlet diverter was significant on the Knitted mesh mist eliminator performance and approx. 88% of it was subject to velocities above the prescribed terminal velocity and would lead to poor vapor liquid separation. Without any hardware change to mitigate this underperformance, it would be required to drop the capacity of the VLS by at least 5 times. On the other hand, if two layers of mist pads with 75% size of full mesh pad was used, 26% recovery in performance can be achieved. The higher separation performance of dual-mesh pad configuration can be attributed to the inherent design of the dual mesh pad configuration and the increase of the total mesh pad volume by 60.7% in comparison to the single mesh pad configuration.

The model proposed in this work provides the basis for future development of parametric study on various configurations of mesh pad that can ultimately improve the capacity and performance of the VLS.

5.1. Introduction

Vapour-liquid Separator (VLS) is one of the most commonly found unit operation in the oil and gas industry. The VLS is often used in conjunction with other unit operations (i.e. heat exchangers and compressors) and it plays a critical role to obtain a hydrocarbon dew point specification, which must be fulfilled to transport and commercialise the gas (Perez, 2012). It is also employed to remove liquid from the gas stream and mitigate the adverse effect of the dispersed phase. For example, free liquid can damage or destroy a compressor, water carried from a boiler can erode the blades of a turbine, and gas dehydration equipment can lose operation efficiency when contaminated with liquid hydrocarbons (Stewart & Arnold, 2008). Hence, the VLS is important to protect downstream equipment from scaling or corrosive liquids, recover valuable products, and improve emission controls (Brunazzi & Paglianti, 1998).

Major parts of a VLS includes the feed pipe, inlet diverter, gravity-settling section, and mist elimination devices (coalescing media). The vapour stream enters through the feed pipe and then passed to an inlet diverter, where bulk of the liquid phase is removed from the vapour phase. The Shell Schoepentoeter is a well-known example of an inlet diverter. According to (Chemtech, 2014), it operates by utilizing properly oriented and distributed vanes that slices up the mixed-phase feed into a series of flat jets. The vanes then dissipate a large part of the kinetic energy from the jets allowing the vapour stream to enter the gravity settling section of in a uniform and smooth manner. It also enhances liquid separation through centrifugal acceleration of the flow. In the gravity settling section, the heaviest and largest particles are separated through gravity forces acting upon them. However, separation through gravity alone is insufficient to accomplish the desired separation efficiency since only droplets up to 100 μm are removed. Additional mist elimination devices are required to remove smaller droplets from the vapour stream by utilizing momentum through tortuous paths (Svrcek & Monnery, 1993). Installing mist eliminators can increase the separation efficiency of an economically sized separator from 95% (without mist eliminator) to 100% (Stewart & Arnold, 2008). These mist elimination devices includes knitted mesh mist eliminators (mesh pads), vane packs, baffles, and cyclones.

There are three separation mechanisms used in various mist eliminators, that includes, *Inertial Capture*, *Interception Interception*, and *Diffusion Capture*. Mist eliminators can be of various designs exploiting one or more of these mechanisms. *Inertial Capture* occurs when heavier particles deviate from the air/gas flow streamline due to its mass, causing a strong

variation in velocity and direction where it eventually hits the filter media (wire mesh) (Brunazzi & Paglianti, 1998; Swanborn, 1988). *Interception* involves particles/drops that is adequately light to follow the streamline, but is brushed against the wire mesh due to its particle size (Brunazzi & Paglianti, 1998). *Diffusion Capture* affects sub-micron particles where its particle movement is governed by the Brownian Motion, which is essentially the random movements of particles not following the streamline, increasing its probability of encountering a filter media (Brunazzi & Paglianti, 1998; Swanborn, 1988).

Various studies had been done on mist elimination devices at macro-scale. For wire mesh mist eliminators (mesh pads), (El-Dessouky et al., 2000) had developed an experimental setup to analyse the performance of the wire mesh mist eliminator. This experiment confirmed the basic understanding, underlying theories, and expectations towards the nature and behaviour of separation devices like the knitted mesh mist eliminator. A study by (Al-Dughaiter et al., 2011) investigated the pressure drop across wire mesh mist eliminators in a bubble column. Results of this experiment follows the same pattern and agrees with the result presented by (El-Dessouky et al., 2000). Besides experimental studies, CFD simulation studies were also conducted. A multiphase 2D CFD simulation study was conducted by (Rahimi & Abbaspour, 2008) to analyse the performance of the wire-mesh mist eliminator and compared it with the experimental study results by (El-Dessouky et al., 2000). (Al-Fulaij et al., 2014) showed that the correlation developed by (El-Dessouky et al., 2000) offers less flexibility in comparison with its developed CFD model. Another research study by (Sun et al., 2015) provided a different approach. This study focused on providing a method of geometrical simplification for numerical simulations and conducted a wind tunnel experiment under different air velocities for two different mesh pads.

The literature review reveals that majority of the work done previously focuses on understanding the hydrodynamics of the separation devices mentioned above. However, understanding the fluid flow distribution from the inlet diverter is equally important since it can significantly affect the performance of the mist eliminators. (Pham et al., 2018) made a gas-phase CFD model in 3D of various inlet diverters used in an amine absorber to understand the hydrodynamic performance of the Schoepentoeter compared to other inlet diverters (gas distributor) system. It was concluded that simple tubular inlet diverter designs were insufficient to equally distribute the gas over the vessel and a complex design like the Schoepentoeter were required to achieve better performance.

Therefore, based on the literature review provided above, this paper was aimed to further investigate the fluid flow distribution after passing through the Schoepentoeter by

studying the effect of inlet Reynolds number on the cross-sectional variance of velocity. Additionally, this study also conducted a parametric study to investigate the separation performance of a dual mesh pad configuration in comparison to a conventional single mesh pad setup.

5.2. CFD Model

CFD simulations were carried out to investigate the hydrodynamic performance of an existing inlet diverter design (Schoepentoeter) and to conduct parametric study of a novel VLS design with a dual mesh pad configuration. The models were solved using pressure-based solver in ANSYS 18.2 as single-phase steady-state incompressible flow with constant density. The two-dimensional (2D) (Figure 64) and three-dimensional (3D) (Figure 63 and Figure 65) fluid domains were discretised using a combination of quadrilateral and polyhedral meshes. The Standard K-epsilon viscous model was used for the 2D models, while the 3D models used the SST K-Omega due to its capability on handling complex geometry with a turbulent flow. The Semi-Implicit Method for Pressure-Linked Equation (SIMPLE) scheme was chosen as the pressure-velocity coupling algorithm with second-order upwind scheme for the momentum equation. Each simulation was initialised from the inlet at different Reynolds numbers, represented as inlet velocity.

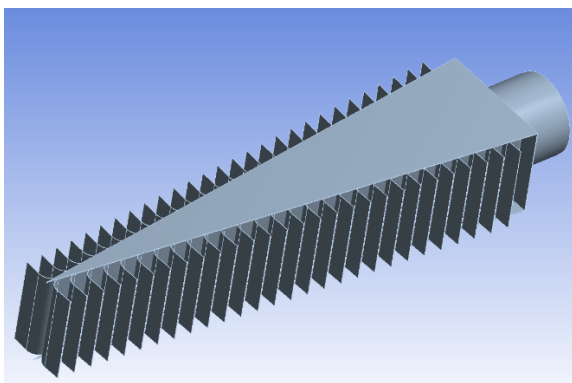


Figure 62: CAD Model of Schoepentoeter

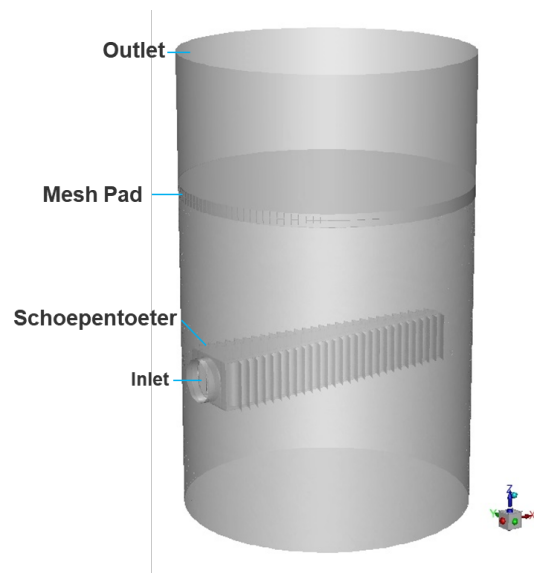


Figure 63: Fluid domain of a vapour-liquid separator with a Schoepentoeter and a single mesh pad configuration

For the inlet diverter study, a 3D model of Schoepentoeter was developed based on a technical drawing that was provided by the industry, as shown in Figure 62. The 3D model of the Schoepentoeter was then integrated into a 3D fluid domain of a vapour-liquid separator with a single mesh pad placed above the Schoepentoeter, as shown in Figure 63. The single-mesh pad fluid domain (Figure 63) was used to numerically investigate the hydrodynamic performance of the Schoepentoeter, that includes the fluid flow distribution and the average velocity of the fluid flow after passing through the Schoepentoeter. The fluid domain (Figure 63) was also used as a baseline case for the subsequent parametric study.

The parametric study investigated the effect of height and mesh pad opening towards the separation performance of a novel VLS design proposed in this work, which has a dual-mesh pad configuration. A 2D fluid domain, as shown in Figure 64, was used to minimise the computational time of the 50+ designs generated in this work. The components featured in the fluid domain includes the Schoepentoeter as the inlet diverter, a vane in the centre of the fluid domain, and two mesh pads (*Porous 1* and *Porous 2*) that were located at different height in the fluid domain. The centrally located vane has a symmetric geometry that was designed to maintain equal pressure on both sides of the fluid domain. The parametric design variables are tabulated in Table 9. Velocity sensors were added to the fluid domain to provide velocity distribution data along both mesh pad inlet, which are marked by the red lines in Figure 64.

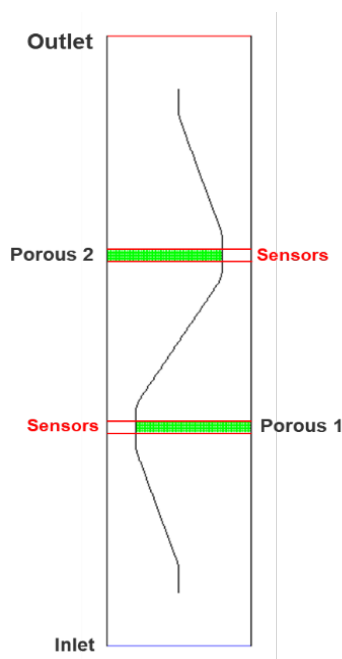


Figure 64: Diagram of vapour-liquid separator with a dual mesh pad configuration in 2D

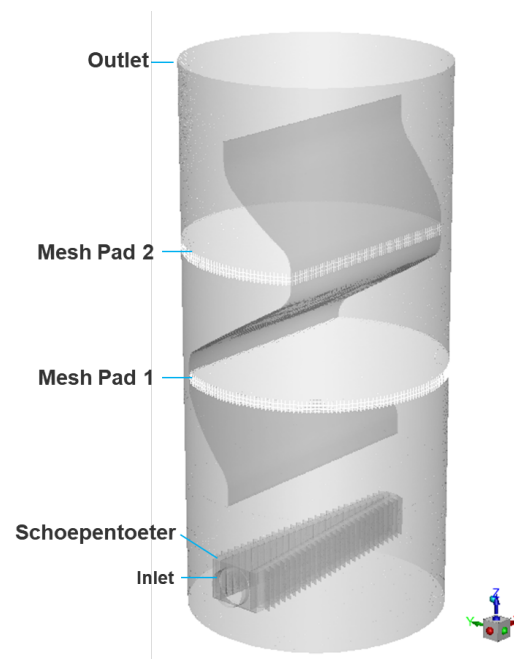


Figure 65: Fluid domain of a vapour-liquid separator with a Schoepentoeter and dual mesh pad configuration

Table 9: Variables of 2D Dual Mesh Pad Configuration Parametric Study	
Variable	Value
Mesh Pad Thickness [m]	0.2
Mesh Pad Length [m]	1.75 – 2
Distance between Mesh Pad [m]	1 – 6
Vessel Length [m]	2.5

To determine the optimum configuration for maximum separation efficiency, the calculated fluid velocity from the numerical CFD simulation reaching the surface of the mesh pad (mesh pad inlet velocity) was compared with the $V_{t,max}$ of each design. The $V_{t,max}$ is the maximum terminal velocity at which the droplets are captured by the mesh pad, which is calculated by using the modified Souders-Brown equation as a function of the load factor (K-value) and the fluid densities (gas and liquid). The K-value is typically an empirical value provided in different research studies or by vendors. For the mesh pad to reach maximum separation efficiency, the fluid velocity reaching the surface of the mesh pad (mesh pad inlet) must be lower than the calculated $V_{t,max}$. Eq. 12 can also be used to determine the cross-section area of the mesh pad based on the $V_{t,max}$ (Brunazzi and Paglianti 2001).

$$V_{t,max} = K \sqrt{\frac{\rho_l - \rho_v}{\rho_v}} \quad \text{Eq. 12}$$

5.3. Mesh Pad Modelling Methodology and Validation

The mesh pad used in the fluid domain was modelled as a porous zone that requires inertial and viscous resistance values. These values were calculated using a non-linear pressure drop correlation, as shown by Eq. 13, which is a second order polynomial trendline curve that was derived from a literature data (Rahimi & Abbaspour, 2008).

$$y = 21.081x^2 + 59.677x \quad \text{Eq. 13}$$

To validate the model, the single mesh pad VLS fluid domain shown in Figure 63 was used, which is the same configuration used in the literature study (Rahimi and Abbaspour, 2008). The numerical CFD simulation was carried out with the same physical properties of fluid given in the literature study (Rahimi and Abbaspour, 2008) at an inlet velocity ranging

from 1 m/s to 7 m/s. The comparison between the experimental data given in the literature against the numerical CFD simulation result from the present study is shown in Figure 66. The values of pressure drop at all inlet velocity tested (1 – 7 m/s) were in good agreement with a variance of 5%.

It must be noted that since the inertial and viscous resistance values were calculated using a non-linear pressure drop correlation, the obtained values from the might only be true for the exact physical properties of fluid given in the literature study (Rahimi & Abbaspour, 2008). To analyse various gas compositions and mixtures, the Ergun can be used. However, this method was not used in this study due to its complexity to accurately predict the average particle size and simply because testing different gas compositions was not included in the scope of the study.

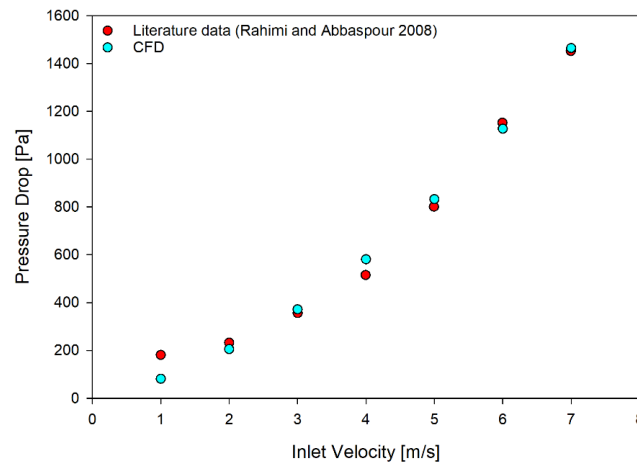


Figure 66: Comparison of Literature Experimental Data against CFD Simulation Result

5.4. Results and Discussion

5.4.1. Inlet Diverter

The fluid flow distribution and average velocity at different height of the VLS vessel were analysed using iso-surfaces in ANSYS Fluent. The location of the iso-surfaces along with an example of the velocity contour produced through the CFD simulation is shown by . The three iso-surfaces used are equidistant to each other at 1 metre intervals. The first iso-surface is located 1 metre above the inlet of the Schoepentoeter while the third iso-surface is located at the outlet of the fluid domain. Table 10 shows the standard deviation of velocities at different heights of the VLS vessel. At laminar flow ($Re = 1 \times 10^{-3}$), the variation in velocity is very minimal, indicating the fluid flow is well distributed. With the increase of the Reynolds number, the standard deviation of velocity also increases. At an industrially relevant

turbulent flow ($Re = 4.8 \times 10^5$), the variation in velocity increased by ten times (986%) in comparison to laminar flow ($Re = 1 \times 10^3$). This result shows that the Schoepentoeter only works best at laminar flow and cannot provide an equal fluid flow distribution at an industrially relevant condition. The same result is qualitatively shown in Figure 68, which shows the velocity contours at different Reynolds number at a height of a 3 metre above the Schoepentoeter inlet.

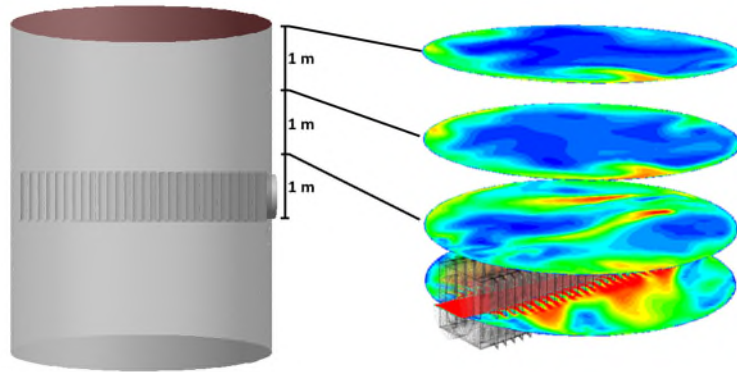


Figure 67: 3D Fluid Domain of Inlet Diverter with Location of Iso-surfaces and Velocity Contours

Table 10: Standard Deviation of Velocities at Different Heights of the Vessel

Re	Inlet Velocity [m/s]	Z = 1 m	Z = 2 m	Z = 3 m
1×10^3	0.023	0.000381	0.000509	0.000489
1×10^4	0.228	0.006639	0.009690	0.008384
1×10^5	2.280	0.075014	0.087933	0.079746
4.8×10^5	11.03	0.375875	0.372512	0.317920
1×10^6	22.80	0.758281	0.888574	0.732157

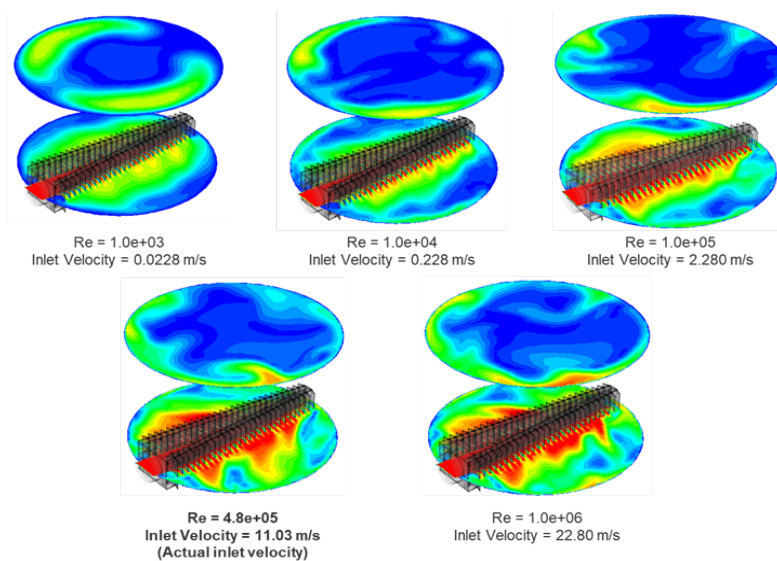


Figure 68: Velocity Contours at Various Inlet Velocities/Re Number

Furthermore, from Figure 68, at all Reynolds number tested, the area in the middle section area of the vessel was observed to have a lower velocity in comparison with the higher velocity along the wall of the vessel. This velocity profile pattern was created by the vanes that slices up the gas stream into a series of jet stream, eventually creating vortexes in the vessel. Furthermore, the average velocity at different height of the fluid domain in shown in Table 11. Results calculated in Table 11 were calculated with Reynolds number of 4.8×10^5 (inlet velocity of 11.03 m/s), which was the VLS inlet velocity given by the industry. Due to the inability of the Schoepentoeter being modelled in 2D, the average velocity at a height of 1.5 m above the Schoepentoeter, which was 0.460 m/s, was chosen as the inlet velocity for the 2D parametric study.

Height [m]	Average Velocity [m/s]
1	0.663
1.5	0.460
2	0.448
3	0.39

5.4.2. Mesh Pad

5.4.2.1. Single Mesh Pad with Inlet Diverter: Baseline Case Study

For the baseline case study, the 3D fluid domain that includes an inlet diverter and a single mesh pad (Figure 63) was used as a basis for the separation performance comparison against the novel dual mesh pad configuration. For this fluid domain (Figure 63), the calculated $V_{t,max}$ was 0.35 m/s. The $V_{t,max}$ was calculated using Eq. 12 with fluid properties given in the literature (Rahimi and Abbaspour, 2008) and a load factor (K-value) given by the supplier of the *KnitMeshTM* Mist Eliminator (Chemtech, 2014).

The fraction of velocity above $V_{t,max}$ on the mesh pad inlet at different inlet velocity is shown in Figure 8. At an inlet velocity of 11.03 m/s, 88% of the fraction of the velocity was above the prescribed terminal velocity (0.35 m/s) and would lead to poor vapour liquid separation. Without any hardware change to mitigate the underperformance, the capacity of the VLS is required to be reduced by at least 5 times or to install additional mist elimination devices after the mesh pad, which includes vanes and cyclones. These devices introduce additional layers of complexity to the overall design of the VLS, contributing to the increase in both capital and operating expenditures. If the separation performance of the mesh pad can

be optimised, it would reduce the need for additional mist elimination devices to improve the separation performance of the VLS. Consequently, a novel dual-mesh pad configuration presented in this study was proposed.

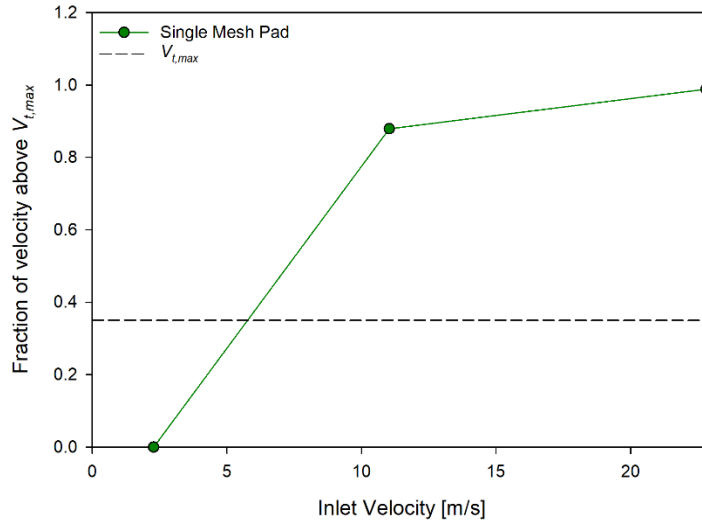


Figure 69: Fraction of Velocity above $V_{t,max}$ on the Mesh Pad Inlet against Various Inlet Velocity

5.4.2.2. Effect of Height and Opening

For the 2D parametric study, to investigate the effect of height and mesh pad opening towards the separation performance of the dual mesh configuration, the 2D fluid domain as shown in Figure 64 was used. The velocity sensors on the inlet the two mesh pads (Porous 1 and Porous 2) were used to provide velocity distribution data along both mesh pad inlet, as shown by the red lines in Figure 64. In this study, only the inlet velocity on *Porous 2* was analysed since it is highly affected by different height and opening while *Porous 1* is not immediately affected. The parametric operating parameters used in the parametric study are tabulated in Table 9 and the result from the 2D parametric study is shown in Figure 70. Figure 70 shows the relationship of the velocity fraction above the $V_{t,max}$ at different distances (height) between the two mesh pads (Porous 1 and Porous 2).

For the effect of height, at all inlet openings, as the distance between the mesh pad was increased, the velocity at the mesh pad inlet decreases, as shown in Figure 70. The larger volume of area or distance between the inlet and the two mesh pads (*Porous 1* and *Porous 2*) allowed more energy to dissipate before the reaching the mesh pad inlet, especially for *Porous 2*, resulting the velocity of the fluid flow to be lower than the maximum terminal velocity. Additionally, for the effect of opening, it was expected that as the mesh pad diameter of

Porous 1 increases, the velocity at the mesh pad inlet of *Porous 2* would increase, as a result of the smaller opening or gap between the vane and the wall of the vapour liquid separator. However, that was not the case. At a mesh pad coverage of 70 - 75% (mesh pad diameter = 1.750 - 1.875 m), the smaller gap (0.625 – 0.750 m) next created next to *Porous 1* increased the rate of energy dissipation of the fluid flow. As an example, in Figure 70, at a distance between mesh pad of 3 – 4 m, a lower mesh pad inlet velocity was observed at a mesh pad coverage of 75% instead of 70%. In contrast, a different phenomenon was observed at the highest mesh pad coverage tested of 80% (mesh pad diameter = 2.000 m), which resulted the smallest gap (0.5 m) between the vane and the wall of the vapour liquid separator in study. The very small gap of 0.5 m generated a high-velocity jet stream, inducing an unequal velocity profile on the mesh pad inlet of *Porous 2* with a majority of the mesh pad area subjected to a fluid flow velocity higher than the maximum terminal velocity.

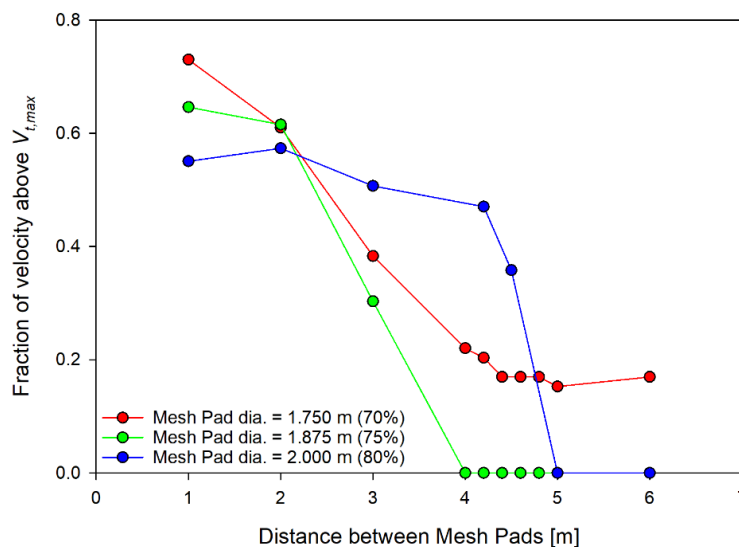


Figure 70: Fraction of Velocity above $V_{t,max}$ against Various Distances between Mesh Pads ($v=0.46$ m/s; $Re=5.69 \times 10^6$)

From this parametric simulation study, it was concluded that the 75% mesh pad coverage ($d = 1.875$ m) performed better in comparison to the other mesh pad sizes tested. A better balance of energy dissipation inside the VLS model was achieved. In addition to that, increasing the distance between the mesh pad from 1 m to 4 m at $d = 1.875$ m shows an increase of the VLS capacity by 64.6%. In conclusion, the optimised VLS configuration achieved from this study would have a mesh pad coverage of 75% ($d = 1.875$ m) and a distance between mesh pad of 4 m. However, this configuration is impractical for industrial application and operation since it would result in a total column height of 14 m.

5.4.2.3. 3D Simulation of Dual Mesh-pad Configuration

A numerical study (CFD simulation) was conducted using the commercial package ANSYS-Fluent to investigate the separation performance of dual mesh pad configuration. To further investigate the separation performance of the novel, the 3D fluid domain of the novel dual mesh pad was used, shown in Figure 65. The design was based on the research outcome of the 2D parametric study, as presented in Section 5.4.2.2, that has a mesh pad coverage of 75% ($d = 1.875$ m) and a distance between mesh pad of 4 m. The comparison of separation performance of the dual-mesh pad configuration against the single-mesh pad configuration is shown in Figure 71. At industrially relevant conditions ($v = 11.03$ m/s), an average of 26% recovery in performance was achieved by the dual-mesh pad configuration. The higher separation performance of dual-mesh pad configuration can be attributed to the inherent design of the dual mesh pad configuration and the increase of the total mesh pad volume by 60.7% in comparison to the single mesh pad configuration.

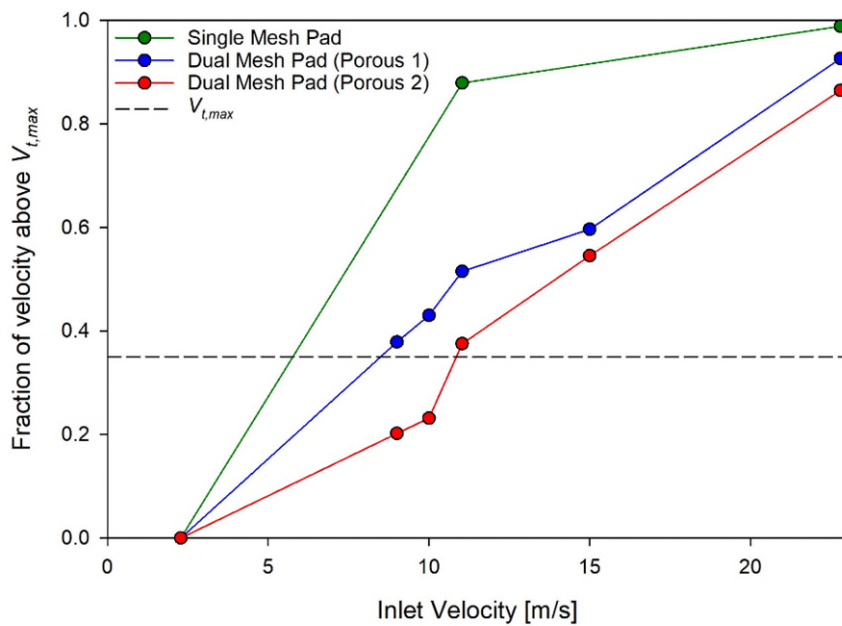


Figure 71: Fraction above $V_{t,max}$ on the Mesh Pad Inlet against Various Inlet Velocity (Dual Mesh Pad Configuration 3D Model)

5.5. Conclusions

In this work, a series of CFD simulations were conducted using the commercial package ANSYS-Fluent version 18.2 to investigate the fluid flow distribution performance of an existing inlet diverter design (Schoepentoeter) and to conduct parametric study of a novel VLS design with a dual mesh pad configuration. 2D and 3D fluid domains were used in this study and velocity sensors were added at different locations of the fluid domains. From this study, the following key findings were concluded:

- From the Schoepentoeter inlet diverter study, it was concluded that the Schoepentoeter is only effective at laminar flow and cannot provide an equal fluid flow distribution at an industrially relevant condition. Additionally, the average velocity of the fluid flow after passing through the Schoepentoeter at different height of the VLS vessel were calculated.
- From the baseline case study that used a 3D fluid domain that includes an inlet diverter and a single mesh pad (Figure 63), it was found that 88% of the fraction of the velocity was above the prescribed terminal velocity (0.35 m/s) and would lead to poor vapour liquid separation.
- From the 2D parametric study of the novel VLS design that has a dual mesh pad configuration (Figure 64), the optimised VLS configuration achieved from this study would have a mesh pad coverage of 75% ($d = 1.875$ m) and a distance between mesh pad of 4 m. However, this configuration is impractical for industrial application and operation since it would result in a total column height of 14 m.
- From the 3D numerical simulation study of the dual mesh pad configuration (Figure 65), at industrially relevant conditions ($v = 11.03$ m/s), an average of 26% recovery in performance was achieved by the dual-mesh pad configuration in comparison to the single mesh pad configuration. The higher separation performance of dual-mesh pad configuration can be attributed to the inherent design of the dual mesh pad configuration and the increase of the total mesh pad volume by 60.7% in comparison to the single mesh pad configuration.

The novel dual mesh pad VLS design presented in this work, provides the basis for different mesh pad configurations and parametric studies that can ultimately improve the capacity and performance of the VLS.

Chapter 6 Conclusions and Recommendations

6.1. Conclusions

Vapour-liquid separation is one of the key functions for unit operations in the chemical and processing industries that is typically carried out in a vapour-liquid separator (two-phase system). This thesis aims to understand the hydrodynamics of the key components (inlet diverter and mist eliminator) at micro- and milli-scale, which is important in improving the overall efficiency of a vapour-liquid separator. In the case of the inlet diverter, the research conducted was focused on understanding the hydrodynamics of an existing and a novel inlet diverter design that includes key parameters such as fluid flow distribution performance. In the case of the knitted mesh pad (mist eliminator), the research was focused on understanding the hydrodynamics of droplet capture on thin wires. The key findings and contributions from the main chapters (Chapter 2 to 5) of the thesis are summarised below:

Chapter 2: Hydrodynamics of Droplet Capture on Thin Wires

The hydrodynamics of droplet interaction between a droplet and a wire was investigated in this chapter. Numerical, experimental, and analytical studies were conducted to understand the relationship between the governing forces of the phases, the physical properties of the phases, and the surface properties of the knitted mesh (i.e. wires). The following key findings for this chapter were concluded:

- High-speed imaging experiment to obtain empirical data of droplet capture on different material of contact surfaces.
 - Static contact angle was measured for different contact surfaces.
 - $V_{t,max}$ was calculated for different wire surfaces (stainless steel and copper) and wire-to-droplet ratios.
- Improved analytical model to better predict the $V_{t,max}$ that includes variable value of C_d .
 - The improved analytical model was derived from the force balance equation by balancing different forces on an impacting droplet.
 - The correlation for the variable C_d was developed as a function of fundamental physical properties of the fluid (the ratio of viscosities) and operating parameters (ratio of diameters).
 - The three constants used in the correlation of C_d was obtained using the droplet capture experiment data.

- The analytical model was better in predicting $V_{t,max}$ values in the range of 0.3 to 0.7 m/s with the data points within +/- 25%.
- Results from the experiment were used to estimate the parameters in the newly developed correlation for the variable C_d using a hybrid genetic algorithm (GA) and Levenberg-Marquadt algorithm (LMA) method.
- The analytical model was also used to investigate the effect of wire size and fluid properties towards the $V_{t,max}$. In the context of a vapour-liquid separator, the ability to predict the $V_{t,max}$ with different wire size would help in controlling the porosity of the mesh pad. Additionally, the ability to predict the $V_{t,max}$ for different fluid properties would help in anticipating different types of feeds that is passing through the vapour-liquid separator.
- 2D numerical CFD model to investigate the effect of wire shapes and size towards the $V_{t,max}$
 - A parametric numerical CFD study using ANSYS Fluent was conducted to investigate the effect of wire shapes and sizes towards the $V_{t,max}$ in a system of a single droplet impacting upon a single thin wire.
 - It was concluded that an optimum combination of ratio of diameters, mesh pad porosity, and wire shape can lead to a knitted mesh pad specification with an improved separation efficiency and reduced pressure drop.
 - This study can be used as a basis to additively manufacture knitted mesh pads with different wire geometries or cross-section.

Chapter 3: Gas-gas Hydrodynamics of a Fractal Flow Mixer

In Chapter 3, the hydrodynamic performance of the fractal flow mixer was numerically characterised using CFD with a gas mixture of air and methane. The following key findings for this chapter were concluded:

- A novel flow distributor design was proposed, called the fractal flow mixer (Chapter 4).
 - The fractal flow mixer was designed using the concept of self-similar bifurcating channels and combines the function of a flow distributor and a mixer into a single device. The device has two inlets which are recursively bifurcated over four stages resulting in 16 outlet channels per pathway. The outlets from each of the two pathways are then combined to mix the two fluid streams.

- The fractal flow mixer was successfully additively manufactured without the use of supports. Two additive manufacturing techniques were demonstrated. The first technique is vat-photopolymerisation using a resin precursor, and the second technique is the laser powder bed fusion using a titanium alloy.
- 3D numerical CFD to investigate the hydrodynamics of a gas-gas flow passing through the fractal flow mixer (Chapter 4).
 - A parametric study was conducted to investigate the effect of Reynolds number and inlet flow ratio was investigated.
 - Single-phase flow with two gases of air and methane.
 - It was concluded that uniform flow distribution was achieved with a maximum relative standard deviation of 8%.

Chapter 4: Gas-liquid Hydrodynamics of a Fractal Flow Mixer

In Chapter 4, the hydrodynamic performance of the fractal flow mixer was experimentally characterised with a gas-liquid flow of air and water. The following key findings for this chapter were concluded:

- Experiment using high-speed imaging and optical probe was conducted to investigate the hydrodynamics of a gas-liquid flow passing through the fractal flow device and also the feasibility of producing Taylor flow within its microchannels (Chapter 5).
 - The effect of Reynolds number and inlet flow ratio was investigated.
 - Two-phase flow with air and water.
- High speed imaging was used to identify the flow regimes in the channels of the fractal flow mixer.
 - Four different types of flow regimes were identified: bubbly flow, slug flow, annular flow, and churn flow.
 - At different combinations of velocities, two or more flow patterns (low flow, annular flow, slug flow and churn flow) were observed simultaneously in different outlet microchannels of the fractal flow mixer.
 - A new flow regime map was developed for the specific fractal flow mixer presented in this thesis.
- An optical probe was used to analyse the fluid flow distribution of the fractal flow mixer
 - The optical probe was used to measure the bubble mean size and bubble mean velocity from each outlet.

- It was found that the fractal flow mixer was able to generate equal flow distribution across the 16 outlets and maintain a Taylor flow over a range of V_{SL}/V_{SG} . However, the bubble/slug size varies to a certain extent, depending on the V_{SL}/V_{SG} that are governed by the capillary effect and the back-pressure.
- Results from this study shows the potential of the fractal flow mixer to be used as an inlet diverter at a larger scale, enhancing the separation efficiency of the mesh pad.

Chapter 5: CFD Simulations of Vapour-Liquid Separator

In Chapter 5, the vapour-liquid separation performance of an existing inlet diverter design (Schoepentoeter) and a novel vapour-liquid separator configuration were investigated. The following key findings for this chapter were concluded:

- Numerical CFD study to investigate the flow distribution performance of an existing inlet diverter design (Schoepentoeter) (Chapter 6).
 - The fluid flow distribution and average velocity at different height of the VLS vessel were analysed using iso-surfaces in ANSYS Fluent.
 - The Schoepentoeter only works best at laminar flow but cannot provide an equal fluid flow distribution at an industrially relevant condition.
- Numerical CFD study to investigate the separation performance of a novel vapour-liquid separator configuration.
 - A dual-mesh pad configuration was proposed. A conventional vertical vapour-liquid separator typically only uses a single knitted mesh pad above the inlet diverter.
 - A parametric study was conducted with different mesh pad diameters/area coverage and different distances between the two mesh pads.
 - The optimum dual-mesh pad configuration had a diameter of 1.875 m (75% mesh pad coverage) with a distance between the mesh pad of 4 m. This configuration provided an increase of the VLS capacity by 64.6% in comparison to a single-mesh pad configuration.
 - Using the dual-mesh pad configuration, a recovery in performance of 26% can be achieved at an industrially relevant condition.

6.2. Challenges and Recommendations

Based on the research outcomes presented in this thesis, which includes the multiphase hydrodynamic characterisation of the two physical systems in a vapour-liquid separator and the proposal of a novel inlet diverter design, the following studies are recommended:

Chapter 2: Hydrodynamics of Droplet Capture on Thin Wires

There are two key outcomes in Chapter 2, which include the improved analytical model in predicting the $V_{t,max}$ that contain a variable C_d value and the numerical CFD study to investigate the effect of wire shapes and size towards the $V_{t,max}$. For the improved analytical model in predicting $V_{t,max}$, it was found that the prediction of $V_{t,max}$ for <0.3 m/s and >0.7 m/s can be further improved, and the material of the contact surface was limited to only two materials, that includes copper and stainless-steel. To improve the accuracy and the scalability of the model, further fine-tuning of the constants (a_1 , b_1 , and c_1) used in predicting the variable C_d value is required. Fine-tuning can be done by expanding the empirical database of $V_{t,max}$ from the high-speed imaging experiment to include different materials of contact surfaces, different droplet properties, and an increased range of wire-to-droplet diameter ratio. Alternatively, a different set of constants can be used for <0.3 m/s and >0.7 m/s. Furthermore, a surface tension coefficient should be added to the correlation of the variable C_d to better predict the $V_{t,max}$ for different materials of wire or contact surfaces. Trials were conducted to include the surface tension coefficient in this study, however, the prediction of $V_{t,max}$ was still inaccurate. For the numerical CFD study to investigate the effect of wire shapes and size towards the $V_{t,max}$, the study can be further extended to adapt the 2D domain into a 3D domain to take into account the surface area of the droplet impact more accurately.

Chapter 3: Gas-gas Hydrodynamics of a Fractal Flow Mixer

In Chapter 3, the gas-gas hydrodynamics of a fractal flow mixer was numerically investigated with a gas mixture of air and methane. The CFD model used in this study can be further improved by testing different materials of construction for the fractal flow mixer to consider different surface roughness. The effect of inlet feed with different fluid properties should also be investigated. Additionally, the study can be further extended by experimentally investigating the gas-gas hydrodynamics of the fractal flow mixer. An anemometer can be used to measure the velocity of air from each outlet to quantify the fluid flow distribution from each outlet of the fractal flow mixer.

Chapter 4: Gas-liquid Hydrodynamics of a Fractal Flow Mixer

In Chapter 4, the gas-liquid hydrodynamics of a fractal flow mixer was experimentally investigated using high-speed imaging and an optical probe. Since the fractal flow mixer is additively manufactured, the experiment study can be further extended by investigating the effect of different material properties towards the hydrodynamics of the fractal flow mixer. Consequently, new flow regime maps can be developed for different materials. Furthermore, the effect of design modification can also be investigated (i.e. number of bifurcation stages and outlet design). The size of the fractal flow mixer can be gradually scaled up to reflect the potential of the fractal flow mixer to be used as an inlet diverter at an industrial scale. A design strategy is also required to adapt the geometries of the fractal flow mixer to the vessel of a vapour-liquid separator, i.e. a radial design of a fractal flow mixer. A numerical CFD study was also initiated to investigate the hydrodynamics of a gas-liquid flow passing through the fractal flow mixer. However, there were issues with the convergence of the results. Thus, it was not included in this thesis. It is recommended to extend the numerical CFD study for a gas-liquid flow. A validated model would help analyse the forces inside the channels, which would not be feasible through an experimental study.

Chapter 5: CFD Simulations of Vapour-Liquid Separator

In Chapter 5, CFD simulations of a Vapour-Liquid Separator (VLS) were conducted to investigate the separation performance of an existing inlet diverter design (Schoepentoeter) and a novel VLS configuration. The study can be extended to include a multiphase flow in the CFD simulation to be able to predict the fluid flow distribution of the inlet diverter and the separation performance of the knitted mesh pad more accurately. A lab-scale VLS can also be commissioned to investigate the separation performance of the novel VLS configuration experimentally. Additionally, an experiment study was initiated to investigate the performance of additively manufactured mesh pads, which is shown in Appendix A. The dry pressure drop was measured at different heights of the mesh pad. The separation efficiency and wet pressure drop of these mesh pads were also planned to be investigated. Unfortunately, the experiment rig was not optimised to accurately measure the two variables (separation efficiency and wet pressure drop). Further optimisation of the additively manufactured mesh pad design is also required. It is recommended that the study of additively manufactured mesh pads to be continued to take advantage of the advancement in additive manufacturing.

References

- Abadie, T., Aubin, J., Legendre, D., & Xuereb, C. (2012). Hydrodynamics of gas–liquid Taylor flow in rectangular microchannels. *Microfluidics and Nanofluidics*, 12(1), 355-369. <https://doi.org/10.1007/s10404-011-0880-8>
- Abiev, R., Svetlov, S., & Haase, S. (2017). Hydrodynamics and Mass Transfer of Gas-Liquid and Liquid-Liquid Taylor Flow in Microchannels [<https://doi.org/10.1002/ceat.201700041>]. *Chemical Engineering & Technology*, 40(11), 1985-1998. <https://doi.org/https://doi.org/10.1002/ceat.201700041>
- Abishek, S., Mead-Hunter, R., King, A. J. C., & Mullins, B. J. (2019). Capture and re-entrainment of microdroplets on fibers. *Physical Review E*, 100(4), 042803. <https://doi.org/10.1103/PhysRevE.100.042803>
- Afshari, E., Mosharaf-Dehkordi, M., & Rajabian, H. (2017). An investigation of the PEM fuel cells performance with partially restricted cathode flow channels and metal foam as a flow distributor. *Energy*, 118, 705-715. <https://doi.org/https://doi.org/10.1016/j.energy.2016.10.101>
- Al-Dughaiter, A. A., Ibrahim, A. A., & Al-Masry, W. A. (2011). Investigating pressure drop across wire mesh mist eliminators in bubble column. *Journal of Saudi Chemical Society*, 15(1), 1-9. <https://doi.org/https://doi.org/10.1016/j.jscs.2010.09.008>
- Al-Dughaiter, A. S., Ibrahim, A. A., & Al-Masry, W. A. (2010). Investigating droplet separation efficiency in wire-mesh mist eliminators in bubble column. *Journal of Saudi Chemical Society*, 14(4), 331-339. <https://doi.org/https://doi.org/10.1016/j.jscs.2010.04.001>
- Al-Fulaij, H., Cipollina, A., Micale, G., Ettouney, H., & Bogle, D. (2014). Eulerian-Eulerian modelling and computational fluid dynamics simulation of wire mesh demisters in MSF plants. *Engineering Computations*, 31(7), 1242-1260. <https://doi.org/doi:10.1108/EC-03-2012-0063>
- American Petroleum Institute. (2008). *API Specification 12J.: Specification for Oil and Gas Separators*. American Petroleum Institute (API).
- Amrei, M. M., Venkateshan, D. G., D'Souza, N., Atulasimha, J., & Tafreshi, H. V. (2016). Novel Approach to Measuring the Droplet Detachment Force from Fibers. *Langmuir*, 32(50), 13333-13339. <https://doi.org/10.1021/acs.langmuir.6b03198>
- Angeli, P., & Gavrilidis, A. (2008). Hydrodynamics of Taylor flow in small channels: A Review. *Proceedings of the Institution of Mechanical Engineers, Part C: Journal of Mechanical Engineering Science*, 222(5), 737-751. <https://doi.org/10.1243/09544062JMES776>
- Asadolahi, A. N., Gupta, R., Leung, S. S. Y., Fletcher, D. F., & Haynes, B. S. (2012). Validation of a CFD model of Taylor flow hydrodynamics and heat transfer. *Chemical Engineering Science*, 69(1), 541-552. <https://doi.org/https://doi.org/10.1016/j.ces.2011.11.017>
- Ascough, G., & Kiker, G. (2002). The effect of irrigation uniformity on irrigation water requirements. *Water Sa*, 28(2), 235-242. <https://doi.org/10.4314/wsa.v28i2.4890>
- Aubin, J., Ferrando, M., & Jiricny, V. (2010). Current methods for characterising mixing and flow in microchannels. *Chemical Engineering Science*, 65(6), 2065-2093. <https://doi.org/https://doi.org/10.1016/j.ces.2009.12.001>
- Aziz, H., Farhan, N. M., & Vahedi Tafreshi, H. (2018). Effects of fiber wettability and size on droplet detachment residue. *Experiments in Fluids*, 59(7), 122. <https://doi.org/10.1007/s00348-018-2579-z>
- Bajura, R. A. (1971). A Model for Flow Distribution in Manifolds. *Journal of Engineering for Power*, 93(1), 7-12. <https://doi.org/10.1115/1.3445410>
- Barbosa, I. S. O., Costa, J. M., Manrique, Y. A., Dias, M. M., Faria, J. L., Santos, R. J., Silva, C. G., & Brito, M. S. C. A. (2023). ChannelCOMB Device for Mesostructured Reactors and Networks of Reactors [<https://doi.org/10.1002/ceat.202200560>]. *Chemical Engineering & Technology*, 46(6), 1241-1250. <https://doi.org/https://doi.org/10.1002/ceat.202200560>
- Barbosa, I. S. O., Santos, R. J., Silva, C. G., & Brito, M. S. C. A. (2021). Consecutive Flow Distributor Device for Mesostructured Reactors and Networks of Reactors. *Chemical Engineering and Processing - Process Intensification*, 167, 108541. <https://doi.org/https://doi.org/10.1016/j.cep.2021.108541>

- Bassiouny, M. K., & Martin, H. (1984). Flow distribution and pressure drop in plate heat exchangers—I U-type arrangement. *Chemical Engineering Science*, 39(4), 693-700. [https://doi.org/https://doi.org/10.1016/0009-2509\(84\)80176-1](https://doi.org/https://doi.org/10.1016/0009-2509(84)80176-1)
- Bejan, A. (2000). *Shape and structure, from engineering to nature*. Cambridge university press.
- Berk, Z. (2018). 7.5.2 Quality of Mixing, the Concept of "Mixedness". In *Food Process Engineering and Technology (3rd Edition)* (pp. 203-205). Elsevier. <https://app.knovel.com/hotlink/pdf/id:kt011Q1C68/food-process-engineering/quality-mixing-concept>
- Bothamley, M. (2015). Gas/Liquid Separators: Quantifying Separation Performance - Part 1. *Oil and Gas Facilities*, 2, 21-29. <https://doi.org/10.2118/0813-0021-OGF>
- Boyer, R., Welsch, G., & Collings, E. W. (1994). In *Materials Properties Handbook - Titanium Alloys*. ASM International. <https://app.knovel.com/hotlink/pdf/id:kt007TGFO1/materials-properties/front-matter>
- Brandt, M., Sun, S., Leary, M., Feih, S., Elambasseril, J., & Liu, Q. (2013). High-Value SLM Aerospace Components: From Design to Manufacture. *Advanced Materials Research*, 633, 135-147. <https://doi.org/10.4028/www.scientific.net/AMR.633.135>
- Brunazzi, E., & Paglianti, A. (1998). Design of wire mesh mist eliminators [<https://doi.org/10.1002/aic.690440302>]. *AIChE Journal*, 44(3), 505-512. <https://doi.org/https://doi.org/10.1002/aic.690440302>
- Camarrì, S., Mariotti, A., Galletti, C., Brunazzi, E., Mauri, R., & Salvetti, M. V. (2020). An Overview of Flow Features and Mixing in Micro T and Arrow Mixers. *Industrial & Engineering Chemistry Research*, 59(9), 3669-3686. <https://doi.org/10.1021/acs.iecr.9b04922>
- Campanelli, S., Contuzzi, N., Angelastro, A., & Antonio Domenico, L. (2010). Capabilities and Performances of the Selective Laser Melting Process. In *New Trends in Technologies: Devices, Computer, Communication and Industrial Systems* (pp. 233-252). <https://doi.org/10.5772/10432>
- Cao, J., Kraut, M., Dittmeyer, R., Zhang, L., & Xu, H. (2018). Numerical analysis on the effect of bifurcation angle and inlet velocity on the distribution uniformity performance of consecutive bifurcating fluid flow distributors. *International Communications in Heat and Mass Transfer*, 93, 60-65. <https://doi.org/https://doi.org/10.1016/j.icheatmasstransfer.2017.04.017>
- Chandra, S., & Avedisian, C. (1991). On the collision of a droplet with a solid surface. *Proceedings of the Royal Society of London. Series A: Mathematical and Physical Sciences*, 432(1884), 13-41.
- Chemtech, S. (2014). *Gas/Liquid Separation Technology* https://www.sulzer.com/-/media/files/products/separation-technology/feed-inlet-devices/gas_liquid_separation_technology.ashx
- Chen, L., Tian, Y. S., & Karayiannis, T. G. (2006). The effect of tube diameter on vertical two-phase flow regimes in small tubes. *International Journal of Heat and Mass Transfer*, 49(21), 4220-4230. <https://doi.org/https://doi.org/10.1016/j.ijheatmasstransfer.2006.03.025>
- Comtet, J., Keshavarz, B., & Bush, J. W. (2016). Drop impact and capture on a thin flexible fiber. *Soft Matter*, 12(1), 149-156.
- Don, W. G., & Robert, H. P. (2008). *Perry's Chemical Engineers' Handbook, Eighth Edition* (8th ed. / ed.). McGraw-Hill Education. <https://www.accessengineeringlibrary.com/content/book/9780071422949>
- Dong, J., Xu, X., & Xu, B. (2017). CFD analysis of a novel modular manifold with multi-stage channels for uniform air distribution in a fuel cell stack. *Applied Thermal Engineering*, 124, 286-293. <https://doi.org/https://doi.org/10.1016/j.applthermaleng.2017.06.030>
- Dong, Z., Wen, Z., Zhao, F., Kuhn, S., & Noël, T. (2021). Scale-up of micro- and milli-reactors: An overview of strategies, design principles and applications. *Chemical Engineering Science: X*, 10, 100097. <https://doi.org/https://doi.org/10.1016/j.cesx.2021.100097>
- Dressaire, E., Sauret, A., Boulogne, F., & Stone, H. A. (2016). Drop impact on a flexible fiber [10.1039/C5SM02246K]. *Soft Matter*, 12(1), 200-208. <https://doi.org/10.1039/C5SM02246K>
- Duroudier, J.-P. (2016). 2 - Gas-Liquid Separator Vats and Drums. In *Liquid-Gas and Solid-Gas Separators* (pp. 47-65). Elsevier. <https://doi.org/https://doi.org/10.1016/B978-1-78548-181-9.50002-5>

- El-Dessouky, H. T., Alatiqi, I. M., Ettouney, H. M., & Al-Deffeeri, N. S. (2000). Performance of wire mesh mist eliminator. *Chemical Engineering and Processing: Process Intensification*, 39(2), 129-139. [https://doi.org/https://doi.org/10.1016/S0255-2701\(99\)00033-1](https://doi.org/https://doi.org/10.1016/S0255-2701(99)00033-1)
- Etmnan, A., Muzychka, Y. S., & Pope, K. (2021). A Review on the Hydrodynamics of Taylor Flow in Microchannels: Experimental and Computational Studies. *Processes*, 9(5).
- Farhan, N. M., & Tafreshi, H. V. (2018). Universal expression for droplet–fiber detachment force. *Journal of Applied Physics*, 124(7), 075301. <https://doi.org/10.1063/1.5032106>
- Frazier, W. E. (2014). Metal Additive Manufacturing: A Review. *Journal of Materials Engineering and Performance*, 23(6), 1917-1928. <https://doi.org/10.1007/s11665-014-0958-z>
- Gac, J. M., & Gradoń, L. (2012). Analytical investigation and numerical modeling of collisions between a droplet and a fiber. *Journal of Colloid and Interface Science*, 369(1), 419-425. <https://doi.org/https://doi.org/10.1016/j.jcis.2011.12.018>
- Gan, M. X., & Wong, C. H. (2016). Practical support structures for selective laser melting. *Journal of materials processing technology*, 238, 474-484. <https://doi.org/10.1016/j.jmatprotec.2016.08.006>
- Gas Processors Suppliers Association. (2004). *Engineering data book* (12th , FPS. ed.). Gas Processors Suppliers Association (GPSA).
- Ghanem, A., Lemenand, T., Della Valle, D., & Peerhossaini, H. (2014). Static mixers: Mechanisms, applications, and characterization methods – A review. *Chemical Engineering Research and Design*, 92(2), 205-228. <https://doi.org/https://doi.org/10.1016/j.cherd.2013.07.013>
- Gibson, I., Rosen, D., & Stucker, B. (2015). *Additive Manufacturing Technologies* (2nd ed.). <https://doi.org/10.1007/978-1-4939-2113-3>
- Gilet, T., Terwagne, D., & Vandewalle, N. (2010). Droplets sliding on fibres. *The European Physical Journal E*, 31(3), 253-262. <https://doi.org/10.1140/epje/i2010-10563-9>
- Goldshmid, J., Samet, M., & Wagner, M. (1986). Turbulent mixing at high dilution ratio in a Sulzer-Koch static mixer. *Industrial & Engineering Chemistry Process Design and Development*, 25(1), 108-116. <https://doi.org/10.1021/i200032a017>
- Gu, W., Yan, S., & Bai, Z. (2020). A study on a droplet impact on a fiber during coalescence-separation: Phenomena and models. *Chemical Engineering Science*, 212, 115337. <https://doi.org/https://doi.org/10.1016/j.ces.2019.115337>
- Guo, R., Fu, T., Zhu, C., Yin, Y., & Ma, Y. (2019). Hydrodynamics and mass transfer of gas-liquid flow in a tree-shaped parallel microchannel with T-type bifurcations. *Chemical Engineering Journal*, 373, 1203-1211. <https://doi.org/https://doi.org/10.1016/j.cej.2019.05.124>
- Gupta, R., Fletcher, D. F., & Haynes, B. S. (2009). On the CFD modelling of Taylor flow in microchannels. *Chemical Engineering Science*, 64(12), 2941-2950. <https://doi.org/https://doi.org/10.1016/j.ces.2009.03.018>
- Gupta, R., Fletcher, D. F., & Haynes, B. S. (2010). Taylor Flow in Microchannels: A Review of Experimental and Computational Work. *The Journal of Computational Multiphase Flows*, 2(1), 1-31. <https://doi.org/10.1260/1757-482X.2.1.1>
- Haghshenasfard, M., Zivdar, M., Rahimi, R., & Nasr Esfahany, M. (2007). CFD Simulation of Gas Distribution Performance of Gas Inlet Systems in Packed Columns. *Chemical Engineering & Technology*, 30(9), 1176-1180. <https://doi.org/https://doi.org/10.1002/ceat.200700102>
- Harlow, F. H., & Shannon, J. P. (1967). The splash of a liquid drop. *Journal of Applied Physics*, 38(10), 3855-3866.
- He, X., Chen, S., & Zhang, R. (1999). A Lattice Boltzmann Scheme for Incompressible Multiphase Flow and Its Application in Simulation of Rayleigh–Taylor Instability. *Journal of Computational Physics*, 152(2), 642-663. <https://doi.org/https://doi.org/10.1006/jcph.1999.6257>
- Hessel, V., Löwe, H., & Schönfeld, F. (2005). Micromixers—a review on passive and active mixing principles. *Chemical Engineering Science*, 60(8), 2479-2501. <https://doi.org/https://doi.org/10.1016/j.ces.2004.11.033>

- Holland, J. H. (1992). *Adaptation in natural and artificial systems: an introductory analysis with applications to biology, control, and artificial intelligence*. MIT press.
- Hung, L. S., & Yao, S. C. (1999). Experimental investigation of the impaction of water droplets on cylindrical objects. *International Journal of Multiphase Flow*, 25(8), 1545-1559. [https://doi.org/https://doi.org/10.1016/S0301-9322\(98\)00085-8](https://doi.org/https://doi.org/10.1016/S0301-9322(98)00085-8)
- Hung, L. S., & Yao, S. C. (2002). Dripping phenomena of water droplets impacted on horizontal wire screens. *International Journal of Multiphase Flow*, 28(1), 93-104. [https://doi.org/https://doi.org/10.1016/S0301-9322\(01\)00061-1](https://doi.org/https://doi.org/10.1016/S0301-9322(01)00061-1)
- Jähnisch, K., Hessel, V., Löwe, H., & Baerns, M. (2004). Chemistry in Microstructured Reactors [<https://doi.org/10.1002/anie.200300577>]. *Angewandte Chemie International Edition*, 43(4), 406-446. <https://doi.org/https://doi.org/10.1002/anie.200300577>
- Jiang, Y., Zhang, Y., Zhang, J., & Tang, Z. (2022). Characteristics of Gas–Liquid Slug Flow in Honeycomb Microchannel Reactor. *Energies*, 15(4).
- Karki, K. C., & Patankar, S. V. (2006). Airflow distribution through perforated tiles in raised-floor data centers. *Building and Environment*, 41(6), 734-744. <https://doi.org/https://doi.org/10.1016/j.buildenv.2005.03.005>
- Khalili, M., Yahyazadeh, H., Gorji-Bandpy, M., & Ganji, D. D. (2016). Application of volume of fluid method for simulation of a droplet impacting a fiber. *Propulsion and Power Research*, 5(2), 123-133. <https://doi.org/https://doi.org/10.1016/j.jprr.2016.04.003>
- Kim, S.-G., & Kim, W. (2016). Drop impact on a fiber. *Physics of Fluids*, 28(4), 042001. <https://doi.org/10.1063/1.4945103>
- Koopman, H. K., Köksoy, Ç., Ertunç, Ö., Lienhart, H., Hedwig, H., & Delgado, A. (2014). An analytical model for droplet separation in vane separators and measurements of grade efficiency and pressure drop. *Nuclear Engineering and Design*, 276, 98-106. <https://doi.org/https://doi.org/10.1016/j.nucengdes.2014.05.034>
- Kouhikamali, R., Noori Rahim Abadi, S. M. A., & Hassani, M. (2014). Numerical study of performance of wire mesh mist eliminator. *Applied Thermal Engineering*, 67(1), 214-222. <https://doi.org/https://doi.org/10.1016/j.applthermaleng.2014.02.073>
- Kukukova, A., Aubin, J., & Kresta, S. M. (2009). A new definition of mixing and segregation: Three dimensions of a key process variable. *Chemical Engineering Research and Design*, 87(4), 633-647. <https://doi.org/https://doi.org/10.1016/j.cherd.2009.01.001>
- Kumar, V., Paraschivoiu, M., & Nigam, K. D. P. (2011). Single-phase fluid flow and mixing in microchannels. *Chemical Engineering Science*, 66(7), 1329-1373. <https://doi.org/https://doi.org/10.1016/j.ces.2010.08.016>
- Lacey, P. M. C. (1954). Developments in the theory of particle mixing. *Journal of Applied Chemistry*, 4(5), 257-268. <https://doi.org/https://doi.org/10.1002/jctb.5010040504>
- Lee, S. J., Cha, J. H., Kim, K. M., & Choi, W. (2019). Dynamics of drop impact on heated metal wires: Thermally induced transition from tail to splash to jumping modes. *International Journal of Heat and Mass Transfer*, 131, 226-236. <https://doi.org/https://doi.org/10.1016/j.ijheatmasstransfer.2018.11.063>
- Lei, L., Zhao, Y., Wang, X., Xin, G., & Zhang, J. (2022). Experimental and numerical studies of liquid-liquid slug flows in micro channels with Y-junction inlets. *Chemical Engineering Science*, 252, 117289. <https://doi.org/https://doi.org/10.1016/j.ces.2021.117289>
- Leung, S. S. Y., Liu, Y., Fletcher, D. F., & Haynes, B. S. (2010). Heat transfer in well-characterised Taylor flow. *Chemical Engineering Science*, 65(24), 6379-6388. <https://doi.org/https://doi.org/10.1016/j.ces.2010.09.014>
- Levenberg, K. (1944). A method for the solution of certain non-linear problems in least squares. *Quarterly of applied mathematics*, 2(2), 164-168.
- Levin, Z., & Hobbs, P. V. (1971). Splashing of water drops on solid and wetted surfaces: hydrodynamics and charge separation. *Philosophical Transactions of the Royal Society of London. Series A, Mathematical and Physical Sciences*, 269(1200), 555-585.

- Lim, A. E., & Lam, Y. C. (2021). Vertical Squeezing Route Taylor Flow with Angled Microchannel Junctions. *Industrial & Engineering Chemistry Research*, 60(39), 14307-14317. <https://doi.org/10.1021/acs.iecr.1c02324>
- Liu, H., Li, P., Lew, J. V., & Juarez-Robles, D. (2012). Experimental study of the flow distribution uniformity in flow distributors having novel flow channel bifurcation structures. *Experimental Thermal and Fluid Science*, 37, 142-153. <https://doi.org/https://doi.org/10.1016/j.expthermflusci.2011.10.015>
- Liu, H., & Zhang, Y. (2009). Droplet formation in a T-shaped microfluidic junction. *Journal of Applied Physics*, 106(3), 034906. <https://doi.org/10.1063/1.3187831>
- Lorenceanu, É., Clanet, C., & Quéré, D. (2004). Capturing drops with a thin fiber. *Journal of Colloid and Interface Science*, 279(1), 192-197. <https://doi.org/https://doi.org/10.1016/j.jcis.2004.06.054>
- Lorenceanu, E., Clanet, C., Quéré, D., & Vignes-Adler, M. (2009). Off-centre impact on a horizontal fibre. *The European Physical Journal Special Topics*, 166(1), 3-6. <https://doi.org/10.1140/epjst/e2009-00868-0>
- Lu, F., Luo, Y.-h., & Yang, S.-m. (2008). Analytical and Experimental Investigation of Flow Distribution in Manifolds for Heat Exchangers. *Journal of Hydrodynamics, Ser. B*, 20(2), 179-185. [https://doi.org/https://doi.org/10.1016/S1001-6058\(08\)60044-X](https://doi.org/https://doi.org/10.1016/S1001-6058(08)60044-X)
- Luo, L., Fan, Y., Zhang, W., Yuan, X., & Midoux, N. (2007). Integration of constructal distributors to a mini crossflow heat exchanger and their assembly configuration optimization. *Chemical Engineering Science*, 62(13), 3605-3619. <https://doi.org/https://doi.org/10.1016/j.ces.2007.02.058>
- Luo, L., Fan, Z., Le Gall, H., Zhou, X., & Yuan, W. (2008). Experimental study of constructal distributor for flow equidistribution in a mini crossflow heat exchanger (MCHE). *Chemical Engineering and Processing: Process Intensification*, 47(2), 229-236. <https://doi.org/https://doi.org/10.1016/j.cep.2007.02.028>
- Ma, D., Wang, G., Ma, Y., Zhu, C., & Tang, X. (2023). Hydrodynamics behavior and mass transfer performance of gas-liquid two-phase flow in the honeycomb fractal microreactor. *Chemical Engineering Journal*, 462, 142228. <https://doi.org/https://doi.org/10.1016/j.cej.2023.142228>
- Mariotti, A., Galletti, C., Brunazzi, E., & Salvetti, M. V. (2019). Steady flow regimes and mixing performance in arrow-shaped micro-mixers. *Physical Review Fluids*, 4(3), 034201. <https://doi.org/10.1103/PhysRevFluids.4.034201>
- Marquardt, D. W. (1963). An Algorithm for Least-Squares Estimation of Nonlinear Parameters. *Journal of the Society for Industrial and Applied Mathematics*, 11(2), 431-441. <https://doi.org/10.1137/0111030>
- Mazur, M., Bhatelia, T., Kuan, B., Patel, J., Webley, P. A., Brandt, M., Pareek, V., & Utikar, R. (2019). Additively manufactured, highly-uniform flow distributor for process intensification. *Chemical Engineering and Processing - Process Intensification*, 143, 107595. <https://doi.org/https://doi.org/10.1016/j.cep.2019.107595>
- Merdasi, A., Ebrahimi, S., Moosavi, A., Shafii, M. B., & Kowsary, F. (2018). Simulation of a falling droplet in a vertical channel with rectangular obstacles. *European Journal of Mechanics - B/Fluids*, 68, 108-117. <https://doi.org/https://doi.org/10.1016/j.euromechflu.2017.11.002>
- Mishima, K., & Hibiki, T. (1996). Some characteristics of air-water two-phase flow in small diameter vertical tubes. *International Journal of Multiphase Flow*, 22(4), 703-712. [https://doi.org/https://doi.org/10.1016/0301-9322\(96\)00010-9](https://doi.org/https://doi.org/10.1016/0301-9322(96)00010-9)
- Mohiuddin Mala, G., Li, D., & Dale, J. D. (1997). Heat transfer and fluid flow in microchannels. *International Journal of Heat and Mass Transfer*, 40(13), 3079-3088. [https://doi.org/https://doi.org/10.1016/S0017-9310\(96\)00356-0](https://doi.org/https://doi.org/10.1016/S0017-9310(96)00356-0)
- Mokhatab, S., Poe, W. A., & Mak, J. Y. (2015). Chapter 4 - Phase Separation. In *Handbook of Natural Gas Transmission and Processing (Third Edition)* (3rd ed., pp. 137-167). Gulf Professional Publishing. <https://doi.org/https://doi.org/10.1016/B978-0-12-801499-8.00004-3>
- Mullins, B. J., Agranovski, I. E., Braddock, R. D., & Ho, C. M. (2004). Effect of fiber orientation on fiber wetting processes. *Journal of Colloid and Interface Science*, 269(2), 449-458. [https://doi.org/https://doi.org/10.1016/S0021-9797\(03\)00729-X](https://doi.org/https://doi.org/10.1016/S0021-9797(03)00729-X)
- Narayana N. Pillai, C. R. R., & Ramakrishnan, C. R. (2006). *Principles Of Fluid Mechanics And Fluid Machines (second Edition)*. Universities Press (India) Pvt. Limited. <https://books.google.com.au/books?id=ih402g7bNXYC>

- Ohadi, M., Choo, K., Dessiatoun, S., & Cetegen, E. (2013). *Next generation microchannel heat exchangers*. Springer.
- Ojaghloou, N., Tafreshi, H. V., Bratko, D., & Luzar, A. (2018). Dynamical insights into the mechanism of a droplet detachment from a fiber [10.1039/C8SM01257A]. *Soft Matter*, 14(44), 8924-8934. <https://doi.org/10.1039/C8SM01257A>
- Park, S., Jung, I., Lee, Y., Kshetrimayum, K. S., Na, J., Park, S., Shin, S., Ha, D., Lee, Y., Chung, J., Lee, C.-J., & Han, C. (2016). Design of microchannel Fischer–Tropsch reactor using cell-coupling method: Effect of flow configurations and distribution. *Chemical Engineering Science*, 143, 63-75. <https://doi.org/https://doi.org/10.1016/j.ces.2015.12.012>
- Perez, C. E. S. (2012). *Decision Making Methodology for the Selection of Gas-liquid Separators* (Publication Number EPT-M-2012-106) Norwegian University of Science and Technology]. Trondheim.
- Pham, H. H., Lim, Y.-I., Han, S., Lim, B., & Ko, H.-S. (2018). Hydrodynamics and design of gas distributor in large-scale amine absorbers using computational fluid dynamics [journal article]. *Korean Journal of Chemical Engineering*, 35(5), 1073-1082. <https://doi.org/10.1007/s11814-018-0006-z>
- Pigford, R. L., Ashraf, M., & Miron, Y. D. (1983). Flow distribution in piping manifolds. *Industrial & Engineering Chemistry Fundamentals*, 22(4), 463-471. <https://doi.org/10.1021/i100012a019>
- Piroird, K., Clanet, C., Lorenceau, É., & Quéré, D. (2009). Drops impacting inclined fibers. *Journal of Colloid and Interface Science*, 334(1), 70-74. <https://doi.org/https://doi.org/10.1016/j.jcis.2009.03.004>
- Prakash, B., Parmar, H., Shah, M. T., Pareek, V. K., Anthony, L., & Utikar, R. P. (2019). Simultaneous measurements of two phases using an optical probe. *Experimental and Computational Multiphase Flow*, 1(4), 233-241. <https://doi.org/10.1007/s42757-019-0025-y>
- Prakash, B., Shah, M. T., Pareek, V. K., & Utikar, R. P. (2018). Impact of HSPBT blade angle on gas phase hydrodynamics in a gas–liquid stirred tank. *Chemical Engineering Research and Design*, 130, 219-229. <https://doi.org/https://doi.org/10.1016/j.cherd.2017.12.028>
- Priyambodo, M. D. M., Mazur, M., Patel, J., Shah, M., Sun, B., Pareek, V., Brandt, M., Webley, P. A., & Bhatelia, T. (2022). Numerical evaluation of an additively manufactured uniform fractal flow mixer. *Chemical Engineering and Processing - Process Intensification*, 179, 109047. <https://doi.org/https://doi.org/10.1016/j.cep.2022.109047>
- Rahimi, R., & Abbaspour, D. (2008). Determination of pressure drop in wire mesh mist eliminator by CFD. *Chemical Engineering and Processing: Process Intensification*, 47(9), 1504-1508. <https://doi.org/https://doi.org/10.1016/j.cep.2007.06.016>
- Rein, M. (1993). Phenomena of liquid drop impact on solid and liquid surfaces. *Fluid Dynamics Research*, 12(2), 61-93. [https://doi.org/https://doi.org/10.1016/0169-5983\(93\)90106-K](https://doi.org/https://doi.org/10.1016/0169-5983(93)90106-K)
- Safavi, M., & Nourazar, S. S. (2019). Experimental, analytical, and numerical study of droplet impact on a horizontal fiber. *International Journal of Multiphase Flow*, 113, 316-324. <https://doi.org/https://doi.org/10.1016/j.ijmultiphaseflow.2018.10.018>
- Safavi, M., & Nourazar, S. S. (2021). Droplet capture with a wetted fiber. *Theoretical and Computational Fluid Dynamics*, 35(3), 331-343. <https://doi.org/10.1007/s00162-021-00561-3>
- Sahu, R. P., Sinha-Ray, S., Yarin, A. L., & Pourdeyhimi, B. (2013). Blowing drops off a filament [10.1039/C3SM50618E]. *Soft Matter*, 9(26), 6053-6071. <https://doi.org/10.1039/C3SM50618E>
- Shen, P. (1992). The effect of friction on flow distribution in dividing and combining flow manifolds.
- Sher, E., Haim, L. F., & Sher, I. (2013). Off-centered impact of water droplets on a thin horizontal wire. *International Journal of Multiphase Flow*, 54, 55-60. <https://doi.org/https://doi.org/10.1016/j.ijmultiphaseflow.2013.03.002>
- Sinnott, R., & Towler, G. (2019a). *Chemical Engineering Design* (6th Edition). In: Elsevier.
- Sinnott, R., & Towler, G. (2019b). *Chemical engineering design: SI Edition*. Butterworth-Heinemann.
- Sivanandam, S., & Deepa, S. (2008). Genetic algorithms. In *Introduction to genetic algorithms* (pp. 15-37). Springer.

- Stalder, A. F., Kulik, G., Sage, D., Barbieri, L., & Hoffmann, P. (2006). A snake-based approach to accurate determination of both contact points and contact angles. *Colloids and Surfaces A: Physicochemical and Engineering Aspects*, 286(1), 92-103. <https://doi.org/https://doi.org/10.1016/j.colsurfa.2006.03.008>
- Stewart, M., & Arnold, K. (2008). Chapter 3 - Two-Phase Gas-Liquid Separators. In *Gas-Liquid And Liquid-Liquid Separators* (pp. 65-130). Gulf Professional Publishing. <https://doi.org/https://doi.org/10.1016/B978-0-7506-8979-3.00003-9>
- Sulzer. (2022). Gas/Liquid Separation Technology. In Sulzer (Ed.): Sulzer.
- Sulzer. (2023a). KnitMesh™ wire mesh mist eliminators. In ct_122_knitmesh_1920x1280 (Ed.): Sulzer.
- Sulzer. (2023b). Shell Schoepentoeter™. In ct_129_2_inlet_device_installed_column_1920x1280 (Ed.), (Vol. 1920x1280, pp. Shell Schoepentoeter™): Sulzer.
- Sun, H., Bu, S., & Luan, Y. (2015). A high-precision method for calculating the pressure drop across wire mesh filters. *Chemical Engineering Science*, 127, 143-150. <https://doi.org/https://doi.org/10.1016/j.ces.2015.01.023>
- Svrcek, W., & Monnery, W. (1993). Design two-phase separators within the right limits. *Chemical Engineering Progress*, 89(10), 53-60.
- Swanborn, R. A. (1988). *A new approach to the design of gas-liquid separators for the oil industry* <http://resolver.tudelft.nl/uuid:aa5fc516-6b58-4900-90d8-e15a6f332c84>
- Tiwari, A., Maheshwari, A., Rajesh, V. M., & Singh, K. B. (2019). Experimental characterization of gas-liquid flows in splitting distributor for parallel micro-channels. *Chemical Engineering Journal*, 377, 120602. <https://doi.org/https://doi.org/10.1016/j.cej.2018.12.062>
- Tomor, A., & Kristóf, G. (2016). Validation of a Discrete Model for Flow Distribution in Dividing-Flow Manifolds: Numerical and Experimental Studies. *Periodica Polytechnica Mechanical Engineering*, 60, 41-49. <https://doi.org/10.3311/PPme.8518>
- Triplett, K. A., Ghiaasiaan, S. M., Abdel-Khalik, S. I., & Sadowski, D. L. (1999). Gas-liquid two-phase flow in microchannels Part I: two-phase flow patterns. *International Journal of Multiphase Flow*, 25(3), 377-394. [https://doi.org/https://doi.org/10.1016/S0301-9322\(98\)00054-8](https://doi.org/https://doi.org/10.1016/S0301-9322(98)00054-8)
- VanGilder, J. W., & Schmidt, R. R. (2005). Airflow uniformity through perforated tiles in a raised-floor data center. International Electronic Packaging Technical Conference and Exhibition,
- Wang, C., Wu, X., Zhang, H., Hao, P., He, F., & Zhang, X. (2021). A many-body dissipative particle dynamics study of eccentric droplets impacting inclined fiber. *Physics of Fluids*, 33(4), 042001. <https://doi.org/10.1063/5.0044065>
- Wang, J. (2008). Pressure drop and flow distribution in parallel-channel configurations of fuel cells: U-type arrangement. *International Journal of Hydrogen Energy*, 33(21), 6339-6350. <https://doi.org/https://doi.org/10.1016/j.ijhydene.2008.08.020>
- Wang, J., Gao, Z., Gan, G., & Wu, D. (2001). Analytical solution of flow coefficients for a uniformly distributed porous channel. *Chemical Engineering Journal*, 84(1), 1-6. [https://doi.org/https://doi.org/10.1016/S1385-8947\(00\)00263-1](https://doi.org/https://doi.org/10.1016/S1385-8947(00)00263-1)
- Wang, L., Kong, X., & Qi, Y. (2016). Optimal design for split-and-recombine-type flow distributors of microreactors based on blockage detection. *Chinese Journal of Chemical Engineering*, 24(7), 897-903. <https://doi.org/https://doi.org/10.1016/j.cjche.2016.04.021>
- Wang, S., & Desjardins, O. (2018). Numerical study of the critical drop size on a thin horizontal fiber: Effect of fiber shape and contact angle. *Chemical Engineering Science*, 187, 127-133. <https://doi.org/https://doi.org/10.1016/j.ces.2018.04.040>
- Wechsato, W., Lorente, S., & Bejan, A. (2002). Optimal tree-shaped networks for fluid flow in a disc-shaped body. *International Journal of Heat and Mass Transfer*, 45(25), 4911-4924. [https://doi.org/https://doi.org/10.1016/S0017-9310\(02\)00211-9](https://doi.org/https://doi.org/10.1016/S0017-9310(02)00211-9)
- Wen, J., Li, Y., Zhou, A., & Zhang, K. (2006). An experimental and numerical investigation of flow patterns in the entrance of plate-fin heat exchanger. *International Journal of Heat and Mass Transfer*, 49(9), 1667-1678. <https://doi.org/https://doi.org/10.1016/j.ijheatmasstransfer.2005.10.029>

- Weyer, F., Duchesne, A., & Vandewalle, N. (2017). Switching behavior of droplets crossing nodes on a fiber network. *Scientific Reports*, 7(1), 13309. <https://doi.org/10.1038/s41598-017-13009-8>
- Wichangarm, M., Matthujak, A., Sriveerakul, T., Sucharitpwatskul, S., & Phongthanapanich, S. (2020). Investigation on thermal efficiency of LPG cooking burner using computational fluid dynamics. *Energy*, 203, 117849. <https://doi.org/https://doi.org/10.1016/j.energy.2020.117849>
- Yue, J., Chen, G., Yuan, Q., Luo, L., & Gonthier, Y. (2007). Hydrodynamics and mass transfer characteristics in gas–liquid flow through a rectangular microchannel. *Chemical Engineering Science*, 62(7), 2096-2108. <https://doi.org/https://doi.org/10.1016/j.ces.2006.12.057>
- Yue, J., Luo, L., Gonthier, Y., Chen, G., & Yuan, Q. (2008). An experimental investigation of gas–liquid two-phase flow in single microchannel contactors. *Chemical Engineering Science*, 63(16), 4189-4202. <https://doi.org/https://doi.org/10.1016/j.ces.2008.05.032>
- Zhang, S., Lu, Y., Gu, Y., Zhang, X., Sun, J., & Tang, Z. (2018). The process intensification of CO₂ absorption in honeycomb fractal reactor fabricated by 3D printer. *Chemical Engineering and Processing - Process Intensification*, 132, 42-47. <https://doi.org/https://doi.org/10.1016/j.cep.2018.08.013>
- Zhang, Y., Zhang, J., Tang, Z., & Wu, Q. (2021). Gas–Liquid Taylor Flow Characteristics in a Fractal Microchannel Network during Numbering-up and Sizing-up. *Industrial & Engineering Chemistry Research*, 60(21), 7935-7949. <https://doi.org/10.1021/acs.iecr.1c00448>
- Zhao, L., Li, J., Battaglia, F., & He, Z. (2016). Computational investigation of the flow field contribution to improve electricity generation in granular activated carbon-assisted microbial fuel cells. *Journal of Power Sources*, 333, 83-87. <https://doi.org/https://doi.org/10.1016/j.jpowsour.2016.09.113>
- Zheng, J., Wang, J., Yu, Y., & Chen, T. (2018). Hydrodynamics of Droplet Impingement on a Thin Horizontal Wire. *Mathematical Problems in Engineering*, 2018, 9818494. <https://doi.org/10.1155/2018/9818494>
- Zhu, P., Wang, W., Chen, X., Lin, F., Wei, X., Ji, C., & Zou, J. (2019). Experimental study of drop impact on a thin fiber. *Physics of Fluids*, 31(10), 107102. <https://doi.org/10.1063/1.5116845>

Appendices

APPENDIX A: Experiment Study on Additively Manufactured Mesh Pads

Setup

The vapour liquid separator experiment was used to investigate the separation performance of additively manufactured mesh pads by measuring the wet and dry pressure drop. The experiment rig, shown in Figure AB1, consists of two feed inlets of water and air, a cylindrical column, an air compressor, an air inlet distributor, a water pump, a hydraulic atomising nozzle, needle valves (water and air), flowmeters (water and air), a weight scale, and the additively manufactured mesh pads.

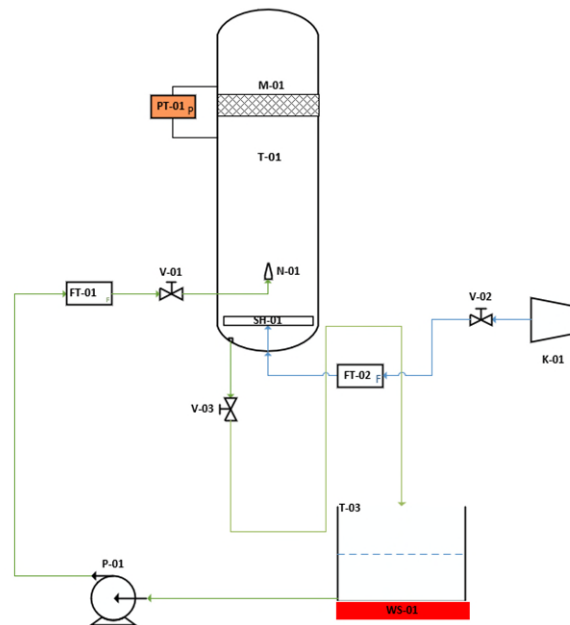


Figure AB1: P&ID of vapour-liquid separator experiment rig

The cylindrical column had a diameter of 200 mm and a height of 1000 mm. The inlet compressed air was regulated using a needle valve and a flowmeter before passing through the inlet distributor. The inlet distributor was installed at the bottom of the cylindrical column to promote equal flow distribution. The inlet water feed was provided through a closed-loop system from a water tank. The purpose of using a closed loop water system was to measure the separation efficiency by measuring weight loss in water tank after a certain period of time. The water inlet feed was regulated using a needle valve and a flowmeter before passing through the spray nozzle. The spray nozzle has a full circle pattern and was installed 50 mm above the air inlet distributor and 200 mm below the mesh pads to ensure that the entire

surface of the mesh pad was covered. For the additively manufactured mesh pads, as shown in Figure AB2, each mesh pad has a diameter of 200 mm and a height of 13.2 mm. These mesh pads have a laves lattice structure design and were additively manufactured using the filament deposit method (FDM) with a wire thickness of 20 mm. Multiple configurations of mesh pads were tested, from 2 to 8 mesh pads, corresponding to 26.2 mm to 105.6 mm in height. The mesh pads were placed at a height of 400 mm from the bottom of the cylindrical column. The pressure drop before and after passing through the mesh pads was measured using a manometer.



Figure AB2: P&ID of vapour-liquid separator experiment rig

Results and Discussion

The measured dry pressure drop at different heights of the mesh pad is shown in AB3. The increase in the height of the mesh pad resulted in the increase of pressure drop. The effect of the mesh pad height was less significant at a lower inlet flowrate (i.e. 100 l/min) where difference of pressure drop was minimal, with the difference between $h = 26.4$ mm and $h = 105.6$ mm was 1.63 Pa. At a higher flowrate (i.e. 1000 l/min), the difference of pressure drop was higher, the difference between $h = 26.4$ mm and $h = 105.6$ mm was 43.48 Pa.

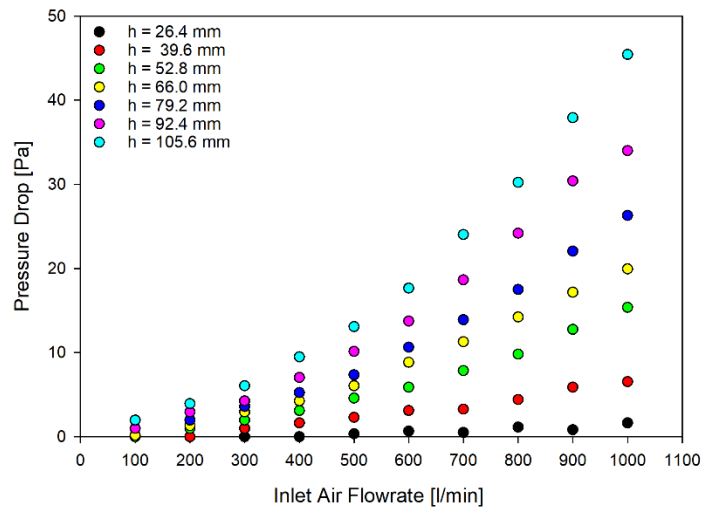


Figure AB3: Measured dry pressure drop at different height of the mesh pad

APPENDIX B: Copyrights

12/08/2023, 00:13

Rightslink® by Copyright Clearance Center

Home Help Live Chat Sign in Create Account

Analytical Model for Droplet Capture on a Thin Wire

Author:
Muhammad Dary Mahadika Priyambodo, Milinkumar T. Shah, Tejas Bhatelia, et al

Publication: Industrial & Engineering Chemistry Research

Publisher: American Chemical Society

Date: Dec 1, 2022

Copyright © 2022, American Chemical Society

PERMISSION/LICENSE IS GRANTED FOR YOUR ORDER AT NO CHARGE

This type of permission/license, instead of the standard Terms and Conditions, is sent to you because no fee is being charged for your order. Please note the following:

- Permission is granted for your request in both print and electronic formats, and translations.
- If figures and/or tables were requested, they may be adapted or used in part.
- Please print this page for your records and send a copy of it to your publisher/graduate school.
- Appropriate credit for the requested material should be given as follows: "Reprinted (adapted) with permission from {COMPLETE REFERENCE CITATION}. Copyright {YEAR} American Chemical Society." Insert appropriate information in place of the capitalized words.
- One-time permission is granted only for the use specified in your RightsLink request. No additional uses are granted (such as derivative works or other editions). For any uses, please submit a new request.

If credit is given to another source for the material you requested from RightsLink, permission must be obtained from that source.

[BACK](#) [CLOSE WINDOW](#)

© 2023 Copyright - All Rights Reserved | [Copyright Clearance Center, Inc.](#) | [Privacy statement](#) | [Data Security and Privacy](#)
| [For California Residents](#) | [Terms and Conditions](#) Comments? We would like to hear from you. E-mail us at customer-care@copyright.com

The content of *Chapter 2: Hydrodynamics of Droplet Capture on Thin Wires*, is reprinted (adapted) with permission and modified from this journal article.



Home



Help ▾



Live Chat



Sign in



Create Account



Numerical evaluation of an additively manufactured uniform fractal flow mixer

Author:

Muhammad Dary M. Priyambodo, Maciej Mazur, Jim Patel, Milinkumar Shah, Biao Sun, Vishnu Pareek, Milan Brandt, Paul A. Webley, Tejas Bhatelia

Publication: Chemical Engineering and Processing: Process Intensification**Publisher:** Elsevier**Date:** September 2022

© 2022 Elsevier B.V. All rights reserved.

Journal Author Rights

Please note that, as the author of this Elsevier article, you retain the right to include it in a thesis or dissertation, provided it is not published commercially. Permission is not required, but please ensure that you reference the journal as the original source. For more information on this and on your other retained rights, please visit: <https://www.elsevier.com/about/our-business/policies/copyright#Author-rights>

BACK

CLOSE WINDOW

The content of *Chapter 3: Gas-gas Hydrodynamics of a Fractal Flow Mixer*, is reprinted (adapted) with permission and modified from this journal article.



RightsLink



Gas-liquid hydrodynamics of a fractal flow mixer

Author:

Muhammad Dary M. Priyambodo, Tejas Bhatelia, Milinkumar Shah, Jim Patel, Maciej Mazur, Vishnu Pareek

Publication: Chemical Engineering and Processing: Process Intensification

Publisher: Elsevier

Date: November 2023

© 2023 The Authors. Published by Elsevier B.V.

Creative Commons

This is an open access article distributed under the terms of the [Creative Commons CC-BY](#) license, which permits unrestricted use, distribution, and reproduction in any medium, provided the original work is properly cited.

You are not required to obtain permission to reuse this article.

To request permission for a type of use not listed, please contact [Elsevier](#) Global Rights Department.

Are you the [author](#) of this Elsevier journal article?

© 2024 Copyright - All Rights Reserved | [Copyright Clearance Center, Inc.](#) | [Privacy statement](#) | [Data Security and Privacy](#)
| [For California Residents](#) | [Terms and Conditions](#) Comments? We would like to hear from you, E-mail us at customer@copyright.com

The content of *Chapter 4: Gas-liquid Hydrodynamics of a Fractal Flow Mixer*, is reprinted (adapted) with permission and modified from this journal article.

APPENDIX C: Attribution of Authorship Statement

The content of Chapter 2: Hydrodynamics of Droplet Capture on Thin Wires is reprinted (adapted) with permission and modified from the following publication:

“Analytical Model for Droplet Capture on a Thin Wire”

Industrial & Engineering Chemistry Research, 2022, 61, 18914-18927

Muhammad Dary Mahadika Priyambodo^a, Milinkumar T. Shah^{a*}, Tejas Bhatelia^{a*}, Biao Sun^a, and Vishnu Pareek^a

^aWA School of Mines, Minerals Energy and Chemical Engineering, Curtin University, Bentley, WA 6102, Australia

Conception and Design	Manuscript Preparation	Acquisition of Data and Method	Analysis and Statistical Method	Interpretation and Discussion	Manuscript Review
Co-author 1: Muhammad Dary Mahadika Priyambodo (First Author)					
✓	✓	✓	✓	✓	✓
I acknowledge that these represent my contributions to the above research output.					
Signature:					

Conception and Design	Manuscript Preparation	Acquisition of Data and Method	Analysis and Statistical Method	Interpretation and Discussion	Manuscript Review
Co-author 2: Milinkumar T. Shah (Corresponding Author)					
✓	✓		✓	✓	✓
I acknowledge that these represent my contributions to the above research output.					
Signature:					

The content of Chapter 2: Hydrodynamics of Droplet Capture on Thin Wires is reprinted (adapted) with permission and modified from the following publication:

“Analytical Model for Droplet Capture on a Thin Wire”

Industrial & Engineering Chemistry Research, 2022, 61, 18914-18927

Muhammad Dary Mahadika Priyambodo^a, Milinkumar T. Shah^{a*}, Tejas Bhatelia^{a*}, Biao Sun^a, and Vishnu Pareek^a

^aWA School of Mines, Minerals Energy and Chemical Engineering, Curtin University, Bentley, WA 6102, Australia

Conception and Design	Manuscript Preparation	Acquisition of Data and Method	Analysis and Statistical Method	Interpretation and Discussion	Manuscript Review
Co-author 3: Tejas Bhatelia (Corresponding Author)					
✓	✓		✓	✓	✓
I acknowledge that these represent my contributions to the above research output.					
Signature:					

Conception and Design	Manuscript Preparation	Acquisition of Data and Method	Analysis and Statistical Method	Interpretation and Discussion	Manuscript Review
Co-author 4: Biao Sun					
				✓	✓
I acknowledge that these represent my contributions to the above research output.					
Signature:					

The content of Chapter 2: Hydrodynamics of Droplet Capture on Thin Wires is reprinted (adapted) with permission and modified from the following publication:

“Analytical Model for Droplet Capture on a Thin Wire”

Industrial & Engineering Chemistry Research, 2022, 61, 18914-18927

Muhammad Dary Mahadika Priyambodo^a, Milinkumar T. Shah^{a*}, Tejas Bhatelia^{a*}, Biao Sun^a, and Vishnu Pareek^a

^aWA School of Mines, Minerals Energy and Chemical Engineering, Curtin University, Bentley, WA 6102, Australia

Conception and Design	Manuscript Preparation	Acquisition of Data and Method	Analysis and Statistical Method	Interpretation and Discussion	Manuscript Review
Co-author 5: Vishnu Pareek					
✓					✓
I acknowledge that these represent my contributions to the above research output.					
Signature:					

The content of Chapter 3: Gas-gas Hydrodynamics of a Fractal Flow Mixer is reprinted (adapted) with permission and modified from the following publication:

“Numerical evaluation of an additively manufactured uniform fractal flow mixer”

Chemical Engineering and Processing – Process Intensification, 2022, 179, 109047

Muhammad Dary M. Priyambodo^a, Maciej Mazur^b, Jim Patel^c, Milinkumar Shah^a, Biao Sun^a, Vishnu Pareek^a, Milan Brandt^b, Paul A. Webley^d, and Tejas Bhatelia^{a*},

^aWA School of Mines, Minerals Energy and Chemical Engineering, Curtin University, Bentley, WA 6102, Australia

^bRMIT Centre for Additive Manufacturing, School of Engineering, RMIT University, Melbourne, Australia

^cCSIRO Energy, 71 Normanby Road, Clayton North, Victoria 3189, Australia

^dDepartment of Chemical and Biological Engineering, Monash University, Victoria 3800, Australia

Conception and Design	Manuscript Preparation	Acquisition of Data and Method	Analysis and Statistical Method	Interpretation and Discussion	Manuscript Review
Co-author 1: Muhammad Dary Mahadika Priyambodo (First Author)					
✓	✓	✓	✓	✓	✓
I acknowledge that these represent my contributions to the above research output.					
Signature:					

Conception and Design	Manuscript Preparation	Acquisition of Data and Method	Analysis and Statistical Method	Interpretation and Discussion	Manuscript Review
Co-author 2: Maciej Mazur					
✓	✓	✓		✓	✓
I acknowledge that these represent my contributions to the above research output.					
Signature:					

The content of Chapter 3: Gas-gas Hydrodynamics of a Fractal Flow Mixer is reprinted (adapted) with permission and modified from the following publication:

“Numerical evaluation of an additively manufactured uniform fractal flow mixer”

Chemical Engineering and Processing – Process Intensification, 2022, 179, 109047

Muhammad Dary M. Priyambodo^a, Maciej Mazur^b, Jim Patel^c, Milinkumar Shah^a, Biao Sun^a, Vishnu Pareek^a, Milan Brandt^b, Paul A. Webley^d, and Tejas Bhatelia^{a*},

^aWA School of Mines, Minerals Energy and Chemical Engineering, Curtin University, Bentley, WA 6102, Australia

^bRMIT Centre for Additive Manufacturing, School of Engineering, RMIT University, Melbourne, Australia

^cCSIRO Energy, 71 Normanby Road, Clayton North, Victoria 3189, Australia

^dDepartment of Chemical and Biological Engineering, Monash University, Victoria 3800, Australia

Conception and Design	Manuscript Preparation	Acquisition of Data and Method	Analysis and Statistical Method	Interpretation and Discussion	Manuscript Review
Co-author 3: Jim Patel					
✓			✓		✓
I acknowledge that these represent my contributions to the above research output.					
Signature:					

Conception and Design	Manuscript Preparation	Acquisition of Data and Method	Analysis and Statistical Method	Interpretation and Discussion	Manuscript Review
Co-author 4: Milinkumar T. Shah					
	✓		✓		✓
I acknowledge that these represent my contributions to the above research output.					
Signature:					

The content of Chapter 3: Gas-gas Hydrodynamics of a Fractal Flow Mixer is reprinted (adapted) with permission and modified from the following publication:

“Numerical evaluation of an additively manufactured uniform fractal flow mixer”

Chemical Engineering and Processing – Process Intensification, 2022, 179, 109047

Muhammad Dary M. Priyambodo^a, Maciej Mazur^b, Jim Patel^c, Milinkumar Shah^a, Biao Sun^a, Vishnu Pareek^a, Milan Brandt^b, Paul A. Webley^d, and Tejas Bhatelia^{a*},

^aWA School of Mines, Minerals Energy and Chemical Engineering, Curtin University, Bentley, WA 6102, Australia

^bRMIT Centre for Additive Manufacturing, School of Engineering, RMIT University, Melbourne, Australia

^cCSIRO Energy, 71 Normanby Road, Clayton North, Victoria 3189, Australia

^dDepartment of Chemical and Biological Engineering, Monash University, Victoria 3800, Australia

Conception and Design	Manuscript Preparation	Acquisition of Data and Method	Analysis and Statistical Method	Interpretation and Discussion	Manuscript Review
Co-author 5: Biao Sun					
		✓			✓
I acknowledge that these represent my contributions to the above research output.					
Signature:					

Conception and Design	Manuscript Preparation	Acquisition of Data and Method	Analysis and Statistical Method	Interpretation and Discussion	Manuscript Review
Co-author 6: Vishnu Pareek					
✓					✓
I acknowledge that these represent my contributions to the above research output.					
Signature:					

The content of Chapter 3: Gas-gas Hydrodynamics of a Fractal Flow Mixer is reprinted (adapted) with permission and modified from the following publication:

“Numerical evaluation of an additively manufactured uniform fractal flow mixer”

Chemical Engineering and Processing – Process Intensification, 2022, 179, 109047

Muhammad Dary M. Priyambodo^a, Maciej Mazur^b, Jim Patel^c, Milinkumar Shah^a, Biao Sun^a, Vishnu Pareek^a, Milan Brandt^b, Paul A. Webley^d, and Tejas Bhatelia^{a*},

^aWA School of Mines, Minerals Energy and Chemical Engineering, Curtin University, Bentley, WA 6102, Australia

^bRMIT Centre for Additive Manufacturing, School of Engineering, RMIT University, Melbourne, Australia

^cCSIRO Energy, 71 Normanby Road, Clayton North, Victoria 3189, Australia

^dDepartment of Chemical and Biological Engineering, Monash University, Victoria 3800, Australia

Conception and Design	Manuscript Preparation	Acquisition of Data and Method	Analysis and Statistical Method	Interpretation and Discussion	Manuscript Review
Co-author 7: Milan Brandt					
✓					✓
I acknowledge that these represent my contributions to the above research output.					
Signature:					

Conception and Design	Manuscript Preparation	Acquisition of Data and Method	Analysis and Statistical Method	Interpretation and Discussion	Manuscript Review
Co-author 8: Paul A. Webley					
✓					✓
I acknowledge that these represent my contributions to the above research output.					
Signature:					

The content of Chapter 3: Gas-gas Hydrodynamics of a Fractal Flow Mixer is reprinted (adapted) with permission and modified from the following publication:

“Numerical evaluation of an additively manufactured uniform fractal flow mixer”

Chemical Engineering and Processing – Process Intensification, 2022, 179, 109047

Muhammad Dary M. Priyambodo^a, Maciej Mazur^b, Jim Patel^c, Milinkumar Shah^a, Biao Sun^a, Vishnu Pareek^a, Milan Brandt^b, Paul A. Webley^d, and Tejas Bhatelia^{a*},

^aWA School of Mines, Minerals Energy and Chemical Engineering, Curtin University, Bentley, WA 6102, Australia

^bRMIT Centre for Additive Manufacturing, School of Engineering, RMIT University, Melbourne, Australia

^cCSIRO Energy, 71 Normanby Road, Clayton North, Victoria 3189, Australia

^dDepartment of Chemical and Biological Engineering, Monash University, Victoria 3800, Australia

Conception and Design	Manuscript Preparation	Acquisition of Data and Method	Analysis and Statistical Method	Interpretation and Discussion	Manuscript Review
Co-author 9: Tejas Bhatelia (Corresponding Author)					
✓			✓	✓	✓
I acknowledge that these represent my contributions to the above research output.					
Signature:					

The content of Chapter 4: Gas-liquid Hydrodynamics of a Fractal Flow Mixer is reprinted (adapted) with permission and modified from the following publication:

“Gas-liquid Hydrodynamics of a fractal flow mixer”

Chemical Engineering and Processing – Process Intensification, 2023, 193, 109558

Muhammad Dary M. Priyambodo^a, Tejas Bhatelia^{a*}, Milinkumar Shah^a, Jim Patel^b, Maciej Mazur^c, and Vishnu Pareek^a

^aWA School of Mines, Minerals Energy and Chemical Engineering, Curtin University, Bentley, WA 6102, Australia

^bCSIRO Energy, 71 Normanby Road, Clayton North, Victoria 3189, Australia

^cRMIT Centre for Additive Manufacturing, School of Engineering, RMIT University, Melbourne, Australia

Conception and Design	Manuscript Preparation	Acquisition of Data and Method	Analysis and Statistical Method	Interpretation and Discussion	Manuscript Review
Co-author 1: Muhammad Dary Mahadika Priyambodo (First Author)					
✓	✓	✓	✓	✓	✓
I acknowledge that these represent my contributions to the above research output.					
Signature:					

Conception and Design	Manuscript Preparation	Acquisition of Data and Method	Analysis and Statistical Method	Interpretation and Discussion	Manuscript Review
Co-author 2: Tejas Bhatelia (Corresponding Author)					
✓			✓	✓	✓
I acknowledge that these represent my contributions to the above research output.					
Signature:					

The content of Chapter 4: Gas-liquid Hydrodynamics of a Fractal Flow Mixer is reprinted (adapted) with permission and modified from the following publication:

“Gas-liquid Hydrodynamics of a fractal flow mixer”

Chemical Engineering and Processing – Process Intensification, 2023, 193, 109558

Muhammad Dary M. Priyambodo^a, Tejas Bhatelia^{a*}, Milinkumar Shah^a, Jim Patel^b, Maciej Mazur^c, and Vishnu Pareek^a

^aWA School of Mines, Minerals Energy and Chemical Engineering, Curtin University, Bentley, WA 6102, Australia

^bCSIRO Energy, 71 Normanby Road, Clayton North, Victoria 3189, Australia

^cRMIT Centre for Additive Manufacturing, School of Engineering, RMIT University, Melbourne, Australia

Conception and Design	Manuscript Preparation	Acquisition of Data and Method	Analysis and Statistical Method	Interpretation and Discussion	Manuscript Review
Co-author 3: Milinkumar Shah					
✓			✓	✓	✓
I acknowledge that these represent my contributions to the above research output.					
Signature:					

Conception and Design	Manuscript Preparation	Acquisition of Data and Method	Analysis and Statistical Method	Interpretation and Discussion	Manuscript Review
Co-author 4: Jim Patel					
✓					✓
I acknowledge that these represent my contributions to the above research output.					
Signature:					

The content of Chapter 4: Gas-liquid Hydrodynamics of a Fractal Flow Mixer is reprinted (adapted) with permission and modified from the following publication:

“Gas-liquid Hydrodynamics of a fractal flow mixer”

Chemical Engineering and Processing – Process Intensification, 2023, 193, 109558

Muhammad Dary M. Priyambodo^a, Tejas Bhatelia^{a*}, Milinkumar Shah^a, Jim Patel^b, Maciej Mazur^c, and Vishnu Pareek^a

^aWA School of Mines, Minerals Energy and Chemical Engineering, Curtin University, Bentley, WA 6102, Australia

^bCSIRO Energy, 71 Normanby Road, Clayton North, Victoria 3189, Australia

^cRMIT Centre for Additive Manufacturing, School of Engineering, RMIT University, Melbourne, Australia

Conception and Design	Manuscript Preparation	Acquisition of Data and Method	Analysis and Statistical Method	Interpretation and Discussion	Manuscript Review
Co-author 5: Maciej Mazur					
✓					✓
I acknowledge that these represent my contributions to the above research output.					
Signature:					

Conception and Design	Manuscript Preparation	Acquisition of Data and Method	Analysis and Statistical Method	Interpretation and Discussion	Manuscript Review
Co-author 6: Vishnu Pareek					
✓					✓
I acknowledge that these represent my contributions to the above research output.					
Signature:					